



UNIVERSITÀ DEGLI STUDI DI MILANO

DOTTORATO DI RICERCA IN SCIENZE DELLA TERRA

*Ciclo XXXIV*

DIPARTIMENTO DI SCIENZE DELLA TERRA

---



Mesozoic episodes of C-cycle and climate perturbations: geochemical signatures of the oceanic ecosystem dynamics across the Toarcian Oceanic Anoxic Event and the Valanginian Weissert Event

GEO/02

Liyenne Cavalheiro

Prof.ssa Elisabetta Erba

Co-supervisor: Prof. Thomas Wagner

COORDINATORE DEL DOTTORATO

Prof. Fernando Camara Artigas

## Abstract

This Ph.D. research project investigated two paleo-environmental dynamics under extreme Mesozoic carbon cycle and climate perturbations evidenced by major anomalies in the carbon isotope record ( $\delta^{13}\text{C}$ ) of the Early Jurassic and Early Cretaceous, namely the Toarcian Ocean Anoxic Event (T-OAE) and the Valanginian Weissert Event, respectively. The material selected for the study of the T-OAE is from two new cores (Sogno and Gajum), which represent pelagic deepest records (1000-1500 paleo-water depth) of the Lombardy Basin (Southern Alps, Italy). Both cores record an expanded black shale interval (the Fish Level) of 5 m and 16 m at Sogno and Gajum, respectively, representing the lithostratigraphic expression of the T-OAE *sensu* Jenkyns (1985, 1988). The Fish Level correlates with the early Toarcian negative  $\delta^{13}\text{C}$  anomaly named 'Jenkyns Event'. The Weissert Event was studied in a unique southern polar location, where a 40 m thick Lower Cretaceous black shale section was recovered at Ocean Drilling Program (ODP) Site 692, in the Weddell Sea, nearshore Antarctica. The two case studies were selected in distinct and very different paleo-settings and latitudes, in order to explore how global climate perturbations translate into local paleo-environmental responses in the sedimentary record, documenting potentially different pathways in the bio-geochemical cycles. A detailed characterization of  $\delta^{13}\text{C}$  stratigraphy, calibrated with nannofossil biostratigraphy, was the basis for a univocal identification of the T-OAE (including the Jenkyns Event) and the Valanginian Weissert Event anomalies. Multi-proxy based organic and inorganic geochemical analyses were used to reconstruct OC burial and preservation rates, the nature and sources of organic matter, carbonate chemistry, the evolution of paleo-temperatures, the paleo-depositional environment and redox conditions. Both case studies confirm that local sedimentary records of strongly restricted and/or deep marine basins register the  $\delta^{13}\text{C}$  signals of global perturbations and associated environmental variables. This has been demonstrated at both locations by reconstructing proxy variations in ocean temperatures, drastic changes in carbonate chemistry and the biologic response, linked to the T-OAE and the Weissert Event. In contrast, both case studies emphasize that basin physiography and local climatic and environmental conditions play a major role in controlling OC rates even across such extreme carbon-cycle perturbations. Notably, the aim of this Ph.D. research was to design and apply an integrated approach combining modelling and multi-proxy data to demonstrate an innovative way forward to decouple uncertainties and limitations of individual proxy results and locations from regional to global scale interpretations. New temperature/ $p\text{CO}_2$  relationships based on multi-proxy data and modelling were reconstructed for the Weissert Event case study. The analytical approach was not identical for the two case studies. Modelling and part of the geochemical analyses were not applied to the T-OAE section due to pandemic restrictions that prevented laboratory work and subsequent elaborations. The outcome suggests that the established strategy for the Weddell Sea case study may now serve as a conceptual framework to advance research on the Italian Jurassic sections, and other OAE examples. This research points out that more emphasis should be made in understanding temperature/ $p\text{CO}_2$  relationships to evaluate processes, rates, and dimensions of climate and environmental change back in time, setting boundaries either for the study of past carbon-cycle/climate perturbations and for projecting future climate and environmental response.

## **Acknowledgments**

Writing these lines, I recall my very first days in the laboratory, the excitement but also concern to check the new results, the continuous state of mind of trying to create ideas and connections in my head that contributed day by day to this final thesis.

I want to express all my gratitude to Elisabetta and Tom, thank you for your dedicated supervision and guidance. You are an example of perseverance and integrity at work. It has been an intellectual, but above all, a personal pleasure to work with you during these five years, from the beginning of my MSc to the end of my Ph.D. I want to especially thank you for having always trusted more than I do in my capabilities and encouraging me to move further and aim to great intents. At Milan and Edinburgh, I could not have asked for better colleagues and great collaborations with Cologne and Bristol Universities, and the GEOMAR.

I feel grateful to have had the chance to travel around Europe thanks to the ERASMUS program, meet people with different cultural and scientific backgrounds, and attend multidisciplinary courses and congresses that enriched my vision and research skills. I would also like to thank my colleagues at the Ph.D., with whom I shared all the joys and plenitude of emotions during this Ph.D. journey.

Thank you to all my loved ones, my dear family, and friends who have always supported me.

## Table of contents

<b>1. Introduction.....</b>	<b>5</b>
1.1 Thesis structure and declaration of authorship .....	5
1.2 State of the Art of Ocean Anoxic Events (OAEs) .....	8
1.3 The Early Jurassic T-OAE versus the Early Cretaceous Weissert Event .....	13
1.4 Materials and objectives of the thesis .....	20
<b>2. Coring the sedimentary expression of the early Toarcian Oceanic Anoxic Event: new stratigraphic records from the Tethys Ocean .....</b>	<b>24</b>
<b>3. Carbon- and oxygen-isotope signature of the Toarcian Oceanic Anoxic event: insights from two Tethyan pelagic sequences (Gajum and Sogno Cores - Lombardy Basin, northern Italy).....</b>	<b>36</b>
<b>4. New organic carbon content and geochemical paleoenvironmental reconstructions from the Toarcian Fish Level (Sogno Core - Lombardy Basin, northern Italy). .....</b>	<b>64</b>
<b>5. Impact of global cooling on Early Cretaceous high <math>p\text{CO}_2</math> world during the Weissert Event.....</b>	<b>83</b>
<b>6. Global and local dynamics on biogeochemical carbon cycling in the Early Cretaceous proto-Weddell Sea (Eastern Antarctica).....</b>	<b>95</b>
<b>7. Bottom water conditions during the Early Cretaceous at ODP Hole 692B -Weddell Sea (Antarctica) - paleoenvironmental changes through the Weissert Event.....</b>	<b>133</b>
<b>8. Discussions and implications .....</b>	<b>148</b>
8.1 The Valanginian (Early Cretaceous) Weissert Event .....	148
8.2 The early Toarcian (Early Jurassic) T-OAE. ....	151
8.3 Implications from this research and future perspectives .....	155
<b>9. References.....</b>	<b>158</b>

# 1. Introduction

## 1.1 Thesis structure and declaration of authorship

The present Ph.D.-thesis consists of 9 chapters.

Chapter 1 is introductory and consists of a) state of the art of the topic; b) the objectives; c) the materials and methods applied in this study.

Chapters 2, 3, 4, 5, 6, and 7 are independent manuscripts that either are published or are under peer-reviewed with international journals, or are in preparation for submission to peer reviewed journals.

Chapter 8 provides the discussion and implications of the main results and conclusions of the six manuscripts included in this thesis (chapters 2 to 7), and also presents the perspectives for future research.

In chapter 9 are listed the references of the introductory and conclusive chapters 1 and 8. References of chapters 2 to 7 are included at the end of each chapter, as reported in the original manuscripts.

All published manuscripts included in this thesis (chapters 2, 3, 5, and 7) were not modified from published versions.

**Chapter 1** is an introduction to this thesis. It is subdivided into four main parts: it presents the general structure of the thesis, the state of the art of Ocean Anoxic Events, and an overview of the Early Jurassic (Toarcian, ~183 Ma) Toarcian Event and the Early Cretaceous (Valanginian, ~133 Ma) Weissert Event based on literature. The other sub-paragraphs summarize the material and methods and aims of the present thesis.

**Chapter 2** is a manuscript published in open access in the international peer-reviewed journal *Scientific Drilling* (Volume 26, 17–27, 2019) by E. Erba, G. Gambacorta, S. Visentin, **L. Cavalheiro**, D. Reolon, G. Faucher, and M. Pegoraro. It presents the first report of the drilling and lithostratigraphy of the Sogno and Gajum Cores in the Lombardy Basin (Southern Alps, Italy). The two cores are new reference sections for the pelagic lower Toarcian interval of the western Tethys, including a relatively expanded black shale unit that represents the sedimentary expression of the Jenkyns Event.

Authorship: my contribution as a co-author of this work consisted in assisting the core-drilling operations (Gajum Core), splitting, archiving, and sampling of the cores.

**Chapter 3** is a manuscript published in the international peer-reviewed journal *Newsletters on Stratigraphy*. The authors are E. Erba, **L. Cavalheiro**, A.J. Dickson, G. Gambacorta, H.C. Jenkyns, and T. Wagner. This article presents an extremely detailed chemostratigraphic framing of the Toarcian Oceanic

Anoxic Event, including a detailed characterization of the Jenkyns Event, based on new C and O-isotope, calcium carbonate, and organic carbon records from the Sogno and Gajum Cores (Southern Alps, Italy).

Authorship: I contributed to this work as a co-author in producing and/or processing carbon- and oxygen-isotope, total organic carbon, calcium carbonate data, and the relative supplementary data files and figures. I also contributed to the writing in collaboration with the other co-authors.

**Chapter 4** is a chapter including preliminary geochemical results from the Sogno core. New sulphur, iron, and biomarkers data, along with organic carbon content and Rock-Eval parameters are presented for the Upper Pliensbachian-Lower Toarcian interval. Results of ongoing analyses will further integrate this chapter.

**Chapter 5** is a manuscript published in open access in *Nature Communications* (Volume 12 (1), 1–11, 2021) by **L. Cavalheiro**, T. Wagner, S. Steinig, C. Bottini, W. Dummann, O. Esegbue, G. Gambacorta, V. Giraldo-Gómez, A. Farnsworth, S. Flögel, P. Hofmann, D. J. Lunt, J. Rethemeyer, S. Torricelli, and E. Erba. The work presents new modelling, biostratigraphy, carbon isotope and sea surface temperature proxy data from Ocean Drilling Program (ODP) Site 692 in the Weddell Sea (Eastern Antarctica), integrated with a literature-based ocean temperatures' compilation. The study reconstructs the atmospheric  $p\text{CO}_2$  and temperature change associated with the Early Cretaceous Weissert Event, exploring the potential build-up of local polar ice.

Authorship: I am the first author of this article and I have conducted all isotopic and molecular geochemical analyses, contributed to the model-data comparison, and led the writing of the study.

**Chapter 6** is a manuscript in preparation for submission to an international peer-reviewed journal. The authors are **L. Cavalheiro**, C. Bottini, W. Dummann, E. Erba, G. Gambacorta, V. Giraldo-Gómez, P. Hofmann, and T. Wagner. This work presents new organic (biomarkers,  $\text{TEX}^{86}$ -based sea surface temperatures, and total organic carbon) and inorganic (calcium carbonate and X-ray fluorescence (XRF) based elements) data from the Berriasian–Barremian interval recovered at ODP Site 692. The work disentangles global and local dynamics related to fluctuations in the biogeochemical carbon cycling, redox conditions, and the composition, provenance and weathering state of Berriasian–Barremian marine sediments from the proto-Weddell Sea (Eastern Antarctica).

Authorship: As the first author of this manuscript, I have conducted all isotopic, molecular and inorganic geochemical analyses, and led the writing of the study.

**Chapter 7** is a manuscript published in open access in the international peer-reviewed journal *Palaeogeography, Palaeoclimatology, Palaeoecology* (Volume 587, 1–02, 2022). The authors are V. M. Giraldo-Gómez, C. Bottini, C. Möller, T. Wagner, O. Esegbue, **L. Cavalheiro**, M. R. Petrizzo, G. Gambacorta, and E. Erba. This work presents new benthic foraminifera, total organic carbon and

carbon isotope data from Ocean Drilling Program (ODP) Site 692. The work characterizes changes of the oxygen and organic-matter fluxes, and their relationships to paleoceanographic changes in the bottom waters of the restricted and early emerging proto-Weddell Basin during the Early Cretaceous.

Authorship: As a co-author of this manuscript, I have conducted isotopic and total organic carbon analyses, and led the elaboration of the geochemical data, relative text, and figures.

**Chapter 8** presents an **overview** and link of the **main discussions and implications** of chapters 2 to 7. Moreover, an outlook for further research is given.

## 1.2 State of the Art of Ocean Anoxic Events (OAEs)

The study of extreme carbon-cycle and climate perturbations that punctuated past greenhouse climates, especially during the Mesozoic, provides key insights into the Earth System functioning. Specifically, times of extreme warm are key to understanding and quantifying stressors of stability conditions that forced the systems to climb over tipping points, thus, entering new scenarios of stability. The critical state of near future oceans is widely debated, and a dramatic decline in the uptake of atmospheric CO<sub>2</sub> is predicted because of surface water warming, enhanced acidification (decreasing pH), increased vertical stratification and slowed thermohaline circulation (Solomon et al., 2009).

Mesozoic Oceanic Anoxic Events (OAEs) represent examples of natural global change associated with climate perturbations, variations in *p*CO<sub>2</sub>, ocean chemistry (including global widespread ocean acidification and anoxia) and biota failure/crises (Jenkyns, 2010). The emergence of present climate change made critically important the understanding of “in and out” from icehouse to greenhouse state – and *vice versa* – which is key for contextualizing ongoing and future evolution of ocean, CO<sub>2</sub>, and climate dynamics.

Geological archives contain information on both the inorganic and organic C-cycles, at various spatial and temporal scales. Multiparametric studies based on sedimentology, micro- and macro-palaeontology, stable C and O isotopes, inorganic and organic geochemistry have allowed the compilation of data-sets for the reconstruction of the ocean response and resilience to global changes as reflected in biomineralized part of marine organisms. Unfortunately, the history of organic C is often hampered by the extreme scarcity of organic matter that can accumulate at the seafloor and be preserved in the sedimentary successions. However, OAEs are usually associated with sediments enriched in organic C thanks to deposition under oxygen-depleted conditions (e.g., Jenkyns, 2010).

The ongoing expansion of analytical techniques applied both to modern oceans and to the marine sedimentary archives (e.g., global climate models (GCMs); Lunt et al., 2020) and geochemical paleothermometers (e.g., O’Brien et al., 2017)) has led to a significant advancement in the study of OAEs and deep time climate change.

The original concept of OAEs (Schlanger and Jenkyns, 1976) defined these time intervals as periods of widespread to globally distributed black shales. This initial definition was based only on lithostratigraphic criteria after the recovery of mid-Cretaceous black shales at sites drilled in the Pacific Ocean. It was applied to two time intervals: i) the Aptian–Albian (OAE1), and ii) the Cenomanian–Turonian (OAE2). Later investigations and the development of chemostratigraphy pointed out that OAEs are associated with negative and/or positive anomalies in the carbon isotope curves ( $\delta^{13}\text{C}$ ) measured on sedimentary carbonate and/or organic matter. Consequently, OAE1 was



subdivided into OAE1a (early Aptian), OAE 1b (earliest Albian), questionable OAE 1c (late Albian) and OAE 1d (latest Albian) (Arthur et al., 1990). Moreover, a Coniacian-Santonian OAE3 was recognised although with a regional significance (Wagreich, 2009, 2012). A recent review by Robinson et al. (2017) contextualises Cretaceous OAEs against OAEs (Fig. 1) underlining the major perturbations of the global carbon cycle (Jenkyns, 2010).

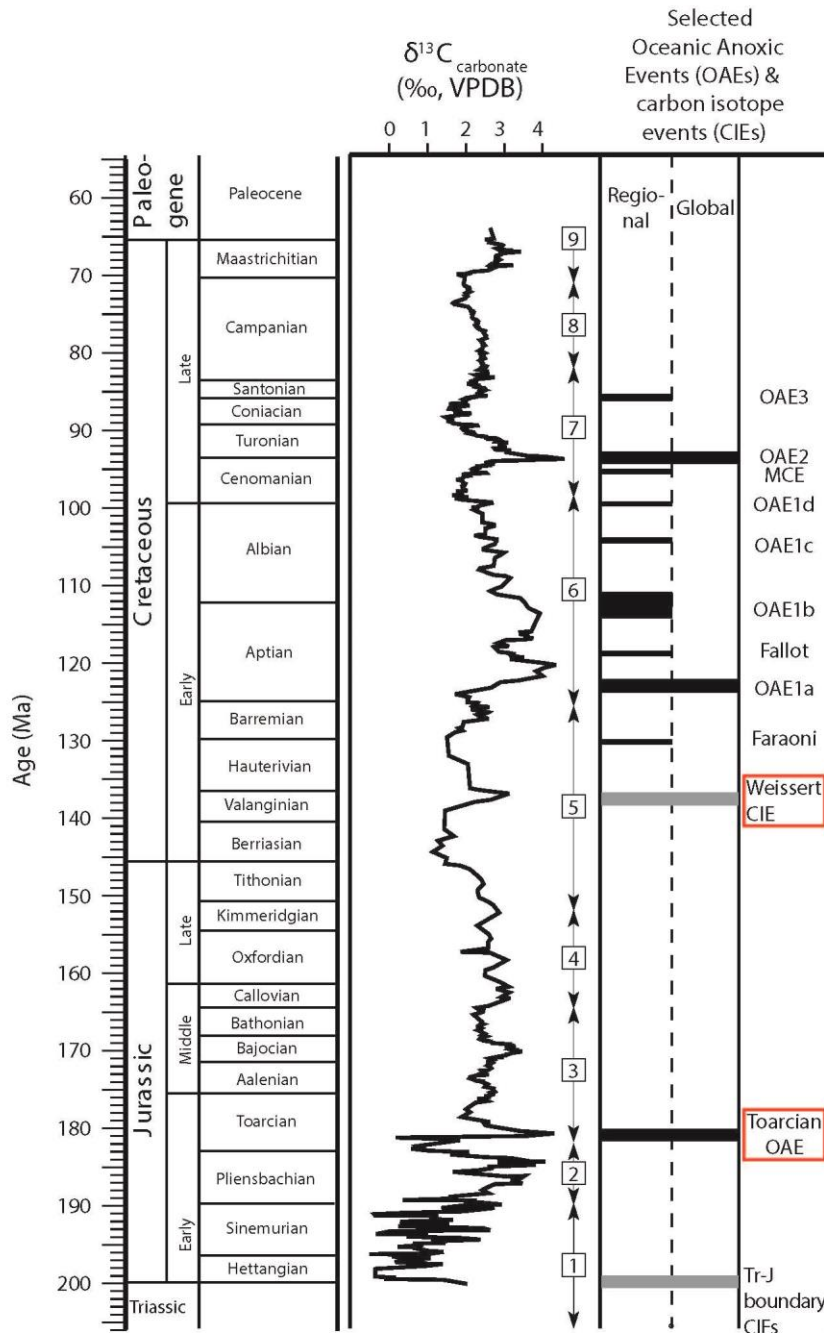


**Fig. 1:** Bulk carbonate carbon isotope ( $\delta^{13}\text{C}_{\text{carb}}$ ) stratigraphy of the Jurassic and Cretaceous, age of prominent Oceanic Anoxic Events (OAEs) and other related phenomena from Robinson et al., 2017. Carbon-isotope data from: (1) Van de Schootbrugge et al. (2005); (2) Hesselbo et al. (2000); (3) Morettini et al. (2002); (4) Dromart et al. (2003); (5) Weissert et al. (1998); (6) Erbacher et al. (1996); (7) Jenkyns et al. (1994); (8) Jarvis et al. (2002); and (9) Abramovich et al. (2003).

As summarized by Erba et al. (2019a), the original definition of OAEs (Schlanger and Jenkyns, 1976) became somehow misleading for the following reasons: i) global anoxia is rarely reached; ii) black shale intervals are not always synchronous; iii) fully oxic continental and shallow marine successions also record global C-cycle anomalies linked to OAEs; iv) anomalies are of long to short duration. Therefore, the first characterization of OAEs (Schlanger and Jenkyns, 1976) has since evolved, and  $\delta^{13}\text{C}$  chemostratigraphy is currently the dominant tool for defining and correlating OAEs (e.g., Erba, 2004; Tsikos et al., 2004; Weissert and Erba, 2004; Jenkyns, 2010; Robinson et al., 2017). Theoretically, the onset of an OAE could be identified at the beginning of a positive or negative  $\delta^{13}\text{C}$  excursion, while the termination could correspond to the level marking the descent/ascent towards stable, pre-excursion values (Jenkyns, 2010). However, these reference points are not always unambiguous hampering unequivocal dating and correlation.

An ongoing debate continues to explore the causes and consequences of OAEs and associated disturbances, involving experts from various disciplines within geosciences. A consensus has been reached for a model for OAEs (Fig. 2; Weissert, 2000; revised by Jenkyns, 2003, 2010) that identifies a volcanic source of  $\text{CO}_2$  altering the climate usually – but not systematically - to a greenhouse mode. When negative carbon isotope signatures are associated to OAEs, presumably the release of isotopically lighter carbon (volcanic  $\text{CO}_2$ , methane hydrates, thermogenic methane) was the triggering mechanism. Greenhouse warming is theorized to imply several processes that ultimately lead to increased rates of organic-carbon burial, including higher nutrients supply, stratification in restricted basins, and enhanced wind-driven upwelling (Jenkyns, 2003, 2010; Robinson et al., 2017). These processes likely sustained increased primary productivity and expansion of oxygen-minimum zones leading to the formation of the characteristic organic carbon (OC)-rich black shales linked to OAEs in many parts of the world oceans. However, understanding how ocean dynamics could sustain such fertile states over long time scales - hundreds of thousands to a million years - raises a major paleoceanographic challenge (Meyer and Kump, 2008). Moreover, according to the general model, the important burial of OC during some OAEs might counter-balance the signal of isotopically light carbon inputs marking positive excursions in carbon-isotope records (Jenkyns, 2003, 2010; Robinson et al., 2017). Importantly, the sequestration of OC during OAEs might have led to reversed greenhouse conditions and global cooling.

It is not trivial to estimate the effective fluxes of organic matter into and out of the surficial carbon reservoirs in the geologic record. Moreover, the amplitude of both negative and positive  $\delta^{13}\text{C}$  anomalies is higher – by as much as a factor two or more – in marine and terrestrial organic matter than in the carbonate record (Jenkyns, 2010). Indeed, differential fractionation effects affecting the

amplitude of  $\delta^{13}\text{C}$  excursions in different sedimentary archives can introduce serious problems for quantitative modelling of the carbon cycle (Jenkyns, 2010).

In general, the most striking effect on the sedimentological and biological record associated with many OAEs remains the lack or paucity of oxygen in the oceanic bottom waters. This aspect has been largely investigated based on the concentrations and isotopes of redox-sensitive elements (e.g., e.g. Jenkyns et al., 2001, 2007, 2016; Kuypers et al., 2002; Pearce et al., 2008; Jenkyns, 2010; Lu et al., 2010; Montoya-Pino et al., 2010; Gill et al., 2011; Nielsen et al., 2011; Owens et al., 2013, 2016; Westermann et al., 2014; Zhou et al., 2015; Dickson et al., 2016, 2017; Gomes et al., 2016; Holmden et al., 2016). Another key sedimentary signature of OAEs is the paucity in carbonate content (Jenkyns, 2003, 2010; Erba, 2004; Robinson et al., 2017). For example, quantitative studies of Cretaceous pelagic sediments comprising OAEs document major shifts in the biogenic component: from carbonate-dominated to siliceous- and/or organic matter dominated (Erba, 1994, 2004; Premoli Silva et al., 1999; Leckie et al., 2002). Yet it remains unclear to what extent this relative drop of biogenic carbonate is related to oceanic acidification as a consequence of excess atmospheric  $\text{CO}_2$  and/or to an overcome of siliceous and organic-walled plankton over calcareous plankton under higher-fertility conditions (Erba, 2004). In addition, many studies (e.g., Neal et al., 2016) have demonstrated the tight temporal coincidence between OAEs and large igneous provinces (LIP), increased weathering, and changes in ocean circulation patterns supporting the general global model summarized above and in Fig.2.

The application of the general model to many OAE or OAE-like events is not straightforward and often provides new questions, pointing out the complexity of the interactions between the C cycle and paleo-climate. In fact, despite general global signatures, the sedimentological and geochemical expression of individual OAEs and, generally,  $\delta^{13}\text{C}$  anomalies can be critically different depending on local-regional conditions (e.g. Bornemann et al., 2017; Müller et al., 2017). In the last decades, many authors highlighted local variations in depositional conditions, types and degrees of diagenesis, preservation, and amount of organic matter characterizing OAEs. Many unanswered questions remain about the timing of environmental processes and consequent changes in the different reservoirs of the lithosphere, hydrosphere, atmosphere and biosphere, especially at higher latitudes (Robinson et al., 2017).

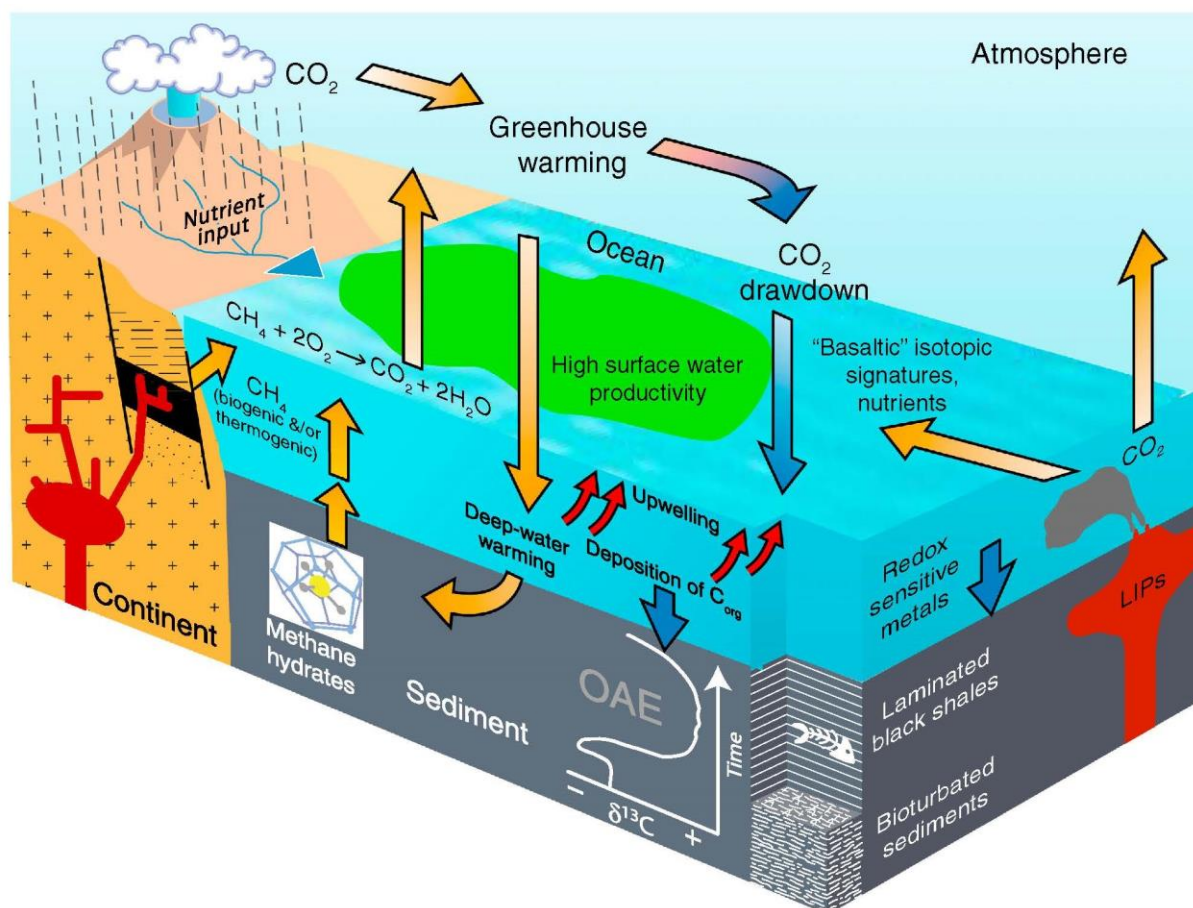


**Fig. 2:** Schematic illustration of the major aspects of the positive and negative feedbacks related to the onset and termination of Ocean Anoxic Events (OAEs), as described in detailed in the text in section 2.1. LIPs = large igneous provinces. The figure is from Robinson et al. (2017), and Jenkyns (2010) modified it following the original scheme presented in Weissert (2000).

This Ph.D. thesis is focused on an integrated multidisciplinary study focused on the Mesozoic carbon cycle and climate change events – presented below in section 2.1 – that represent opposite examples of global warming and cooling linked to fluctuations in atmospheric  $\text{CO}_2$ . Specifically, I considered the early Toarcian OAE (T-OAE) (Jenkyns, 1985, 1988) and the late Valanginian Weissert OAE (Erba et al., 2004). In addition to different geodynamic contexts, a negative and a positive  $\delta^{13}\text{C}$  excursion, respectively, characterize the T-OAE and Weissert Event. More details about the selected case studies are given in the following chapter.

### 1.3 The Early Jurassic T-OAE versus the Early Cretaceous Weissert Event

A detailed summary of named variations in  $\delta^{13}\text{C}$  and identified OAEs across the Jurassic and Cretaceous is provided by the latest GTS2020 time scale (Gradstein et al., 2020) and shown in Fig. 3 and Fig. 4, respectively (see also references in the figures).

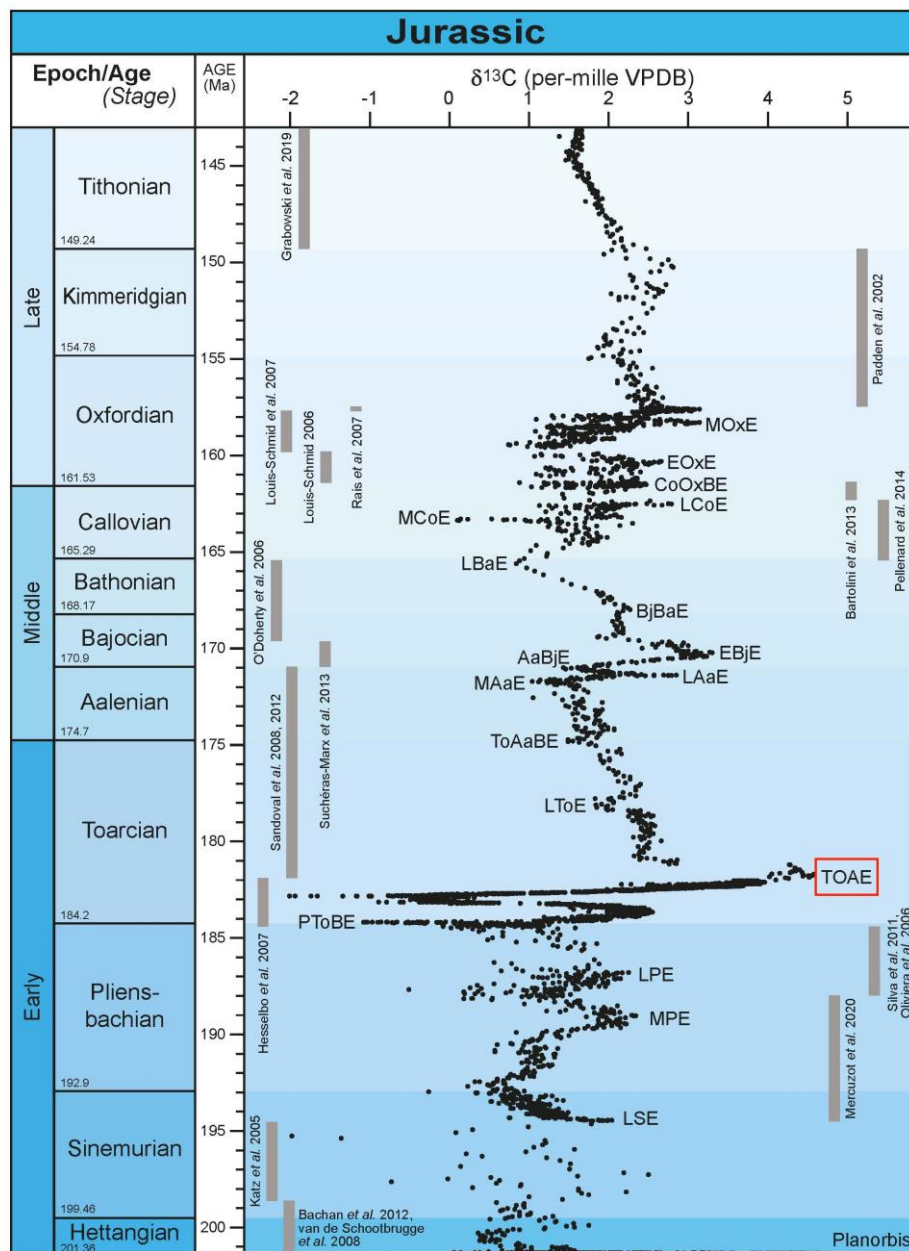


**Fig. 3:** Summary of variations in  $\delta^{13}\text{C}_{\text{carb}}$  through the Jurassic. Vertical bars showing chronostratigraphic interval indicate data sources. See text and references in Gradstein et al.,

2020 for a more detailed discussion of the  $\delta^{13}\text{C}$  composite data. Acronyms used to identify named excursions and boundary events (BE): Late Sinemurarian Event (LSE); MPE, LPE Mid-, Late Pliensbachian events; PToBE Pliensbachian-Toarcian BE; TOAE Toarcian-Oceanic Anoxic Event; LToE Late Toarcian; ToAaBE Toarcian-Aalenian BE; MAaE, LAaE Mid-, and Late Aalenian; AaBjBE Aalenian-Bajocian BE; EBJE Early Bajocian; BjBaBE Bajocian-Bathonian BE; LBaE Late Bathonian; MCoE, LCoE Mid-, Late Collovian; CoOxBE Collovian-Oxfordian BE; and EOxE, MOxE Early, and Mid-Oxfordian.

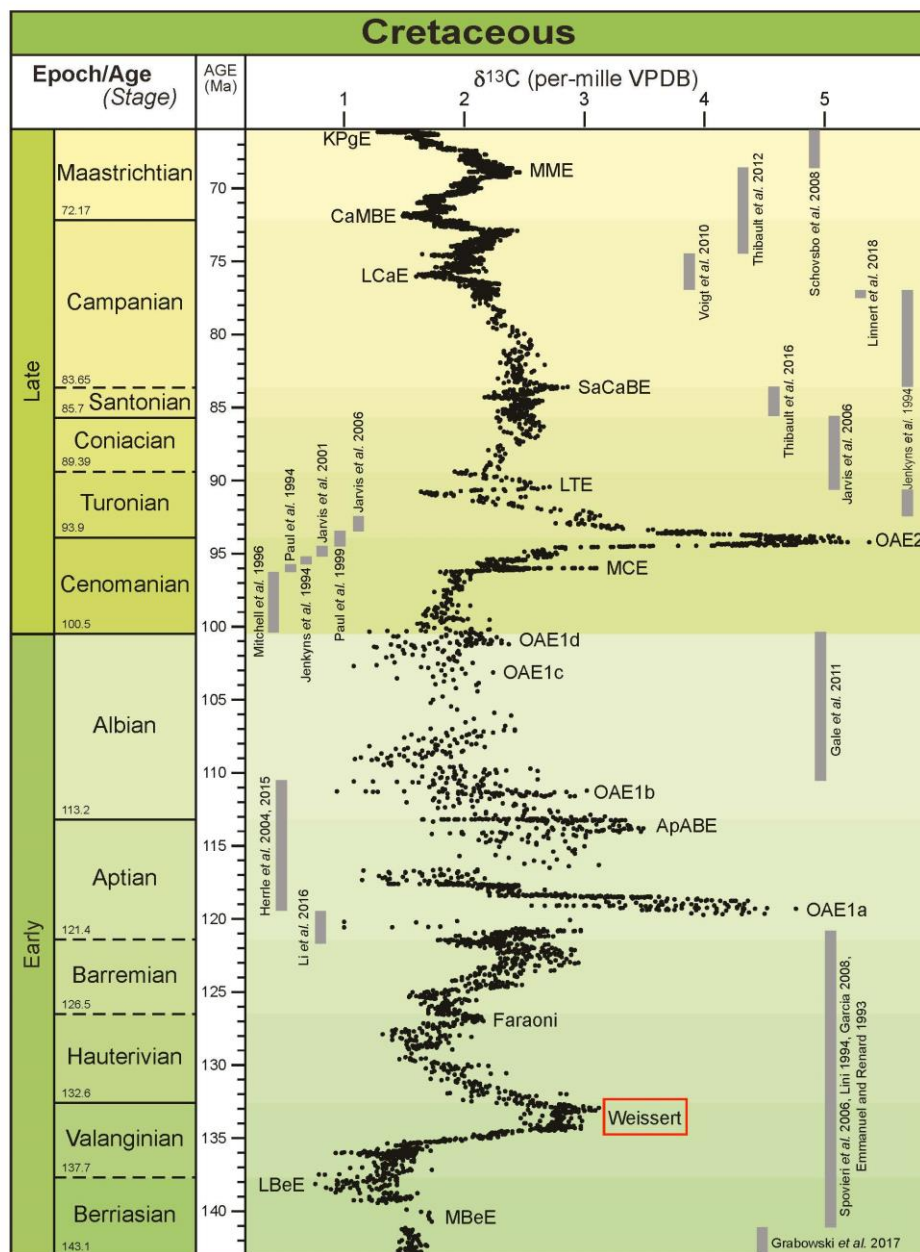


**Fig. 4:** Summary of variations in  $\delta^{13}\text{C}_{\text{carb}}$  through the Cretaceous. Vertical bars showing chronostratigraphic interval indicate data sources. See text and references in Gradstein et al.,

2020 for a more detailed discussion of the  $\delta^{13}\text{C}$  composite data. Acronyms used to identify named excursions and boundary events (BE): MBeE, LBeE Mid-, Late Berriasian events; OAE1a-d and OAE2 suite of Oceanic Anoxic Events; ApABE Aptian-Albian BE; MCE Mid-Cenomanian Event; LTE Late Turonian Event (Hitch Wood); SaCaBE Santonian-Campanian BE; LCaE Late Campanian; CaMBE Campanian-Maastrichtian BE; MME Mid-Masstrichtia; and the KPgE Cretaceous-Paleogene event.

This Ph.D. thesis examined two unique and contrasting case-histories of the Mesozoic: 1) the early Toarcian T-OAE at ~183 Ma (Early Jurassic) (Jenkyns, 1985, 1988), and 2) the late Valanginian Weissert Event at ~138 Ma (Early Cretaceous) (Erba et al., 2004) (see Fig. 2). The two investigated events present critical contrasts in many aspects, making them two interesting case studies to explore the C-cycle and climate dynamics impacting the oceanic ecosystem.

**The Toarcian-OAE.** At the beginning of the XX century, Dal Piaz (1907) documented Toarcian (Early Jurassic) pelagic sediments enriched in OC in the Alpi Feltrine (Southern Alps), similarly to other findings in Germany and Switzerland (Posidonienschiefer), England (Jet Rock and Bituminous Shales) and France (Schistes Cartons). Gaetani and Poliani (1978) also described a lower Toarcian black shale interval, namely the “Livello a Pesci” (Fish Level), in the pelagic succession of the Lombardy Basin. Later Jenkyns (1985, 1988) identified these black shale intervals as the Toarcian-OAE (T-OAE). This lithostratigraphic-based definition was applied in several works and later complemented by a broad  $\delta^{13}\text{C}$  positive excursion interrupted by an abrupt negative “bite” in its central portion (Jenkyns, 2010).

A recent  $\delta^{13}\text{C}$  reference curve for the latest Pliensbachian–middle Toarcian time interval (Ruebsam and Al-Husseine, 2020, modified by Hougård et al., 2021) describes in detail the prolonged positive excursion containing the negative CIE (see Fig. 3 and 5). The broad positive carbon-isotope excursion corresponds to a ~1.5 million-year-long interval based on the latest GTS2020 time scale (Gradstein et al., 2020). The remarkable  $\delta^{13}\text{C}$  negative CIE – of much shorter duration - has been documented at a global scale in a variety of marine and continental settings indicating a global perturbation of the C-cycle (see reviews by Ramirez and Algeo, 2020; Ruebsam and Al-Husseini 2020). A recent revision (Müller et al., 2017) proposed renaming the T-OAE as the Jenkyns Event in which the negative CIE is

distinguished (its interval 2). Reolid et al. (2020) recommended using the term Jenkyns Event to indicate a series of global early Toarcian changes including anoxia, enhanced organic matter burial, biotic crises in marine and terrestrial ecosystems, warming, and sea-level rise. However, a univocal definition of the beginning and end of the Jenkyns Event was not provided, hindering its unambiguous documentation and correlation on a regional to global scale. A summary overview of the chemostratigraphic framework of the T-OAE, including the Jenkyns Event equated to the  $\delta^{13}\text{C}$  negative shift, is presented in Fig.5. A detailed discussion is provided in chapter 3 of this thesis.

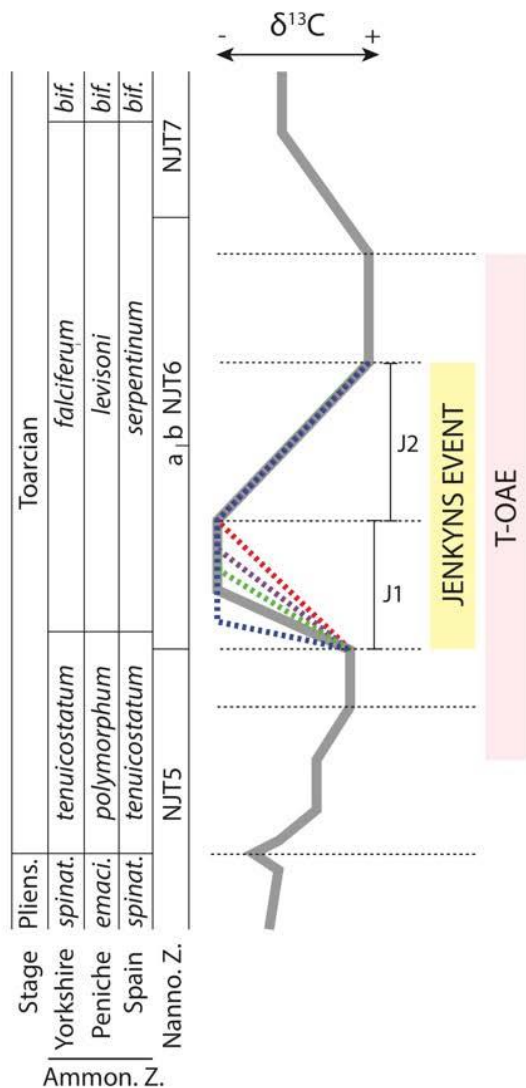


**Fig. 5:** The schematic  $\delta^{13}\text{C}$  reference curve for the latest Pliensbachian–Toarcian time interval is reported (modified after Ruebsam and Al-Husseini (2020), with minor modifications by Hougaard et al. (2021). The stratigraphic extent of the Toarcian Oceanic Anoxic Event (T-OAE) is indicated with a light red box, which includes the interval of the Jenkyns Event (yellow box) as defined in Erba et al. (2022). The Jenkyns Event is also subdivided in a lower J1 and an upper J2 segments. The coloured dashed lines in the reference plot represent the different trends that are worldwide documented in the lower part of the Jenkyns Event (J1). The Figure is modified from Erba et al. (2022).

The release of high amounts of  $\text{CO}_2$  is interpreted as the trigger of extreme paleoenvironmental changes associated with the T-OAE, presumably related to the degassing of the Karoo–Ferrar LIP (Percival et al., 2015; Heimdal et al., 2021). Evidence also suggests that higher  $\text{CO}_2$  levels both in the atmosphere and oceans could be due to the dissociation and



oxidation of methane hydrates along continental margins and/or in high latitude terrestrial environments (Hesselbo et al., 2000; Pálffy and Smith, 2000; McElawin et al., 2005; Svensen et al., 2007; Percival et al., 2015; Them et al., 2017; Ruebsam et al., 2019). Moreover, the T-OAE is further associated with an Osmium isotope anomaly (Cohen et al., 2004; Percival et al., 2016; Them et al., 2017) that documents accelerated weathering (Cohen et al., 2004; Percival et al., 2016; Them et al., 2017) in response to climate change during an extraordinary warmth (Dera et al., 2011; Korte and Hesselbo, 2011; Gómez et al., 2016), and a major marine transgression (Haq et al., 1987; Hardenbol et al., 1998) phase. A biocalcification crisis (Erba, 2004; Mattioli et al., 2004; Casellato and Erba, 2015; Erba et al., 2019a), increased primary productivity (Jenkyns, 2010; Erba et al., 2004), and ocean acidification (Erba et al., 2004; Trecalli et al., 2012; Casellato and Erba, 2015; Posenato et al., 2018) are also documented. Reconstructed atmospheric CO<sub>2</sub> concentrations during the Early Toarcian show a likely doubled increase from ~1000 to ~2000 ppm (i.e., Berner, 2006a, b; Retallack, 2009; Steinthorsdottir and Vajda, 2015), which caused the observed intense and rapid warming linked to the T-OAE (i.e., up to ~8 °C seawater warming in the Asturian Basin at ~40 °N paleolatitude; Gómez et al., 2016).

**The Valanginian Weissert Event.** The original definition of the Weissert Event was not linked to a black shale marker bed. Indeed, in the Maiolica Formation of the Southern Alps a discrete positive carbon isotope excursion of late Valanginian age was identified (Weissert, 1989; Lini et al., 1992) and calibrated with bio-chemostratigraphy (Channell et al., 1993) (see Fig. 4). The anomaly was later recognized in several sections in Europe and the ocean and Erba et al. (2004) formalized the Valanginian Event as the Weissert-OAE. This was based on the occurrence of discrete black shale layers in the interval of the positive C isotopic excursion in the Tethys and Pacific Oceans, although a single lithostratigraphic marker bed was never found. As a consequence, the characterization of this event as an OAE has been debated (i.e., see review in Charbonnier et al., 2020) as late Valanginian global anoxia is not documented, leading some to speculate high OC burial rates on land, instead (e.g., Westermann et al., 2010). Several works discussed a chronostratigraphic link between the initial phase of the event and the timing of the Parana'-Etendeka LIP (Weissert and Erba, 2004; Thiede and Vasconcelos 2010; de Assis Janasi et al., 2011; Dodd et al., 2015; Price et al., 2018; Charbonnier et al., 2020). In this Ph.D. thesis, following the original definition of Erba et al. (2004), we address the Weissert as an OAE-like event, identified by a global positive (on average +1.5‰) CIE, observed both in marine and/or terrestrial organic matter

and carbonate. A revised chemostratigraphic framework of the Weissert Event is shown in Fig.5 from Cavalheiro et al. (2021), which is discussed in detail in chapter 5 of this thesis. In this work revised chronostratigraphy, biostratigraphy and integrated magnetostratigraphy across the Berriasian–Barremian time interval define the stratigraphic framework of the Weissert Event based on the carbon isotope records.

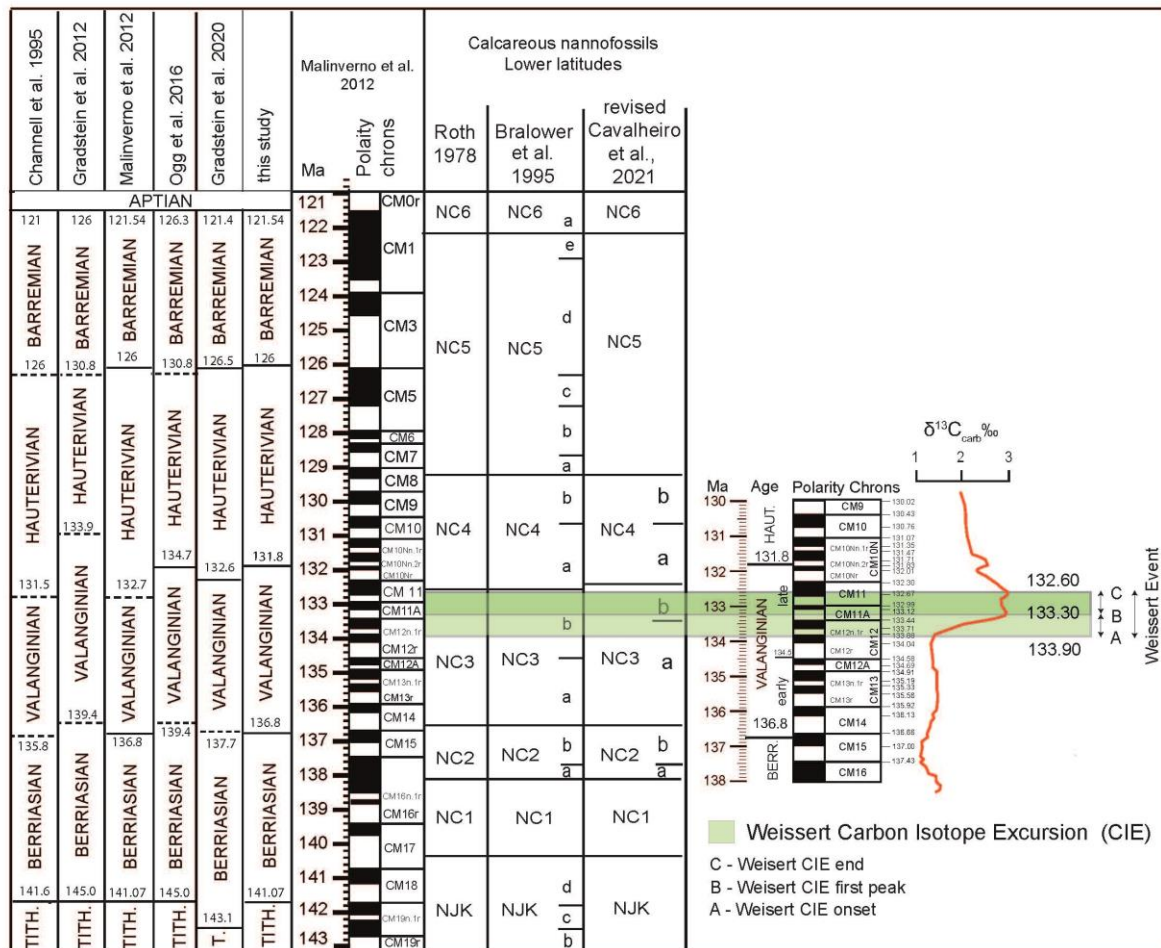


**Fig. 6:** Revised chronostratigraphy, biostratigraphy and integrated magnetostratigraphy across the Berriasian–Barremian time interval showing the chemostratigraphic framework of the Weissert Event based on the carbon isotope record measured from bulk carbonate ( $\delta^{13}\text{C}_{\text{carb}}$ ; Sprovieri et al., 2006). The numerical ages of the Weissert  $\delta^{13}\text{C}_{\text{carb}}$  carbon isotope excursion (CIE) are based on the timescale revisited in Cavalheiro et al. (2021). Figure modified from Cavalheiro et al. (2021).

The Weissert Event is also characterised by a carbonate crisis in pelagic and neritic environments, and local to regional enhanced productivity (Erba et al., 2004, 2019a; Erba and

Tremolada, 2004). Notably, the Weissert Event remains relatively understudied compared to the main OAEs, and estimates of Early Cretaceous atmospheric CO<sub>2</sub> levels are quite uncertain between ~500–1700 ppm (Foster et al., 2017). Notably, the main signature of the Weissert Event is a dramatic OC sequestration – recorded by its diagnostic positive CIE – that is thought to have triggered important atmospheric CO<sub>2</sub> drawdown and global cooling. (Erba et al., 2004; Weissert and Erba, 2004; Erba and Tremolada, 2004; Gröcke et al., 2005; Bornemann and Mutterlose 2008; Price et al., 2018; Charbonnier et al., 2020). Indeed, a latest Valanginian cooling episode is globally documented fostering the debate regarding Early Cretaceous sub-polar glaciation (Miller et al., 2009; Price and Nunn, 2010; Alley et al., 2020). However, contrasting temperature records across the Weissert Event are reported (see Charbonnier et al., 2020).

Both events investigated here represent major episodes of C-cycle and climate perturbations, likely associated with the emplacement of major LIPs. Besides that, yet the two events present critical contrasts both in sedimentary and geochemical signatures, as well as in the resulting impact on climate and C-cycle. Notably, the T-OAE and the Weissert Event represent quite different examples of “in and out” from icehouse to greenhouse state – and *vice versa* – making very important the analysis of the possible mechanisms behind them to understand positive and negative feedback on the C-cycle, climate dynamics, and environmental impact.

## 1.4 Materials and objectives of the thesis

The material selected for the study of the T-OAE is from two Toarcian cores (the Sogno and Gajum Cores) that can be considered reference sections for the pelagic lower Toarcian interval of the western Tethys (Erba et al., 2019b). The Sogno and Gajum Cores recovered 26.83 and 31.18 stratigraphic meters, respectively, of pelagic sediments consisting of marly limestones, marlstone, marly claystone, including a relatively expanded black shale interval, the “Fish Level”, which represents the sedimentary expression of anoxia during the T-OAE (Erba et al., 2019b). The Sogno and Gajum sites were located in relatively restricted and deep basins in a complex low-latitude Toarcian seaway in the western Tethys, which was characterized by a horst and graben topography with deeper zones influenced by local modulation of currents. Particularly, the Sogno site was located in a pelagic plateau (Albenza Plateau), ~1400 m deep, and the Gajum in an inner basin along the slope of a structural high (Corni di Canzo Mt.), ~1800 m deep.

The Weissert Event was studied in a unique southern polar location, thanks to the great opportunity of a considerable good amount of sample material made available by GCR - Gulf Coast Repository Texas A&M University, College Station, Texas, under request 067321-IODP (the International Ocean Drilling Program), which recovered a thick Lower Cretaceous section at Ocean Drilling Program (ODP) Site 692, in the Weddell Sea, nearshore Antarctica. ODP Site 692 recovered a calcium carbonate-rich and finely laminated black shales section of about 40 meters, in a semi-enclosed shelf basin with a paleowater depth of ~500 m and a paleolatitude of ~54 °S (Mutterlose and Wise, 1990). ODP Site 692 was an outer shelf exposed to an open sup-polar basin (Weddell Sea, offshore eastern Antarctica), ~500 m deep. During the Valanginian, the Weddell Basin was an incipient restricted basin with weak replenishment of water masses due to the high degree of hydrographic and bathymetric isolation of the young Early Cretaceous Southern Ocean.

This Ph.D. thesis was designed to study two distinct carbon cycle anomalies evidenced in the carbon isotope record of the Early Jurassic and Early Cretaceous using an integrated analytical strategy to explore paleo-environmental changes, temperature- $p\text{CO}_2$  relations, and bio-geochemical cycle variations. The two selected case studies were investigated in distinct and very different paleo-settings and latitudes, in order to explore how global perturbations

translate into local paleo-environmental responses in the sedimentary record, documenting a different response in the bio-geochemical cycles.

The work strategy of the analytical methods applied in this Ph.D. thesis is shown in Fig. 7, which presents the interdisciplinary analyses carried out for a multi-parametric reconstruction of palaeo-environmental conditions, C-cycle and climate dynamics based on a multi-proxy approach. The core framework of the study is based on an extremely detailed chemostratigraphy reconstruction built on new carbon- and oxygen-isotope data calibrated against nannofossil biostratigraphy. High-resolution inorganic and organic geochemical analyses were addressed to the investigation of major and trace-element concentrations, specific biomarker data and paleo-temperature proxies for a broad and comprehensive paleo-environmental reconstruction. In addition, paleo-climate modelling simulations are integrated with multi-proxy data to explore variations in atmospheric CO<sub>2</sub> levels and global ocean temperatures during major disruptions of the C-cycle across the study time-intervals. In summary, the aims of this Ph.D. thesis are:

1. Investigate two paleo-environments under extreme modes of the Mesozoic climate-carbon cycle, identified by the distinct carbon isotope excursions (CIEs) of the Early Jurassic (T-OAE) and the Early Cretaceous (Weissert-Event).
2. The two case studies are used to identify how global perturbations translate into local paleo-environmental responses in the sedimentary record. The settings are (a) restricted shallow (outer shelf/upper margin) environments along nascent/emerging open marine basins (Early Cretaceous Weddell Sea) and (b) deep water corridors along shelf seaways (Sogno and Gajum locations in the Early Jurassic Lombardy Basin).
3. A precise characterization of carbon-isotope stratigraphy and univocal identification of the T-OAE (including the Jenkyns Event) and the Valanginian Weissert Event anomalies.
4. Design and application of an integrated approach combining modelling and multi-proxy data compilation to demonstrate an innovative way forward to decouple uncertainties and limitations of individual proxy results and locations from regional to global scale interpretations. Especially, reconstruct temperature/*p*CO<sub>2</sub> relationships based on multi-proxy data and modelling to evaluate processes, rates, and dimensions of climate and environmental change back in time, setting boundaries for projecting future climate and environmental response.
5. Reconstruction of OC burial and preservation rates, the nature and sources of organic matter, quality, and thermal maturity.

6. Reconstruction of the paleo-depositional environment and redox conditions using different geochemical (organic and inorganic) proxies
7. Track the evolution of seawater paleo-temperatures based on a literature compilation of available multiple proxies and new high-resolution data across the study CIEs.
8. Combine independent geochemical, geological and climate model simulations to reconstruct variations in global mean surface temperatures (GMSTs) and associated atmospheric CO<sub>2</sub> concentrations across the observed C-cycle and climate change during the study events.
9. Disentangle local/regional versus global isotopic, OC and seawater paleo-temperature signals.
10. Investigate the complex interplay between local and global driving factors acting on different timescales and controlling primary productivity, preservation and dilution dynamics, and ultimately changes in OC signals. Examples are i) plate-tectonic processes transforming basin physiography, ocean gateways and circulation on a multimillion-year (geological) timescale (Donnadieu et al., 2016; Dummann et al., 2020; 2021; Arthur and Natland, 1979; Wagner and Pletsch, 1999); ii) intense carbon-cycle and climate perturbation episodes identified by CIEs (Jenkyns, 2010; Weissert and Erba, 2004). iii) orbital cycles driving changes in oceanic and atmospheric circulation on timescales of tens of thousands to hundreds of thousands of years (Beckmann et al., 2005; Behrooz et al., 2018; Hoffmann and Wagner 2001; Wagner et al., 2013).



## **2. Coring the sedimentary expression of the early Toarcian Oceanic Anoxic Event: new stratigraphic records from the Tethys Ocean**

**In Scientific Drilling**, 26, 17–27, 2019

<https://doi.org/10.5194/sd-26-17-2019>

**Author(s):** E. Erba, G. Gambacorta, S. Visentin, L. Cavalheiro, D. Reolon, G. Faucher, and M. Pegoraro.

### **Abstract**

The Toarcian Oceanic Anoxic Event (T-OAE) interval was cored at Colle di Sogno and Gajum in the Lombardy Basin (Southern Alps, northern Italy). The Sogno and Gajum cores recovered 26.83 and 31.18 stratigraphic metres, respectively, of pelagic sediments consisting of marly limestones, marlstone, marly claystone, and black shale. Drilling at both sites resulted in 100 % recovery of unweathered material. The pelagic succession comprises a relatively expanded black shale interval of 4.98 m in the Sogno core and 15.35 m in the Gajum core, with lower and upper boundaries without evidence of hiatuses. The Sogno and Gajum cores can be considered reference sections for the pelagic lower Toarcian interval of the western Tethys and will provide high-resolution micropaleontological, inorganic and organic geochemical, isotopic multiproxy data. Integrated stratigraphy and cyclostratigraphy are predicted to result in estimates of durations and rates to model the ecosystem resilience to the extreme perturbations of the T-OAE and gain a better understanding of current global changes and help provide better projections of future scenarios.





# Coring the sedimentary expression of the early Toarcian Oceanic Anoxic Event: new stratigraphic records from the Tethys Ocean

Elisabetta Erba, Gabriele Gambacorta, Stefano Visentin, Liyenne Cavalheiro, Dario Reolon, Giulia Faucher, and Matteo Pegoraro

Dipartimento di Science della Terra, Università degli Studi di Milano, Milano, Italy

**Correspondence:** Elisabetta Erba (elisabetta.erba@unimi.it)

Received: 14 June 2019 – Revised: 2 September 2019 – Accepted: 4 September 2019 – Published: 2 December 2019

**Abstract.** The Toarcian Oceanic Anoxic Event (T-OAE) interval was cored at Colle di Sogno and Gajum in the Lombardy Basin (Southern Alps, northern Italy). The Sogno and Gajum cores recovered 26.83 and 31.18 stratigraphic metres, respectively, of pelagic sediments consisting of marly limestones, marlstone, marly claystone, and black shale. Drilling at both sites resulted in 100 % recovery of unweathered material. The pelagic succession comprises a relatively expanded black shale interval of 4.98 m in the Sogno core and 15.35 m in the Gajum core, with lower and upper boundaries without evidence of hiatuses. The Sogno and Gajum cores can be considered reference sections for the pelagic lower Toarcian interval of the western Tethys and will provide high-resolution micropaleontological, inorganic and organic geochemical, isotopic multiproxy data. Integrated stratigraphy and cyclostratigraphy are predicted to result in estimates of durations and rates to model the ecosystem resilience to the extreme perturbations of the T-OAE and gain a better understanding of current global changes and help provide better projections of future scenarios.

## 1 Introduction

The emergence of climate change as a crucial issue for society has urged the understanding of the future state of the planet within the context of increasing carbon dioxide concentrations. The ocean is the oldest ecosystem and the largest on Earth by volume and best records global changes in climate and atmospheric composition. Marine ecosystems are inextricably involved in the physical, chemical, biological processes of global change. In the near future, the ocean's uptake of CO<sub>2</sub> is expected to rapidly decline because of surface water warming, decreasing pH (acidification), increased vertical stratification, and slowed thermohaline circulation (Solomon et al., 2009). Consequently, a very rapid “in and out” from icehouse to greenhouse state – and vice versa – urges comprehension of positive and negative feedbacks on the biosphere.

Understanding of the Earth system at timescales longer than human observations has become imperative, because anthropogenic activities are likely to increase by orders of mag-

nitude the rates of climatic change that usually result from natural processes. The Earth's ecosystems, thus, should be scrutinized on the medium- and long-term scales using geological records of past extreme environmental disturbances that exemplify varied tempos and modes of resilience, occasionally reaching tipping points that triggered permanent modifications.

The Toarcian Oceanic Anoxic Event (T-OAE) is the oldest Mesozoic case of global anoxia with widespread deposition of organic matter-rich sediments in a variety of depositional settings from continental to shallow- and deep-marine (Jenkyns, 1985, 1988, 2010). Available evidence suggests that at ~ 183 Ma the atmosphere and oceans experienced high CO<sub>2</sub>, possibly due to the degassing of lava fields in the Karoo–Ferrar large igneous province and/or from dissociation and oxidation of methane hydrates in continental-margin sediments (Jenkyns, 2010) and/or terrestrial environments (Them et al., 2017). High atmospheric carbon dioxide possibly initiated greenhouse conditions that accelerated

weathering and the hydrological cycle, increasing nutrient recycling into the oceans.

Although the original definition of the T-OAE was based on the presence of a lithostratigraphic marker (Jenkyns, 1985), the development of chemostratigraphy demonstrated that the T-OAE is associated with a negative C isotopic anomaly documented in marine carbonates and organic matter as well as in terrestrial organic matter including fossil wood and specific organic compounds (Jenkyns and Clayton, 1986; Hesselbo et al., 2000, 2007; Schouten et al., 2000; Jenkyns et al., 2002; Emmanuel et al., 2006; Van Breugel et al., 2006; Al-Suwaidi et al., 2010; Caruthers et al., 2011; Izumi et al., 2012; Kafousia et al., 2014; Reolid, 2014; Xu et al., 2017; Them et al., 2017; Fantasia et al., 2018). As shown by Fantasia et al. (2018), such a negative C isotopic anomaly might have resulted from volcanogenic CO<sub>2</sub>, thermogenic methane associated with metamorphism, and dissociation of marine or terrestrial clathrates.

The T-OAE is further marked by an Os anomaly (Cohen et al., 2004; Percival et al., 2016; Them et al., 2017), biocalcification crisis (Erba, 2004; Mattioli et al., 2004; Casellato and Erba, 2015; Erba et al., 2019), increased primary productivity (Jenkyns, 2010; Erba, 2004), and ocean acidification (Erba, 2004; Trecalli et al., 2012; Casellato and Erba, 2015; Posenato et al., 2018), which occurred during an exceptional warming phase (Dera et al., 2011; Korte and Hesselbo, 2011; Gómez et al., 2016) and a major transgression (e.g. Haq et al., 1987; Hardenbol et al., 1998).

Jurassic pelagic successions in the Southern Alps have been extensively investigated for stratigraphy, sedimentology, paleontology, and geochemistry (Bernoulli and Jenkyns, 2009; Erba et al., 2019). In particular, multi- and interdisciplinary studies have demonstrated that the Jurassic pelagic successions of the Lombardy Basin represent “type-sections” of the Tethyan southern margin (Gaetani, 2010). Indeed, the Lombardy Basin is part of the relatively undeformed portion of Adria interpreted as an African “promontory” or as a microplate (Fig. 1). In the latest Triassic–earliest Jurassic a rifting phase caused the breakup of carbonate platforms into a series of “horst and graben” that exerted a physiographic control on sediment type and distribution for most of the Jurassic (Bernoulli and Jenkyns, 1974, 2009; Bosence et al., 2009; Santantonio and Carminati, 2011). As a consequence, sedimentation was differentiated with the deposition of thick complete pelagic successions in the deeper zones, while sedimentation was typically condensed and incomplete on the structural highs.

During the Jurassic the Lombardy Basin was globally a deep area between the Lugano High to the west and the Trento Plateau to the east (Fig. 1). However, the latest Triassic–earliest Jurassic rifting disentangled a number of troughs and paleohighs that are as follows, from west to east: Monte Nudo Trough, Lugano High, Generoso Trough, Corni di Canzo High, Albenza Plateau, Monte Cavallo High, Sebino Trough, Botticino High (Gaetani, 1975, 2010). In the

troughs, partially resedimented Lower Jurassic marlstone–limestone sequences may reach a non-decompacted thickness of 3000 m (e.g. in the Generoso Trough), but condensation and hiatuses characterize the paleohigh sections with reddish nodular facies. Along slopes connecting structural highs to the troughs, sedimentation was marked by slumps, resedimented bodies, and, locally, megabreccias within condensed and occasionally incomplete facies (Gaetani and Erba, 1990; Gaetani, 2010) (Fig. 1). In addition to regional tectonics, the Lombardy Basin successions record global climatic and oceanographic changes, including the T-OAE (Erba et al., 2019). In fact, lower Toarcian black shales have been documented in various sections, offering the opportunity to investigate the consequences of the T-OAE global changes on marine biota in the Tethys Ocean (Erba et al., 2019).

After close investigations of section outcropping in the Lombardy Basin, the Colle di Sogno and Gajum sites were selected as the most promising locations for continuous coring of pelagic records (Gaetani and Erba, 1990; Casellato and Erba, 2015) for continuous coring. In this paper, we document coring operations and lithostratigraphic characterization of both the Sogno and Gajum cores and outline ongoing multidisciplinary research.

## 2 Coring through the sedimentary record of the early Toarcian Oceanic Anoxic Event

The T-OAE is considered a natural Earth system experiment, which allows us to (a) detect and quantify processes associated with emissions of greenhouse gases and natural atmospheric pollutants; (b) understand the role of greenhouse gases on climate dynamics and its influence on the hydrological cycle; (c) characterize changes in ocean and atmospheric chemistry and their interactions; (d) assess changes in biodiversity and dynamics of ecosystems and understand the functioning of biotic sinks; and (e) quantify biosphere–geosphere–atmosphere interactions and their timings or rates.

Analysis of past global change requires the collection of high-resolution data from continuous and ideally unweathered sequences. In surface outcrops, sedimentary rocks and particularly black shales are commonly badly degraded and, consequently, drilling is crucial to ensure the recovery of high-quality fresh cored material. In this paper we identify the T-OAE adopting the original definition by Jenkyns (1985) based on lithostratigraphy. Therefore, the T-OAE in the Lombardy Basin corresponds to the Livello a Pesci (Tintori, 1977; Gaetani and Poliani, 1978; Erba and Casellato, 2010; Erba et al., 2019). This interval has an average thickness of 0.5 to 5 m, but reaches a few tens of metres in the most expanded sections. Black shales are rarely recorded on paleohighs, whereas they are ubiquitous in deeper basins. As the T-OAE occurred at a global scale, the local lack of black shales

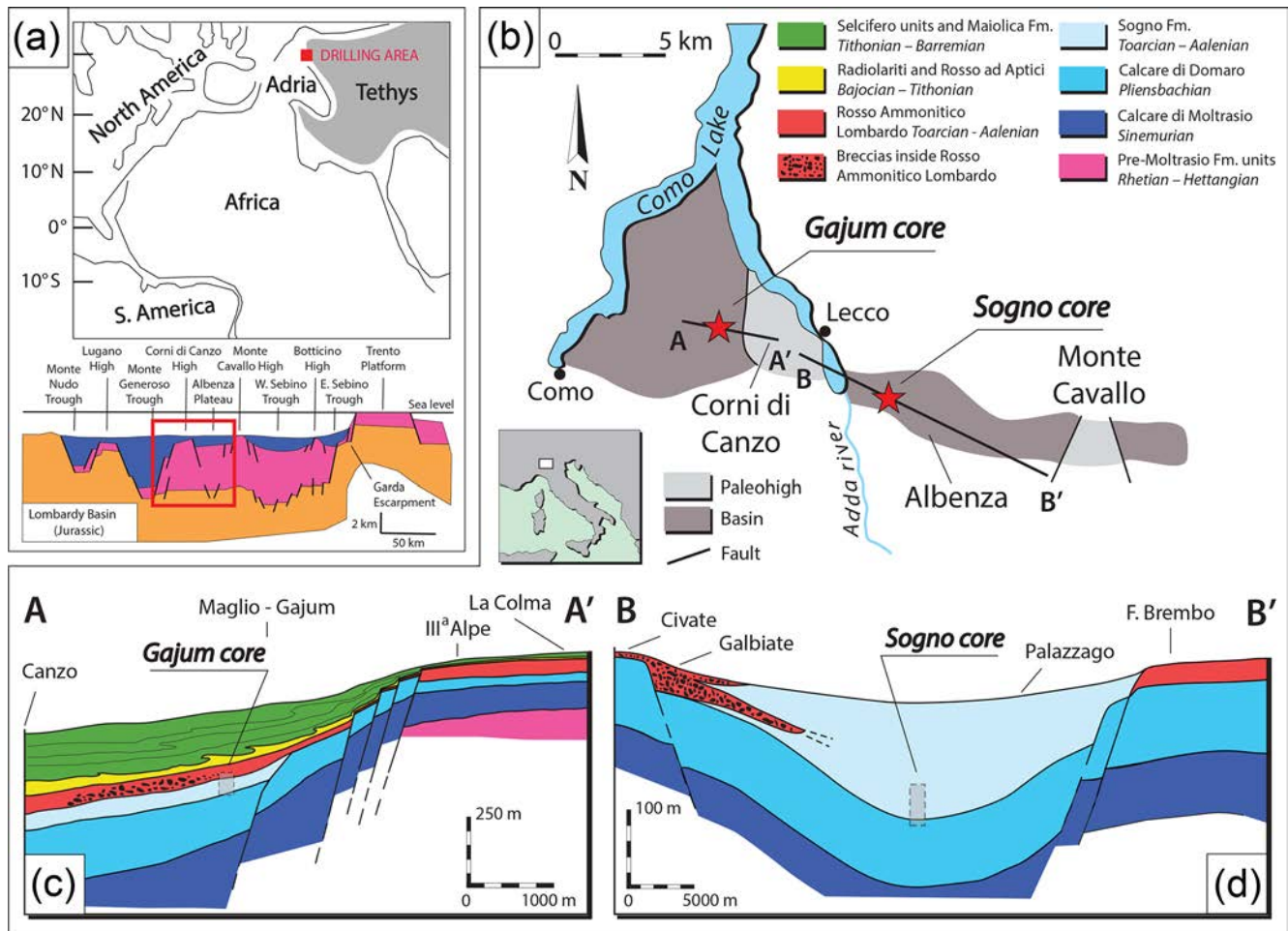


**Figure 1.** Location of the Sogno and Gajum drilling sites relative to (a) paleogeography and (b) current geography. The drilling area was part of the Lombardy Basin (Southern Alps). (c) The Gajum core is sited in an inner basin along the western slope of the Corni di Canzo High while (d) the Sogno core was drilled on the Albenza Plateau as detailed in the geological sections in the lower part of the figure (modified after Gaetani and Poliani, 1978 and Gaetani and Erba, 1990).

in the Lombardy Basin is usually the result of condensation and/or stratigraphic gaps.

#### Location of the drill sites and justification for coring

Two Lower Jurassic sections at Colle di Sogno and Gajum, respectively, were selected for continuous coring through the Toarcian organic-rich black shale interval (Fig. 1). Within the Lombardy Basin, these sections represent significantly different geological settings on a pelagic structural high, namely the Albenza Plateau (Colle di Sogno) and in an inner basin along the slope of the Mt Corni di Canzo structural high (Gajum) (Gaetani and Erba, 1990; Gaetani, 2010). Both successions are relatively expanded and lack the diagenetic manganese-carbonate horizons (present in the Toarcian black shales of the Belluno Basin, Southern Alps, for example) that would compromise primary geochemical signatures

(Farrimond et al., 1988; Jenkyns, 1988; Jenkyns et al., 1991; Bellanca et al., 1999).

The Colle di Sogno site (Fig. 1) was selected because the Jurassic sequence exposed is pelagic, stratigraphically continuous and relatively expanded (Gaetani and Erba, 1990; Muttoni et al., 2005; Channell et al., 2010; Casellato and Erba, 2015). It consists of limestone and marlstone, with chert and marly claystone as minor lithologies. The T-OAE is here represented by ~ 5 m of dark grey to black marly claystones of the Livello a Pesci. At Colle di Sogno, the type-section of the Sogno Formation (Gaetani and Poliani, 1978), located along the road SP 179 on the northern slope of Mt Brughetto, was proved to be suitable for high-resolution multidisciplinary studies of litho-, bio-, chemo-, magneto-, and cyclo-stratigraphy (Gaetani and Poliani, 1978; Jenkyns and Clayton, 1986; Gaetani and Erba, 1990; Hinnov et al., 2000; Channell et al., 2010; Casellato and Erba, 2015).

The Gajum succession crops out in a small lateral cut of the Ravella valley (Fig. 1), where the basal lithofacies of the Moltrasio Limestone Formation suggests sedimentation in shallower water than on the Albenza Plateau (Gaetani and Poliani, 1978; Gaetani and Erba, 1990; Pasquini and Vercesi, 2002). In particular, slumps and resedimented bodies with an eastward-sliding direction document a constant instability of the ramp, indicating that the succession developed in a small inner basin separated by a sill from a deeper basin to the west (Pasquini and Vercesi, 2002). A sharp lithological change marks the boundary between the carbonate-rich lithologies of the Domaro Limestone Formation and the overlying clay-rich lithologies of the lower Sogno Formation consisting of marlstones and marly limestones followed by reddish nodular limestones of the Rosso Ammonitico Lombardo. At Gajum the expanded nature of the black shale interval (~ 15 m) offers the opportunity for studying the inception, evolution, and termination of the T-OAE in great detail.

### 3 Drilling operations and lab core preparation

The Sogno drilling campaign took place in June 2013, while the Gajum core was drilled in February 2016 (Fig. 2). At both Sogno and Gajum sites, drilling operations were performed with the DELTABASE 520 Modular Hydraulic Rotary Drill. The Sogno coring was accomplished with a T2 double corer, using narrow-kerf, sawtoothed drill bits that cut a 101 mm diameter borehole and 84 mm diameter cores. The Gajum core was obtained using a modified T6 triplex corer, including a plastic liner for the best recovery, using narrow-kerf, sawtoothed drill bits that cut a 131 mm diameter borehole and 101 mm diameter cores. At Gajum, after coring, the borehole was logged using a QL40-OBI optical televiewer to obtain high-resolution images of the borehole wall, together with a total gamma radiation tool (Fig. 3).

All cores were initially described on site and a preliminary log was produced. Then, cores were packed, labelled, and put in PVC plastic boxes to prevent contamination and transported to the Department of Earth Sciences in Milan where they are archived. Here, during lab preparation, all cores were longitudinally split along the dip and divided into an archive half and a sampling half, both marked at centimetre scale. The archive half was photographed in high resolution and composite photologs were produced for each site.

### 4 Preliminary results

#### 4.1 Lithostratigraphy of the Sogno core

Four distinct boreholes (S1, S2, S3, and S4) were drilled at Colle di Sogno along the SP 179 road (45°47'20.5" N, 9°28'30.0" E). The outcropping beds show a strike of 150° and a dip of 68° to the southwest (240°).

Initially, a single borehole was planned to penetrate the lower Toarcian–uppermost Pliensbachian interval and reach

the base of the Sogno Formation at ~ 35 m penetration depth. However, at ~ 25 m penetration depth (core S1-27) a sharp dip increase to 88° revealed the occurrence of a fold, partially faulted and reversed, persisting for ~ 4 m (cores S1-27, S1-28, and S1-29). Indeed, core S1-30 perfectly correlates with the lower part of core S1-26 and two black shales were used as lithostratigraphic markers. Coring was extended for ~ 2 m (cores S1-31 and S1-32) penetrating the top of the black shale interval and then operations were interrupted to shift drilling to borehole S2 (Fig. 4). Due to the steep dip, it was decided to perform a 10° inclined coring to decrease the total penetration depth down into the Domaro Limestone Formation. Borehole S2 started just above the top of the black shale interval of the Livello a Pesci, perfectly duplicating core S1-32. However, technical problems prevented coring below a few metres and operations stopped after recovery of core S2-3. The third borehole (S3) was moved 0.5 m relative to S2 and was cored vertically. Again, the recovered succession started from just above the top of the black shale interval with core S3-1 triplicating cores S1-32 and S2-1. Coring was extended to 40 m penetration depth, reaching the uppermost part of the Domaro Limestone Formation (Fig. 4). A fourth borehole (S4) was performed to duplicate the middle and lower portion of the black shale interval to ensure material for multidisciplinary investigations. The recovery percentage for the four boreholes is 99.9 %.

Lithostratigraphic units were defined on the basis of lithological features (i.e. lithology and colours determined with the Munsell Rock Color Chart) and sedimentary structures (i.e. presence or lack of bioturbation and/or lamination). For each core at least four dip measurements were taken during lab preparation to calculate the stratigraphic thickness of the drilled section as 25.33 m under 1.5 m of rubble at the top. A complete composite section, representing the upper Pliensbachian–lower Toarcian interval, was created by combining the data obtained from the S1 and S3 boreholes (Fig. 5). The following key observations were derived:

1. The first 1.5 m of the S1 borehole are represented by soil cover and rubble.
2. The S1 core, despite the occurrence of a faulted fold disturbing the succession, recovered a complete section above the Livello a Pesci. The bottommost part of the well reached the uppermost part of the black shale interval. This correlates with the top black shale interval recovered in the upper part of the S3 core.
3. The upper limit of the black shale interval was cored both at S1 and S3 sites.
4. The S3 core recovered a few metres of succession above the black shale interval, the entire Livello a Pesci, and the lower portion of the Sogno Formation, in addition to the topmost part of the Domaro Limestone. In particular, at 25.47 m, the lithostratigraphic boundary between

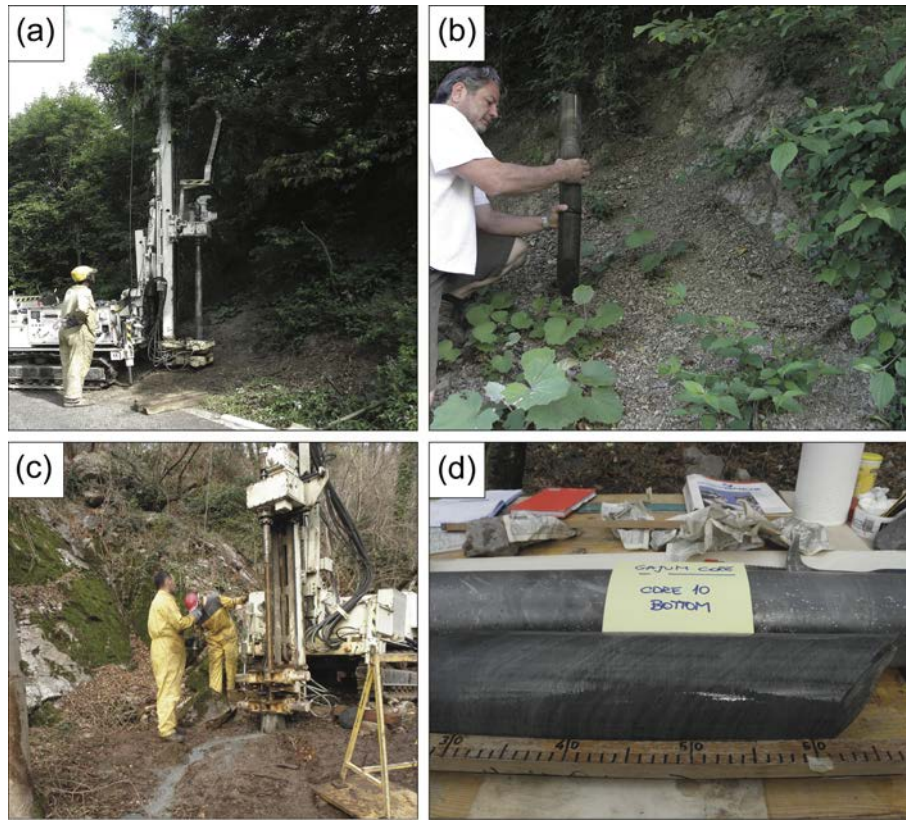


**Figure 2.** Coring operations and results at Sogno and Gajum sites. (a) Coring Sogno Site 4. (b) Livello a Pesci in the Sogno core compared to the equivalent outcropping lithostratigraphic interval. (c) Coring at Gajum. (d) Black shale interval recovered in core 10 of the Gajum core.

the Sogno Formation and Domaro Limestone Formation was recovered.

Combining the above information and considering the dip measured in individual cores (variable in the range of 60 to 87°), the “stratigraphic thickness” of each lithostratigraphic unit was calculated. The overlapping intervals (i.e. U1-5 and U3-1) were matched and duplications were eliminated. The lithologic log of the composite S1–S3 Sogno core, in stratigraphic depths (from 1.5 to 26.83 m), is illustrated in Fig. 5. The composite S1–S3 Sogno core section recovered a complete upper Pliensbachian–lower Toarcian interval, with the S1 core representing its upper portion, and the S3 core the lower part.

The following lithostratigraphic units (U1-1 to U1-5, and U3-2 to U3-11, of the S1 and S3 cores, respectively) are described, from the topmost to the bottommost:

- *Unit 1 (1.50 to 4.82 m): marly limestones, olive-grey in colour.* In the upper and lowermost parts of the unit, high concentrations of reddish mottles and sporadic bioturbation are documented.
- *Unit 2 (4.82 to 9.54 m): marly limestones, olive-grey in colour, characterized by intense bioturbation.* In partic-

ular, the uppermost part of the unit documents the presence of frequent *Planolites*.

- *Unit 3 (9.54 to 10.52 m): marly limestones, grey in colour, characterized by intense bioturbation.* Locally, faintly laminated intervals are observed.
- *Unit 4 (10.52 to 11.87 m): marly limestones with evident and widespread bioturbation.* Locally, 1 to 6 cm thick black shales and laminated intervals are present.
- *Unit 5 (11.87 to 14.55 m): black shales characterized by well-developed lamination, especially in the uppermost part, in addition to pyrite nodules.* In the lower portion, very little bioturbation is documented.
- *Unit 6 (14.55 to 15.93 m): marly limestones, grey to very dark-grey in colour, with reddish to greyish spots.* Bioturbation (burrow) dimensions increase within this unit and thin emerald-green laminae are documented.
- *Unit 7 (15.93 to 16.86 m): marly limestones, with variations in colour from grey, to very dark-grey and dark-red.* In the lowermost portion, bioturbation and lamination are observed.

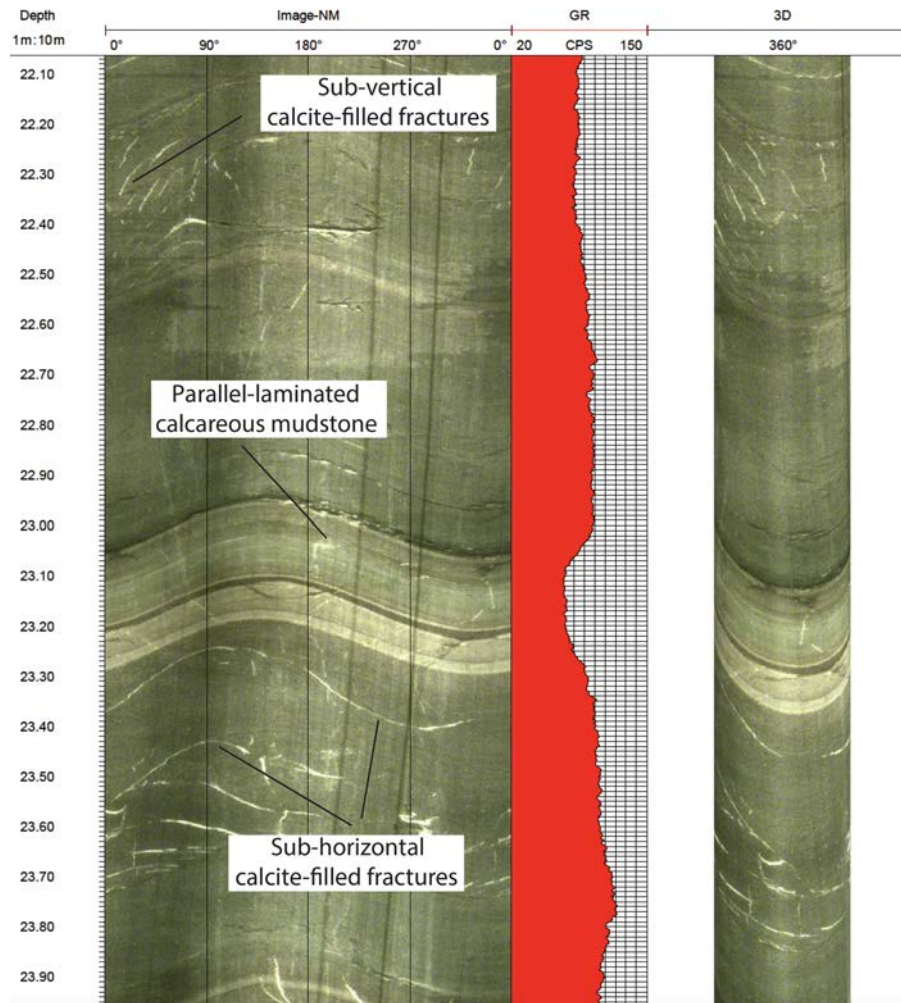


**Figure 3.** Example of Gajum borehole wall image recorded with a QL40-OBI optical televiewer. From left to right: borehole depth, 360° continuous upwrapped digital image of the borehole wall, total natural gamma ray, 3-D log visualization reproducing a virtual core of the borehole.

- Unit 8 (16.86 to 19.10 m): marly limestones, dark-red in colour, with sporadic greyish spots.
- Unit 9 (19.10 to 19.45 m): marly limestones, grey in colour.
- Unit 10 (19.45 to 21.35 m): marly limestones, grey-brown in colour. This is a disturbed interval comprising a level of pebbly marlstones (between 19.45 and 20.03 m), with minor slump structures. Sporadic stylolites are present.
- Unit 11 (21.35 to 22.92 m): marly limestones, grey in colour, characterized by frequent stylolite structures. In addition, 2 cm thick black shale intervals are documented at ~ 21.8 and 22 m, respectively.
- Unit 12 (22.92 to 24.35 m): marly limestones, alternating in colour from reddish to olive-grey. Sporadic bioturbation and lamination can be observed.
- Unit 13 (24.35 to 24.99 m): marly limestones, reddish-greyish in colour.
- Unit 14 (24.99 to 25.47 m): marly limestones, light-brown to grey-brown in colour. Small and large (1 cm thick) burrows are documented. The base of this unit corresponds to the base of the Sogno Formation.
- Unit 15 (25.47 to 26.83 m): marly limestones, olive-grey to dark-grey in colour. Small bioturbations and frequent stylolite structures are observed. This unit corresponds to the uppermost part of the Domaro Limestone Formation.

#### 4.2 Lithostratigraphy of the Gajum core

The Gajum core (45°51'03.2" N, 09°17'19.5" E, at 555 m above sea level) was drilled close to “Fonte Gajum” – Canzo (CO), in the Ravella valley next to the trail named Via delle

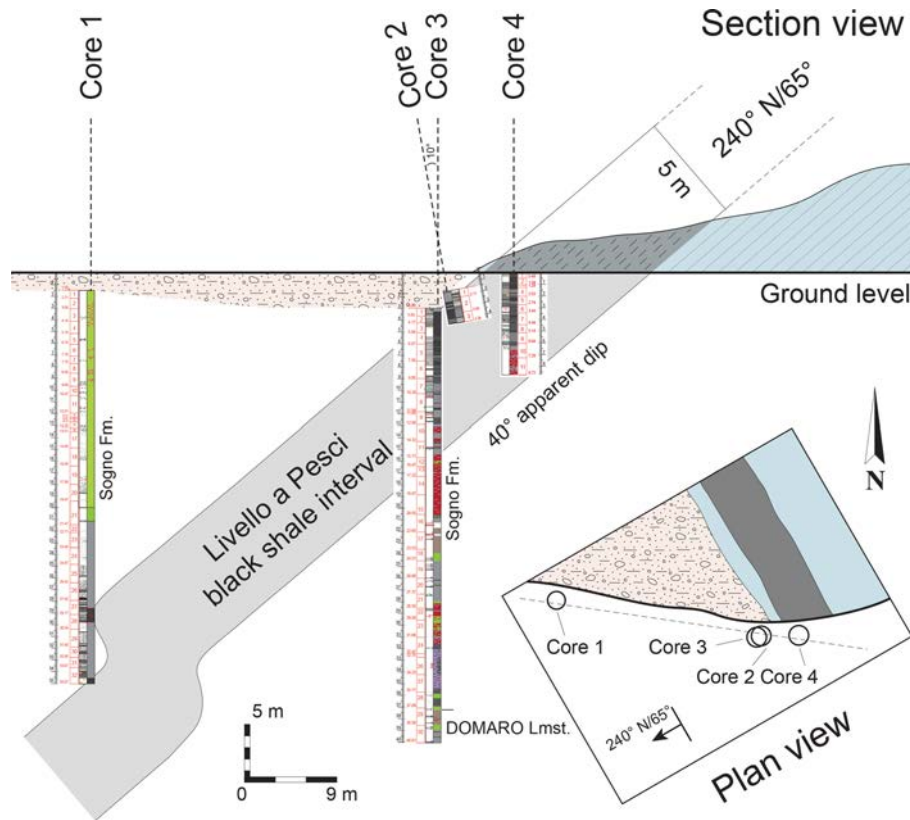


**Figure 4.** Section and plan view of the relative positions of the four boreholes drilled at Colle di Sogno. A pronounced fold was encountered at  $\sim 25$  m penetration depth in Sogno borehole 1 that was abandoned after reaching the topmost part of the black shale interval. Three additional boreholes were cored as explained in the text.

Alpi (Fig. 1). The outcropping beds show a strike of  $245^\circ$  and a dip of  $46^\circ$  to the northwest ( $335^\circ$ ).

A single borehole was drilled at Gajum to a total penetration depth of 42.37 m, with 100 % recovery of excellent-quality material throughout drilling operation. For each core a set of dip measurements was taken during lab preparation, with four measurements on average, and used to calculate the corrected thickness of the drilled section as 28.18 m after removal of 3 m of rubble at the top. As for the Sogno core, lithostratigraphic units were defined based on lithological features and sedimentary structures. The dip measured in individual cores (variable in the range of 40 to  $50^\circ$ ) was used to calculate the “stratigraphic thickness” of each lithostratigraphic unit described below, from the topmost to the bottommost:

- *Unit 1 (3.00 to 4.35 m): dark brown to dusky red nodular limestone.* nodules are 3–5 cm in size and light grey in colour. A resedimented level, consisting of a microbreccia, is detected at 3.92–3.96 m. This unit corresponds to the lower part of the Rosso Ammonitico Lombardo.
- *Unit 2 (4.35 to 7.60 m): marly limestone, grey to olive grey in colour, with dark grey laminated intervals.* Three

black shale intervals occur at 5.24–5.35, 6.26–6.43, and 6.70–6.81 m.

- *Unit 3 (7.60 to 10.60 m): grey to dark grey marly limestone, with heavily bioturbated levels alternating with intervals characterized by faint lamination.* Some pyrite nodules are observed in the lowermost part of the unit.
- *Unit 4 (10.60 to 21.39 m): dark to very dark grey to black marly claystones.* This “black shale” interval is characterized by well-developed lamination and frequent pyrite nodules. In the upper and middle portion, discrete intervals with faint bioturbation are observed.
- *Unit 5 (21.39 to 25.42 m): dark to very dark grey to black marly claystones characterized by well-developed lamination and a few pyrite nodules.* Three intervals of dusky red limy cherts are identified at 21.39–21.87, 23.52–23.81, and 24.30–25.52 m. The highest and lowest cherty reddish levels delimit the top and bottom of this unit, respectively.
- *Unit 6 (25.42 to 26.95 m): dark grey to very dark grey to black marly claystones, with evident laminations and sporadic faint bioturbations.* The base is undulated.

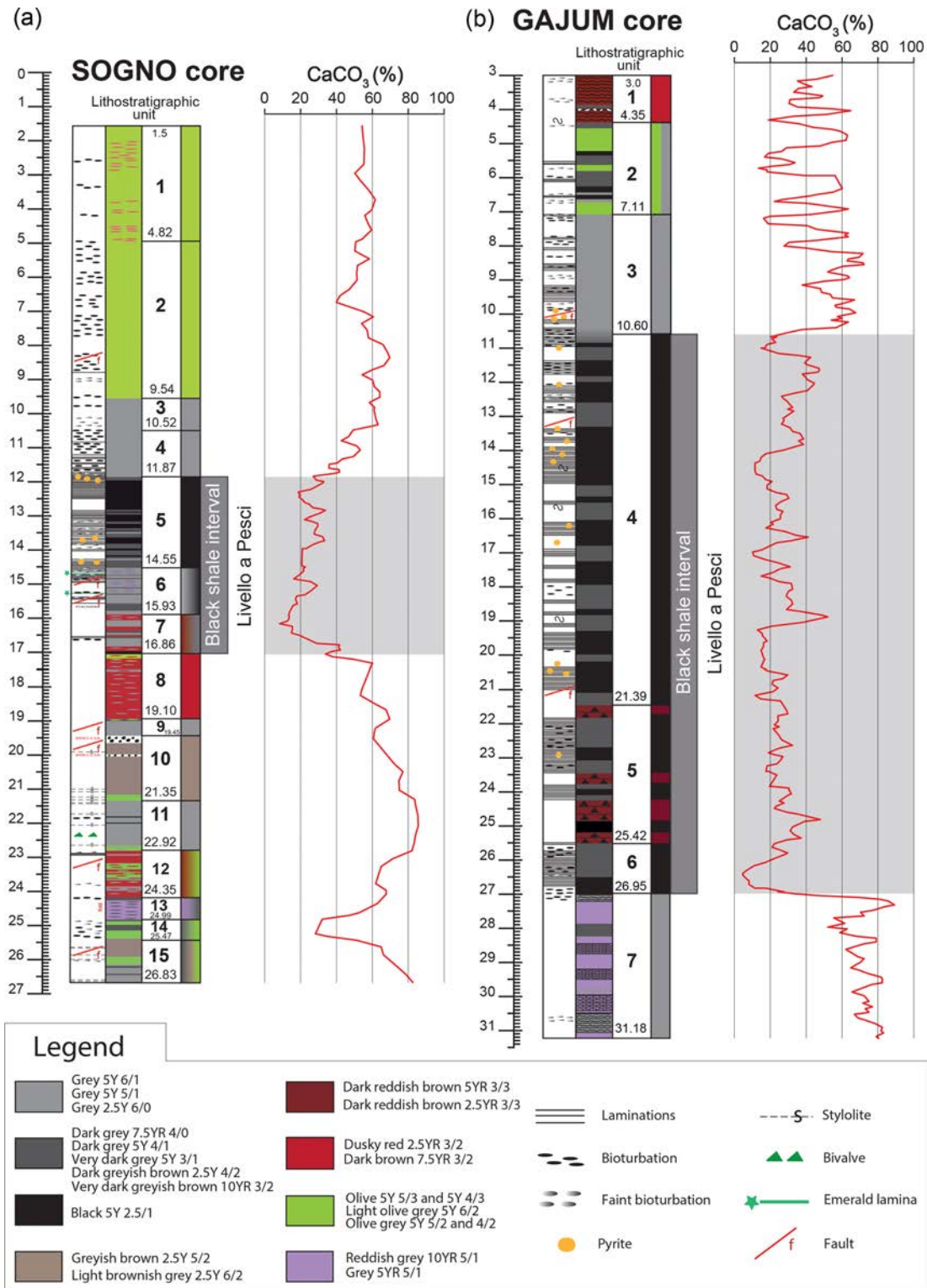


**Figure 5.** Lithostratigraphy and calcium carbonate content of the Sogno (a) and Gajum (b) cores. The grey pattern highlights the Livello a Pesci black shale interval that is the lithostratigraphic record of the T-OAE in the Lombardy Basin. The CaCO<sub>3</sub> content was detected using the Dietrich-Frühling gas volumetric method by measuring evolved CO<sub>2</sub> after acidification of the bulk sample with HCl.



– Unit 7 (26.95 to 31.18 m): grey to reddish grey marly limestones, with fractures filled by diagenetic calcite.

In Fig. 5 the Sogno and Gajum cores are correlated: the T-OAE black shale interval is represented in both sections, but with significantly different thicknesses, namely 4.98 m in the Sogno core and 15.35 m in the Gajum core. The lithostratigraphic onset and termination of the Livello a Pesci black shale interval, based on the lowest and highest black marly claystones, are nicely preserved in both cores, without lithologic evidence of hiatus or disturbance. In the Gajum core the beginning of the anoxic interval is quite abrupt and represented by the change from a few centimetres thick, grey, pseudonodular, and heavily bioturbated marly limestone to black shales with an irregular base mimicking nodularity of the underlying interval: this lithostratigraphic boundary is very similar to the onset of the early Aptian OAE1a in the Cismon core (Erba et al., 2010; Fig. 2). The upper boundary is, conversely, relatively transitional from laminated black shales to dark grey marly limestones. In the Sogno core, instead, both the base and top of the black shale interval are sharp.

The Livello a Pesci is not homogeneous in the Sogno and Gajum cores: in both records, the lower part is characterized by the occurrence of a few reddish levels. These are cherty in the Gajum core (Unit 5) and clayey in the Sogno core (Unit 7). Also, black shales are dominant in the upper part of the Livello a Pesci in both cores (Unit 4 of the Gajum core and Unit 5 of the Sogno core).

As far as the calcium carbonate content is concerned (Fig. 5) in the Sogno and Gajum cores, the interval below the Livello a Pesci is characterized by values of around 60 % and 60 %–80 % CaCO<sub>3</sub>, respectively. A drop in calcium carbonate content to an average of 20 % is recorded within the black shale interval in both cores, with lowermost values of 5 % (Gajum core) to 10 % (Sogno core) in the lowermost part. Above the Livello a Pesci, the calcium carbonate content reverts to 40 %–60 %, with frequent fluctuations.

## 5 Future objectives

The fresh material recovered with the Sogno and Gajum cores provide complete and relatively expanded pelagic records from the western Tethys Ocean. Detailed multidisciplinary investigations are in progress to collect multi-proxy records for building a high-resolution dataset prodromic for modelling the nature and significance of the T-OAE. The specific objectives are as follows:

1. *High-resolution integrated stratigraphy.* This is based on nannofossil biostratigraphy, magnetostratigraphy, chemostratigraphy, and cyclostratigraphy. Milankovitch cycles will be used to estimate durations of the T-OAE.
2. *Detailed studies of critical paleoceanographic parameters.* This includes total organic carbon; isotopic anomalies;

and major, minor and trace elements that will be used to assess changes in surface and bottom water mass characteristics.

3. *Identification and quantification of the response of the biosphere.* This is based on quantitative and high-resolution investigation of calcareous phytoplankton assemblages. In particular, we will focus on the relative timing and possible phase-lag of the response to the overwhelming forcing function/s. These relationships will be used to model the resilience of the oceanic biosphere.
4. *Characterization of the Early Jurassic climate, ocean dynamics, and their response to orbital cyclicity.* In particular, we plan to decipher local from regional and global changes across the paleoenvironmental perturbation. Also, the cyclostratigraphy will allow for the assessment of the influence of eccentricity, obliquity, and precession cycles before, during, and after the T-OAE.

**Data availability.** The Sogno and Gajum cores are stored at the Department of Earth Sciences “Ardito Desio” of the University of Milan (Italy). Data are publicly accessible upon request.

**Author contributions.** EE conceived and executed the Sogno and Gajum coring. She coordinated the lab core work and prepared the paper. GG co-supervised the core description and contributed to the paper. Other co-authors (SV, LC, DR, GF, MP) contributed to core splitting, archiving, and sampling.

**Competing interests.** The authors declare that they have no conflict of interest.

**Acknowledgements.** The T-OAE coring project derived from fieldwork and in-depth discussions with Maurizio Gaetani on Jurassic stratigraphy of the Lombardy Basin. We acknowledge the editor Thomas Wiersberg, and the two reviewers Alicia Fantasia and Stephen Hesselbo, who greatly improved the quality of the paper with their constructive comments.

**Financial support.** This research has been supported by the MIUR (MIUR-PRIN2011 grant no. 2010X3PP8J) awarded to Elisabetta Erba.

**Review statement.** This paper was edited by Thomas Wiersberg and reviewed by Stephen Hesselbo and Alicia Fantasia.

## References

- Al-Suwaidi A. H., Angelozzi, G. N., Baudin F., Damborenea, S. E., Hesselbo, S. P., Jenkyns, H. C., Manceñido M. O., and Riccardi A. C.: First record of the Early Toarcian Oceanic Anoxic Event from the Southern Hemisphere, Neuquén Basin, Argentina, *J. Geol. Soc. London*, 167, 633–636, 2010.
- Bellanca, A., Masetti, D., Neri, R., and Venezia, F.: Geochemical and sedimentological evidence of productivity cycles recorded in Toarcian black shales from the Belluno Basin, Southern Alps, northern Italy, *J. Sediment. Res.*, 69B, 466–476, 1999.
- Bernoulli, D. and Jenkyns, H. C.: Alpine, Mediterranean, and Central Atlantic Mesozoic facies in relation to the early evolution of the Tethys, in: *Modern and Ancient Geosynclinal Sedimentation*, edited by: Dott, R. H. and Shaver R. H., *Soc. Econ. Paleont. Mineral., Spec. Publ.*, 19, 129–160, 1974.
- Bernoulli, D. and Jenkyns, H. C.: Ancient oceans and continental margins of the Alpine-Mediterranean Tethys: Deciphering clues from Mesozoic pelagic sediments and ophiolites, *Sedimentology*, 56, 149–190, 2009.
- Bosence, D., Procter, E., Aurell, M., Kahla, A. B., Boudagher-Fadel, M., Casaglia, F., Cirilli, S., Mehdie, M., Nieto, L., Rey, J., Scherreiks, R., Soussi, M., and Waltham, D.: A Dominant Tectonic Signal in High-Frequency, Peritidal Carbonate Cycles? A Regional Analysis of Liassic Platforms from Western Tethys, *J. Sediment. Res.*, 79, 389–415, 2009.
- Caruthers, A. H., Gröcke, D. R., and Smith, P. L.: The significance of an Early Jurassic (Toarcian) carbon-isotope excursion in Haida Gwaii (Queen Charlotte Islands), British Columbia, Canada, *Earth Planet. Sc. Lett.*, 307, 19–26, 2011.
- Casellato, C. E. and Erba, E.: Calcareous nanofossil biostratigraphy and paleoceanography of the Toarcian Oceanic Anoxic Event at Colle di Sogno section (Southern Alps, Italy), *Riv. Ital. Paleontol. S.*, 105, 343–376, 2015.
- Channell, J. E. T., Casellato, C. E., Muttoni, G., and Erba, E.: Magnetostratigraphy, nanofossil stratigraphy and apparent polar wander for Adria-Africa in the Jurassic–Cretaceous boundary interval, *Palaeogeogr. Palaeoclimatol.*, 293, 51–75, 2010.
- Cohen, A. S., Coe, A. L., Harding, S. M., and Schwark, L.: Osmium isotope evidence for the regulation of atmospheric CO<sub>2</sub> by continental weathering, *Geology*, 32, 157–160, 2004.
- Dera, G., Brigaud, B., Monna, F., Laffont, R., Pucéat, E., Deconinck, J.-F., Pellenard, P., Joachimski, M. M., and Durllet, C.: Climatic ups and downs in a disturbed Jurassic world, *Geology*, 39, 215–218, 2011.
- Emmanuel, L., Renard, M., Cubaynes, R., De Rafelis, M., Hermoso, M., Lecallonnec, L., Le Solleuz, A., and Rey, J.: The “Schistes Carton” of Quercy (Tarn, France): a lithological signature of a methane hydrate dissociation event in the early Toarcian. Implications for correlations between Boreal and Tethyan realms, *Bull. Soc. Géol. Fr.*, 177, 239–249, 2006.
- Erba, E.: Calcareous nanofossils and Mesozoic oceanic anoxic events, *Mar. Micropaleontol.*, 52, 85–106, 2004.
- Erba, E. and Casellato C. E.: Paleoceanografia del Giurassico nella Tetide occidentale: l’archivio geologico del Bacino Lombardo, *Rendiconti dell’Istituto Lombardo, Accademia di Scienze e Lettere, Special Publication on “Una nuova Geologia per la Lombardia”*, 447, 115–140, 2010.
- Erba, E., Bottini, C., Weissert, H. J., and Keller, C. E.: Calcareous nanoplankton response to surface-water acidification around Oceanic Anoxic Event 1a, *Science*, 329, 428–432, 2010.
- Erba, E., Bottini, C., Faucher, G., Gambacorta, G., and Visentin, S.: The response of calcareous nanoplankton to Oceanic Anoxic Events: The Italian pelagic record, *B. Soc. Paleontol. Ital.*, 58, 51–71, 2019.
- Fantasia, A., Föllmi, K. B., Adatte, T., Bernàirdez, E., Spangenberg, J. E., and Mattioli, E.: The Toarcian Oceanic Anoxic Event in southwestern Gondwana: an example from the Andean Basin, northern Chile, *J. Geol. Soc.*, 175, 883–902, 2018.
- Farrimond, P., Englinton, G., Brassell, S. C., and Jenkyns, H. C.: The Toarcian black shale event in northern Italy, *Org. Geochem.*, 13, 823–832, 1988.
- Gaetani, M.: Jurassic stratigraphy of the Southern Alps: a review, *Geology of Italy*, 1, 377–402, 1975.
- Gaetani, M.: From Permian to Cretaceous: Adria as pivotal between extensions and rotations of Tethys and Atlantic Oceans, in: *The Geology of Italy*, edited by: Beltrando, M., Peccerillo, A., Mattei, M., Conticelli, S., and Doglioni, C., *J. Virt. Expl.*, 36, paper 5.a, <https://doi.org/10.3809/jvirtex.2010.00235>, 2010.
- Gaetani, M. and Erba, E.: Il bacino Lombardo: un sistema paleoalto/fossa in un margine continentale passivo durante il Giurassico, 75° Congresso Soc. Geol. It., 10–12 September 1990, Milano, Italy, Guida all’escursione A3, 1990.
- Gaetani, M. and Poliani, G.: Il Toarciano e il Giurassico medio in Albenza (Bergamo), *Riv. Ital. Paleontol. S.*, 84, 349–382, 1978.
- Gómez, J. J., Comas-Rengifo, M. J., and Goy, A.: Palaeoclimatic oscillations in the Pliensbachian (Early Jurassic) of the Asturian Basin (Northern Spain), *Clim. Past*, 12, 1199–1214, <https://doi.org/10.5194/cp-12-1199-2016>, 2016.
- Hardenbol, J., Thierry, J., Farley, M. B., Jacquin, T., de Graciansky, P.-C., and Vail, P. R.: Mesozoic and Cenozoic sequence chronostratigraphic framework of European basins, in: *Mesozoic and Cenozoic sequence stratigraphy of European basins*, edited by: de Graciansky, P.-C., Hardenbol, J., Jacquin T., and Vail, P. R., *SEPM Special Publication*, 60, 3–13, charts 1–8, Tulsa, Oklahoma, 1998.
- Haq, B. U., Hardenbol, J., and Vail, P. R.: Chronology of fluctuating sea-levels since the Triassic, *Nature*, 235, 1156–1167, 1987.
- Hesselbo, S. P., Gröcke, D. R., Jenkyns, H. C., Bjerrum, C. J., Farrimond, P., Morgans Bell, H. S., and Green, O. R.: Massive dissociation of gas hydrate during a Jurassic Oceanic Anoxic Event, *Nature*, 406, 392–395, 2000.
- Hesselbo, S. P., Jenkyns, H. C., Duarte, L. V., and Oliveira, L. C. V.: Carbon-isotope record of the Early Jurassic (Toarcian) Oceanic Anoxic Event from fossil wood and marine carbonate (Lusitanian Basin, Portugal), *Earth Planet. Sc. Lett.*, 253, 455–470, 2007.
- Hinnov, L. A. Park, J., and Erba E.: Lower-Middle Jurassic rhythmites from the Lombard Basin, Italy: a record of orbitally forced carbonate cycles modulated by secular environmental changes in West Tethys, in: *Advances in Jurassic Research*, edited by: Hall R. L. and Smith P. L., *Trans Tech Publications*, 437–454, Zurich, Switzerland, 2000.
- Izumi, K., Miyaji, T., and Tanabe, K.: Early Toarcian (Early Jurassic) oceanic anoxic event recorded in the shelf deposits in the northwestern Panthalassa: evidence from the Nishinakayama for-

- mation in the Toyora area, west Japan, *Palaeogeogr. Palaeoclimatol.*, 315–316, 100–108, 2012.
- Jenkyns, H. C.: The Early Toarcian and Cenomanian-Turonian anoxic events in Europe: comparisons and contrasts, *Geol. Rundsch.*, 74, 505–518, 1985.
- Jenkyns, H. C.: The Early Toarcian (Jurassic) Anoxic Event: stratigraphic, sedimentary and geochemical evidence, *Am. J. Sci.*, 288, 101–151, 1988.
- Jenkyns, H. C.: Geochemistry of oceanic anoxic events, *Geochem. Geophys. Geosyst.*, 11, Q03004, <https://doi.org/10.1029/2009GC002788>, 2010.
- Jenkyns, H. C. and Clayton, C. J.: Black shales and carbon isotopes in pelagic sediments from the Tethyan Lower Jurassic, *Sedimentology*, 33, 87–106, 1986.
- Jenkyns, H. C., Géczy, B., and Marshall, J. D.: Jurassic manganese carbonates of central Europe and the early Toarcian anoxic event, *J. Geol.*, 99, 137–149, 1991.
- Jenkyns, H. C., Jones, C. E., Gröcke, D. R., Hesselbo, S. P., and Parkinson, D. N.: Chemostratigraphy of the Jurassic System: applications, limitations and implications for palaeoceanography, *J. Geol. Soc.*, 159, 351–378, 2002.
- Kafousia, N., Karakitsios, V., Mattioli, E., Kenjo, S., and Jenkyns, H. C.: The Toarcian Oceanic Anoxic Event in the Ionian Zone, Greece, *Palaeogeogr. Palaeoclimatol.*, 393, 135–145, 2014.
- Korte, C. and Hesselbo, S. P.: Shallow marine carbon and oxygen isotope and elemental records indicate icehouse-greenhouse cycles during the early Jurassic, *Paleoceanography*, 26, PA4219, <https://doi.org/10.1029/2011PA002160>, 2011.
- Mattioli, E., Pittet, B., Bucefalo Palliani, R., Rohl, H.-J., Schmid-Rohl, A., and Morettini, E.: Phytoplankton evidence for timing and correlation of palaeoceanographical changes during the Early Toarcian oceanic anoxic event (Early Jurassic), *J. Geol. Soc. London*, 161, 685–693, 2004.
- Muttoni, G., Erba, E., Kent, D. V., and Bachtadse, V.: Mesozoic Alpine facies deposition as a result of past latitudinal plate motion, *Nature*, 434, 59–63, 2005.
- Pasquini, C. and Vercesi, P. L.: Tettonica sinsedimentaria e ricostruzione paleogeografica del margine occidentale dell'Alto dei Corni di Canzo nel Lias inferiore, *Memorie della Società Geologica Italiana*, 57, 107–114, 2002.
- Percival, L. M. E., Cohen, A. S., Davies, M. K., Dickson, A. J., Hesselbo, S. P., Jenkyns, H. C., Leng, M. J., Mather, T. A., Storm, M. S., and Xu, W.: Osmium isotope evidence for two pulses of increased continental weathering linked to Early Jurassic volcanism and climate change, *Geology*, 44, 759–762, 2016.
- Posenato, R., Bassi, D., Trecalli, A., and Parente, M.: Taphonomy and evolution of Lower Jurassic lithotid bivalve accumulations in the Apennine Carbonate Platform (southern Italy), *Palaeogeogr. Palaeoclimatol.*, 489, 261–271, 2018.
- Reolid, M.: Stable isotopes on foraminifera and ostracods for interpreting incidence of the Toarcian Oceanic Anoxic Event in Westernmost Tethys: role of water stagnation and productivity, *Palaeogeogr. Palaeoclimatol.*, 395, 77–91, 2014.
- Santantonio, M. and Carminati, E.: The Jurassic rifting evolution of the Apennines and Southern Alps (Italy): Parallels and differences, *Bull. Geol. Soc. Am.*, 124, 468–484, 2011.
- Schouten, S., van Kaam-Peters, H. M. E., Rijpstra, W. I. C., Schoell, M., and Sinninghe Damsté, J. S.: Effects of an oceanic anoxic event on the stable carbon isotopic composition of early Toarcian carbon, *Am. J. Sci.*, 300, 1–22, 2000.
- Solomon, S., Plattner, G.-K., Knutti, R., and Friedlingstein, P.: Irreversible climate change due to carbon dioxide emissions, *P. Natl. Acad. Sci. USA*, 106, 1704–1709, 2009.
- Them, T. R., Gill, B. C., Selby, D., Gröcke, D. R., Friedman, R. M., and Owens, J. D.: Evidence for rapid weathering response to climatic warming during the Toarcian Oceanic Anoxic Event, *Sci. Rep.*, 7, 5003, <https://doi.org/10.1038/s41598-017-05307-y>, 2017.
- Tintori, A.: Toarcian fishes from the Lombardy Basin, *B. Soc. Paleontol. Ital.*, 16, 143–152, 1977.
- Trecalli, A., Spangenberg, J., Adatte, T., Föllmi, K. B., and Parente, M.: Carbonate platform evidence of ocean acidification at the onset of the early Toarcian oceanic anoxic event, *Earth Planet. Sc. Lett.*, 357–358, 214–225, 2012.
- van Breugel, Y., Baas, M., Schouten, S., Mattioli, E., and Damsté, J. S. S.: Isorenieratane record in black shales from the Paris Basin, France: Constraints on recycling of respired CO<sub>2</sub> as a mechanism for negative carbon isotope shifts during the Toarcian oceanic anoxic event, *Paleoceanography*, 21, PA4220, <https://doi.org/10.1029/2006PA001305>, 2006.
- Xu, W., Ruhl, M., Jenkyns, H. C., Hesselbo, S. P., Riding, J. B., Selby, D., Naafs, B. D. A., Weijers, J. W. H., Pancost, R. D., Tegelaar, E., and Idiz, E.: Carbon sequestration in an expanded lake system during the Toarcian oceanic anoxic event, *Nat. Geosci.*, 10, 129–134, 2017.

---

### 3. Carbon- and oxygen-isotope signature of the Toarcian Oceanic Anoxic event: insights from two Tethyan pelagic sequences (Gajum and Sogno Cores - Lombardy Basin, northern Italy)

In *Newsletters on Stratigraphy*, published online Feb. 2022

10.1127/nos/2022/0690

**Author(s):** E. Erba, L. Cavalheiro, A.J. Dickson, G. Faucher, G. Gambacorta, H.C. Jenkyns, and T. Wagner

#### **Abstract**

The early Toarcian Oceanic Anoxic Event (T-OAE) was associated with major climatic changes involving profound effects on the global carbon cycle. In this study, we present new carbon- and oxygen-isotope, CaCO<sub>3</sub> and total organic carbon (TOC) records from two cores (Sogno and Gajum Cores) that recovered pelagic successions from north-western Tethys. A palaeobathymetry of about 1000 and 1500 m water depth is tentatively reconstructed for the Gajum and Sogno sites, respectively. The investigated sections thereby represent some of the deepest records of the T-OAE in the western Tethys. During the early Toarcian, sedimentation in the Lombardy Basin (Southern Alps, northern Italy) was characterized by the deposition of the Fish Level (Livello a Pesci), a dark grey to black marly claystone with low CaCO<sub>3</sub> content and relatively high TOC content. In the two cores, the Fish Level (~5 m and ~15 m-thick at Sogno and Gajum, respectively) is subdivided into three lithostratigraphic intervals: a lower part, with minimum 28 CaCO<sub>3</sub> (5–10 %) and TOC (~ 0.2–0.3 %) values; a central part with a progressive increase in TOC up to ~ 1.4 %, and an upper part characterized by the highest TOC up to ~ 2.5 %. Within the Fish Level a lower grey interval and an upper black interval are defined based on lithological features. Carbon-isotope chemostratigraphy resolves a  $\delta^{13}\text{C}_{\text{carb}}$  negative excursion of ~ 3 ‰ at Sogno and ~ 6 ‰ at Gajum, and a  $\delta^{13}\text{C}_{\text{org}}$  negative excursion of ~ 7 ‰ at both locations. This global carbon cycle anomaly, named the ‘Jenkyns Event’, is here subdivided into a lower J1 and an upper J2 segment. As highlighted by lithostratigraphic evidence, nannofossil biostratigraphy and chemostratigraphic correlations, a hiatus elides part of the succession below the Fish Level in the Gajum Core, although without compromising the completeness of the Fish Level itself. High resolution  $\delta^{13}\text{C}$  data indicate that the base of the Fish Level is synchronous, but the top diachronous at the two coring sites. The same synchronicity of the base and diachroneity of the top of the black shale interval is identified in the Umbria-Marche Basin, suggesting that the duration of anoxia was not identical over very modest to relatively long distances.



# Carbon- and oxygen-isotope signature of the Toarcian Oceanic Anoxic Event: insights from two Tethyan pelagic sequences (Gajum and Sogno Cores – Lombardy Basin, northern Italy)

Elisabetta Erba<sup>1</sup>, Liyenne Cavalheiro<sup>1</sup>, Alexander J. Dickson<sup>2,3</sup>,  
Giulia Faucher<sup>1</sup>, Gabriele Gambacorta<sup>1\*</sup>, Hugh C. Jenkyns<sup>2</sup>  
and Thomas Wagner<sup>4</sup>

With 11 figures

**Abstract.** The early Toarcian Oceanic Anoxic Event (T-OAE) was associated with major climatic changes involving profound effects on the global carbon cycle. In this study, we present new carbon- and oxygen-isotope, CaCO<sub>3</sub> and total organic carbon (TOC) records from two cores (Sogno and Gajum Cores) that recovered pelagic successions from north-western Tethys. A palaeobathymetry of about 1000 and 1500 m water depth is tentatively reconstructed for the Gajum and Sogno sites, respectively. The investigated sections thereby represent some of the deepest records of the T-OAE in the western Tethys. During the early Toarcian, sedimentation in the Lombardy Basin (Southern Alps, northern Italy) was characterized by the deposition of the Fish Level (Livello a Pesci), a dark grey to black marly claystone with low CaCO<sub>3</sub> content and relatively high TOC content. In the two cores, the Fish Level (~5 m and ~15 m-thick at Sogno and Gajum, respectively) is subdivided into three lithostratigraphic intervals: a lower part, with minimum CaCO<sub>3</sub> (5–10 %) and TOC (~0.2–0.3 %) values; a central part with a progressive increase in TOC up to ~1.4 %, and an upper part characterized by the highest TOC up to ~2.5 %. Within the Fish Level a lower grey interval and an upper black interval are defined based on lithological features. Carbon-isotope chemostratigraphy resolves a  $\delta^{13}\text{C}_{\text{carb}}$  negative excursion of ~3 ‰ at Sogno and ~6 ‰ at Gajum, and a  $\delta^{13}\text{C}_{\text{org}}$  negative excursion of ~7 ‰ at both locations. This global carbon cycle anomaly, named the ‘Jenkyns Event’, is here subdivided into a lower J1 and an upper J2 segment. As highlighted by lithostratigraphic evidence, nannofossil biostratigraphy and chemostratigraphic correlations, a hiatus elides part of the succession below the Fish Level in the Gajum Core, although without compromising the completeness of the Fish Level itself. High-resolution  $\delta^{13}\text{C}$  data indicate that the base of the Fish Level is synchronous, but the top diachronous at the two coring sites. The same synchronicity of the base and diachroneity of the top of the black shale interval is identified in the Umbria-Marche Basin, suggesting that the duration of anoxia was not identical over very modest to relatively long distances.

**Key words.** T-OAE, Toarcian, C- and O-stable isotopes, chemostratigraphy, black shales

---

## Authors' addresses:

<sup>1</sup> Dipartimento di Scienze della Terra “A. Desio”, Università degli Studi di Milano, Via Mangiagalli 34, 20133, Milan, Italy

<sup>2</sup> Department of Earth Sciences, University of Oxford, South Parks Road, Oxford, OX1 3AN, U.K.

<sup>3</sup> Department of Earth Sciences, Royal Holloway University of London, Egham, Surrey, TW20 0EX, U.K.

<sup>4</sup> The Lyell Centre, School of Energy, Geoscience, Infrastructure and Society, Heriot-Watt University, Edinburgh, EH14 4AS, U.K.

\* Corresponding author: gabriele.gambacorta@guest.unimi.it

## 1. Introduction

The Toarcian Oceanic Anoxic Event (T-OAE) represents an episode of globally distributed anoxia with extensive accumulation of organic matter from coastal to pelagic settings (Jenkyns 1985, Jenkyns 1988, Jenkyns 2010). Release of high amounts of CO<sub>2</sub> are interpreted as triggers of extreme palaeoenvironmental change. Possible sources of greenhouse gases are related to the degassing of the Karoo–Ferrar large igneous province (Percival et al. 2015, Heimdal et al. 2021) and/or dissociation of methane hydrates along continental margins and/or terrestrial environments (Hesselbo et al. 2000, Pálffy and Smith 2000, McElwain et al. 2005, Svensen et al. 2007, Percival et al. 2015, Them et al. 2017, Ruebsam et al. 2019). Under greenhouse climatic conditions, an accelerated hydrological cycle, with enhanced continental weathering favoured by the elevated concentrations in atmospheric carbon dioxide, led to increased nutrient input into the oceans (Cohen et al. 2004, Jenkyns 2010, Percival et al. 2016, Izumi et al. 2018, Kemp et al. 2020).

The T-OAE, originally recognized due to the globally distributed record of a coeval lower Toarcian black shale (Jenkyns 1985), is associated with a negative carbonate and organic-carbon isotope anomaly measured both in terrestrial (lacustrine), shallow- and deep-marine archives, including sediments from the ancestral Pacific Ocean (Jenkyns and Clayton 1986, Hesselbo et al. 2000, Hesselbo et al. 2007, Schouten et al. 2000, Röhl et al. 2001, Jenkyns et al. 2001, Jenkyns et al. 2002, McElwain et al. 2002, Kemp et al. 2005, Emmanuel et al. 2006, van Breugel et al. 2006, Sabatino et al. 2009, Al-Suwaidi et al. 2010, Caruthers et al. 2011, Gröcke et al. 2011, Hesselbo and Pieńkowski 2011, Kafousia et al. 2011, Kafousia et al. 2014, Izumi et al. 2012, Trabucho-Alexandre et al. 2012, Reolid 2014, Xu et al. 2017, Them et al. 2017, Fantasia et al. 2018, Ikeda et al. 2018, Filatova et al. 2020, Reolid et al. 2020, Ruebsam and Al-Husseini 2020, Ramirez and Algeo 2020, Hougård et al. 2021).

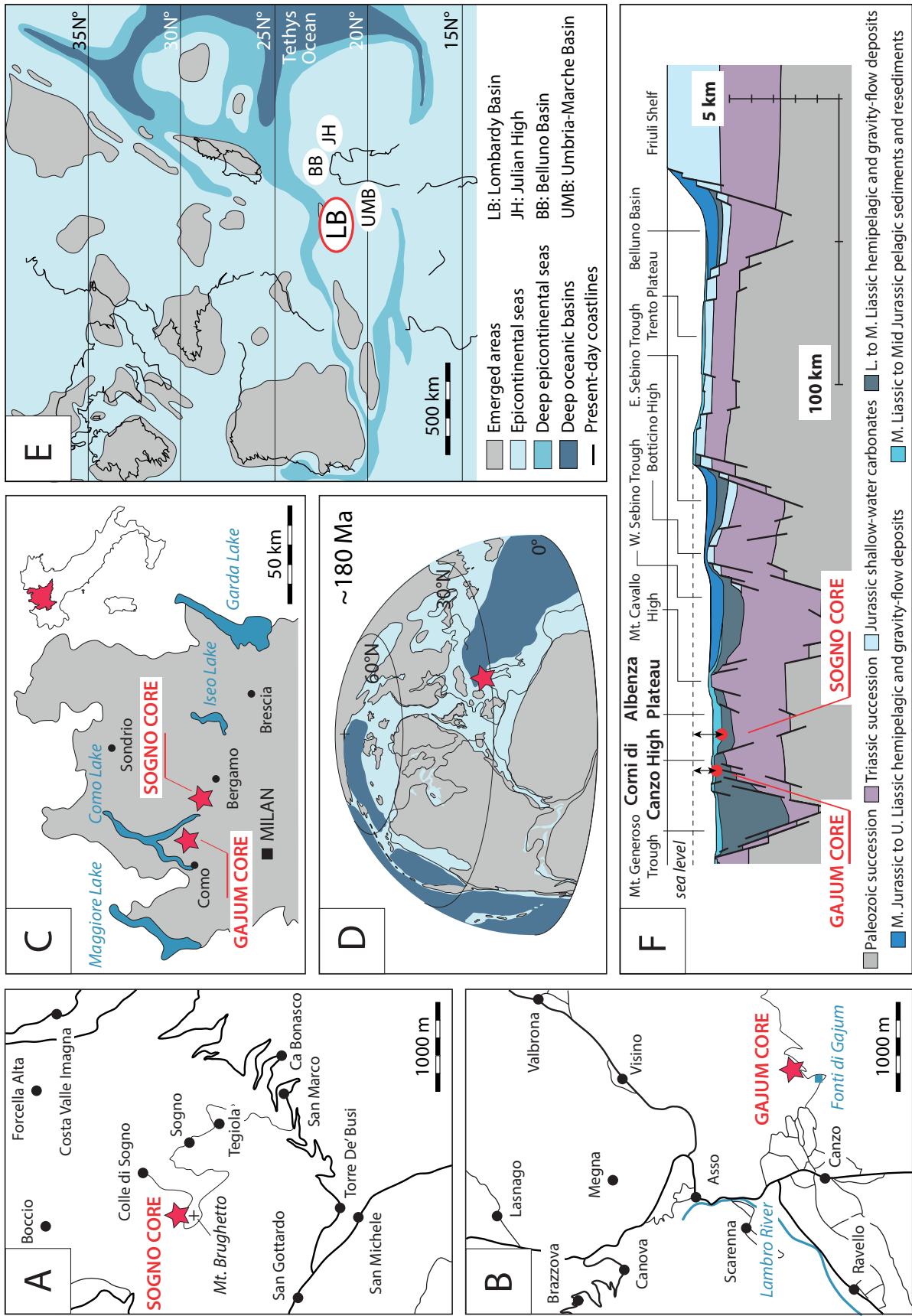
Long time-series show that this negative isotope excursion intersects an overarching positive excursion extending over much of the lower Toarcian (Jenkyns and Clayton 1997, Jenkyns 2003, Xu et al. 2018, Storm et al. 2020). Thermogenic methane associated with metamorphism of organic-rich sediment, dissociation of marine or terrestrial clathrates, and volcanogenic CO<sub>2</sub> have been variously credited with causing the observed negative carbon-isotope anomaly; the exten-

sive broad positive carbon-isotope excursion is attributed to accelerated global marine and lacustrine carbon burial (Jenkyns 1988, Jenkyns 2010, Fantasia et al. 2018, Xu et al. 2018).

Both strontium-isotope (<sup>87</sup>Sr/<sup>86</sup>Sr) and osmium-isotope (<sup>187</sup>Os/<sup>188</sup>Os) anomalies have also been documented as evidence of accelerated continental weathering in response to a global climate change (Jenkyns 2003, Jenkyns 2010, Cohen et al. 2004, Ullmann et al. 2013, Percival et al. 2016, Them et al. 2017, Jenkyns and Macfarlane 2021) with extraordinary warmth (Dera et al. 2011, Korte and Hesselbo 2011, Gómez et al. 2016, Ruebsam et al. 2020) associated with a major marine transgression (Hallam 1981, Haq et al. 1987, Hardenbol et al. 1998). Available records suggest that, in addition to anoxia, these extreme conditions triggered a biocalcification crisis (Erba 2004, Mattioli et al. 2004, Tremolada et al. 2005, Casellato and Erba 2015, Erba et al. 2019a, Reolid et al. 2020), enhanced primary productivity (Erba 2004, Jenkyns 2010), and ocean acidification (Erba 2004, Trecalli et al. 2012, Casellato and Erba 2015, Posenato et al. 2018, Müller et al. 2020, Ettinger et al. 2021).

New carbon- and oxygen-isotope data calibrated against nannofossil biostratigraphy are presented from two Italian pelagic sequences of latest Pliensbachian–early Toarcian age cored in the Lombardy Basin (Southern Alps, northern Italy) (Fig. 1). Excellent recovery of the Sogno and Gajum Cores (Erba et al. 2019b) provided high-quality material for this study. The estimated palaeowater depth of the selected pelagic sites ranges from 1000–2000 m (Gaetani and Poliani 1978), thereby representing some of the deepest records known of the T-OAE and potentially offering new insights into the dynamics of the Tethyan deep carbonate system under environmentally perturbed conditions. The primary objective of this account is to utilize the detailed characterization of the

**Fig. 1.** A. and B. Present-day location of the Sogno and Gajum drilling sites. C. Present-day map of the Lombardy area. D. Palaeogeographic location of the studied successions during the Toarcian (~180 Ma) (modified after Scotese 2011). E. Early Toarcian palaeogeographic map of the western Tethys and European epicontinental sea (modified after Fantasia et al. 2019). F. Schematic section across the Lombardy Basin during the Jurassic (modified after Bernoulli et al. 1979). The palaeo-locations of the two studied sites are indicated.



carbon-isotope stratigraphy of the T-OAE in the Lombardy Basin to investigate the causes and consequences of this major environmental perturbation. In particular, the identification of local/regional versus global isotopic signals should allow the disentangling of small-scale changes from global forcing functions that influenced the ocean/atmosphere system.

## 2. Geological setting

The Lombardy Basin, located in northern Italy (Fig. 1A), was part of the relatively undeformed portion of the continental margin of the Adria microplate in the western Tethys Ocean (Gaetani 2010) (Figs. 1B and 1C). A latest Triassic–earliest Jurassic multiphase rifting, associated with some environmental change, disrupted a relatively continuous carbonate-platform belt producing an articulated “horst and graben” bathymetry in a pelagic setting (Bernoulli and Jenkyns 1974, Bernoulli and Jenkyns 2009, Winterer and Bosellini 1981, Bosence et al. 2009, Santantonio and Carminati 2011, Jenkyns 2020). This palaeogeographic configuration is clearly documented by different sedimentary regimes with deeper zones characterized by thick relatively complete successions, whereas typically condensed and incomplete sequences accumulated on structural highs (Gaetani 1975, Gaetani 2010). During the Early Jurassic the Lombardy Basin became a relatively deep, fully pelagic area between the Lugano High to the west and the Trento Plateau to the east, further subdivided into a number of troughs and palaeohighs that are, from west to east: Monte Nudo Trough, Lugano High, Generoso Trough, Corni di Canzo High, Albenza Plateau, Monte Cavallo High, Sebino Trough, Botticino High (Fig. 1F). Slopes connecting structural highs to troughs were marked by slumps, resedimented bodies, and, locally, megabreccias (Castellarin 1972, Gaetani and Erba 1990, Pasquini and Vercesi 2002, Gaetani 2010).

During the early Toarcian, sedimentation in the Lombardy Basin was characterized by the deposition of the so-called Fish Level (Livello a Pesci) (Tintori 1977, Gaetani and Poliani 1978, Erba and Casellato 2010, Erba et al. 2019a), a typically 0.5 to 5 m-thick dark grey to black marly claystone interval, with a thickness of up to few tens of metres in the most expanded sections.

The Sogno Core (45°47'20.5" N, 9°28'30.0" E) (Erba et al. 2019b) was drilled next to the outcropping type-section of the Sogno Formation (Gaetani and

Poliani 1978), along the road SP 179 on the northern slope of Monte Brughetto (Gaetani and Poliani 1978, Jenkyns and Clayton 1986, Gaetani and Erba 1990, Hinnov et al. 2000, Muttoni et al. 2005, Channell et al. 2010, Casellato and Erba 2015) (Fig. 1A). The lower Toarcian portion of the Sogno Formation, no longer well exposed, consists of about 24 metres of varicoloured limestones and marlstones, with calcareous claystones as minor lithologies overlying the grey, more massive Domaro Limestone Formation, about a metre of which was recovered in the bottom part of the core (Fig. 2). The cored Fish Level (*sensu* Gaetani and Poliani 1978) consists of ~5 m of dark grey to black marly claystones. In particular, following the lithostratigraphy of Erba et al. (2019b), within the Fish Level three intervals are distinguished from bottom to top: an interval consisting of grey to very dark grey and dark red clayey marlstones (Unit 7); grey to very dark grey clayey marlstones with reddish to greyish spots (Unit 6); black shales characterized by well-developed lamination and pyrite nodules (Unit 5).

The Gajum Core (45° 51' 3.2" N, 9° 17' 19.5" E) (Erba et al. 2019b) was drilled close to “Fonte Gajum” located east of Canzo (CO), in a lateral incision of the Ravella Valley next to the trail named Via delle Alpi (Fig. 1B). The marly limestones, marlstones and clayey marlstones of the Sogno Formation (about 22.5 metres) are separated from the underlying Domaro Limestone Formation (about 4 metres) by a sharp undulated lithological contact and overlain by about 1.5 metres of reddish nodular limestones of the Rosso Ammonitico Lombardo Formation (Fig. 3). The Fish Level in the Gajum Core is more expanded than in the Sogno Core, with a thickness of about 16 metres *versus* 5 metres, respectively. Following the lithostratigraphy of Erba et al. (2019b), three units are distinguished within the Fish Level, from bottom to top: an interval consisting of dark grey to very dark grey to black marly claystones, with evident laminations and local faint bioturbated patches (Unit 6); dark to very dark grey to black clayey marlstones interrupted by four intervals of dusky red limy cherts with a few levels characterized by green-coated limy-chert nodules (Unit 5); dark to very dark grey to black marly claystones with evident lamination and common pyrite nodules (Unit 4).

Figure 4 illustrates the lithological variations detected within the Fish Level at Sogno and Gajum showing two distinctive parts, namely a lower grey interval and an upper black interval. The latter is lithologically similar at the two sites, being character-



**SOGNO**

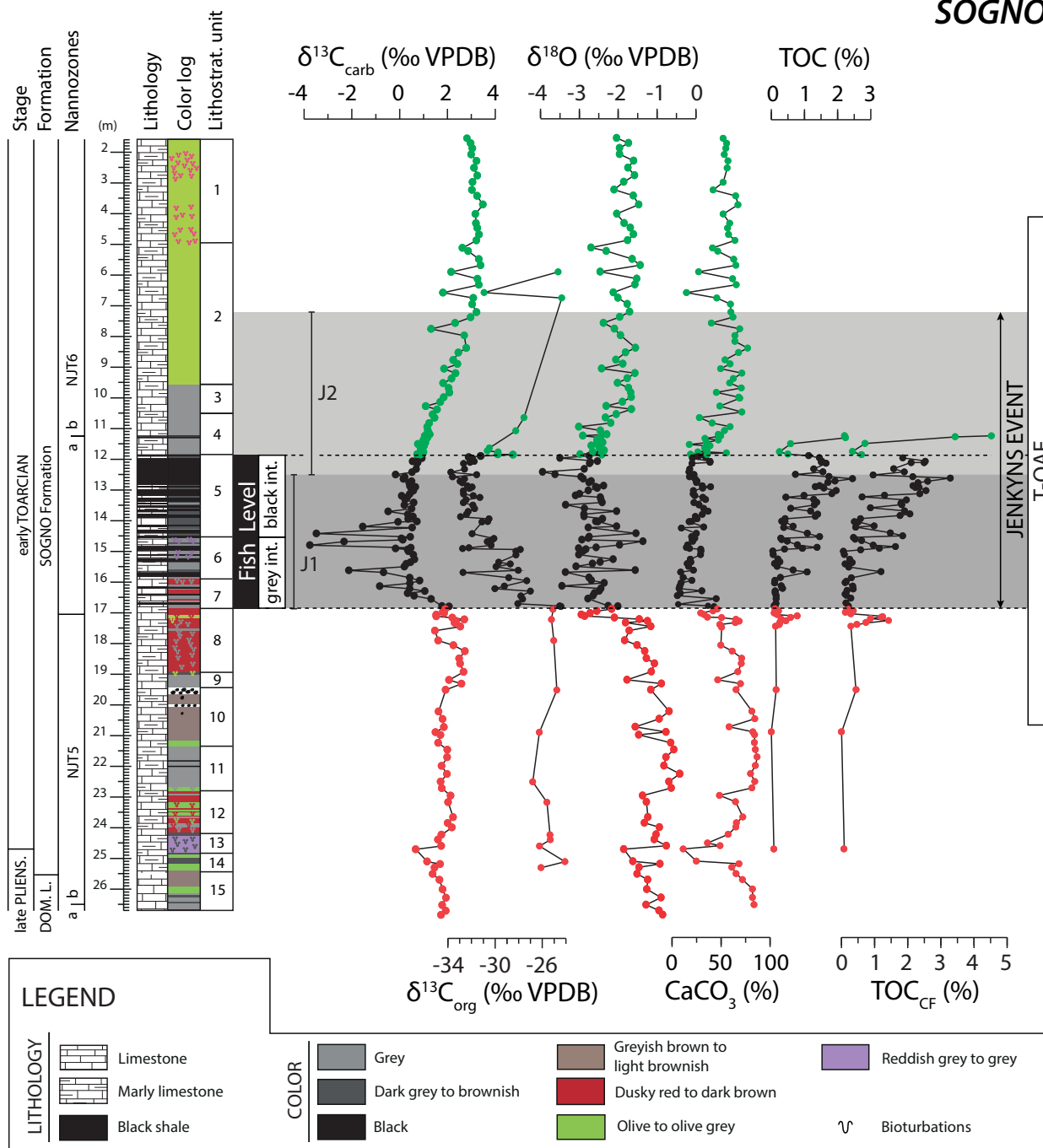


**Fig. 2.** Nannofossil biostratigraphy, lithostratigraphy, isotopic records ( $\delta^{13}C_{carb}$ ,  $\delta^{13}C_{org}$  and  $\delta^{18}O_{carb}$ ),  $CaCO_3$  content, total organic carbon (TOC), and total organic carbon on a carbonate-free basis ( $TOC_{CF}$ ) of the Sogno Core. Nannofossil biostratigraphy from Visentin and Erba (2021); lithostratigraphy and  $CaCO_3$  from Erba et al. (2019b). Samples below, within and above the Fish Level are indicated in red, black and green, respectively. The lower part (J1) and the upper part (J2) of the lithostratigraphic expression of the Jenkyns Event are highlighted with a dark grey and a light grey band, respectively (see text for explanation).

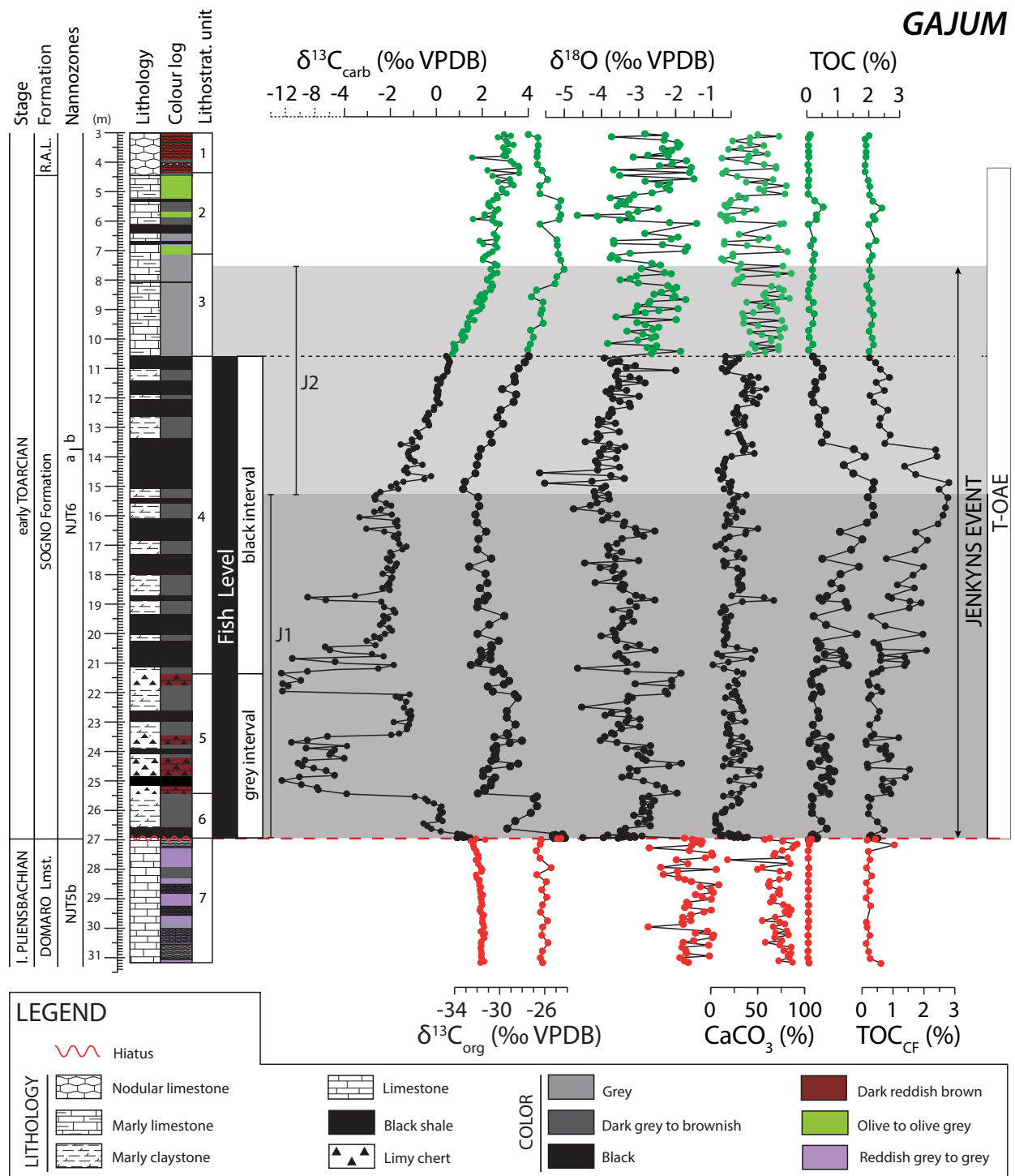


**Fig. 3.** Nannofossil biostratigraphy, lithostratigraphy, isotopic records ( $\delta^{13}\text{C}_{\text{carb}}$ ,  $\delta^{13}\text{C}_{\text{org}}$  and  $\delta^{18}\text{O}_{\text{carb}}$ ),  $\text{CaCO}_3$  content, total organic carbon (TOC), and total organic carbon on a carbonate-free basis ( $\text{TOC}_{\text{CF}}$ ) of the Gajum Core. Nannofossil biostratigraphy from Visentin and Erba (2021); lithostratigraphy and  $\text{CaCO}_3$  from Erba et al. (2019b). The hiatus at the base of the Fish Level is indicated by a red dashed line (see text for explanation). Samples below, within and above the Fish Level are indicated in red, black and green, respectively. For the sake of readability, lower  $\delta^{13}\text{C}_{\text{carb}}$  values are reported using a different scale. The lower part (J1) and the upper part (J2) of the lithostratigraphic expression of the Jenkyns Event are highlighted with a dark grey and a light grey band, respectively (see text for explanation).

ized by laminated fissile black shales, rich in pyrite powder and nodules, and very dark grey, homogenous to faintly bioturbated marly claystones. The lower grey interval, by contrast, predominantly consists of grey and bioturbated marly claystones with different intercalations of reddish lithologies. Whereas in the Sogno Core dusky red clayey marlstones characterize the lowermost part of the Fish Level (Unit 7 in Fig. 2), in the Gajum Core distinctive dark reddish brown limy chert levels occur in the upper part of the grey interval (Unit 5 in Fig. 3). Peculiar emerald-coloured mm-thick laminae are present at 14.69 and 15.28 m within Unit 6 in the Sogno Core (Fig. 4). In the Gajum Core, mm- to cm-sized pea-green coated nodules are documented in the dark red limy chert layers between 23.42 and 23.81 m and between 24.36 and 24.44 m (Fig. 4).

The Sogno and Gajum sites were located in quite different geological settings within the Lombardy Basin, on a pelagic plateau (Albenza Plateau) and in an inner basin along the slope of a structural high (Corni di Canzo Mt.), respectively (Gaetani and Erba 1990, Pasquini and Vercesi 2002, Gaetani 2010) (Fig. 1F). The Late Jurassic palaeobathymetry of the Southern Alps reconstructed by Bernoulli et al. (1979)

potentially provides some estimates of the former water depths of the Sogno and Gajum sites (Fig. 1F). However, these Late Jurassic depth estimates are in no way rigorously quantitative since they rely on regional stratigraphy, sedimentary geometry and thicknesses of the sequences together with the assumed palaeobathymetric significance of characteristic pelagic facies, as suggested by Bosellini and Winterer (1975). Gaetani (2010) detailed the Jurassic evolution of the Southern Alps as part of a passive continental margin adjacent to a spreading centre. The differential subsidence driven by the extensional regime was largely over by late Aalenian times, subsequently becoming more evenly distributed, as documented by the sedimentary successions in various portions of this Tethyan margin (Winterer and Bosellini 1981, Bernoulli and Jenkyns 1974, Bernoulli and Jenkyns 2009, Gaetani 2010). Consequently, following Jenkyns (1988), the position of Early Jurassic sea level can be equated to the top of the Trento Plateau that remained a shallow-water carbonate platform during the Hettangian–earliest Toarcian time interval, allowing an estimate of the palaeowater depths of troughs and highs within the adjacent Lombardy Basin. In this way, the palaeowater

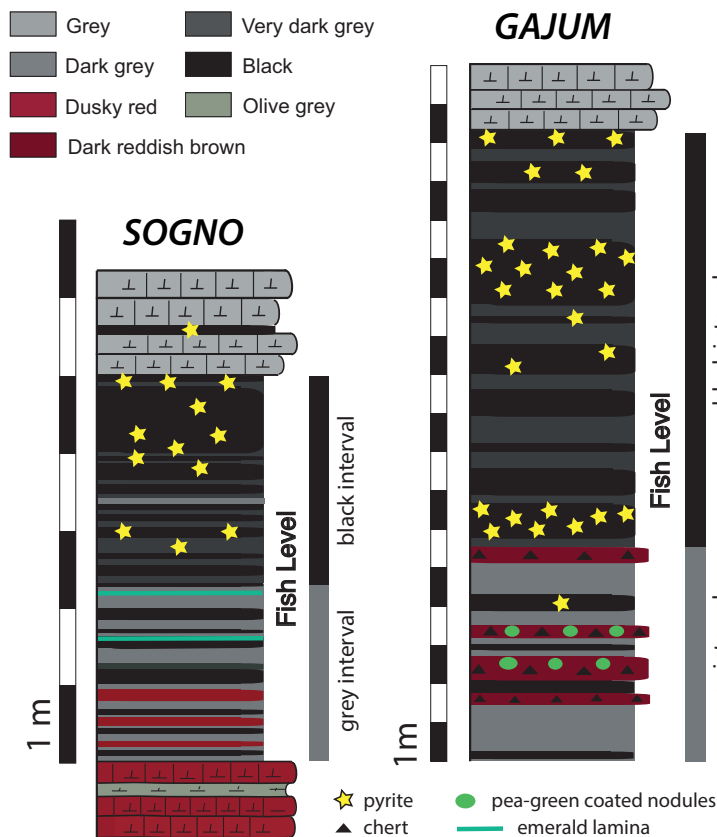


**Fig. 4.** Detailed lithostratigraphy of the Fish Level in the Sogno and Gajum Cores. Two distinctive parts, namely a lower grey interval and an upper black interval are distinguished. See text for details.

depths of the Sogno and Gajum sites are tentatively reconstructed to be about 1500 and about 1000 metres, respectively, during the Early Jurassic.

Generally, the palaeobathymetry of Early Jurassic basins in the southern part of the Tethyan area is poorly quantified. Excluding shallow-water carbonate platforms (e. g., Woodfine et al. 2008, Sabatino et al. 2009, Ettinger et al. 2021), information on water depths for pelagic–hemipelagic settings is scarce, although the reconstructions of Winterer (1998) for the eastern Lombardy Basin (Sebino Trough, Fig. 1F) suggests comparable palaeodepths to those suggested here for the Sogno and Gajum sites. A quantitative water-depth estimate for the Peniche section (Portugal) was given by Bjerrum et al. (2001), who proposed a figure of about 200 m for the shallow westerly dipping homoclinal ramp of the Lusitanian Basin. At the other extreme, the occurrence of radiolarites stratigraphically associated with organic-rich T-OAE shales in the Pindos Zone (northern Peloponnese, Greece) was used to suggest, for the so-called Kastelli Pelites, a water depth greater than that of typical Tethyan continental margins (Kafousia et al. 2011). This example apart, the investigated Sogno and Gajum sites provide some of the deepest records of the T-OAE to complement the information already available for shallower sites in the Tethyan region.

There has been a similar reticence in the literature to giving estimates for the depositional palaeodepths of T-OAE successions in the shelf seas of northern Europe, although studies of relative sea-level change during the Toarcian are relatively plentiful (e. g., Hesselbo and Jenkyns 1998, Röhl and Schmid-Röhl 2005). An overall stratigraphic association with current-bedded clastic sediments of various facies-types, as well as the local presence of silt-grade sedimentary structures in the black shales themselves, likely precludes deposition of the organic-rich sediments in great water depths (e. g., Trabucho-Alexandre et al. 2012). However, the prevailing anoxic to euxinic conditions would have required, during certain intervals at least, the presence of a modestly well-developed and stable water column. Hallam (1967) opted for a relatively shallow 15 to 30 m for the depositional depth of lower Toarcian black shales in Yorkshire, north-east England, whereas Frimmel et al. (2004) and Röhl et al. (2001) suggested figures of ~50 m and 100–150 m, respectively, for coeval facies in south-west Germany. The greater figures seem intrinsically more reasonable given the overall tectonic context of a shelf region undergoing crustal extension and subsidence accom-

panied by a regional sea-level rise. In any event, the contrast in proposed palaeobathymetry when compared with Tethyan pelagic facies in the Lombardy Basin is clear.

### 3. Material and methods

#### 3.1. Carbonate carbon and oxygen isotopes

A total of 173 bulk dried and ground samples of the Sogno Core (one sample every ~10–15 cm) were measured for carbon and oxygen stable isotopes. Measurements were performed at the Open University (U.K.) using a Thermo Delta-Plus Advantage mass spectrometer attached to a Thermo GasBench. Samples were reacted with phosphoric acid ( $\text{H}_3\text{PO}_4$ ) at 60 °C. Data were corrected to the VPDB scale with a linear two-point calibration using NBS-18 and NBS-19 ( $n = 3$  each) and an in-house Maastrichtian limestone. Reproducibility of replicated standards is better than  $\pm 0.1$  ‰ for  $\delta^{13}\text{C}_{\text{carb}}$  and  $\delta^{18}\text{O}_{\text{carb}}$ .

A total of 342 bulk dried and ground samples of the Gajum Core (one sample every 5–10 cm) were measured for stable carbon and oxygen isotopes at the Department of Earth Sciences “A. Desio”, Milan University. Measurements were performed using an automated carbonate preparation device (GasBench II) connected to a Delta V Advantage (Thermo Fisher Scientific Inc.) isotopic ratio mass spectrometer (IRMS). Weighed powders (about 200–1000  $\mu\text{g}$  each depending on sample carbonate content) were reacted with >99 percentage phosphoric acid ( $\text{H}_3\text{PO}_4$ ) at 70 °C. The reference materials used for carbon- and oxygen-isotope analyses are the international standards, IAEA 603 and NBS-18. Analytical reproducibility is better than  $\pm 0.1$  ‰. Stable-isotope ratios are reported using the conventional  $\delta$  notation to indicate per mil (‰) deviation from the VPDB standard (Coplen 1994).

#### 3.2. Organic-carbon isotopes

A sub-set of 77 bulk dried samples, principally covering the Fish Level interval of the Sogno Core, were analysed for bulk organic stable carbon-isotope ratios ( $\delta^{13}\text{C}_{\text{org}}$ ). Samples were crushed with an agate pestle and mortar to <125  $\mu\text{m}$ . Carbonate was removed by treating ~1 g of sample with 20 ml 1 M HCl, and heating on a hot plate for about 2 h. This phase was

repeated until no visible reaction occurred. The acid-treated samples were then washed with distilled deionised water three times to achieve a neutral pH, oven dried at 40 °C and re-crushed. A mass of decarbonated powder equivalent to ~20–100 µg C was then weighed into tin capsules for analysis. Measurements were made at the Open University (U.K.) using a Thermo Flash HT Elemental Analyser coupled to a MAT 253 mass spectrometer. Measured  $\delta^{13}\text{C}$  compositions were corrected to the VPDB scale with a three-point linear calibration using NIST 8572 glutamic acid ( $\delta^{13}\text{C} = -26.39\text{‰}$ ), IAEA CH-6 sucrose ( $\delta^{13}\text{C} = -10.45\text{‰}$ ) and L-Alanine ( $\delta^{13}\text{C} = -23.33\text{‰}$ ), measured in every sample batch. Sample isotopic ratios are reported as per mil deviation from the VPDB international standard (Coplen 1994). Reproducibility of  $\delta^{13}\text{C}_{\text{org}}$ , monitored by standard measurements and duplicates, is better than  $\pm 0.1\text{‰}$ .

For the Gajum Core, a sub-set of 158 bulk dried samples (one sample every ~20 cm) was analysed for  $\delta^{13}\text{C}_{\text{org}}$  at Iso-Analytical, Crewe Cheshire (U.K.). Weighed powdered samples were acidified with 2M HCl (~24 hours), then washed until reaching neutrality and oven-dried at 60 °C. Thereafter, an aliquot of the sample was weighed into a sealed tin capsule, which was loaded into an autosampler and analysed on a Europa Scientific Elemental Analyser – Isotope Ratio Mass Spectrometry (EA-IRMS). The temperature of the furnace was held at 1000 °C and the temperature in the region of the sample reached ~1700 °C. Calibration to the VPDB standard via IAEA-CH-6 sucrose ( $\delta^{13}\text{C} = -10.45\text{‰}$ ) was made daily using the in-house IA-R001 (wheat flour,  $\delta^{13}\text{C} = -26.43\text{‰}$ ), IA-R005 (beet sugar,  $\delta^{13}\text{C} = -26.03\text{‰}$ ) and IA-R006 (cane sugar,  $\delta^{13}\text{C} = -11.64\text{‰}$ ) internal standards. Analytical reproducibility is better than  $\pm 0.1\text{‰}$ .

### 3.3. Calcium carbonate content ( $\text{CaCO}_3$ )

The calcium carbonate ( $\text{CaCO}_3$ ) content of selected samples from both the Sogno ( $N = 163$  samples) and Gajum ( $N = 342$  samples) was measured at the Department of Earth Sciences “A. Desio”, Milan University. The  $\text{CaCO}_3$  content was detected using the Dietrich-Frühling gas volumetric method by measuring evolved  $\text{CO}_2$  after acidification of the bulk sample with HCl (see Erba et al. 2019b).  $\text{CaCO}_3$  results for both the Sogno and Gajum Cores are reported in weight percentage (%) (Figs. 2 and 3).

### 3.4. Total organic carbon (TOC)

A total of 79 samples of the Sogno Core, mainly from the Fish Level, were measured for total organic-carbon (TOC) content by Rock-Eval Pyrolysis 6 at the Department of Earth Sciences at Oxford University (U.K.). The TOC content of 158 samples of the Gajum Core was analysed along with bulk organic stable carbon isotopes at Iso-Analytical, Crewe Cheshire (U.K.), using a Europa Scientific Elemental Analyser – Isotope Ratio Mass Spectrometry (EA-IRMS). The total ion beam data recorded the percentage carbon of the acid-washed samples and was used to calculate the TOC values after subtracting the weight-loss data (total inorganic carbon = TIC) determined at the acid washing stage: i. e.,  $\% \text{TOC} = \% \text{TC} - \% \text{TIC}$ . TOC results for both the Sogno and Gajum Cores are reported in weight percentage (%) (Figs. 2 and 3).

Total organic carbon on a carbonate-free basis ( $\text{TOC}_{\text{CF}}$ ) was computed in order to compensate for the highly variable  $\text{CaCO}_3$  content and evaluate possible dilution effects on the measured total organic matter.  $\text{TOC}_{\text{CF}}$  was calculated using the following formula:

$$\text{TOC}_{\text{CF}} = \text{TOC} * \frac{100}{(100 - \text{CaCO}_3)}$$

## 4. Results

### 4.1. Carbonate carbon and oxygen isotopes

Carbonate carbon isotopes of the Sogno Core range between 3.5 ‰ and -3.8 ‰ (Fig. 2). In the upper Domaro Limestone and the lower Sogno Formation, carbon isotopes are relatively stable with average values of 1.9 ‰ between 26.83 m and 17.22 m. The carbon-isotope chemostratigraphy shows a minor but distinctive negative anomaly previously identified at the Pliensbachian/Toarcian boundary (Littler et al. 2010, da Rocha et al. 2016) at 24.69 m in the lowermost part of the Sogno Formation. Although in previous studies the base of the Toarcian has been placed at the base of the Sogno Formation (Gaetani and Poliani 1978, Casellato and Erba 2015) we believe that, in the Sogno Core, this stage boundary should be placed at the  $\delta^{13}\text{C}_{\text{carb}}$  minor anomaly as documented at the Peniche GSSP (da Rocha et al. 2016) (Fig. 2). Just below the base of the Fish Level,  $\delta^{13}\text{C}_{\text{carb}}$  values decrease sharply to 0.3 ‰, between 17.22 m and

16.36 m, and remain on average around 0.4 ‰ to about 12.51 m. Notably, negative spikes ranging from -0.5 to -3.7 ‰ occur between 16.13 m and 13.70 m. Starting from the topmost part of the Fish Level, the  $\delta^{13}\text{C}_{\text{carb}}$  record gradually increases towards positive values (12.51–6.33 m) until reaching relatively stable values of about 3 ‰ in the upper part of the cored interval (6.33 m–1.56 m). The pioneering work by Jenkyns and Clayton (1986) first documented a negative C-isotopic interval interrupting a positive excursion in the Sogno outcrop (equal to Monte Brughetto section of Gaetani and Poliani 1978). Although the stratigraphic resolution of the C and O stable isotopic analyses was much lower than in the present study, the values documented by Jenkyns and Clayton (1986) compare well with those derived from the Sogno Core.

In the Sogno Core, oxygen isotopes range between -4.4 ‰ and -0.9 ‰ (Fig. 2), generally showing scattered data. A relatively stable trend is observed from the base of the cored section to the interval just below the base of the Fish Level, documenting average values of -1.7 ‰ between 26.83 m and 17.27 m. Across the Fish Level,  $\delta^{18}\text{O}_{\text{carb}}$  data decrease gradually up to 12.42 m, showing average values of -3.1 ‰. Starting from the topmost part of the Fish Level, oxygen isotopes shift towards positive values (12.42–10.39 m), reaching relatively stable values of about -2.4 ‰ in the upper part of the cored interval between 10.39 m and 1.56 m. As for the  $\delta^{13}\text{C}_{\text{carb}}$  record, the oxygen isotope values obtained for the Sogno Core are fully consistent with data documented for the outcrop (Jenkyns and Clayton 1986).

Carbonate carbon isotopes of the Gajum Core range between 3.6 ‰ and -12.5 ‰ (Fig. 3). In the Domaro Limestone, carbon isotopes are stable around average values of 1.9 ‰ between 31.17 m and 26.96 m. At the contact between Domaro Limestone and the Fish Level, based on high-resolution data (one sample every 0.5–1 cm)  $\delta^{13}\text{C}_{\text{carb}}$  values show a minor increase from 1.5 ‰ to 2.1 ‰ (27.04–27.00 m), followed by a sharp decrease down to -0.6 ‰ at 26.44 m. Above, the carbon-isotope trend continues to a slight decrease across the Fish Level, with average values of about -2 ‰ up to 15.47 m. Notably, in the lower part of the Fish Level, three intervals characterized by a series of very negative values are identified: i) the stratigraphically lowest includes 21 negative data points down to -12.5 ‰ between 25.43 m and 23.51 m; ii) the second occurs between 21.97 m and 20.48 m, and includes 10 very negative data-points down to -12.5 ‰; iii) the uppermost interval consists of three data-points show-

ing values down to -9.0 ‰ between 18.88 m and 18.73 m. Starting from the upper part of the Fish Level, the  $\delta^{13}\text{C}_{\text{carb}}$  curve gradually shifts towards positive values (15.47–7.53 m) reaching relatively stable numbers around 2.7 ‰ in the upper part of the Sogno Formation and lower part of the Rosso Ammonitico Lombardo (7.53–3.08 m).

Oxygen isotopes in the Gajum Core range between -5.7 ‰ and -0.8 ‰, generally showing a large amount of data scatter (Fig. 3). The  $\delta^{18}\text{O}_{\text{carb}}$  values show a relatively stable trend from the base of the cored interval up to the base of the Fish Level, with average values of -1.5 ‰ between 31.17 m and 26.96 m. At the boundary between the Domaro Limestone and the Fish Level, a sharp decrease down to values of about -3 ‰ is documented. Across the Fish Level,  $\delta^{18}\text{O}_{\text{carb}}$  data show a gradual decrease up to 14.57 m, with average values of -3.3 ‰. In the upper part of the Fish Level (14.57–10.53 m), oxygen isotopes start shifting towards higher values returning to relatively stable levels, on average -2.7 ‰, between 10.53 m and 3.08 m.

## 4.2. Organic-carbon isotopes

Carbon isotopes on bulk organic matter in the Sogno Core range between -33.7 ‰ and -24.1 ‰ (Fig. 2). In the Domaro Limestone and the lower Sogno Formation,  $\delta^{13}\text{C}_{\text{org}}$  results are relatively stable with average values of -25.5 ‰ between 25.29 m and 16.88 m. At the base of the Fish Level, the  $\delta^{13}\text{C}_{\text{org}}$  curve shifts sharply to lower values of -24.4 ‰ to -27.7 ‰ between 16.79 m and 16.55 m. Across the Fish Level,  $\delta^{13}\text{C}_{\text{org}}$  data continue to decrease up to 12.42 m, with average values of -30.8 ‰. Jenkyns and Clayton (1986) provided  $\delta^{13}\text{C}_{\text{org}}$  data for the Fish Level cropping out at Monte Brughetto that are fully consistent with the Sogno Core record, albeit with lower resolution. Starting from the upper part of the Fish Level (12.42 m),  $\delta^{13}\text{C}_{\text{org}}$  data gradually shift towards higher values up to 10.65 m, reaching values up to -28 ‰. In the overlying organic-lean part of the Sogno Formation, only three samples were measured, which are characterized by an average value of -26.6 ‰ between 6.76 m and 5.91 m.

Carbon isotopes on bulk organic matter of the Gajum Core range between -33.3 ‰ and -24.3 ‰ (Fig. 3). In the Domaro Limestone,  $\delta^{13}\text{C}_{\text{org}}$  data are relatively stable around average values of -26.2 ‰ between 31.17 m and 26.96 m. At the contact between the Domaro Limestone and the Fish Level, high-

resolution data show a minor, initial increase from  $-25\text{‰}$  to  $-24.4\text{‰}$  (27.00–26.93 m), followed by a sharp and more pronounced decrease down to  $-29.4\text{‰}$  at 26.53 m. Across the Fish Level,  $\delta^{13}\text{C}_{\text{org}}$  values continue to decrease up to 15.10 m, reaching values of  $-33.3\text{‰}$ . Starting from the upper part of the Fish Level,  $\delta^{13}\text{C}_{\text{org}}$  values gradually increase (15.11–9.48 m), returning to relatively stable levels, on average  $-25.9\text{‰}$ , in the upper part of the Sogno Formation and Rosso Ammonitico Lombardo (9.48–3.08 m).

### 4.3. Calcium carbonate content ( $\text{CaCO}_3$ )

In the Sogno Core, the calcium carbonate content ranges between 5.5 % and 87.0 % (Fig. 2). In the upper Domaro Limestone and lower part of the Sogno Formation, the  $\text{CaCO}_3$  content is on average 62.9 % between 26.83 m and 16.88 m. However, a sharp decrease, down to 11.4 %, is documented between 26.00 m and 24.69 m.  $\text{CaCO}_3$  values decline from just below the base of the Fish Level, with a minimum of about 5 % in the lower Unit 7. In the Fish Level, the calcium carbonate content remains low, with average values of 23.5 % comparable to those documented by Jenkyns and Clayton (1986) for the Monte Brughetto outcrop.  $\text{CaCO}_3$  starts to rise again above the Fish Level, showing average values of 51.8 % in the upper part of the Sogno Core, between 11.86 m and 1.56 m. However, some fluctuations in the order of about 20–30 % are observed in this interval.

The calcium carbonate content of the Gajum Core ranges between 2.4 % and 92.3 % (Fig. 3). In the Domaro Limestone, the  $\text{CaCO}_3$  values are on average 73 % between 31.17 m and 26.96 m. At the base of the Fish Level,  $\text{CaCO}_3$  values sharply decrease down to  $\sim 10\%$  in the lower part of Unit 6. In the Fish Level, between 26.96 m and 10.60 m, the calcium carbonate content remains low with average values of 25.9 %. Above the Fish Level, the calcium carbonate content rises gradually to average values of 46.9 % in the upper part of the Sogno Formation and the Rosso Ammonitico Lombardo, between 10.60 m and 3.08 m. However, fluctuations up to 40 % are documented in this upper interval of the Gajum Core.

### 4.4. Total organic carbon (TOC)

The TOC values of the Sogno Core fall between 0 % and 2.5 % (Fig. 2). In the lower part of the Sogno Formation, below the Fish Level, TOC content is on

average 0.2 % between 24.69 m and 16.88 m, and increase to about 0.8 % just below the base of the Fish Level at  $\sim 17.1$  m. In the lowermost part of the Fish Level (Unit 7) TOC values are very low (0.2 %). Within lithological Unit 6, TOC starts to increase at 15.6 m reaching values up to  $\sim 1.4\%$ , with an average of 0.5 %. The uppermost part of the Fish Level (Unit 5) is characterized by the highest TOC values, on average 1.3 %, with peaks up to 2.5 %. These data are fully consistent with the TOC values obtained by Jenkyns and Clayton (1986) for the outcropping Fish Level. The interval immediately above the Fish Level is characterized by low values in the lowermost part ( $\sim 0.4\%$ ), followed by two samples with TOC content of  $\sim 2.2\%$ .

In the Gajum Core, the TOC values range between 0 % and 2.2 % (Fig. 3). In the Domaro Limestone (31.17–26.96 m), the TOC content is stable and extremely low, on average about 0.1 %. The lowermost and central lithostratigraphical units of the Fish Level (Units 6 and 5) are characterized by rather stable low values of about 0.3 % and 0.4 %, respectively. Unit 4 is characterized by a lowermost part (21.39–13.74 m) marked by a progressive increase in TOC up to 2.2 % (average of 1.1 %) and an upper part (13.74–10.60 m) with a low TOC content of  $\sim 0.4\%$ . In the upper part of the Gajum Core above the Fish Level and in the Rosso Ammonitico Lombardo (10.60–3.08 m), TOC values are very low, on average 0.1 %. Only a limited increase is observed in the interval between 5.95 and 5.31 m with an average value of  $\sim 0.3\%$  and a maximum of  $\sim 0.5\%$  at 5.53 m.

## 5. Discussion

### 5.1. The Fish Level in the Sogno and Gajum Cores

The Fish Level was originally described by Tintori (1977) in the section cropping out south of Monte Brughetto as a 1.75 m-thick interval consisting of fissile, brownish to black claystones and clayey marlstones, with planar alignments of small pyritic crystals. Gaetani and Poliani (1978) established the type section of the Sogno Formation on the road north of Monte Brughetto and described, in the middle part of lithozone 1, a 4.3 m-thick clayey interval containing common fish remains. According to Gaetani and Poliani (1978), the Fish Level *sensu stricto* can reach a thickness of 50 cm and is present only in the most

expanded sequences. However, the precise position of the Fish Level in the Colle di Sogno reference section or in other localities was not defined and, consequently, Casellato and Erba (2015) applied the name to the entire clayey interval of Gaetani and Poliani (1978). The same criteria were followed by Erba et al. (2019b) for the identification of the Fish Level in the Sogno and Gajum Cores, and used to identify the lithostratigraphic signature of the T-OAE, as suggested by Jenkyns (1985 1988).

The detailed sedimentological characterization of the Fish Level recovered with the Sogno and Gajum Cores was used to identify a lower grey interval and an upper black interval (Figs. 2, 3, and 4). The variable thickness of these two intervals as well as of the total thickness of the Fish Level appears dependent on the location within specific morphostructural features of the Lombardy Basin. It is worthwhile noting that the upper black interval is lithologically similar in the two cores, whereas the lower grey interval is rather variable. Most probably the Fish Level reported by Tintori (1977) corresponds to the sole upper black interval that should therefore be considered the Fish Level *sensu stricto*.

The expanded nature of the Fish Level in the Sogno and Gajum Cores offers the opportunity to investigate in detail the lithostratigraphic variations associated with the C-isotope anomaly. At both sites, the Fish Level base and top are identified as corresponding with the lowermost and uppermost dark grey to black shale, respectively (Erba et al. 2019b). Nevertheless, the Fish Level basal and top contacts are different in the two cores. Notably, in the Sogno Core the upper boundary corresponds to the top of the continuous black-shale interval overlain by grey marlstones, whereas the base is fixed at the bottom of the lowermost dark grey marlstone overlying a reddish interval (Unit 8). As described above (Fig. 4), the basal part of the Fish Level (Unit 7) is developed as greyish marly claystones with a few black shales, but also some reddish levels. On the contrary, in the Gajum Core the base of the Fish Level is well defined due to the abrupt occurrence of black shales, whereas the top is characterized by a transition from black shales to progressively dark grey to grey marly claystones and marlstones (Figs. 2, 3, and 4). The sharp lithological nature of the lower boundary of the Fish Level in the Gajum Core is related to the occurrence of a hiatus that may cover ~600 kyrs based on nannofossil biostratigraphy (Visentin and Erba 2021). Indeed, from a lithological point of view, the hiatus coincides with the boundary

between light grey limestones of the Domaro Limestone Formation and the grey interval of the Fish Level, thereby eliding the lowermost Toarcian part of the Sogno Formation. Moreover, as illustrated in Figure 5, the uppermost centimetres of the Domaro Limestone are characterized by a pseudo-nodular facies and an undulating surface with the overlying grey interval of the Fish Level. However, calcareous nannofossil biostratigraphy and geochemical data suggest that the basal part of the Fish Level is most probably complete.

The hiatus detected at the base of the Fish Level is interpreted as the result of downslope sediment (mass) transport as documented by megabreccia bodies occurring in various palaeo-locations near to the Gajum drillsite, at the foot or in lower parts of the slopes of the Mt. Corni di Canzo palaeohigh (Gaetani and Erba 1990, Pasquini and Vercesi 2002). Sedimentary discontinuities of similar age and duration have been documented for several lower Toarcian sections from the Lusitanian Basin as well as in Western Tethyan sections and have been ascribed to rapid regression/transgression phases around Pliensbachian/Toarcian boundary time, in the earliest *polymorphum* Zone and immediately before the T-OAE negative CIE: some authors have attributed such putative sea-level oscillations to glacio-eustatic control (Pittet et al. 2014). A rapid glacio-eustatic sea-level fall preceding the T-OAE negative CIE was also suggested, based on the presence of deeply incised valleys in marine sections exposed in Greenland and Morocco (Krencker et al. 2019). However, the palaeowater depth of the Gajum site (about 1000 m) excludes a similar cause for the hiatus dated in this core. This contention is further reinforced by the occurrence of continuous and complete sequences in several parts of the Lombardy Basin, as at Sogno on the Albenza Plateau. Rather, an early Toarcian tectonic phase associated with the rifting that propagated eastwards in the Southern Alps during the Late Triassic (Norian) to Middle Jurassic, was responsible for gaps and massive re-sedimentation in various parts of the Lombardy Basin (Gaetani 2010).

Despite the lithostratigraphical differences, related to the specific palaeo-physiography of the Gajum (Corni di Canzo High) and Sogno (Albenza Plateau) sites, some common geochemical features are observed within the Fish Level in the Sogno and Gajum Cores. The lower part of the grey interval, with minimum CaCO<sub>3</sub> values (5–10%) and TOC (~0.2%), is characterized by bioturbated, grey to very dark grey, and dark red marlstones in the Sogno Core (Unit 7) and bioturbated, dark grey to very dark



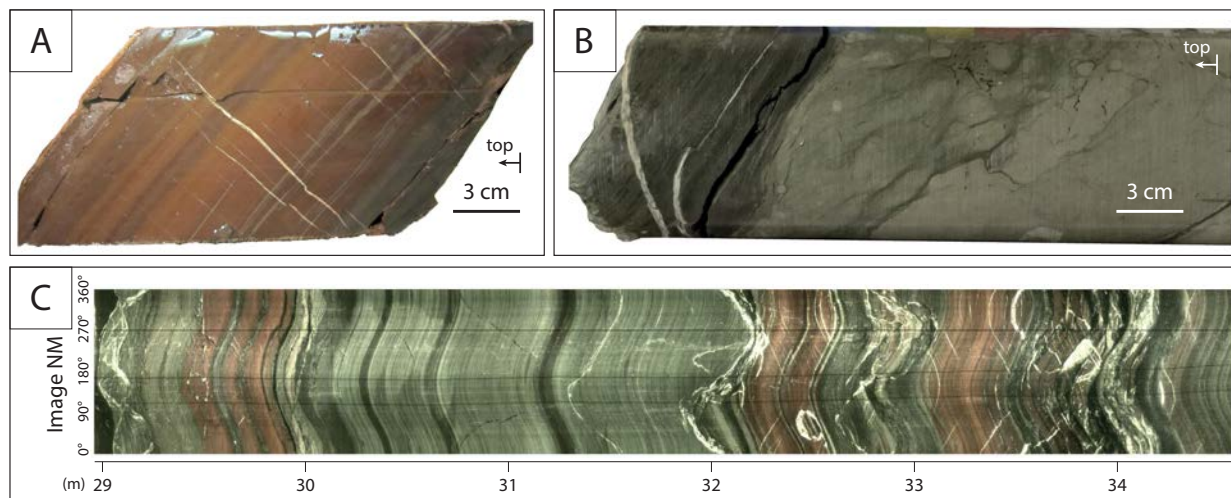


**Fig. 5.** A. Dusky red limy chert interval in the Gajum Core (slabbed core 22; ~32.4 m – penetration depth, ~23.7 m – stratigraphic depth). B. Boundary between the Domaro Limestone (on the right) and Sogno Formation (on the left) (core 25; ~36.78 m, – penetration depth, ~26.95 m – stratigraphic depth). An undulated surface marks the sharp boundary between the pseudo-nodular limestones and the Fish Level. C. Gajum borehole well image (from ~29 to ~34.5 m – penetration depth; from ~21 to ~25.3 m – stratigraphic depth). Three intervals of dusky red limy cherts interspersed with the grey to black marly claystones can be observed.

grey marly claystones in the Gajum Core (Unit 6). At Sogno, the onset of the Fish Level is marked by a drop in  $\text{CaCO}_3$  associated with the “*Schizosphaerella* crisis” (Erba 2004, Casellato and Erba 2015) documented at supra-regional scale (Tremolada et al. 2005, Visentin et al. 2021). It is characterized by the drastic reduction in abundance of schizosphaerellids that begins just stratigraphically preceding the negative CIE of the T-OAE and represents the wide-scale temporary collapse of a rock-forming taxon within the calcareous nannoplankton (Claps et al. 1995, Erba 2004, Tremolada et al. 2005, Mattioli et al. 2008, Fraguas et al. 2012, Hermoso et al. 2012, Erba et al. 2019a, Reolid et al. 2020, Visentin et al. 2021). In the Lombardy Basin, the “*Schizosphaerella* crisis” is paralleled by a substantial decrease in abundance of another well-calcified nanofloral taxon, namely *Mitrolithus jansae* (Casellato and Erba 2015, Visentin and Erba 2021). In the negative CIE interval of the T-OAE *Schizosphaerella* is also characterized by reduced sizes (Mattioli and Pittet 2002, Mattioli et al. 2004, Mattioli et al. 2009, Suan et al. 2008, Suan et al. 2010, Reolid et al. 2014, Reolid et al. 2020, Clémence et al. 2015, Erba et al. 2019). These drastic reductions in calcareous nannoplankton calcification, also described as a ‘calcareous nannofossil crisis’ or ‘disappearance event’ (Bucefalo Palliani et al. 2002, Mattioli et al. 2004, Mattioli et al. 2008, Suan et al. 2008, Fraguas et al. 2012, Clémence

et al. 2015), were translated into the drop in pelagic carbonate sedimentation as a consequence of combined warming, ocean fertilization and acidification influencing calcareous phytoplankton abundance and species-specific biocalcification. The increase in calcium carbonate above the Fish Level in both the Sogno and Gajum Cores (Figs. 2 and 3) records the resumption of *Schizosphaerella* production (Casellato and Erba 2015, Erba et al. 2019a, Visentin and Erba 2021), further highlighting the rock-forming role of this highly calcified taxon.

Jenkyns and Clayton (1986) observed a near-linear relationship ( $R^2 = 0.94$ ) between carbon isotopes in organic matter and the calcium-carbonate content of the Fish Level formerly cropping out at Monte Brughetto. They interpreted this relationship as the result of the replacement of calcareous nannofossils by non-carbonate-secreting phytoplankton that preferentially fixed  $^{12}\text{C}$ . However, the new data from the Sogno and Gajum Cores do not display such a linear relationship (Fig. 6). In fact,  $R^2$  is equal to 0.006 and 0.002 for the Fish Level interval at Sogno and Gajum, respectively and a  $R^2$  for the entire dataset equal to 0.26 and 0.10 at Sogno and Gajum, respectively. Furthermore, micropaleontological characterization of the Fish Level in the Colle di Sogno section (Casellato and Erba 2015), as well as in the Sogno and Gajum Cores (Visentin and Erba 2021), demonstrated that calcareous nannofossils

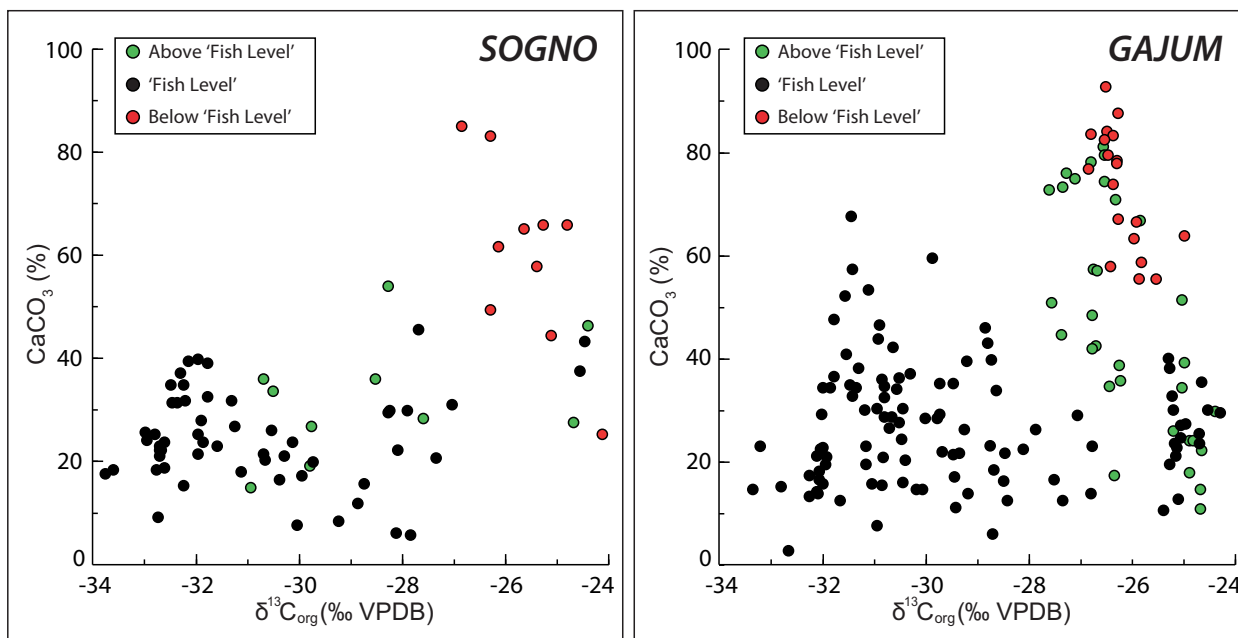


**Fig. 6.** Cross-plot of  $\text{CaCO}_3$  versus  $\delta^{13}\text{C}_{\text{org}}$  data for the Sogno and Gajum Cores. Samples below, within and above the Fish Level are indicated in red, black and green, respectively.

are present throughout the Fish Level, as in the intervals below and above. Consequently, the T-OAE negative excursion cannot be ascribed to a change in the nature and isotopic composition of the planktonic components due to local upwelling conditions, as hypothesized by Jenkyns and Clayton (1986). Moreover, the negative CIE has been documented in all complete marine and terrestrial archives, indicating that the whole ocean-atmosphere system was affected by a major change in the carbon pool.

The upper part of the grey interval within the Fish Level is characterized in both cores by a progressive increase in TOC up to  $\sim 1.4\%$ , with an average calcium carbonate content of 20–28%. In both cores, the upper black interval displays the highest TOC content (up to  $\sim 2.5\%$ ) associated with low  $\text{CaCO}_3$  content ( $\sim 27\%$ ) (Unit 5 and Unit 4 in the Sogno and Gajum Cores, respectively). However, it should be noticed that in the Gajum Core a sharp decrease in TOC down to values of about 0.3% was recognized in the very uppermost part of the Fish Level.

Possible dilution effects of organic matter by calcium carbonate were estimated by comparing measured TOC values with  $\text{CaCO}_3$  content. In particular, TOC on a carbonate-free basis ( $\text{TOC}_{\text{CF}}$ ) was calculated for both cores, in order to compensate for variable calcium carbonate amounts.  $\text{TOC}_{\text{CF}}$  curves do not

show substantial variations with respect to TOC profiles, thus indicating a negligible impact of carbonate dilution on organic-matter content. This result is further confirmed by the lack of a direct correlation between TOC and  $\text{CaCO}_3$ , as shown in the cross-plot in Figure 7.

## 5.2. The carbon-isotope record in the Sogno and Gajum Cores

The  $\delta^{13}\text{C}$  record of the latest Pliensbachian–early Toarcian time interval in both cores is characterized by common trends that ensure high-resolution dating and correlation between the two (Figs. 2 and 3). As described in section 4.1, the negative excursion in the Gajum Core is also marked by three lithostratigraphic intervals with particularly low  $\delta^{13}\text{C}_{\text{carb}}$  values, from about  $-9\%$  to about  $-12\%$ . Such punctuated very negative values (from  $-1\%$  to  $-4\%$ ) are also noted in the lower and middle part of the CIE of the Sogno Core (Fig. 2).

Although the overall trends in both carbonate and organic-carbon isotopes are similar in the Sogno and Gajum Cores, some differences exist in the  $\delta^{13}\text{C}_{\text{carb}}$  absolute values of the two cores. In fact, the  $\delta^{13}\text{C}_{\text{org}}$  values are practically identical, with the T-OAE chemostratigraphic anomaly represented by a negative

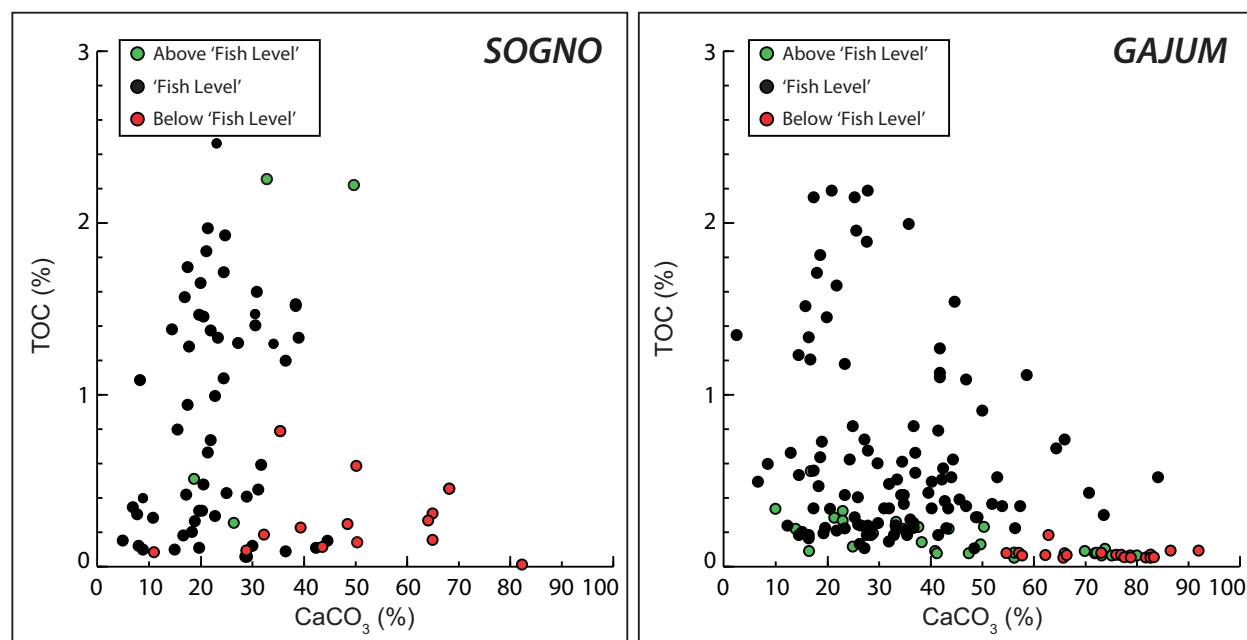


**Fig. 7.** Cross-plot of total organic carbon (TOC) versus  $\text{CaCO}_3$  data for the Sogno and Gajum Cores. Samples below, within and above the Fish Level are indicated in red, black and green, respectively.

excursion of about 7‰ (Figs. 2 and 3). On the contrary,  $\delta^{13}\text{C}_{\text{carb}}$  records of the two cores exhibit different values, with the amplitude of the T-OAE negative excursion reaching  $\sim 3$ ‰ (from about 3‰ to about 0‰) in the Sogno Core, while this decrease is about twice as large (from about 3‰ to about  $-3$ ‰) in the Gajum Core (Figs. 2 and 3). We speculate that these extremely negative values are related to the remineralization of organic matter and the fixation of relatively isotopically light carbon released below the sediment-water interface into authigenic carbonates. The preferential fixation of the released light carbon in the carbonate phase is illustrated by the occurrence of the very negative values exclusively in the carbonate-carbon but not in the organic-carbon isotopic record. Observed differences in the two  $\delta^{13}\text{C}_{\text{carb}}$  records testify to the occurrence of variable early diagenetic patterns that acted to a different extent in the two locations.

An extensive discussion on the role of diagenesis was given by Jenkyns and Clayton (1986) to explain the low  $\delta^{13}\text{C}$  values measured from several T-OAE organic-rich shales and intercalated manganian carbonate from the Tethyan region, including the Monte Brughetto outcrop. They described the shift to lower values as the result of a negative local diagenetic trend unrelated to a change in the oceanic carbon-isotope reservoir. In particular, according to these authors, the

negative values reflect a mixture of isotopically heavier primary marine carbonate and isotopically lighter diagenetic cement precipitated in equilibrium with  $\text{CO}_2$  derived from bacterial oxidation of organic matter. The same interpretation was also given by Bellanca et al. (1999) to explain the low  $\delta^{13}\text{C}_{\text{carb}}$  values in the lower Toarcian bioturbated manganian limestones, grey marlstones, and thinly laminated, organic-carbon-rich black shales in the Belluno Basin (northeastern Italy) (Figs. 1E and 1F). Sabatino et al. (2011) described very negative  $\delta^{13}\text{C}_{\text{carb}}$  values from manganian and siliceous limestone interbedded within the T-OAE black-shale interval in the Julian Alps (Monte Mangart section). The authors suggested that the negative C-isotopic values coincident with high Mn contents indicate the effects of organic matter in the mineralization process during early diagenetic precipitation of manganese carbonates; the same interpretation is adopted here. As far as the Gajum Core is concerned, two of the three most negative  $\delta^{13}\text{C}_{\text{carb}}$  intervals correlate with reddish limy cherts within Unit 5 (Figs. 2 and 3). Although the  $\delta^{13}\text{C}_{\text{carb}}/\delta^{18}\text{O}_{\text{carb}}$  cross-plot (see below) is comparable with negligible diagenetic alteration, we cannot exclude the likely role of diagenesis due to the development of the limy cherts whose genesis necessarily involved dissolution-precipitation phenomena.

### 5.3. Oxygen-isotope variations

A cross-plot of  $\delta^{13}\text{C}_{\text{carb}}$  values against the  $\delta^{18}\text{O}_{\text{carb}}$  data for all the analysed samples of the two sections is given in Figure 8. A correlation between the two isotopic ratios is generally observed in samples affected by diagenesis due to the presence of variable quantities of isotopically homogeneous, isotopically negative calcite cementing primary marine carbonate (e. g., Marshall 1992, Blanchet et al. 2012). Our data show absence of correlation ( $R^2$  equal to 0.21 and 0.07 in the Sogno and Gajum Cores, respectively) when considering all the analysed samples together. By grouping data according to their position relative to the Fish Level, no correlation between the  $\delta^{13}\text{C}_{\text{carb}}$  and the  $\delta^{18}\text{O}_{\text{carb}}$  is observed ( $R^2$  from 0 to 0.19), with the exception of the interval above the Fish Level in the Gajum Core ( $R^2 = 0.56$ ). These data suggest that diagenesis may have had little effect, with moderate impact only in the upper interval of the Gajum Core. Thus, the occurrence of common patterns in the oxygen-isotope record in the two sections suggests a relatively modest overprint of the original isotopic signal.

Some cautious considerations in terms of relative temperature variations can therefore be made. In both sections, a progressive shift of  $\delta^{18}\text{O}_{\text{carb}}$  from heavier to lighter values is observed in correspondence with the Fish Level, possibly due to a gradual change towards warmer conditions. By considering the typical  $\Delta^{18}\text{O}_{\text{carb}}$  gradients between 0.2–0.3 ‰ per °C for

marine carbonates (Leng and Marshall 2004, Maslin and Dickson 2015), the observed  $\delta^{18}\text{O}_{\text{carb}}$  decrease of about 2 ‰ in amplitude in both the Sogno and Gajum Cores would imply a warming of about 7–10 °C. This magnitude of warming is in good agreement with  $\text{TEX}_{86}$  based sea-surface temperatures reconstructions for the Tethyan region for the same time interval (Ruebsam et al. 2020).

In the Sogno Core, where the lowermost part of the Sogno Formation is preserved, the progressive shift in  $\delta^{18}\text{O}_{\text{carb}}$  towards lower values begins before the deposition of the Fish Level, suggesting that the onset of warmer conditions pre-dated the deposition of the black-shale interval. In fact, oxygen-isotope values start to gently decrease from about 3 metres below the Fish Level and then are marked by a sharp shift to lighter ratios at the onset level of the negative carbon-isotope anomaly, about 0.5 m below the base of the black-shale interval. Oxygen-isotope values in the uppermost part of the succession record a progressive shift back to higher values, probably resulting from a gradual cooling. In the Gajum Core, the abrupt shift to lighter  $\delta^{18}\text{O}_{\text{carb}}$  values coincides with the base of the Fish Level and is consistent with the occurrence of a hiatus at the Domaro Limestone/Sogno Formation boundary. The most negative values are reached in the uppermost part of the black-shale interval (from about 16.2 to 12.8 m) followed by a gradual increase. We note particularly that, in both cores, the gradual shift back to higher oxygen-isotope ratios occurs prior to the end of the negative carbon-isotope anomaly,

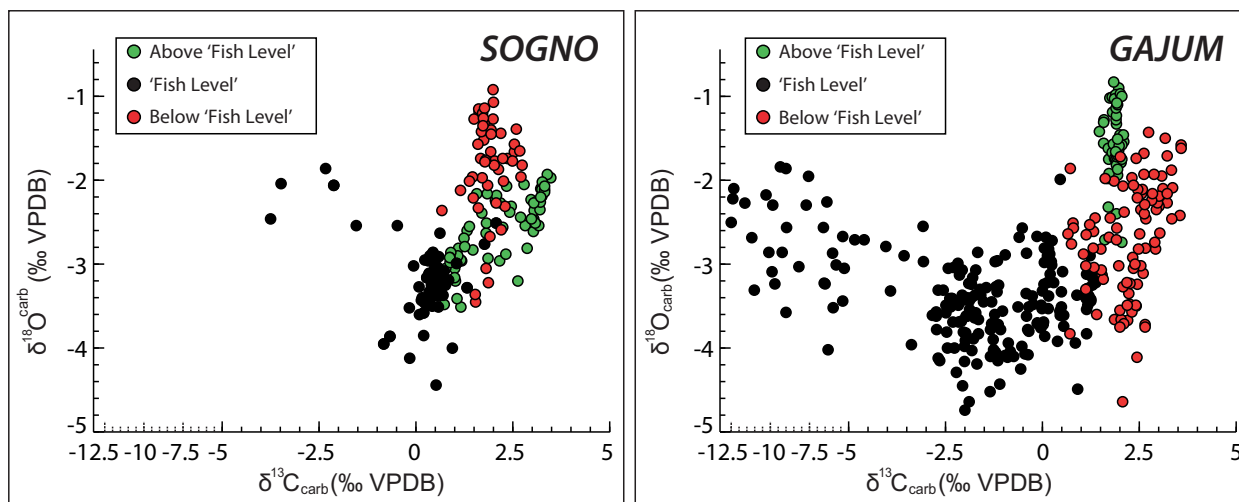


**Fig. 8.** Cross-plot of  $\delta^{18}\text{O}_{\text{carb}}$  versus  $\delta^{13}\text{C}_{\text{carb}}$  data for the Sogno and Gajum Cores. Samples below, within and above the Fish Level are indicated in red, black and green, respectively. For the sake of readability, lower  $\delta^{13}\text{C}_{\text{carb}}$  values are reported using a different scale.

indicating that the transition towards cooler conditions started before the return back to post-T-OAE  $\delta^{13}\text{C}$  background values. Indeed, it should be pointed out that local variations in salinity might have influenced the observed  $\delta^{18}\text{O}_{\text{carb}}$  record, in addition to temperature. However, such effects cannot be constrained with available data.

The lowest  $\delta^{18}\text{O}_{\text{carb}}$  values measured in the upper part of the negative  $\delta^{13}\text{C}$  anomaly in both the Sogno and Gajum Cores are consistent with other Tethyan sequences observed in Spain (Tremolada et al. 2005, Gómez et al. 2016), Portugal (Oliveira et al. 2006, Suan et al. 2008), Greece (Kafousia et al. 2014), and north European localities in France (Emmanuel et al. 2006) and Germany (Röhl et al. 2001).

#### 5.4. The T-OAE in the western Tethys

Recently, Hougård et al. (2021) documented the T-OAE anomalies in the Swabo-Franconian Basin (SW Germany) and discussed the extension of anoxia relative to carbon-isotope chemostratigraphy. Results were compared to similar datasets from the Paris Basin, the Cleveland Basin and the Swiss Jura to assess synchronicity/diachroneity of the termination of anoxia in different parts of the seaway connecting the Tethys to the Boreal Oceans. Hougård et al. (2021) raised the critical issue of the definition of the T-OAE that hitherto has not been systematically applied, thereby introducing artefacts and/or misunderstandings in correlations and modelling at supra-regional scale.

Following the original definition of OAEs by Schlanger and Jenkyns (1976), Jenkyns (1988) described the lithological T-OAE signature based on globally distributed apparently coeval organic-rich black shales dated to the early Toarcian *falciferum* Zone. This lithostratigraphy-based definition was applied in several subsequent papers and complemented by a broad  $\delta^{13}\text{C}$  positive excursion interrupted by an abrupt negative “bite” in its central portion (Jenkyns 2010). In Figure 9, the  $\delta^{13}\text{C}$  reference curve for the latest Pliensbachian–middle Toarcian time interval (Ruebsam and Al-Husseine 2020, modified by Hougård et al. 2021), shows the prolonged positive excursion containing the negative CIE. The extremely detailed record of the Mochras borehole (Xu et al. 2018, Storm et al. 2020) documents the T-OAE positive excursion (from the mid-*tenuicostatum* Zone to the mid-*serpentinum* Zone) and the negative CIE (*exaratum* Subzone). Applying the GTS2020 time

scale (Gradstein et al. 2020) the broad positive carbon-isotope excursion corresponds to a  $\sim 1.5$  million-year-long interval. The remarkable  $\delta^{13}\text{C}$  negative CIE has been documented at global scale in a variety of marine and continental settings indicating a global perturbation of the C cycle (see reviews by Remirez and Algeo 2020, Ruebsam and Al-Husseini 2020). Arguably, such a negative CIE is the most consistently recognizable feature that accompanies the T-OAE.

Müller et al. (2017) proposed renaming the T-OAE as the Jenkyns Event in which they distinguished the negative CIE (their interval 2). Recently, Reolid et al. (2020) recommended using the term Jenkyns Event for the global early Toarcian changes including anoxia, enhanced organic-matter burial, biotic crises in marine and terrestrial ecosystems, warming and sea-level rise. However, a precise definition of the beginning and end of the Jenkyns Event is not provided, hampering its unambiguous identification and correlation on a regional, supra-regional and global scale.

Here, we suggest labelling as the Jenkyns Event only the  $\delta^{13}\text{C}$  negative CIE of the T-OAE. As such, the Jenkyns Event correlates with the uppermost *tenuicostatum* Zone–*exaratum* Subzone and falls within the NJT6 nannofossil Zone (Ferreira et al. 2019, Visentin and Erba 2021). Inspection of medium- to high-resolution records allows a further subdivision of the Jenkyns Event into: a) a lower part where, after a marked decrease, the carbon-isotope curve remains at minimum values, and b) an upper part that features a gradual increase back to pre-anomaly values (Fig. 9). It is worth pointing out that the chemostratigraphic expression of the lower part of the Jenkyns Event (J1) can have very different shapes, while the upper part (J2) is similar in the currently available documented records. Adopting the above subdivision, three time-lines can be used for global correlations, namely the base of J1, the base of J2, and the top of J2.

The comparison of lithostratigraphy and chemostratigraphy (both  $\delta^{13}\text{C}_{\text{carb}}$  and  $\delta^{13}\text{C}_{\text{org}}$  data) highlights analogies and differences in the timing and depositional style of the Fish Level in the Sogno and Gajum Cores (Fig. 9). At both sites, the lowermost part of the lithostratigraphically constrained T-OAE (Fish Level) corresponds to carbonate- and TOC-poor marlstones and marly claystones, followed in the middle and upper parts by more organic-rich dark grey marly claystones and black shales. The coherence in stratigraphic position of the TOC content in the two cores seems to imply some remineralization of organic matter (hence lower TOC) in the early stages of the Jenkyns Event (lower

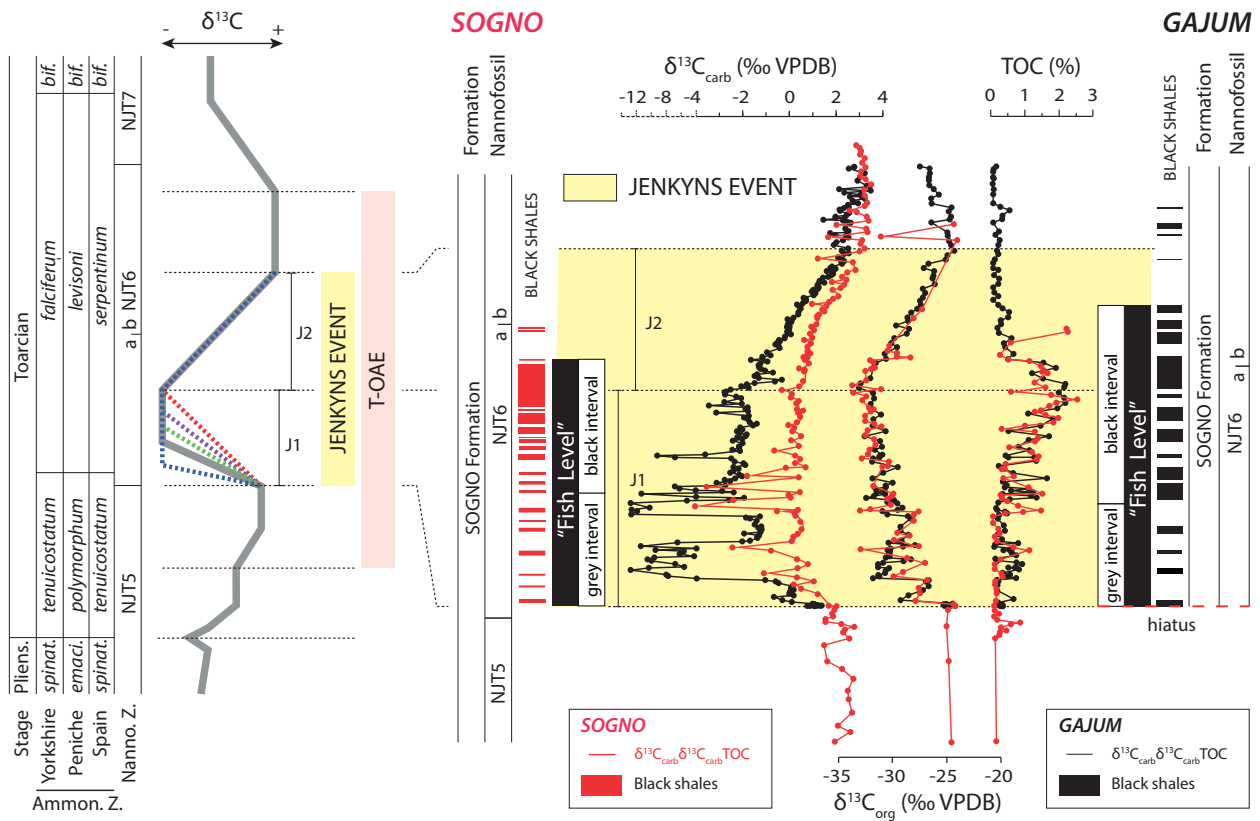


**Fig. 9.** On the left, the schematic  $\delta^{13}\text{C}$  reference curve for the latest Pliensbachian–Toarcian time interval is reported (modified after Ruebsam and Al-Husseini (2020), with minor modifications by Hougård et al. 2021). The stratigraphic extent of the T-OAE is indicated with a light red rectangle, while the proposed interval of the Jenkyns Event is indicated by a yellow band. Extent of the lower J1 and the upper J2 segments of the Jenkyns Event is also illustrated. Coloured dashed lines in the reference plot represent the different trends documented in the lower part of the Jenkyns Event (J1). On the right, chemostratigraphic correlation of the Sogno and Gajum Cores is based on overlapped  $\delta^{13}\text{C}_{\text{carb}}$  and  $\delta^{13}\text{C}_{\text{org}}$  isotope profiles and TOC data. The extent of the Fish Level and its internal subdivision into a grey interval and a black interval is reported for the two records.

half of the J1) that could have fuelled authigenic carbonate precipitation after burial.

In both the Sogno and Gajum Cores, the base of the Fish Level coincides with the chemostratigraphic onset of the Jenkyns Event (Figs. 2, 3, and 9). This correlation implies that the hiatus at the Domaro Limestone/Sogno Formation boundary in the Gajum Core does not cut out the basal part of the Fish Level. We underscore the fact that, in the Sogno Core, decreases in  $\text{CaCO}_3$  and  $\delta^{18}\text{O}$  start  $\sim 20$  cm below the base level of the signature of the Jenkyns Event, in a similar way to records from the Sancerre section (Hermoso et al. 2013). In the Gajum Core, the coeval interval seems either extremely condensed or absent/elided.

The timing of initial deposition of the Fish Level relative to the CIE is synchronous at both Sogno and

Gajum sites. Conversely, the upper boundary of the black-shale interval appears diachronous in the two records (Fig. 9) suggesting a delayed re-establishment of well-oxygenated conditions at Gajum. Moreover, the top of the black-shale interval is abrupt at Sogno, whereas a gradual change from black shales to organic-lean pale marlstones is documented in the Gajum Core (Figs. 2, 3 and 4). This observed disparity is interpreted to reflect the different geological settings: on a pelagic plateau at about 1500 m water depth (Sogno Core) and in an inner basin along the slope of a structural high at about 1000 m water depth (Gajum Core). Therefore, the lithostratigraphic expression of the T-OAE, namely the Fish Level, was of similar inception, but different termination and duration depending on local conditions even within the same basin.

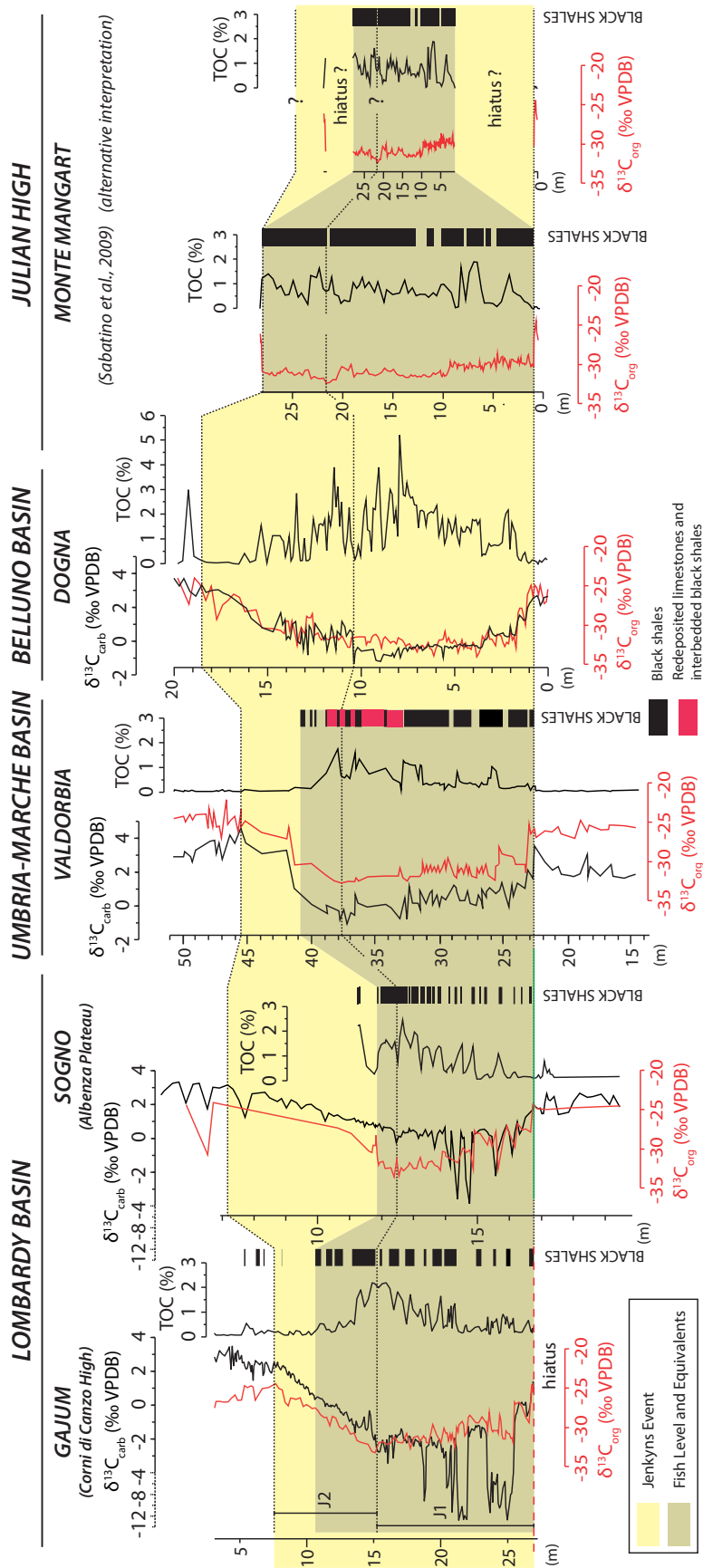


**Fig. 10.** Correlation of carbon-isotope profiles ( $\delta^{13}\text{C}_{\text{carb}}$  in black and  $\delta^{13}\text{C}_{\text{org}}$  in red), TOC and black-shale occurrence for the Jenkyns Event interval at Sogno (Lombardy Basin, this study), Gajum (Lombardy Basin, this study), Valdorbria (Umbria-Marche Basin, Sabatino et al. 2009), Dogna (Belluno Basin, Jenkyns et al. 2001, Sabatino et al. 2009), and the Monte Mangart section (Julian High, Sabatino et al. 2011). An alternative interpretation of the Monte Mangart data is also reported. See text for details. The stratigraphic position of the Fish Level and Fish Level Equivalent is indicated by a grey band, while the position of the Jenkyns Event interval is highlighted by a yellow band.

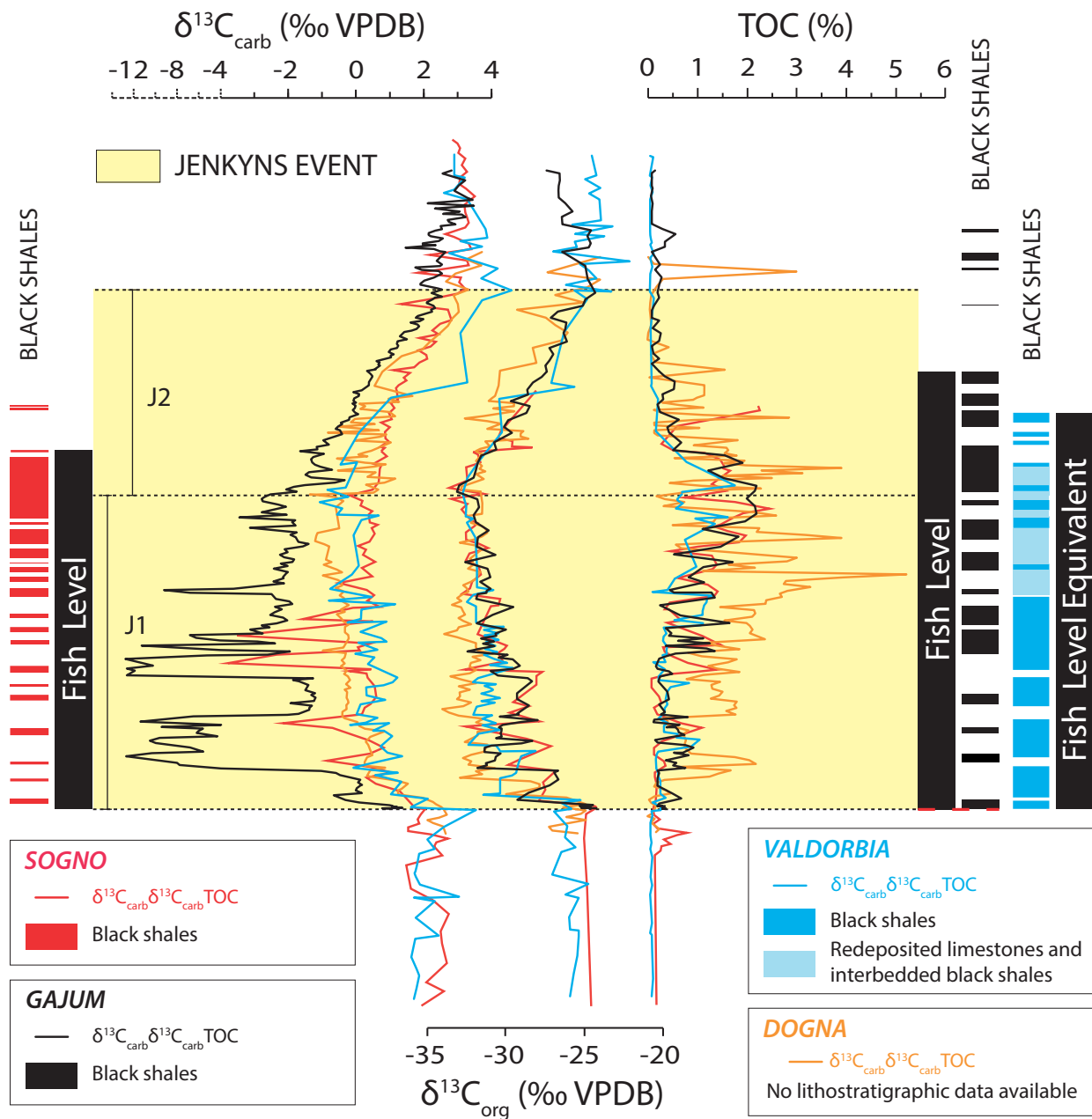


**Fig. 11.** Overlain  $\delta^{13}\text{C}_{\text{carb}}$ ,  $\delta^{13}\text{C}_{\text{org}}$ , and TOC profiles for the Sogno Core (Lombardy Basin, this study), Gajum Core (Lombardy Basin, this study), Valdorbis (Umbria-Marche Basin, Sabatino et al. 2009), Dogna (Belluno Basin, Jenkyns et al. 2001, Sabatino et al. 2009). The distribution of the black-shale intervals (Fish Level and Fish Level Equivalent) is also reported.

In Figure 10 the Sogno and Gajum C-isotopic, black-shale and TOC records are compared to analogous data from the Umbria-Marche Basin (Valdorbis section, Sabatino et al. 2009), Belluno Basin (Dogna section; in Jenkyns et al. 2001, Sabatino et al. 2009) and Julian High (Monte Mangart section in Sabatino et al. 2009, Sabatino et al. 2011). The negative CIE at Valdorbis

and Dogna unambiguously allows the identification and correlation of the J1 and J2 segments at supra-regional scale. The  $\delta^{13}\text{C}_{\text{org}}$  record of the Monte Mangart section was interpreted as complete, allowing the identification of the base and top of the negative CIE (Sabatino et al. 2009). However, based on values and trends, we propose a revised chemostratigraphic cor-



relation suggesting that hiatuses have removed the oldest and youngest parts of the record of the Jenkyns Event (Fig. 10).

From a lithostratigraphic point of view, a Fish Level Equivalent is recognizable in the Valdorbja and Monte Mangart sections, whereas lithological data are not provided for Dogna, preventing the identification of a Fish Level Equivalent in the Belluno Basin. Chemostratigraphy indicates that the Fish Level Equivalent corresponds to the entire J1 and lower J2 in the Umbria-Marche Basin, similarly to the Lombardy Basin (Fig. 11). While the base of the Fish Level Equivalent is synchronous to the base of the Fish Level, in the Umbria-Marche Basin (Valdorbja section) the termination of anoxia (= top of the Fish Level Equivalent) is younger than at Sogno and older than at Gajum (Figs. 10 and 11). Depending on the interpretation of the carbon-isotope record, at Monte Mangart the Fish Level Equivalent might coincide with the entire Jenkyns Event interval following the interpretation of Sabatino et al. (2009). Thus, the base of the Fish Level Equivalent would be synchronous with the records in the Lombardy and Umbria-Marche Basins while the top would be delayed for at least one locality on the Julian High (Monte Mangart). The revised chemostratigraphy (this study), implying stratigraphic gaps at the base and top of the Fish Level Equivalent, hampers the assessment of synchronicity/diachroneity of inception and/or termination of oxygen depletion in the Julian High area.

As far as the TOC is concerned (Figs. 10 and 11), the Valdorbja and Dogna records are similar to those of Sogno and Gajum, with an increase from the beginning of the negative CIE to the J1/J2 boundary interval. However, whereas at Valdorbja the TOC values are comparable to the Sogno and Gajum data, values are higher at Dogna (from 0.3 to 5%). Moreover, in the Dogna section, the increase in TOC begins lower in the section and terminates higher than at Sogno, Gajum and Valdorbja.

At supra-regional scale within the western Tethys litho-geochemical data indicate that features were very similar in the Lombardy and Umbria-Marche Basins, but slightly different in the Belluno Basin. The onset of black-shale deposition (Fish Level and Fish Level Equivalent) was coeval at inter-basinal scale since it coincides with the beginning of the Jenkyns Event in the Lombardy and Umbria-Marche Basins. Termination of black-shale deposition, however, was diachronous at intra- and inter-basinal scale, possibly depending on specific morphostructural settings.

## 6. Conclusions

New carbon- and oxygen-isotope,  $\text{CaCO}_3$  and TOC data from the Sogno and Gajum Cores provide a high-resolution record of the T-OAE in the Lombardy Basin. The reconstructed palaeobathymetry is about 1000 and 1500 m water depth for the Gajum and Sogno sites, respectively. Thus, the investigated sections provide some of the deepest records of the T-OAE in the western Tethyan region. During the early Toarcian, sedimentation shifted to a depositional style characterized by dark grey to black marly claystones with low  $\text{CaCO}_3$ , corresponding to the Fish Level. This interval is lithologically variable and of significantly different thickness in the Sogno (~5 m) and Gajum (~16 m) Cores. Notwithstanding these differences, in both cores the Fish Level is marked by a lower part characterized by minimum  $\text{CaCO}_3$  (5–10%) and TOC (~0.2%), a central part with a progressive shift in TOC up to ~1.4%, and an upper part with the highest TOC values reaching up to ~2.5%. Based on detailed lithostratigraphy, the Fish Level is subdivided into a lower grey interval and an upper black interval, the latter being the Fish Level *sensu stricto*.

In the Sogno Core, the carbon-isotope chemostratigraphy allows the identification of the minor negative anomaly at the Pliensbachian/Toarcian boundary followed by a broad positive excursion. A hiatus elides the lowermost part of the Sogno Formation below the Fish Level in the Gajum Core, so that the Pliensbachian/Toarcian boundary interval is not preserved. Across the Fish Level, the negative carbonate carbon-isotope anomaly shows a shift of ~3‰ in the Sogno and ~6‰ in the Gajum Core, respectively, and a  $\delta^{13}\text{C}_{\text{org}}$  negative shift of ~7‰ in both successions. We propose naming the  $\delta^{13}\text{C}$  negative anomaly the 'Jenkyns Event' (further subdivided into the J1 and J2 segments) and use this diagnostic geochemical feature to unambiguously identify the T-OAE at a global scale. Calcareous nannofossil biostratigraphy constrains the Jenkyns Event to the NJT 6 Zone.

In both cores, oxygen-isotope data document a progressive shift to lighter values suggestive of warmer conditions starting before the deposition of the Fish Level. The lowest oxygen-isotope ratios are recorded within the Fish Level itself, consistent with warmest ocean temperatures during its deposition in the early Toarcian. Data indicate a return back to higher oxygen-isotope values before the end of the black-shale deposition, thus suggesting that a change to cooler conditions occurred before the termination of the Jenkyns Event.

High-resolution correlation of the new cored sequences from the Lombardy Basin highlights the fact that the onset of deposition of the Fish Level was synchronous, but its termination was diachronous at the two sites, suggesting a delayed re-establishment of oxygenated bottom-water conditions at Gajum. Also, the top of the black-shale interval is abrupt at Sogno, whereas black shales gradually change to grey marlstones in the Gajum Core.

The records from the Lombardy Basin can be compared to sections from the Umbria-Marche and Belluno Basins and the Julian High with the  $\delta^{13}\text{C}_{\text{carb}}$  and  $\delta^{13}\text{C}_{\text{org}}$  data providing the chemostratigraphic framework (J1 and J2 segments) to assess the wider distribution of TOC and black shales. As is the case for other OAEs (see discussion in Tsikos et al. 2004 and Kolonic et al. 2005 for OAE2, and Wagner et al. 2013 for OAE3), the organic-rich and/or carbonate-poor lithologies (black shales) are diachronous relative to carbon-isotope stratigraphy. Specifically, the onset of the T-OAE black shale deposition in the western Tethys was coeval in different basins and started at the beginning of the Jenkyns Event, but the return to more oxygenated bottom waters was diachronous at local to inter-basinal scales.

**Acknowledgements.** The authors are grateful to Guillaume Suan and an anonymous Reviewer who, with their valuable comments, greatly contributed to improving the quality of the manuscript. We thank C. Compostella, E. S. Ferrari and M. Pegoraro (University of Milano) and S. Nicoara (Open University) for their technical help. The research was conducted within the PRIN 2017RX9XXXY awarded to EE and the Italian Ministry of Education (MIUR) project “Dipartimenti di Eccellenza 2018–2022, Le Geoscienze per la Società: Risorse e loro evoluzione”.

## References

- Al-Suwaidi, A. H., Angelozzi, G. N., Baudin, F., Damborenea, S. E., Hesselbo, S. P., Jenkyns, H. C., Manceñido, M. O., Riccardi, A. C., 2010. First record of the Early Toarcian Oceanic Anoxic Event from the Southern Hemisphere, Neuquén Basin, Argentina. *Journal of the Geological Society of London* 167, 633–636.
- Bellanca, A., Masetti, D., Neri, R., Venezia, F., 1999. Geochemical and sedimentological evidence of productivity cycles recorded in Toarcian black shales from the Belluno Basin, Southern Alps, Northern Italy. *Journal of Sedimentary Research* 69, 466–476.
- Bernoulli, D., Homewood, P., Kálin, O., van Stuijvenberg, J., 1979. Evolution of continental margins in the Alps. *Schweizerische Mineralogische und Petrographische Mitteilungen* 59, 165–170.
- Bernoulli, D., Jenkyns, H. C., 1974. Alpine, Mediterranean, and Central Atlantic Mesozoic facies in relation to the early evolution of the Tethys. In: Dott, R. H., Shaver, R. H. (Eds.), *Modern and Ancient Geosynclinal Sedimentation*. Society of Economic Paleontologists and Mineralogists, Special Publication 19, 129–160.
- Bernoulli, D., Jenkyns, H. C., 2009. Ancient oceans and continental margins of the Alpine-Mediterranean Tethys: Deciphering clues from Mesozoic pelagic sediments and ophiolites. *Sedimentology* 56, 149–190.
- Bjerrum, C. J., Surlyk, F., Callomon, J. H., Slingerland, R. L., 2001. Numerical paleoceanographic study of the Early Jurassic transcontinental Laurasian Seaway. *Paleoceanography* 16, 390–404.
- Blanchet, C. L., Kasten, S., Vidal, L., Poulton, S. W., Ganeshram, R., Thouveny, N., 2012. Influence of diagenesis on the stable isotopic composition of biogenic carbonates from the Gulf of Tehuantepec oxygen minimum zone. *Geochemistry, Geophysics, Geosystems* 13, Q04003, doi: 10.1029/2011GC003800.
- Bosellini, A., Winterer, E. L., 1975. Pelagic limestone and radiolarite of the Tethyan Mesozoic: a genetic model. *Geology* 3, 279–282.
- Bosence, D., Procter, E., Aurell, M., Kahla, A. B., Boudagher-Fadel, M., Casaglia, F., Cirilli, S., Mehdie, M., Nieto, L., Rey, J., Scherreiks, R., Soussi, M., Waltham, D., 2009. A Dominant Tectonic Signal in High-Frequency, Peritidal Carbonate Cycles? A Regional Analysis of Liassic Platforms from Western Tethys. *Journal of Sedimentary Research* 79, 389–415.
- Bucefalo Palliani, R., Mattioli, E., Riding, J. B., 2002. The response of marine phytoplankton and sedimentary organic matter to the Early Toarcian (Lower Jurassic) oceanic anoxic event in northern England. *Marine Micropaleontology* 46, 223–245.
- Caruthers, A. H., Gröcke, D. R., Smith, P. L., 2011. The significance of an Early Jurassic (Toarcian) carbon-isotope excursion in Haida Gwaii (Queen Charlotte Islands), British Columbia, Canada. *Earth and Planetary Science Letters* 307, 19–26.
- Casellato, C. E., Erba, E., 2015. Calcareous nannofossil biostratigraphy and paleoceanography of the Toarcian Oceanic Anoxic Event at Colle di Sogno section (Southern Alps, Italy). *Rivista Italiana di Paleontologia e Stratigrafia* 105, 343–376.
- Castellarin, A., 1972. Evoluzione paleotettonica sinsedimentaria del limite tra ‘Piattaforma Veneta’ e ‘Bacino Lombardo’, a nord di Riva del Garda. *Giornale di Geologia, serie 2a* 38, 11–212.
- Channell, J. E. T., Casellato, C. E., Muttoni, G., Erba, E., 2010. Magnetostratigraphy, nannofossil stratigraphy and apparent polar wander for Adria-Africa in the Jurassic–Cretaceous boundary interval. *Palaeogeography, Palaeoclimatology, Palaeoecology* 293, 51–75.
- Claps, M., Erba, E., Masetti, D., Melchiorri, F., 1995. Milankovitch-type cycles recorded in Toarcian black

- shales from Belluno Trough (Southern Alps, Italy). *Memorie di Scienze Geologiche*, Università di Padova 47, 179–188.
- Clémence, M. E., Gardin, S., Bartolini, A., 2015. New insights in the pattern and timing of the Early Jurassic calcareous nannofossil crisis. *Paleogeography, Paleoclimatology, Paleocology* 427, 100–108.
- Cohen, A. S., Coe, A. L., Harding, S. M., Schwark, L., 2004. Osmium isotope evidence for the regulation of atmospheric CO<sub>2</sub> by continental weathering. *Geology* 32, 157–160.
- Coplen, T. B., 1994. Reporting of stable hydrogen, carbon, and oxygen isotopic abundances. *Pure and Applied Chemistry* 66, 273–276.
- da Rocha, R. B., Mattioli, E., Duarte, L. V., Pittet, B., Elmi, S., Mouterde, R., Cabral, M. C., Comas-Rengifo, M. J., Gómez, J. J., Goy, A., Hesselbo, S. P., Jenkyns, H. C., Littler, K., Mailliot, S., de Oliveira, L. C. V., Osete, M. L., Perilli, N., Pinto, S., Ruget, C., Suan, G., 2016. Base of the Toarcian Stage of the Lower Jurassic defined by the Global Boundary Stratotype Section and Point (GSSP) at the Peniche section (Portugal). *Episodes* 39, 460–481.
- Dera, G., Brigaud, B., Monna, F., Laffont, R., Pucéat, E., Deconinck, J.-F., Pellenard, P., Joachimski, M. M., Durllet, C., 2011. Climatic ups and downs in a disturbed Jurassic world. *Geology* 39, 215–218.
- Emmanuel, L., Renard, M., Cubaynes, R., De Rafelis, M., Hermoso, M., Lecallonnec, L., Le Solleuz, A., Rey, J., 2006. The “Schistes Carton” of Quercy (Tarn, France): a lithological signature of a methane hydrate dissociation event in the early Toarcian. Implications for correlations between Boreal and Tethyan realms. *Bulletin de la Société Géologique de France* 177, 239–249.
- Erba, E., 2004. Calcareous nannofossils and Mesozoic oceanic anoxic events. *Marine Micropaleontology* 52, 85–106.
- Erba, E., Bottini, C., Faucher, G., Gambacorta, G., Visentin, S., 2019a. The response of calcareous nannoplankton to Oceanic Anoxic Events: The Italian pelagic record. *Bollettino della Società Paleontologica Italiana* 58, 51–71.
- Erba, E., Casellato, C. E., 2010. Paleocanografia del Giurassico nella Tetide occidentale: l’archivio geologico del Bacino Lombardo. *Rendiconti dell’Istituto Lombardo. Accademia di Scienze e Lettere, Special Publication on “Una nuova Geologia per la Lombardia”* 447, 115–140.
- Erba, E., Gambacorta, G., Visentin, S., Cavalheiro, L., Reolon, D., Faucher, G., Pegoraro, M., 2019b. Coring the sedimentary expression of the early Toarcian Oceanic Anoxic Event: new stratigraphic records from the Tethys Ocean. *Scientific Drilling* 26, 17–27.
- Ettinger, N. P., Larson, T. E., Kerans, C., Thibodeau, A. M., Hattori, K. E., Kacur, S. M., Martindale, R. C., 2021. Ocean acidification and photic-zone anoxia at the Toarcian Oceanic Anoxic Event: Insights from the Adriatic Carbonate Platform. *Sedimentology* 68, 63–107.
- Fantasia, A., Föllmi, K. B., Adatte, T., Bernardez, E., Spangenberg, J. E., Mattioli, E., 2018. The Toarcian Oceanic Anoxic Event in southwestern Gondwana: an example from the Andean Basin, northern Chile. *Journal of the Geological Society* 175, 883–902.
- Fantasia, A., Föllmi, K. B., Adatte, T., Spangenberg, J. E., Mattioli, E., 2019. Expression of the Toarcian Oceanic Anoxic Event: New insights from a Swiss transect. *Sedimentology* 66, 262–284.
- Ferreira, J., Mattioli, E., Sucheràs-Marx, B., Giraud, F., Duarte, V. L., Pittet, B., Suan, G., Hassler, A., Spangenberg, J. E., 2019. Western Tethys Early and Middle Jurassic calcareous nannofossil biostratigraphy. *Earth-Science Reviews* 197, 1–19.
- Filatova, N. I., Konstantinovskaya, E., Vishnevskaya, V., 2020. Jurassic–Lower Cretaceous siliceous rocks and black shales from allochthonous complexes of the Koryak–Western Kamchatka orogenic belt, East Asia. *International Geology Review*, doi: 10.1080/00206814.2020.1848649.
- Fraguas, A., Comas-Rengifo, M. J., Gómez, J., Goy, A., 2012. The calcareous nannofossil crisis in Northern Spain (Asturias province) linked to the Early Toarcian warming-driven mass extinction. *Marine Micropaleontology* 94–95, 58–71.
- Frimmel, A., Oschmann, W., Schwark, L., 2004. Chemos-tratigraphy of the Posidonia Black Shale, SW Germany: I. Influence of sea-level variation on organic facies evolution. *Chemical Geology* 206, 199–230.
- Gaetani, M., 1975. Jurassic stratigraphy of the Southern Alps: a review. In: Squyres, C. H. (Ed.), *Geology of Italy*, I, Earth Sciences Society of the Libyan Arab Republic, Tripoli, Libya, 377–402.
- Gaetani, M., 2010. From Permian to Cretaceous: Adria as pivotal between extensions and rotations of Tethys and Atlantic Oceans. In: Beltrando, M., Peccerillo, A., Mattei, M., Conticelli, S., Doglioni, C. (Eds.), *The Geology of Italy*. *Journal of the Virtual Explorer* 36, paper 5.a, <https://doi.org/10.3809/jvirtex.2010.00235>, 2010.
- Gaetani, M., Erba, E., 1990. Il Bacino Lombardo: un sistema paleoalto/fossa in un margine continentale passivo durante il Giurassico. 75° Congresso Società Geologica Italiana, 10–12 September 1990, Milano, Italy. Guida all’escursione A3.
- Gaetani, M., Poliani, G., 1978. Il Toarciano e il Giurassico medio in Albenza (Bergamo). *Rivista Italiana di Paleontologia e Stratigrafia* 84, 349–382.
- Gómez, J. J., Comas-Rengifo, M. J., Goy, A., 2016. Palaeoclimatic oscillations in the Pliensbachian (Early Jurassic) of the Asturian Basin (Northern Spain). *Climate of the Past* 12, 1199–1214.
- Gradstein, F. M., Ogg, J. G., Schmitz, M. D., Ogg, G. M., 2020. *Geological Time Scale 2020*. Elsevier, 2 volumes, 1390 p.
- Gröcke, D. R., Hori, R. S., Trabucho-Alexandre, J., Kemp, D. B., Schwark, L., 2011. An open ocean record of the Toarcian oceanic anoxic event. *Solid Earth* 2, 245–257.
- Hallam, A., 1967. The depth significance of shales with bituminous laminae. *Marine Geology* 5, 481–493.
- Hallam, A., 1981. A revised sea-level curve for the early Jurassic. *Journal of the Geological Society* 138, 735–743.

- Haq, B. U., Hardenbol, J., Vail, P. R., 1987. Chronology of fluctuating sea-levels since the Triassic. *Nature* 235, 1156–1167.
- Hardenbol, J., Thierry, J., Farley, M. B., Jacquin, T., de Graciansky, P.-C., Vail, P. R., 1998. Mesozoic and Cenozoic sequence chronostratigraphic framework of European basins. In: de Graciansky, P.-C., Hardenbol, J., Jacquin, T., Vail, P. R. (Eds.), *Mesozoic and Cenozoic sequence stratigraphy of European basins*. Society for Sedimentary Geology (SEPM), Special Publication 60, 3–13, charts 1–8, Tulsa, Oklahoma.
- Heimdal, T. H., Godd eries, Y., Jones, M. T., Svensen, H. H., 2021. Assessing the importance of thermogenic degassing from the Karoo Large Igneous Province (LIP) in driving Toarcian carbon cycle perturbations. *Nature Communications* 12, doi: 10.1038/s41467-021-26467-6.
- Hermoso, M., Minoletti, F., Pellenard, P., 2013. Black shale deposition during Toarcian super-greenhouse driven by sea level. *Climate of the Past* 9, 2703–2712.
- Hermoso, M., Minoletti, F., Rickaby, R. E. M., Hesselbo, S. P., Baudin, F., Jenkyns, H. C., 2012. Dynamics of a stepped carbon-isotope excursion: Ultra high-resolution study of Early Toarcian environmental change. *Earth and Planetary Science Letters* 319–320, 45–54.
- Hesselbo, S. P., Gr ocke, D. R., Jenkyns, H. C., Bjerrum, C. J., Farrimond, P., Morgans Bell, H. S., Green, O. R., 2000. Massive dissociation of gas hydrate during a Jurassic Oceanic Anoxic Event. *Nature* 406, 392–395.
- Hesselbo, S. P., Jenkyns, H. C., 1998. British Lower Jurassic sequence stratigraphy. In: de Graciansky, P. C., Hardenbol, J., Jacquin, T., Farley, M., Vail, P. R. (Eds.), *Mesozoic–Cenozoic Sequence Stratigraphy of European Basins*, Society for Sedimentary Geology (SEPM), Special Publication 60, 561–581.
- Hesselbo, S. P., Jenkyns, H. C., Duarte, L. V., Oliveira, L. C. V., 2007. Carbon-isotope record of the Early Jurassic (Toarcian) Oceanic Anoxic Event from fossil wood and marine carbonate (Lusitanian Basin, Portugal). *Earth and Planetary Science Letters* 253, 455–470.
- Hesselbo, S. P., Pieńkowski, G., 2011. Stepwise atmospheric carbon-isotope excursion during the Toarcian Oceanic Anoxic Event (Early Jurassic, Polish Basin). *Earth and Planetary Science Letters* 301, 365–372.
- Hinnov, L. A., Park, J., Erba, E., 2000. Lower–Middle Jurassic rhythmites from the Lombard Basin, Italy: a record of orbitally forced carbonate cycles modulated by secular environmental changes in West Tethys. In: Hall, R. L., Smith, P. L. (Eds.), *Advances in Jurassic Research*, Trans Tech Publications, Z urich, Switzerland, 437–454.
- Houg ard, I. W., Bojese-Koefoed, J. A., Vickers, M. L., Ullmann, C. V., Bjerrum, C. J., Rizzi, M., Korte, C., 2021. Redox element record shows that environmental perturbations associated with the T-OAE were of longer duration than the carbon isotope record suggests – the Aubach section, SW Germany. *Newsletters on Stratigraphy* 54, 229–246.
- Ikeda, M., Hori, R. S., Ikehara, M., Miyashita, R., Chino, M., Yamada, K., 2018. Carbon cycle dynamics linked with Karoo-Ferrar volcanism and astronomical cycles during Pliensbachian-Toarcian (Early Jurassic). *Global and Planetary Change* 170, 163–171.
- Izumi, K., Kemp, D. B., Itamiya, S., Inui, M., 2018. Sedimentary evidence for enhanced hydrological cycling in response to rapid carbon release during the early Toarcian oceanic anoxic event. *Earth and Planetary Science Letters* 481, 162–170.
- Izumi, K., Miyaji, T., Tanabe, K., 2012. Early Toarcian (Early Jurassic) oceanic anoxic event recorded in the shelf deposits in the northwestern Panthalassa: evidence from the Nishinakayama formation in the Toyora area, west Japan. *Palaeogeography, Palaeoclimatology, Palaeoecology* 15–316, 100–108.
- Jenkyns, H. C., 1985. The Early Toarcian and Cenomanian-Turonian anoxic events in Europe: comparisons and contrasts. *Geologische Rundschau* 74, 505–518.
- Jenkyns, H. C., 1988. The Early Toarcian (Jurassic) Anoxic Event: stratigraphic, sedimentary and geochemical evidence. *American Journal of Science* 288, 101–151.
- Jenkyns, H. C., 2003. Evidence for rapid climate change in the Mesozoic–Palaeogene greenhouse world. *Philosophical Transactions of the Royal Society of London, Series A* 361, 1885–1916.
- Jenkyns, H. C., 2010. Geochemistry of oceanic anoxic events. *Geochemistry, Geophysics, Geosystems* 11, Q03004, doi: 10.1029/2009GC002788.
- Jenkyns, H. C., 2020. The demise and drowning of Early Jurassic (Sinemurian) carbonate platforms: stratigraphic evidence from the Italian peninsula, Sicily and Spain. In: *L’Eredit  scientifica di Paolo Scandone, Atti dei Convegni Lincei* 335, 55–82.
- Jenkyns, H. C., Clayton, C. J., 1986. Black shales and carbon isotopes in pelagic sediments from the Tethyan Lower Jurassic. *Sedimentology* 33, 87–106.
- Jenkyns, H. C., Clayton, C. J., 1997. Lower Jurassic epicontinental carbonates and mudstones from England and Wales: chemostratigraphic signals and the early Toarcian anoxic event. *Sedimentology* 44, 687–706.
- Jenkyns, H. C., Gr ocke, D. R., Hesselbo, S. P., 2001. Nitrogen isotope evidence for water mass denitrification during the early Toarcian (Jurassic) oceanic anoxic event. *Paleoceanography* 16, 593–603.
- Jenkyns, H. C., Jones, C. E., Gr ocke, D. R., Hesselbo, S. P., Parkinson, D. N., 2002. Chemostratigraphy of the Jurassic System: applications, limitations and implications for palaeoceanography. *Journal of the Geological Society* 159, 351–378.
- Jenkyns, H. C., MacFarlane, S., 2021. The chemostratigraphy and environmental significance of the Marlstone and Junction Bed (Beacon Limestone, Toarcian, Lower Jurassic, Dorset, UK). *Geological Magazine*, doi: 10.1017/S0016756821000972.
- Kafousia, N., Karakitsios, V., Jenkyns, H. C., Mattioli, E., 2011. A global event with a regional character: the Early Toarcian Oceanic Anoxic Event in the Pindos Ocean (northern Peloponnese, Greece). *Geological Magazine* 148, 619–631.

- Kafousia, N., Karakitsios, V., Mattioli, E., Kenjo, S., Jenkyns, H. C., 2014. The Toarcian Oceanic Anoxic Event in the Ionian Zone, Greece. *Palaeogeography, Palaeoclimatology, Palaeoecology* 393, 135–145.
- Kemp, D. B., Coe, A. L., Cohen, A. S., Schwark, L., 2005. Astronomical pacing of methane release in the Early Jurassic period. *Nature* 437, 396–399.
- Kemp, D. B., Selby, D., Izumi, K., 2020. Direct coupling between carbon release and weathering during the Toarcian oceanic anoxic event. *Geology* 48, 976–980.
- Kolonic, S., Wagner, T., Forster, A., Sinnighe Damsté, J. S., Waslworth-Bell, B., Erba, E., Turgeon, S., Brumsack, H.-J., Chellai, E. H., Tsikos, H., Kuhnt, W., Kuypers, M. M. M., 2005. Black shale deposition on the northwest African Shelf during the Cenomanian/Turonian oceanic anoxic event: Climate coupling and global organic carbon burial. *Paleoceanography* 20, PA1006, doi: 10.1029/2003PA000950.
- Korte, C., Hesselbo, S. P., 2011. Shallow marine carbon and oxygen isotope and elemental records indicate icehouse-greenhouse cycles during the early Jurassic. *Paleoceanography* 26, PA4219, doi: 10.1029/2011PA002160.
- Krenker, F.-N., Lindström, S., Bodin, S., 2019. A major sea-level drop briefly precedes the Toarcian oceanic anoxic event: implication for Early Jurassic climate and carbon cycle. *Scientific Reports* 9, 12518, doi: 10.1038/s41598-019-48956-x.
- Leng, M. J., Marshall, J. D., 2004. Palaeoclimate interpretation of stable isotope data from lake sediment archives. *Quaternary Science Reviews* 23, 811–831.
- Littler, K., Hesselbo, S. P., Jenkyns, H. C., 2010. A carbon-isotope perturbation at the Pliensbachian–Toarcian boundary: evidence from the Lias Group, NE England. *Geological Magazine* 147, 181–192.
- Marshall, J. D., 1992. Climatic and oceanographic isotopic signals from the carbonate rock record and their preservation. *Geological Magazine* 129, 143–160.
- Maslin, M., Dickson, A. J., 2015. O-Isotopes. In: Harff, J., Meschede, M., Petersen, S., Thiede, J. (Eds.), *Encyclopedia of Marine Geosciences*, doi: 10.1007/978-94-007-6644-0\_81-1.
- Mattioli, E., Pittet, B., Bucefalo Palliani, R., Röhl, H.-J., Schmid-Röhl, A., Morettini, E., 2004. Phytoplankton evidence for timing and correlation of palaeoceanographical changes during the Early Toarcian oceanic anoxic event (Early Jurassic). *Journal of the Geological Society of London* 161, 685–693.
- Mattioli, E., Pittet, B., Petitpierre, L., Mailliot, S., 2009. Dramatic decrease of pelagic carbonate production by nannoplankton across the Early Toarcian anoxic event (TOAE). *Global and Planetary Change* 65, 134–145.
- Mattioli, E., Pittet, B., Suan, G., Mailliot, S., 2008. Calcareous nannoplankton changes across the early Toarcian oceanic anoxic event in the western Tethys. *Paleoceanography* 23, PA3208, doi: 10.1029/2007PA001435.
- Mattioli, M., Pittet, B., 2002. Contribution of calcareous nannoplankton to carbonate deposition: a new approach applied to the Lower Jurassic of Central Italy. *Marine Micropaleontology* 45, 175–190.
- McElwain, J. C., Wade-Murphy, J., Hesselbo, S. P., 2005. Changes in carbon dioxide during an oceanic anoxic event linked to intrusion into Gondwana coals. *Nature* 435, 479–482.
- Müller, T., Jurikova, H., Gutjahr, M., Tomašových, A., Schlögl, J., Liebetrau, V., Duarte, L. V., Milovský, R., Suan, G., Mattioli, E., Pittet, B., Eisenhauer, A., 2020. Ocean acidification during the early Toarcian extinction event: Evidence from boron isotopes in brachiopods. *Geology* 48, 1184–1188.
- Müller, T., Price, G. D., Bajnai, D., Nyerges, A., Kesjár, D., Raucsik, B., Varga, A., Judik, K., Fekete, J., May, Z., Pálffy, J., 2017. New multiproxy record of the Jenkyns Event (also known as the Toarcian Oceanic Anoxic Event) from the Mecsek Mountains (Hungary): Differences, duration and drivers. *Sedimentology* 64, 66–86.
- Muttoni, G., Erba, E., Kent, D. V., Bachtadse, V., 2005. Mesozoic Alpine facies deposition as a result of past latitudinal plate motion. *Nature* 434, 59–63.
- Oliveira, L. C. V., Rodrigues, R., Duarte, L. V., Lemos, V. B., 2006. Avaliação do potencial gerador de petróleo e interpretação paleoambiental com base em biomarcadores e isótopos estáveis de carbono da seção Pliensbachiano–Toarciano inferior (Jurássico Inferior) da região de Peniche (Bacia Lusitânica, Portugal). *Boletim de Geociências da Petrobras* 14, 207–234.
- Pálffy, J., Smith, P. L., 2000. Synchrony between Early Jurassic extinction, oceanic anoxic event, and the Karoo–Ferrar flood basalt volcanism. *Geology* 28, 747–750.
- Pasquini, C., Vercesi, P. L., 2002. Tettonica sinsedimentaria e ricostruzione paleogeografica del margine occidentale dell’Alto dei Corni di Canzo nel Lias inferiore. *Memorie della Società Geologica Italiana* 57, 107–114.
- Percival, L. M. E., Cohen, A. S., Davies, M. K., Dickson, A. J., Hesselbo, S. P., Jenkyns, H. C., Leng, M. J., Mather, T. A., Storm, M. S., Xu, W., 2016. Osmium isotope evidence for two pulses of increased continental weathering linked to Early Jurassic volcanism and climate change. *Geology* 44, 759–762.
- Percival, L. M. E., Witt, M. L. I., Mather, T. A., Hermoso, M., Jenkyns, H. C., Hesselbo, S. P., Al-Suwaidi, A. H., Storm, M. S., Xu, W., Ruhl, M., 2015. Globally enhanced mercury deposition during the end-Pliensbachian extinction and Toarcian OAE: A link to the Karoo–Ferrar Large Igneous Province. *Earth and Planetary Science Letters* 428, 267–280.
- Pittet, B., Suan, G., Lenoir, F., Duarte, L. V., Mattioli, E., 2014. Carbon isotope evidence for sedimentary discontinuities in the lower Toarcian of the Lusitanian Basin (Portugal): Sea level change at the onset of the Oceanic Anoxic Event. *Sedimentary Geology* 303, 1–14.
- Posenato, R., Bassi, D., Trecalli, A., Parente, M., 2018. Taphonomy and evolution of Lower Jurassic lithiotid bivalve accumulations in the Apennine Carbonate Platform (southern Italy). *Palaeogeography, Palaeoclimatology, Palaeoecology* 489, 261–271.

- Remirez, M. N., Algeo, T. J., 2020. Carbon-cycle changes during the Toarcian (Early Jurassic) and implications for regional versus global drivers of the Toarcian oceanic anoxic event. *Earth-Science Reviews* 209, 103283.
- Reolid, M., 2014. Stable isotopes on foraminifera and ostracods for interpreting incidence of the Toarcian Oceanic Anoxic Event in Westernmost Tethys: role of water stagnation and productivity. *Palaeogeography, Palaeoclimatology, Palaeoecology* 395, 77–91.
- Reolid, M., Mattioli, E., Duarte, L. V., Marok, A., 2020. The Toarcian Oceanic Anoxic Event and the Jenkyns Event (IGCP-655 final report). *Episodes* 43, 833–844.
- Reolid, M., Mattioli, E., Nieto, L. M., Rodríguez-Tovar, F. J., 2014. The Early Toarcian Oceanic Anoxic Event in the External Subbetic (Southiberian Paleomargin, Westernmost Tethys): Geochemistry, nannofossil and ichnology. *Palaeogeography, Palaeoclimatology, Palaeoecology* 411, 79–94.
- Röhl, H. J., Schmid-Röhl, A., 2005. Lower Toarcian (Upper Liassic) black shales of the Central European epicontinental basin: a sequence stratigraphic case study from the SW German Posidonia Shale. In: Harris, N. B. (Ed.), *The Deposition of Organic-Carbon-Rich Sediments: Models, Mechanisms, and Consequences*, Society for Sedimentary Geology (SEPM), Special Publication 82, 165–189.
- Röhl, H.-J., Schmid-Röhl, A., Oschmann, W., Frimmel, A., Schwark, L., 2001. The Posidonia Shale (Lower Toarcian) of SW-Germany: an oxygen-depleted ecosystem controlled by sea level and palaeoclimate. *Palaeogeography, Palaeoclimatology, Palaeoecology* 165, 27–52.
- Ruebsam, W., Al-Husseini, M., 2020. Calibrating the Early Toarcian (Early Jurassic) with stratigraphic black holes (SBH). *Gondwana Research* 82, 317–336.
- Ruebsam, W., Mayer, B., Schwark, L., 2019. Cryosphere carbon dynamics control early Toarcian global warming and sea level evolution. *Global and Planetary Change* 172, 440–453.
- Ruebsam, W., Reolid, M., Sabatino, N., Masetti, D., Schwark, L., 2020. Molecular paleothermometry of the early Toarcian climate perturbation. *Global and Planetary Change* 195, 103351.
- Sabatino, N., Neri, R., Bellanca, A., Jenkyns, H. C., Baudin, F., Parisi, G., Masetti, D., 2009. Carbon-isotope records of the Early Jurassic (Toarcian) oceanic anoxic event from the Valdorbica (Umbria-Marche Apennines) and Monte Mangart (Julian Alps) sections: palaeoceanographic and stratigraphic implications. *Sedimentology* 56, 1307–1328.
- Sabatino, N., Neri, R., Bellanca, A., Jenkyns, H. C., Masetti, D., Scopelliti, G., 2011. Petrography and high-resolution geochemical records of Lower Jurassic manganese-rich deposits from Monte Mangart, Julian Alp. *Palaeogeography, Palaeoclimatology, Palaeoecology* 299, 97–109.
- Sabatino, N., Vlahović, I., Jenkyns, H. C., Scopelliti, G., Neri, R., Prtoljan, B., Velić, I., 2013. Carbon-isotope record and palaeoenvironmental changes during the early Toarcian oceanic anoxic event in shallow-marine carbonates of the Adriatic Carbonate Platform in Croatia. *Geological Magazine* 150, 1085–1102.
- Santantonio, M., Carminati, E., 2011. The Jurassic rifting evolution of the Apennines and Southern Alps (Italy): Parallels and differences. *Bulletin of the Geological Society of America* 124, 468–484.
- Schlanger, S. O., Jenkyns, H. C., 1976. Cretaceous oceanic anoxic events: causes and consequences. *Geologie en Mijnbouw* 55, 179–184.
- Schouten, S., van Kaam-Peters, H. M. E., Rijpstra, W. I. C., Schoell, M., Sinninghe Damsté, J. S., 2000. Effects of an oceanic anoxic event on the stable carbon isotopic composition of early Toarcian carbon. *American Journal of Science* 300, 1–22.
- Scotese, C. R., 2011. The PALEOMAP Project PaleoAtlas for ArcGIS, Volume 3, Jurassic and Triassic Paleogeographic and Plate Tectonic Reconstructions, version (9.2r). PALEOMAP Project, Arlington, Texas.
- Storm, M. S., Hesselbo, S. P., Jenkyns, H. C., Ruhl, M., Ullmann, C. V., Xu, W., Leng, M. J., Riding, J. B., Gorbatenko, O., 2020. Orbital pacing and secular evolution of the Early Jurassic carbon cycle. *Proceedings of the National Academy of Sciences* 117, 3974–3982.
- Suan, G., Mattioli, E., Pittet, B., Lécuyer, C., Suchera-Marx, B., Duarte, L. V., Philippe, M., Reggiani, L., Martineau, F., 2010. Secular environmental precursor to Early Toarcian (Jurassic) extreme climate changes. *Earth and Planetary Science Letters* 290, 448–458.
- Suan, G., Mattioli, E., Pittet, B., Mailliot, S., Lécuyer, C., 2008. Evidence for major environmental perturbation prior to and during the Toarcian (Early Jurassic) oceanic anoxic event from the Lusitanian Basin, Portugal. *Paleoceanography* 23, PA1202, doi: 10.1029/2007PA001459.
- Svensen, H. H., Planke, S., Chevallier, L., Malthes-Sørensen, A., Corfu, F., Jamtveit, B., 2007. Hydrothermal venting of greenhouse gases triggering Early Jurassic global warming. *Earth Planet. Sci. Lett.* 256, 554–566.
- Them, T. R., Gill, B. C., Selby, D., Gröcke, D. R., Friedman, R. M., Owens, J. D., 2017. Evidence for rapid weathering response to climatic warming during the Toarcian Oceanic Anoxic Event. *Scientific Reports* 7, 5003, doi: 10.1038/s41598-017-05307-y.
- Tintori, A., 1977. Toarcian fishes from the Lombardy Basin. *Bollettino della Società Paleontologica Italiana* 16, 143–152.
- Trabucho-Alexandre, J., Dirks, R., Veld, H., Klaver, G., De Boer, P., 2012. Toarcian black shales in the Dutch Central Graben: record of energetic, variable depositional conditions during an oceanic anoxic event. *Journal of Sedimentary Research* 82, 104–120.
- Trecalli, A., Spangenberg, J., Adatte, T., Föllmi, K. B., Parente, M., 2012. Carbonate platform evidence of ocean acidification at the onset of the early Toarcian oceanic anoxic event. *Earth and Planetary Science Letters* 357–358, 214–225.
- Tremolada, F., van de Schootbrugge, B., Erba, E., 2005. Early Jurassic schizosphaerellid crisis in Cantabria, Spain: Implications for calcification rates and phytoplankton evolution across the Toarcian oceanic anoxic

- event. *Paleoceanography* 20, PA2011, doi: 10.1029/2004PA001120.
- Tsikos, H., Jenkyns, H. C., Walsworth-Bell, B., Petrizzo, M. R., Forster, A., Kolonic, S., Erba, E., Premoli Silva, I., Baas, M., Wagner, T., Sinninghe Damsté, J. S., 2004. Carbon-isotope stratigraphy recorded by the Cenomanian–Turonian Oceanic Anoxic Event: correlation and implications based on three key localities. *Journal of the Geological Society London* 161, 711–719.
- Ullmann, C. V., Hesselbo, S. P., Korte, C., 2013. Tectonic forcing of Early to Middle Jurassic seawater Sr/Ca. *Geology* 41, 211–214.
- van Breugel, Y., Baas, M., Schouten, S., Mattioli, E., Damsté, J. S. S., 2006. Isorenieratane record in black shales from the Paris Basin, France: Constraints on recycling of respired CO<sub>2</sub> as a mechanism for negative carbon isotope shifts during the Toarcian oceanic anoxic event. *Paleoceanography*, 21, PA4220, <https://doi.org/10.1029/2006PA001305>.
- Visentin, S., Erba, E., 2021. High-resolution calcareous nannofossil biostratigraphy 1 across the Toarcian Oceanic Anoxic Event in northern Italy: clues from the Sogno and Gajum Cores (Lombardy Basin, Southern Alps). *Rivista Italiana di Paleontologia e Stratigrafia* 127, 539–556.
- Visentin, S., Erba, E., Mutterlose, J., 2021. Bio- and chemostratigraphy of the Posidonia Shale: a new database for the Toarcian Anoxic Event from northern Germany. *Newsletters on Stratigraphy*, doi: 10.1127/nos/2021/0658.
- Wagner, T., Hofmann, P., Flögel, S., 2013. Marine black shale deposition and Hadley Cell dynamics: A conceptual framework for the Cretaceous Atlantic Ocean. *Marine and Petroleum Geology* 43, 222–238.
- Winterer, E. L., 1998. Paleobathymetry of Mediterranean Tethyan Jurassic pelagic sediments. *Memorie della Società Geologica Italiana* 53, 97–131.
- Winterer, E. L., Bosellini, A., 1981. Subsidence and sedimentation on Jurassic passive continental margin, Southern Alps, Italy. *American Association of Petroleum Geologists Bulletin* 65, 394–421.
- Woodfine, R. G., Jenkyns, H. C., Sarti, M., Baroncini, F., Violante, C., 2008. The response of two Tethyan carbonate platforms to the early Toarcian (Jurassic) oceanic anoxic event: environmental change and differential subsidence. *Sedimentology* 55, 1011–1028.
- Xu, W., Ruhl, M., Jenkyns, H. C., Hesselbo, S. P., Riding, J. B., Selby, D., Naafs, B. D. A., Weijers, J. W. H., Pancost, R. D., Tegelaar, E., Idiz, E., 2017. Carbon sequestration in an expanded lake system during the Toarcian oceanic anoxic event. *Nature Geoscience* 10, 129–134.
- Xu, W., Ruhl, M., Jenkyns, H. C., Leng, M. J., Huggett, J. M., Minisini, D., Ullmann, C. V., Riding, J. B., Weijers, J. W., Storm, M. S., Percival, L. M., 2018. Evolution of the Toarcian (Early Jurassic) carbon-cycle and global climatic controls on local sedimentary processes (Cardigan Bay Basin, UK). *Earth and Planetary Science Letters* 484, 396–411.
- Manuscript received: June 18, 2021  
Revisions required: July 23, 2021  
Revised version received: November 12, 2021  
Manuscript accepted: November 15, 2021

**The pdf version of this paper includes an electronic supplement**

Please save the electronic supplement contained in this pdf-file by clicking the blue frame above. After saving rename the file extension to .zip (for security reasons Adobe does not allow to embed .exe, .zip, .rar etc. files).

**Table of contents – Electronic Supplementary Material (ESM)**

Supplementary material consists of isotopic data ( $\delta^{13}\text{C}_{\text{carb}}$ ,  $\delta^{13}\text{C}_{\text{org}}$ ,  $\delta^{18}\text{O}_{\text{carb}}$ ), CaCO<sub>3</sub> content and Total Organic Carbon (TOC) for the Sogno and Gajum cores.

## **4. New organic carbon content and geochemical paleoenvironmental reconstructions from the Toarcian Fish Level (Sogno Core - Lombardy Basin, northern Italy).**

**Draft chapter of preliminary geochemical results of the Sogno core**

### **Abstract**

This chapter presents a preliminary organic geochemical characterisation of the black shales interval (Fish Level) cored at Colle di Sogno (Southern Alps, Italy). The Fish Level correlates with the early Toarcian negative  $\delta^{13}\text{C}$  anomaly named Jenkyns Event, which is associated with major disturbances in both the global carbon and biogeochemical cycles. The Fish Level is here divided into three distinct lithostratigraphic intervals that document a progressive upward increase in organic carbon (OC) content, reaching values up to ~2.5 % in the uppermost part. Particularly, OC fluctuations of about 0.5% are also documented across the overall black shales interval. New sulphur, iron and biomarkers data, along with organic carbon content and Rock-Eval parameters are presented for the Upper Pliensbachian-Lower Toarcian interval. Variations in redox state, organic matter type, and carbon burial trends are reconstructed. Further results of ongoing analyses will present new biomarkers data aiming to contribute to shed new light on outstanding questions concerning the extent of ocean anoxia/dysoxia and related changes in OM type in the Western Tethyan area.



## 1. Introduction

This chapter presents preliminary results of geochemical analyses carried out for the Sogno core, in the Lombardy Basin (Southern Alps, northern Italy) (Fig. 1), which includes a relatively expanded black shale section containing the Fish Level (Erba et al., 2019, b). The chemostratigraphic framework of the Sogno core (see Fig. 1 a) has been investigated in detail in Erba et al., 2022. The Jenkyns Event is the oldest Mesozoic case of global anoxia (~180 Myr; Jenkyns, 2010), documenting extensive accumulation of organic matter from coastal to pelagic settings (Jenkyns, 1985, 1988, 2010). Release of high amounts of greenhouse gases possibly related to the degassing of the Karoo–Ferrar large igneous province (LIP) and/or dissociation of methane hydrates (Hesselbo et al., 2000; Them et al., 2017; Reolid et al., 2020) are inferred to be the triggers of this extreme paleoenvironmental change, and its globally documented diagnostic carbon isotope anomaly ( $\delta^{13}\text{C}$ ) (Hesselbo et al., 2000, 2007; Schouten et al., 2000; Röhl et al., 2001; Jenkyns et al., 2002; Emmanuel et al., 2006; van Breugel et al., 2006; Al-Suwaidi et al., 2010; Gröcke et al., 2011; Kafousia et al., 2011, 2014; Izumi et al., 2012; Reolid, 2014; Xu et al., 2017; Them et al., 2017; Fantasia et al., 2018; Ikeda et al., 2018; Reolid et al., 2020; Hougard et al., 2021).

As redox conditions and the type (origin) of organic matter constituents and their (related) lability toward oxic degradation control OM accumulation, degradation and preservation (Arndt et al., 2013), this work examined high-resolution 1) variations in redox state, and 2) the organic matter type across the study black shale interval. Geochemical parameters such as TOC, sulphur (S), sulphur/iron (S/Fe) and S/TOC ratios were examined together with pyrite and bioturbation amount distribution. Molecular data of specific biomarkers (*n*-alkanes and regular steranes) and Rock-Eval data are also presented. In a high-resolution black-shale section, this research explores how variations in oxic, sub-oxic-anoxic conditions are linked to lithostratigraphy and OC content, its quality and preservation. These new geochemical observations contribute to exploring OC dynamics and related paleoenvironmental reconstructions in the Tethyan area. Notably, this high-resolution Toarcian black shale section aims to make a case-study to evaluate OC information in relation to paleoenvironmental reconstructions, especially in changing redox dynamics, where drastic alterations of oxygenation levels play a key role in controlling the ultimate fate of organic matter.

## 1.1 Geological framework of the Sogno core

The Lombardy Basin is a well-known Mesozoic study area in northern Italy (Fig. 1 b-c), which identifies a relatively undeformed portion of the Adria microplate in the Tethyan southern margin (Gaetani, 2010). During the Jurassic, sedimentation was controlled by a characteristic horst and graben topography with deeper zones that developed thick complete pelagic successions (Gaetani, 1975, 2010) such as the Sogno Formation. The Sogno Core (Erba et al., 2019b) was drilled next to the type-section of the Sogno Formation (Gaetani and Poliani 1978) (Fig. 1 d), which consists of ~24 metres of limestones and marlstones, including also minor cherts and marly claystones. Notably, the Fish Level (Livello a Pesci, *sensu* Gaetani and Poliani 1978) here records about 5 m; following the lithozones defined by Erba et al. (2019b) it is divided into three lithostratigraphic units (LU) from bottom to top: an interval of grey to very dark-grey and dark red marly limestones (LU-7); grey to very dark-grey marly limestones with reddish to greyish spots (LU-6); black shales characterized by well-developed lamination and pyrite nodules (LU-5).

## 2. Material and methods

Based on a published data-set of the Sogno core, (Erba et al., 2022; Fig. 1), we have selected different sub-sets of samples for new geochemical analysis described below and focused on a high-resolution study of the Fish Level. Personal communication of ongoing analyses of Rock-Eval data from a total of 79 samples of the Sogno core analysed the Department of Earth Sciences at Oxford University (UK), Fe data from coupled plasma mass spectrometer (ICP-MS) analysis at Oldenburg University, and Sulphur concentrations from a vario MICRO CUBE elemental analyser (elementar Corp., USA) at Heriot-Watt University are also presented.

### 2.1 Pyrite and bioturbation distribution

A rectangular-shaped mask, as wide as the diameter of the Sogno core, was used to carry out semi-quantitative analysis of pyrite and bioturbation distribution. The mask, with a 2-cm wide slit relatively to the core center and parallel to the stratification/lamination of the analysed lithology was moved upwards every 2 cm across the Sogno core. The presence and absence of bioturbation, maximum and minimum dimensions, and percentage abundance of burrows is determined following Droser and Bottjer (1986).

## 2.2 Lipid biomarker measurements

Aliquots (~6 grams) from a sub-set of 14 samples (freeze-dried and ground) were extracted with an Accelerated Solvent Extractor (DIONEX ASE 350 System), using a mixture of dichloromethane (DCM)/methanol (MeOH) (5:1, v/v) at a temperature of 100 °C and pressure of 69±10 psi. Sulphur-free extracts (desulfurization by acid-activated copper turnings) were purified by column chromatography over self-packed silica gel (deactivated with 1% ultrapure H<sub>2</sub>O) columns using hexane, hexane:DCM (2:1, v/v), and MeOH as subsequent eluents. The hexane-fraction (dissolved in 50µL hexane) was analysed at the Lyell Centre (Heriot-Watt University) on a Thermo Scientific Trace 1310 GC fitted with a split splitless injector (at 280 °C) and linked to a Single Quadrupole Mass Spectrometer using electron ionization (electron voltage 70eV, source temperature 230 °C, quadrupole temperature 150 °C, multiplier voltage 1800V, interface temperature 310 °C). Samples were investigated both in selected ion monitoring (SIM) and in full scan acquisition mode (50–600 amu/sec), using a thermo fused silica capillary column (60 m x 0.25 mm i.d) coated with 0.25 µm 5 % phenylmethylpolysiloxane phase. The GC temperature was gradually (5 °C/min) increased from 50 to 310 °C, holding the final temperature for 10 minutes and using helium as carrier gas (flow rate of 1 ml/min, initial inlet pressure of 50 kPa, split at 30 ml/min). Reproducibility was monitored using an in-house standard with all targeted compounds and it was better than 10% for all reported biomarkers ratios.

## 3. Results

### 3.1 TOC-S-Fe relationships

The down-core distribution of TOC, S and Fe is shown in Fig. 2 and described below from bottom to top. Fe-S, S-TOC, and Fe-S-TOC relationships are also plotted in diagrams in Fig. 3a, b, and c, respectively.

- Marly limestones below the Fish Level (LU-8 to 13) characterized by widespread bioturbation, olive grey, dark grey, grey, and brown to reddish in colour, document very low TOC (average (avg.) 0.30%; red dots in Fig. 2) and S (avg. 0.01%; red dots in Fig. 2) concentrations. Fe-S-TOC relationships indicate that most samples have also a low and constant S/Fe ratio of 0.01 and no systematic relation between Fe and S content is documented, i.e., R-squared (R<sup>2</sup>) for a

linear regression trend line is close to 0. Fe content varies between ~0.5 and 4 % (Fig. 3a). All samples (red dots in Fig. 3b and c) fall within or below the dashed line ( $S/C=0.4$ ) that correspond to the line defined by Berner and Raiswell (1983) for normal marine sediments, documenting also a quite scattered S-TOC relation ( $R^2 \sim 0.1$ ).

- Marly limestones with variations in colour from grey, to very dark grey and dark red of the lower lithostratigraphic unit of the Fish Level (LU-7) document on average very low TOC (0.16%; grey dots in Fig. 2) and S (avg. 0.14%; grey dots in Fig. 2). Fe-S-TOC relationships show a low and constant S/Fe ratio of 0.04 and the S-Fe  $R^2$  is close to zero, with the Fe content varying between ~2.5 and 5.5 % (Fig. 3a). All samples (grey dots in Fig. 3b and c) fall within or slightly above the dashed line for normal marine sediments ( $S/C=0.4$ ; Berner and Raiswell (1983) and show a positive S-TOC relation with a  $R^2$  of 0.6.
- Marly limestones grey to very dark grey in colour, with reddish to greyish spots, document a general upward increase in TOC (avg. 0.47%; dark grey dots in Fig. 2) and S (avg. 0.61%; dark grey dots in Fig. 2) content in LU-6, in the mid part of the Fish Level. Fe-S-TOC relationships show higher variability but in general S/Fe ratio is on average low, ~0.14 (dark grey dots in Fig. 2 and Fig.3c). A positive S-Fe relation with a high R-squared of 0.83 (Fig. 3a) is documented, with Fe content varying between ~2.5 and 5.5 % (Fig. 3a). Overall all samples (dark grey dots in Fig. 3b and c) fall within or above the dashed line for normal marine sediments ( $S/C=0.4$ ; Berner and Raiswell (1983)), documenting a highly positive S-TOC relation with  $R^2$  of 0.8, excluding a single (outlier) data-point (TOC% 1.38 and S% 0.07 at 14.9 m). Notably, concurrent spikes of S, TOC, and S/Fe slightly above 1%, 2%, and 0.40, respectively, are also documented in dark-grey to black, non-bioturbated, and laminated thin intervals (at ~15.6 and 14.8 meters in Fig. 2).
- Black shales characterized by well-developed lamination in the upper part of the Fish Level (LU-5) document generally higher TOC (avg. 1.26%; black dots in Fig. 2) and S (avg. 2.50%; black dots in Fig. 2) concentrations. Particularly, oscillations in the TOC, S and S/Fe content are documented, showing minimum values of about 0.30%, 2%, and 0.16, and maximum values of about 2.5%, 6.5% and 0.9, respectively (black dots in Fig.2). All samples show a highly positive Fe-S relation with  $R^2 > 0.9$  and S/Fe ratio is on average higher, ~0.60. Moreover, overall all samples (black dots in Fig. 3b and c) fall above the dashed line for normal marine sediments ( $S/C=0.4$ ; Berner and Raiswell (1983)), although documenting a scattered S-TOC relation with a  $R^2$  of 0.2.
- Marly limestones above the Fish Level (LU-4) characterized by widespread bioturbation, dark grey to grey in colour, document a general sharp decrease in TOC (avg. 0.44%; blue dots in

Fig. 2) and S (avg. 1.16%; blue dots in Fig. 2) concentrations. Fe-S-TOC relationships show an average low S/Fe ratio of 0.32 (blue dots in Fig. 2), and a highly positive correlation of S-Fe with  $R^2 > 0.9$  (blue dots Fig. 3a). Note an organic-rich thin layer of few centimeters (at ~11.3 meters in Fig. 2) documents concurrent higher TOC, S and S/Fe concentrations up to about 2%, 5% and 0.9, respectively (blue boxes in Fig. 2). All samples (blue dots and boxes in Fig. 3b and c) sit above the dashed line for normal marine sediments ( $S/C=0.4$ ; Berner and Raiswell (1983) and show a positive S-TOC relation with a  $R^2$  of 0.6.

### 3.2 Pyrite and bioturbation distribution

Fossil traces (*Planolites* and *Chondrites*) are identified in all lithostratigraphic units. Bioturbation is very high in the reddish limestone of LU-8, in the range of 50-100%, and it progressively decreases upwards, within the Fish Level (Fig. 2), with average values of about 20%. Discontinuous well laminated black shales intervals document faded or lack of bioturbation. Minimum values are documented in the upper lithostratigraphic unit of the Fish Level. On top of LU-5, the bioturbation amount increases again to average values of 50%, showing minimum values only in a thin OC-rich layer.

Pyrite is identified within and slightly above the Fish Level. The nodular, powdery and laminar (maximum thickness 5 mm) pyrite distribution is reported in Fig. 2. Nodular pyrite is the most common, with nodules reaching a maximum diameter and abundance of about 10mm, and 7 to 9 nodules per stratigraphic centimeter, respectively. Laminar pyrite is generally rare, documenting discontinuous laminae with a maximum length of 10-11 cm and a maximum thickness of 0.5 cm. Powdery pyrite is identified and very abundant only in the topmost part of the Fish level and in an OC-rich black shale layer in LU-4.

### 3.3 Organic carbon sources

OC sources are assessed based on the relative abundances of chain lengths of *n*-alkanes, which range from  $nC_{15}$  to  $nC_{35}$ . High molecular weight (HMW)  $nC_{25}$  to  $nC_{35}$  *n*-alkanes show no odd-over-even pre-dominance, i.e., the avg. carbon preference index  $CPI_{25-34}$  is ~1. The average chain length ratio (ACL from Peters et. al., 2005) is overall always <25. Regular steranes homologues are the major compounds in the m/z 217 fragmentograms, which is the dominant ion in the mass spectra. The different isomers,  $5\alpha(H), 14\alpha(H), 17\alpha(H)$  (abbreviated

$\alpha\alpha\alpha$ ) and  $5\alpha(H),14\beta(H),17\beta(H)$  (abbreviated  $\alpha\beta\beta$ ), were recognised evaluating the ratios of two specific molecular ions,  $m/z$  149 and  $m/z$  151, or in alternative  $m/z$  217 and  $m/z$  218; the ratios were estimated using peak heights. In addition, the 22S and 22R epimers were distinguished, for both  $\alpha\alpha\alpha$  and  $\alpha\beta\beta$  isomer types. Overall, consistent distribution of the regular steranes ( $C_{27}$ ,  $C_{29}$ ,  $C_{30}$ ) is documented. In particular, for all samples, the evaluation of the relative abundance of the  $C_{27}$ ,  $C_{28}$ ,  $C_{29}$   $\alpha\alpha\alpha$  isomers was possible. Thus, the relative abundance of  $C_{27}$  *iso*-steranes was calculated with the  $\alpha\alpha\alpha$  isomers (S+R epimers), using *p:IGI software*. The following equation was employed:

$$\text{St27Iso} = \text{C27 Iso-steranes} / \text{C27 to C29 iso-steranes}$$

Where:

$$\text{C27 iso-steranes} = 217\text{St } 27\text{IsoR and } 217\text{St } 27\text{IsoS}$$

$$\text{C28 iso-steranes} = 217\text{St } 28\text{IsoR and } 217\text{St } 27\text{IsoS}$$

$$\text{C29 iso-steranes} = 217\text{St } 29\text{IsoR and } 217\text{St } 29\text{IsoS}$$

Thereafter, the ratio was plotted against the St28Iso and St29Iso (relative abundance of the  $C_{28}$  and  $C_{29}$  *iso*-steranes, respectively) in triangular diagrams. In the ternary diagrams, the plot locations show a general dominance of  $C_{27}$  *iso*-sterane, indicating dominant marine OM.

### 3.4 Water column stratification and paleo-redox conditions

Ratios of pristanes (Pr) and phytanes (Py) were also used to explore the sources of OM and redox conditions. Pristane and phytane were found in all samples analysed, with an overall predominance of pristane over phytane. Pristane/Phytane (Pr/Py) ratios range between ~1 and 1.9, interrupted only in the upper part of the Fish Level (at ~13 to 12.5 meters), where ratios of about 0.7-0.8 are documented. All higher-TOC and sulphur samples within the Fish Level were screened for lycopane, isorenieratene derivatives and related compounds, the occurrence of which is limited to anoxic depositional settings (Sinnighe Damste' et al., 2003) and imply photic zone euxinia (Koopmans et al., 1996), respectively. However, none of these compounds were detected in any of the measured samples. Moreover, quantification of gammacerane was not possible because of impractical separation of this compound, which is nearly co-eluting with the 22R epimer of  $C_{31}$ -homohopane.

### 3.5 Rock-Eval pyrolysis

In the Sogno core, HI ranges from 0 to 438 mg HC/g TOC. Values close to zero are recorded in the lithostratigraphic units below the black shale interval and there is a clear upward increasing trend within the Fish Level. On top of that, values return close to zero, remaining high (>200) only in an organic-rich layer in LU-4. The highest HI values are measured in the topmost part of the black shale interval, in LU-5.  $T_{max}$  values range between 426 and 439°C ° in all samples. For the given HI and  $T_{max}$  results, screened samples with TOC >0.5 are classified as kerogens types II and mixed type II/III hydrocarbons within and above the Fish Level. Low TOC samples ( $\leq 0.5\%$ ), below and above the Fish Level, and in its lower lithostratigraphic units (LU -7 and 6), plot as kerogens type III to IV. The calculated oxygen index (OI) is very scattered and varies between extremely low values (<10) and up to >100, showing no systematic relation with HI and  $T_{max}$ .

## 4. Discussions

### 4.1 Thermal maturity and organic carbon sources

$T_{\max}$  values of  $\sim 426\text{-}439^{\circ}\text{C}$  consistent for type II and type III kerogens (HI  $\sim 200\text{-}440$ ) indicate low stage thermal maturity. Particularly,  $T_{\max}$  results do not increase downcore and similar values are reconstructed in all screened samples, also in those plotting as kerogens type III to IV that document very low residual TOC and HI. Moreover, incomplete homohopane and iso-sterane isomerisation with average 22S C<sub>32</sub>  $\alpha\beta$  hopane and 20S C<sub>29</sub>  $\alpha\alpha\alpha$  sterane values  $<0.5$  and  $<0.6$ , respectively, suggest no relevant thermal maturity impacting the study biomarker compounds (Peters et al., 2005). Therefore, CPI values of  $\sim 1$  likely arise from a predominance of marine input rather than indicating thermal maturity in all screened samples below, within, and above the Fish Level. This is consistent with Rock-Eval data that document dominant marine kerogen type II/III hydrocarbons in all screened samples with TOC values  $>0.5$ . Note that low TOC ( $\leq 0.5\%$ ) samples documenting low HI values (in this study  $<170$ ), which plot as kerogen types III to IV types are to be treated with cautious (Peters et al., 2005). In fact, all these samples come from the lower LU-7 and 6 of the Fish Level, and/or samples below or above the black shale interval, which contains OM deposited under very well oxygenated conditions (see discussion below), implying relevant aerobic decay (Peters et al., 2005). Relatively low Pr/Py ratios (always  $<2$ ) - consistent with *n*-alkanes distributions and regular steranes - also document OM with dominant marine sources (Peters et al., 2005).

### 4.2 Evolution of redox conditions across the Jenkyns Event

The reddish and greyish marly limestones below and in the lowermost portion of the Fish Level, which identifies the interval preceding the Jenkyns Event and its early onset phase, document a well oxygenated depositional setting. Very high bioturbation amount, and extremely low S/Fe and TOC concentrations are indeed documented in these intervals. Particularly, besides recording almost identical geochemical characteristics (TOC, S, S/Fe values) to the sediments underneath, the lowermost LU-7 of the Fish Level registers a progressive decrease in bioturbation following the onset of the Jenkyns Event; this is consistent with a drastic depletion in calcium carbonate that marks the onset of the event (Erba et al., 2022), explained as the result of a crisis of the heavily calcified nannoplankton, due to CO<sub>2</sub> –



induced ocean acidification (Casellato and Erba, 2015). The mid greyish to dark-grey limestones within the Fish Level mark a transitional phase, which registers peaks in TOC >1% (Erba et al., 2022), concurrent with changes in redox parameters, such as peaks in S/Fe ratios and depletion in bioturbation amount, suggesting swings from oxic to more de-oxygenated conditions. In well laminated black shales from the upper part of the Fish Level – the high TOC-black shale *sensu strictu* – and in a thin OC-rich interval on top of LU-5, sub-oxic to anoxic conditions are inferred by S/Fe ratios >0.45, which are supported by TOC values up to 2% (on avg. >1%), as well as abundant powdery pyrite, and extremely faded to almost absent bioturbation. Notably, also Pr/Py ratios become <0.1 only in the topmost part of the Fish Level, suggesting a distinct oxygen-depleted environment (Peters et al., 2005). In contrast, the higher Pr/Py ratios of about 1-1.5 documented in the other intervals point out more oxic conditions (Peters et al., 2005). Furthermore, in the upper part of the black shale interval, sporadic peaks in pyrite and S/Fe ratios >0.75 might suggest a restricted intensification of de-oxygenation, possibly reaching euxinia. However, it is not recognized the occurrence of any organic compound supporting a proper anoxic depositional setting and/or photic zone euxinia. Particularly, superimposed on the generally high TOC and dysoxic trend described above, the upper part of the Fish Level also documents minor oscillations to more oxic conditions, which are inferred by a decrease in S/Fe ratios (<0.45), concurrent with a decrease in TOC (<1%), and an increase in bioturbation amount (up to 25%). Therefore, in accordance with other black shales from the Tethyan region (Pancost et al., 2004; Sabatino et al., 2009), we exclude the development of persistent bottom water anoxia in the study Albenza region even during the more extreme paleo-environmental conditions recorded during the Jenkyns Event.

On top of the black shale interval, in the early recovery phase of the Jenkyns Event (lowermost part of J2 in Fig.2), a prompt increase in bioturbation suggests a recovery in oxygenation levels, as also indicated by a rise in the CaCO<sub>3</sub>% content in Erba et al., 2022. Despite the limited sample geochemical analysis, we identify on top of the Fish Level another transitional phase, characterized by swings in redox parameters with varying TOC and S/Fe concentrations, culminating with the latest thin OC-rich layer.

## 5. Preliminary conclusions and implications

1. Both inorganic (S/Fe) and organic redox proxies (Pr/Py, TOC) together with bioturbation and lithology evidence, including pyrite distribution, suggest an upward decrease in oxygenation levels across the Fish Level, which documents an initial oxic environment with poor preservation conditions of the organic matter. The topmost part of the black shale unit shows progressively more dysoxic to anoxic conditions, although recording intermittent minor fluctuations towards euxinia as well as towards more oxygenated intervals. Therefore, we exclude the development of persistent bottom water anoxia in the study Albenza region even during the more extreme paleo-environmental conditions recorded during the Jenkyns Event.
2. The TOC and HI contents of the black shale interval of the Sogno core increase upward, reaching the highest values in the topmost part of the Fish Level; this interval, which records the lowest paleo-oxygenations levels, thus documents the greatest preservation of organic material (TOC and HI up to 2% and 400 HC/g TOC, respectively). Note that all samples analysed show the same low range of thermal maturity based on  $T_{\max}$  data, but are heterogeneous in kerogen type, including type II, mixed II/II, III and IV. However, samples classified as type III to IV, accordingly to molecular analysis, are not inferred by a different origin of the OM but are due to different aerobic decay. Samples from the lower portion of the Fish Level thus contain oxidised organic matter with extremely low TOC (<0.5%) and HI (<170 HC/g TOC) values.
3. Molecular data reconstruct dominant pelagic organic matter, consistent with kerogen type II and mixed type II/III in well-preserved samples in the top part of the Fish Level. No evidence of relevant terrestrial input is documented.
4. The overall homogenous thermal maturity stage and good correlation between the paleo-redox parameters and TOC content implies that paleoenvironment had a strong controlling effect on the accumulation and preservation of organic matter in the Albenza Basin.

## 6. Figures

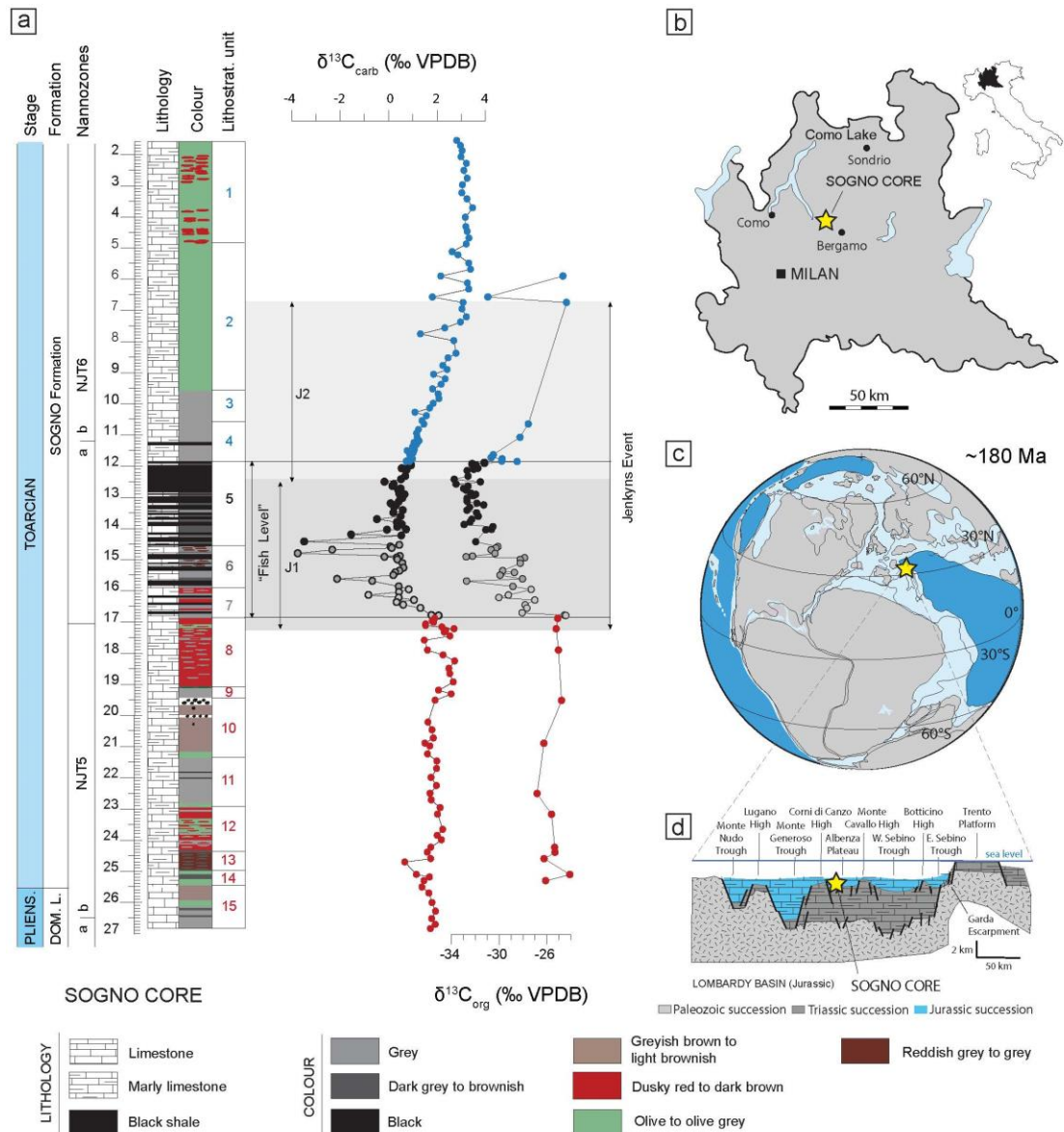


**Fig. 1:** **a.** Nannofossil biostratigraphy (from Visentin and Erba (2021)), lithostratigraphy (from Erba et al. (2019b)), and chemostratigraphy (from Erba et al., 2022) of the Sogno core. Carbon isotopes on bulk carbonate ( $\delta^{13}\text{C}_{\text{carb}}$ ) and bulk organic matter ( $\delta^{13}\text{C}_{\text{org}}$ ) show samples below (red dots), within (grey, dark grey, and black dots), and above the “Fish Level” (blue dots). The lower and the upper part of the Jenkyns Event, J1 (dark grey box) and J2 (grey box), are indicated as defined in Erba et al., 2022. **b.** Present-day location of the Sogno core in the Lombardy area (Italy), and paleogeographic position of the study area in **(c)** paleo-map and **(d)** schematic section across the Lombardy basin during the Toarcian (~180 Ma) (modified after Erba et al., 2022).

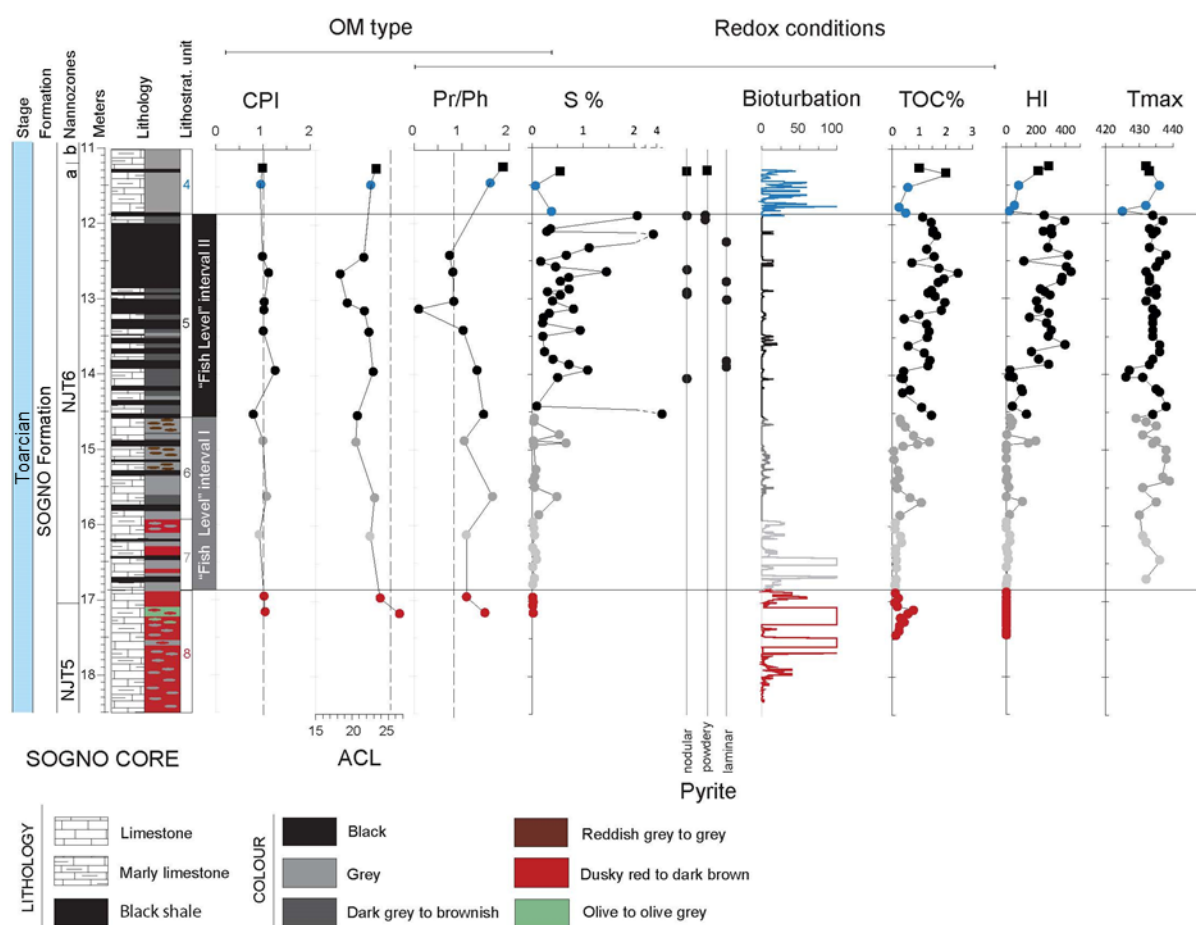


**Fig. 2:** Down-core distribution of selected biomarkers ratios used to reconstruct redox conditions and organic matter (OM) type: carbon preference index (CPI), average chain length (ACL), and pristane/phytane (Pr/Py) ratios as defined in Peter et al. (2005); pyrite distribution and bioturbation amount in percentage; percentages of TOC, TS, and S/Fe ratios (with redox states as proposed by Raisswell et al. (1998), Leventhal (1983), and Berner and Raiswell (1983)).

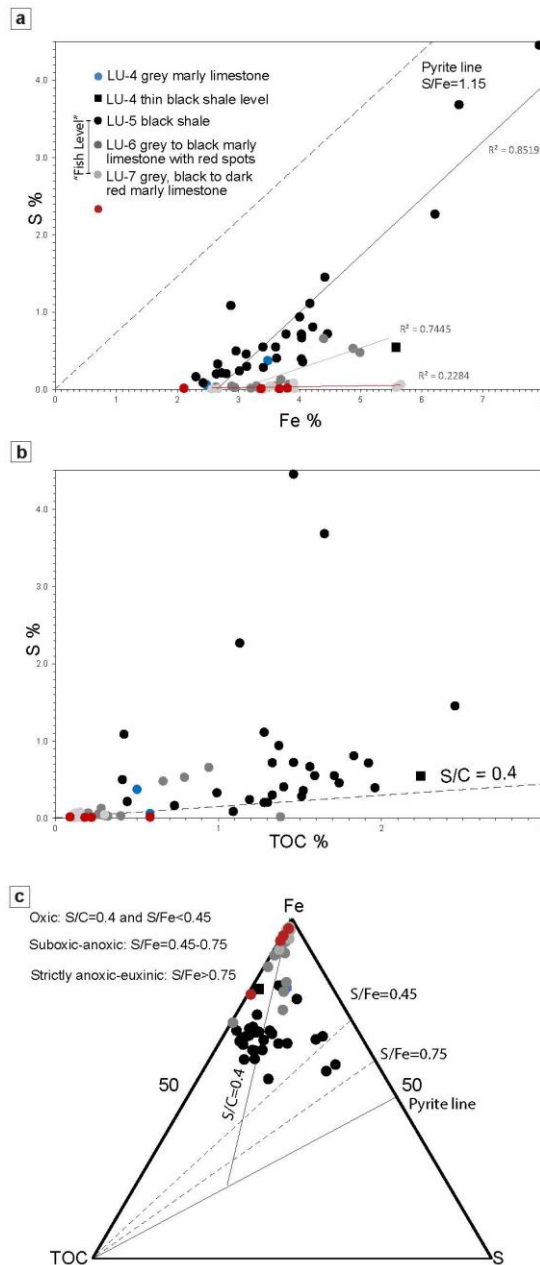


**Fig. 3:** Samples (dots) from lithostratigraphic units above (blue), within (black, dark grey, and grey), and below (red) the “Fish Level” are represented. Linear trend lines and respective R-squared values are reported for distinct samples distributions discussed in the text. **a.** Total sulphur (S) versus total iron (Fe) concentrations. The dashed line corresponds to the pyrite line ( $S/Fe=1.15$ ). **b.** S versus total organic carbon (TOC) concentrations. Dashed lines correspond to the line defined by Berner and Raiswell (1983) for normal marine sediments ( $S/C=0.4$ ). **c.** Ternary diagram illustrating TOC, S, and Fe relationships with characteristic  $S/Fe$  and  $S/C$  ratios used to discriminate redox states (i.e., oxic conditions:  $S/C=0.4$  and; sub-oxic-anoxic conditions:  $S/Fe=0.45-0.75$ ; and strictly anoxic-euxinic conditions:  $S/Fe > 0.75$ ) as proposed by Raiswell et al. (1988), Leventhal (1983), and Berner and Raiswell (1983).

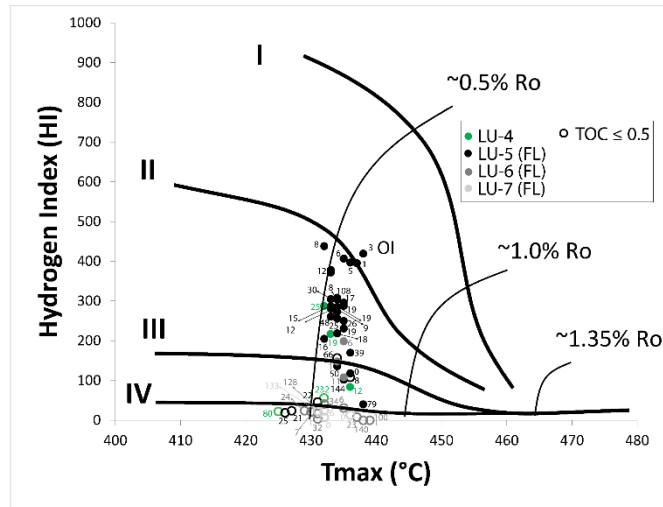


**Fig. 4:** Van Krevelen Diagram showing kerogen type of the Sogno core based on Hydrogen Index (HI) and  $T_{max}$  Rock-Eval data.

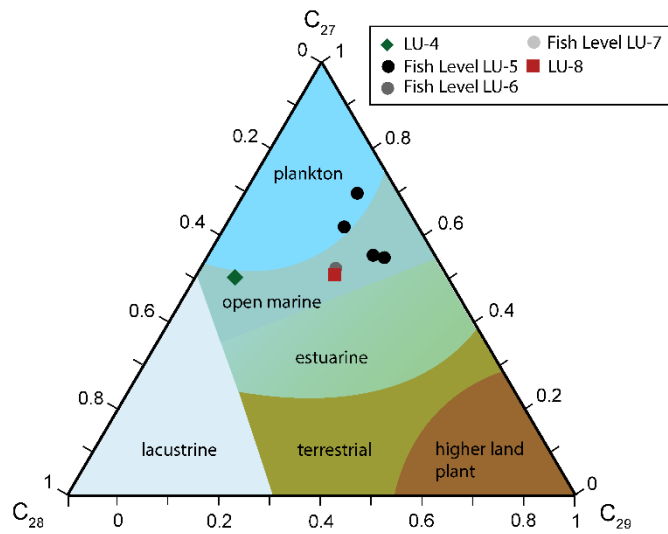


**Fig. 5:** Ternary diagram showing distribution of  $C_{27}$ ,  $C_{28}$ ,  $C_{29}$   $\alpha\alpha\alpha$  regular steranes in the lithostratigraphic units above, within and below the Fish Level in the Sogno core.

## 7. References

1. Arndt S, Jørgensen B. B., LaRowe D. E., Middelburg J. J., Pancost R. D., Regnier P., 2013. Quantifying the degradation of organic matter in marine sediments: a review and synthesis. *Earth-Science Reviews* 123, 53–86.
2. Al-Suwaidi, A.H., Angelozzi, G.N., Baudin F., Damborenea, S.E., Hesselbo, S.P., Jenkyns, H.C., Manceñido, M.O., Riccardi, A.C., 2010. First record of the Early Toarcian Oceanic Anoxic Event from the Southern Hemisphere, Neuquén Basin, Argentina. *Journal of the Geological Society of London* 167, 633–636.
3. Berner, R. A., Raiswell, R., 1983. Burial of organic carbon and pyrite sulfur in sediments over Phanerozoic time: a new theory, *Geochimica et Cosmochimica Acta* 47, 855–862
4. Bray, E.E. and Evans, E.D., 1961. Distribution of n-paraffins as a clue to recognition of source beds. *Geochimica et Cosmochimica Acta* 22(1), 2–15.
5. Casellato, C.E., Erba, E., 2015. Calcareous nannofossil biostratigraphy and paleoceanography of the Toarcian Oceanic Anoxic Event at Colle di Sogno section (Southern Alps, Italy). *Rivista Italiana di Paleontologia e Stratigrafia* 105, 343–376.
6. Castellarin, A., 1972. Evoluzione paleotettonica sinsedimentaria del limite tra ‘Piattaforma Veneta’ e ‘Bacino Lombardo’, a nord di Riva del Garda. *Giornale di Geologia serie 2a*, 38, 11–212.
7. Droser, M.L. and Bottjer, D.J., 1986. A semiquantitative field classification of ichnofabric. *Journal of Sedimentary Research* 56(4).
8. Emmanuel, L., Renard, M., Cubaynes, R., De Rafelis, M., Hermoso, M., Lecallonnec, L., Le Solleuz, A., and Rey, J., 2006. The “Schistes Carton” of Quercy (Tarn, France): a lithological signature of a methane hydrate dissociation event in the early Toarcian. Implications for correlations between Boreal and Tethyan realms. *Bulletin de la Société Géologique de France* 177, 239–249.
9. Erba, E., Bottini, C., Faucher, G., Gambacorta, G., Visentin, S., 2019a. La risposta del nannoplancton calcareo agli Eventi Anossici Oceanici: il record pelagico in Italia [The response of calcareous nannoplankton to Oceanic Anoxic Events: The Italian pelagic record]. In *Symposium on Environmental Crises and Biotic Responses in the History of the Earth-An Italian Perspective at the Congress of the Italian-Paleontological-Society (SPI)*. Società Paleontologica Italiana 58 (1), 51–71.
10. Erba, E., Gambacorta, G., Visentin, S., Cavalheiro, L., Reolon, D., Faucher, G., Pegoraro, M.,

- 2019b. Coring the sedimentary expression of the early Toarcian Oceanic Anoxic Event: new stratigraphic records from the Tethys Ocean. *Scientific Drilling* 26, 17–27.
11. Fantasia, A., Föllmi, K.B., Adatte, T., Bernàrdez, E., Spangenberg, J.E., and Mattioli, E., 2018. The Toarcian Oceanic Anoxic Event in southwestern Gondwana: an example from the Andean Basin, northern Chile. *Journal of the Geological Society* 175, 883–902.
  12. Gaetani, M., 1975. Jurassic stratigraphy of the Southern Alps: a review. In: Squyres, C.H. (Ed.), *Geology of Italy, I*, Earth Sciences Society of the Libyan Arab Republic, Tripoli, Libya 377–402.
  13. Gaetani, M., 2010. From Permian to Cretaceous: Adria as pivotal between extensions and rotations of Tethys and Atlantic Oceans. In: Beltrando, M., Peccerillo, A., Mattei, M., Conticelli, S., Doglioni, C. (Eds), *The Geology of Italy*. *Journal of the Virtual Explorer* 36, 5.a.
  14. Gaetani, M., Poliani, G., 1978. Il Toarciano e il Giurassico medio in Albenza (Bergamo). *Rivista Italiana di Paleontologia e Stratigrafia* 84, 349–382.
  15. Gröcke, D.R., Hori, R.S., Trabucho-Alexandre, J., Kemp, D.B., Schwark, L., 2011. An open ocean record of the Toarcian oceanic anoxic event. *Solid Earth*, 2, 245–257.
  16. Hallam, A., 1967. The depth significance of shales with bituminous laminae. *Marine Geology* 5, 481–493.
  17. Hesselbo, S. P., Gröcke, D., Jenkyns, H. C., Bjerrum, C.J., Farrimond, P., Bell, H. S. M., Green, O. R., 2000. Massive dissociation of gas hydrate during a Jurassic oceanic anoxic event. *Nature* 406, 392–395.
  18. Hesselbo, S. P., Jenkyns, H. C., Duarte, L. V., Oliveira, L. C., 2007. Carbon-isotope record of the Early Jurassic (Toarcian) Oceanic Anoxic Event from fossil wood and marine carbonate (Lusitanian Basin, Portugal). *Earth and Planetary Science Letters* 253(3–4), 455–470.
  19. Hougård, I.W., Bojese-Koefoed, J.A., Vickers, M.L., Ullmann, C.V., Bjerrum, C.J., Rizzi, M., Korte, C., 2021. Redox element record shows that environmental perturbations associated with the T-OAE were of longer duration than the carbon isotope record suggests – the Aubach section, SW Germany. *Newsletters on Stratigraphy* 54, 229–246.
  20. Ikeda, M., Hori, R.S., Ikehara, M., Miyashita R., Chino, M., Yamada. K., 2018. Carbon cycle dynamics linked with Karoo-Ferrar volcanism and astronomical cycles during Pliensbachian-Toarcian (Early Jurassic). *Global and planetary Change* 170, 163–171.
  21. Izumi, K., Miyaji, T., Tanabe, K., 2012. Early Toarcian (Early Jurassic) oceanic anoxic event recorded in the shelf deposits in the northwestern Panthalassa: evidence from the Nishinakayama formation in the Toyora area, west Japan. *Palaeogeography, Palaeoclimatology, Palaeoecology* 15–316, 100–108.



22. Kafousia, N., Karakitsios, V., Jenkyns, H.C. and Mattioli, E., 2011. A global event with a regional character: the Early Toarcian Oceanic Anoxic Event in the Pindos Ocean (northern Peloponnese, Greece). *Geological Magazine* 148, 619–631.
23. Kafousia, N., Karakitsios, V., Mattioli, E., Kenjo, S., Jenkyns H.C., 2014. The Toarcian Oceanic Anoxic Event in the Ionian Zone, Greece. *Palaeogeography, Palaeoclimatology, Palaeoecology* 393, 135–145.
24. Koopmans, M. P., Köster, J., Van Kaam-Peters, H. M. E., Kenig, F., Schouten, S., Hartgers, W. A., de Leeuw, J. W., Sinninghe Damsté, J. S., 1996. Diagenetic and catagenetic products of isorenieratene: molecular indicators for photic zone anoxia, *Geochimica et Cosmochimica Acta* 60, 4467–4496.
25. Leventhal, J. S., 1983. An interpretation of carbon and sulfur relationships in Black Sea sediments as indicators of environments of deposition. *Geochimica et Cosmochimica Acta* 47, 133–137.
26. Jenkyns, H. C., 1985. The Early Toarcian and Cenomanian-Turonian anoxic events in Europe: comparisons and contrasts. *Geologische Rundschau* 74(3), 505–518.
27. Jenkyns, H., 1988. The early Toarcian (Jurassic) anoxic event-stratigraphic, sedimentary, and geochemical evidence. *American Journal of Science* 288(2), 101–151.
28. Jenkyns, H. C., 2010. Geochemistry of oceanic anoxic events. *Geochemistry, Geophysics, Geosystems* 11, Q03004.
29. Jenkyns, H.C., Jones, C.E., Gröcke, D.R., Hesselbo, S.P., Parkinson, D.N., 2002. Chemostratigraphy of the Jurassic System: applications, limitations and implications for palaeocoenography. *Journal of the Geological Society* 159, 351–378.
30. Pancost, R.D., Crawford, N., Magness, S., Turner, A., Jenkyns, H.C., Maxwell, J.R., 2004. Further evidence for the development of photic-zone euxinic conditions during Mesozoic oceanic anoxic events. *Journal of the Geological Society* 161(3), 353–364.
31. Peters, K.E., Peters, K.E., Walters, C.C., Moldowan, J.M., 2005. *The biomarker guide*. Cambridge university press, 1.
32. Raiswell, R., Buckley, F., Berner, R. A., Anderson, T. F., 1988. Degree of pyritization of iron as a paleoenvironmental indicator of bottomwater oxygenation. *Journal of Sedimentary Research* 58, 812–819.
33. Reolid, M., 2014. Stable isotopes on foraminifera and ostracods for interpreting incidence of the Toarcian Oceanic Anoxic Event in Westernmost Tethys: role of water stagnation and productivity. *Palaeogeography, Palaeoclimatology, Palaeoecology* 395, 77–91.
34. Reolid, M., Mattioli, E., Duarte, L. V., Marok, A., 2020. The Toarcian Oceanic Anoxic Event

- and the Jenkyns Event (IGCP-655 final report). *Episodes* 43(2), 833–844.
35. Röhl, H.-J., Schmid-Röhl, A., Oschmann, W., Frimmel, A., Schwark, L., 2001. The Posidonia Shale (Lower Toarcian) of SW-Germany: an oxygen-depleted ecosystem controlled by sea level and palaeoclimate. *Palaeogeography, Palaeoclimatology, Palaeoecology* 165, 27–52.
  36. Sabatino, N., Neri, R., Bellanca, A., Jenkyns, H.C., Baudin, F., Parisi, G., Masetti, D., 2009. Carbon-isotope records of the Early Jurassic (Toarcian) oceanic anoxic event from the Valdorbia (Umbria–Marche Apennines) and Monte Mangart (Julian Alps) sections: Palaeoceanographic and stratigraphic implications. *Sedimentology* 56(5), 1307–1328.
  37. Schouten, S., van Kaam-Peters, H.M.E., Rijpstra, W.I.C., Schoell, M., Sinninghe Damsté, J.S., 2000. Effects of an oceanic anoxic event on the stable carbon isotopic composition of early Toarcian carbon. *American Journal of Science* 300, 1–22.
  38. Sinninghe Damsté, J. S., Kuypers, M. M. M., Schouten, S., Schulte, S., Rullkötter, J., 2003. The lycopane/C31 n-alkane ratio as a proxy to assess palaeoxicity during sediment deposition, *Earth and Planet Science Letters* 209, 215–226.
  39. Them, T. R., Gill, B. C., Selby, D., Gröcke, D. R., Friedman, R. M., Owens, J. D., 2017. Evidence for rapid weathering response to climatic warming during the Toarcian Oceanic Anoxic Event. *Scientific reports* 7(1), 1–10.
  40. van Breugel, Y., Baas, M., Schouten, S., Mattioli, E., Damsté, J.S.S., 2006. Isorenieratane record in black shales from the Paris Basin, France: Constraints on recycling of respired CO<sub>2</sub> as a mechanism for negative carbon isotope shifts during the Toarcian oceanic anoxic event. *Paleoceanography* 21, PA4220.
  41. Visentin, S., Erba, E., 2021. High-resolution calcareous nannofossil biostratigraphy 1 across the Toarcian Oceanic Anoxic Event in northern Italy: clues from the Sogno and Gajum Cores (Lombardy Basin, Southern Alps). *Rivista Italiana di Paleontologia e Stratigrafia* 127, 539–556.
  42. Xu, W., Ruhl, M., Jenkyns, H.C., Hesselbo, S.P., Riding, J.B., Selby, D., Naafs, B.D.A., Weijers, J.W.H., Pancost, R.D., Tegelaar, E., Idiz, E., 2017. Carbon sequestration in an expanded lake system during the Toarcian oceanic anoxic event. *Nature Geoscience* 10, 129–134.

---

## 5. Impact of global cooling on Early Cretaceous high $p\text{CO}_2$ world during the Weissert Event

In *Nature Communications*, 12(1), 1–11, 2021








<https://doi.org/10.1038/s41467-021-25706-0>

**Author(s):** L. Cavalheiro, T. Wagner, S. Steinig, C. Bottini, W. Dummann, O. Esegbue, G. Gambacorta, V. Giraldo-Gómez, A. Farnsworth, S. Flögel, P. Hofmann, D. J. Lunt, J. Rethemeyer, S. Torricelli, and E. Erba.

### Abstract

The Weissert Event ~133 million years ago marked a profound global cooling that punctuated the Early Cretaceous greenhouse. We present modelling, high-resolution bulk organic carbon isotopes and chronostratigraphically calibrated sea surface temperature (SSTs) based on an organic paleothermometer (the  $\text{TEX}_{86}$  proxy), which capture the Weissert Event in the semi-enclosed Weddell Sea basin, offshore Antarctica (paleolatitude ~54 °S; paleowater depth ~500 meters). We document a ~3–4 °C drop in SST coinciding with the Weissert cold end, and converge the Weddell Sea data, climate simulations and available worldwide multi-proxy based temperature data towards one unifying solution providing a best-fit between all lines of evidence. The outcome confirms a 3.0 °C ( $\pm 1.7$  °C) global mean surface cooling across the Weissert Event, which translates into a ~40% drop in atmospheric  $p\text{CO}_2$  over a period of ~700 thousand years. Consistent with geologic evidence, this  $p\text{CO}_2$  drop favoured the potential build-up of local polar ice.

# Impact of global cooling on Early Cretaceous high $p\text{CO}_2$ world during the Weissert Event

Liyenne Cavalheiro <sup>1</sup>, Thomas Wagner <sup>2</sup>✉, Sebastian Steinig<sup>3</sup>, Cinzia Bottini <sup>1</sup>, Wolf Dummann<sup>4,8</sup>, Onoriode Esegbue<sup>2,9</sup>, Gabriele Gambacorta<sup>5</sup>, Victor Giraldo-Gómez <sup>1</sup>, Alexander Farnsworth <sup>3,10</sup>, Sascha Flögel<sup>6</sup>, Peter Hofmann<sup>4</sup>, Daniel J. Lunt <sup>3</sup>, Janet Rethemeyer<sup>4</sup>, Stefano Torricelli<sup>7</sup> & Elisabetta Erba <sup>1</sup>

The Weissert Event ~133 million years ago marked a profound global cooling that punctuated the Early Cretaceous greenhouse. We present modelling, high-resolution bulk organic carbon isotopes and chronostratigraphically calibrated sea surface temperature (SSTs) based on an organic paleothermometer (the  $\text{TEX}_{86}$  proxy), which capture the Weissert Event in the semi-enclosed Weddell Sea basin, offshore Antarctica (paleolatitude ~54 °S; paleowater depth ~500 meters). We document a ~3–4 °C drop in SST coinciding with the Weissert cold end, and converge the Weddell Sea data, climate simulations and available worldwide multi-proxy based temperature data towards one unifying solution providing a best-fit between all lines of evidence. The outcome confirms a 3.0 °C ( $\pm 1.7$  °C) global mean surface cooling across the Weissert Event, which translates into a ~40% drop in atmospheric  $p\text{CO}_2$  over a period of ~700 thousand years. Consistent with geologic evidence, this  $p\text{CO}_2$  drop favoured the potential build-up of local polar ice.

<sup>1</sup>Department of Earth Sciences Arditio Desio, University of Milan, Milan, Italy. <sup>2</sup>The Lyell Centre, Heriot-Watt University, Edinburgh, UK. <sup>3</sup>School of Geographical Sciences, University of Bristol, Bristol, UK. <sup>4</sup>Institute of Geology and Mineralogy, University of Cologne, Cologne, Germany. <sup>5</sup>Eni S.p.A. Natural Resources–Geology and Geophysics Research and Technological Innovation, San Donato Milanese, Milan, Italy. <sup>6</sup>GEOMAR Helmholtz Centre for Ocean Research, Kiel, Germany. <sup>7</sup>Eni S.p.A. Natural Resources–Sedimentology, Stratigraphy and Petrography Department, San Donato Milanese, Milan, Italy. <sup>8</sup>Present address: Institute of Geosciences, Goethe-University Frankfurt, Frankfurt am Main, Germany. <sup>9</sup>Present address: School of Natural and Environmental Science, Newcastle University, Newcastle, UK. <sup>10</sup>Present address: State Key Laboratory of Tibetan Plateau Earth System, Resources and Environment (TPESRE), Institute of Tibetan Plateau Research, Chinese Academy of Sciences, Beijing 100101, China. ✉email: [t.wagner@hw.ac.uk](mailto:t.wagner@hw.ac.uk)

The greenhouse world of the Mesozoic–Paleogene is a primary target for understanding the behaviour of the Earth system during periods of extreme warmth and its response to recurrent episodes of short-term warming<sup>1–4</sup> and cooling<sup>5–7</sup>, including the possible build-up of polar ice<sup>8</sup>. The Late Valangian (Early Cretaceous) Weissert Event, calibrated in the uppermost part of magnetic chron CM12 through the upper part of magnetic chron CM11<sup>9</sup> (~133.9–132.6 million years ago; updated chronological framework in this study) has large potential to shed light on the climate-carbon-ice relationships at elevated but not very high atmospheric  $p\text{CO}_2$  levels (~500–1700 ppm<sup>10</sup>). The Weissert perturbation is globally documented in the sedimentary record by a positive (+1.5‰) carbon isotope excursion (CIE) observed both in organic and inorganic records<sup>9</sup>. The Weissert CIE, like other Cretaceous climate perturbations<sup>5–7</sup>, is associated with extended volcanism (Paraná-Etendeka Large Igneous Province<sup>9</sup>), a carbonate crisis in pelagic and neritic environments, local to regional enhanced productivity, and oceanic dysoxia/anoxia that likely boosted marine organic carbon ( $C_{\text{org}}$ ) burial, in combination triggering atmospheric  $p\text{CO}_2$  drawdown and global cooling<sup>9,11–16</sup>. However, there are only few proxy records<sup>6,15–18</sup> that document the complete temperature evolution across the Weissert Event. Even less is known about absolute atmospheric  $p\text{CO}_2$  levels and the extent of transient polar ice buildup. Many temperature proxy records are inconsistent in their interpretation due to contrasting ocean temperature reconstructions based on  $\text{TEX}_{86}$ <sup>17</sup>, oxygen isotopes<sup>16,18</sup> and Mg/Ca palaeothermometers<sup>15</sup>, no systematic comparison with independent evidence, such as climate model simulations, and a lack of alignment against unified chronological frameworks. Furthermore, Valangian stratigraphic sections from the climatically sensitive sub-polar/polar regions are particularly rare<sup>16,17,19,20</sup>, fostering the debate regarding whether the Weissert cooling led to sub-polar glaciation<sup>8,19,21</sup>, as suggested by the occurrence of Late Valangian glendonites, dropstones, tillites, and ice-rafted debris both in sub-Arctic and sub-Antarctic regions (see<sup>16</sup>).

Here we present high-resolution data from a ~14 metres long, calcium carbonate-rich and finely laminated black shale section (78.61–93 metres below seafloor (mbsf); cores 113–692–10R and 113–692–12R) from Ocean Drilling Program (ODP) Site 692 (Leg 113) in the Weddell Sea (East Antarctica)<sup>22</sup>. Sample material was provided by GCR—Gulf Coast Repository Texas A&M University, College Station, Texas, under request 067321IODP. Site 692 was located in a semi-enclosed shelf basin with a paleowater depth of ~500 m and a paleolatitude of ~54 °S<sup>22</sup>. The Valangian paleogeography with the location of ODP 692 is shown in Fig. 1. The study section covers ~5 Myr of climate history from the Late Berriasian–Early Valangian (~135 Myr; updated chronostratigraphy in Fig. 2) to the Early Hauterivian (~130.5 Myr). A total of 81 samples with an average time resolution of around ~25–50 kyr (Fig. 2) were measured for total organic carbon (TOC) concentration and bulk organic carbon isotopes ( $\delta^{13}\text{C}_{\text{org}}$ ), resolving the entire Weissert Event. We also present a detailed ( $N=48$  samples) sea surface temperature (SST) profile derived from the organic glycerol dialkyl glycerol tetraether (GDGT) paleothermometry  $\text{TEX}_{86}$ <sup>23</sup>. 65 samples were used for calcareous nannofossil investigation to refine the original biostratigraphy<sup>22</sup> and 31 samples were investigated for benthic foraminifera assemblages to reconstruct paleowater depths. These data enable us to constrain the SST evolution of the Early Cretaceous Weddell Sea within a refined chronological framework. In order to contextualize the local Weddell Sea results in the global climate evolution of the Weissert Event, we supplement these data with other available Valangian proxy temperature evidence from mid-latitude and tropical ocean basins, including  $\text{TEX}_{86}$ , oxygen isotopes, clumped isotopes and Mg/Ca measurements. In

particular, we assess uncertainties in absolute  $\text{TEX}_{86}$ -derived temperatures and possible regional changes in the  $\text{TEX}_{86}$ -SST relation for young, restricted ocean basins<sup>24</sup>. The temperature data from all study sites are aligned against a refined chronological framework, defined by the Weissert CIE. By comparing this chronologically aligned multi-proxy ocean temperature database to global paleoclimate modelling results we present a best-fit approach to resolve the Weissert carbon-climate perturbation. It is important to note that this best fit approach does not prefer any specific temperature calibration or location, however, it identifies techniques and study sites that are more consistent with available global observations and global modelling systematics than others. Based on this outcome we estimate the global mean surface temperatures and associated model  $p\text{CO}_2$  concentrations for the different phases of the perturbation. This unified solution is then used to explore the probability of ice build-up around Antarctica as a result of atmospheric  $\text{CO}_2$  drawdown during the Weissert Event.

## Results

**Weissert Event chrono- and chemostratigraphy at Site 692.** We started by combining calcareous nannofossil data and chemostratigraphy ( $\delta^{13}\text{C}_{\text{org}}$ ) to identify the Weissert Event based on its biostratigraphically constrained positive CIE<sup>9</sup> (Fig. 2, Supplementary Figs. 1 and 2 and ‘Methods’ section). Consistent with other study sites<sup>9,16,25</sup>, we find an average amplitude of about 1.5‰ (~−31.5 to −30‰) and identify the onset of the event (A in Fig. 2), and two distinct maxima (B and C in Fig. 2), suggesting that the Weddell Sea record encompasses the full magnitude and duration of the Weissert CIE. The onset of the event is placed at the base of the positive CIE at ~90.5 mbsf (A in Fig. 2) and the end at ~83.5 mbsf (top of the CIE plateau, C in Fig. 2) following the original definition<sup>9</sup>. The recovery period, marking the return of isotope trends towards pre-perturbation levels, follows point C in Fig. 2, the end of the Weissert perturbation.

**Contrasting  $\text{TEX}_{86}$ -derived temperatures across the Weissert Event.** Our  $\text{TEX}_{86}$  profile from Site 692 documents variable values between 0.77 and 0.63 (Eq. 1 and ‘Methods’ section) over a time period of approximately 750 kyr (Fig. 2). Independent of the choice of  $\text{TEX}_{86}$ -SST calibration, the record shows the highest (warmest)  $\text{TEX}_{86}$  values in the Late Berriasian–Early Valangian interval and during the initial warm phase of the Weissert Event (~0.74 in A–B in Fig. 2). Two minima (coolest temperatures, ~0.66) in the  $\text{TEX}_{86}$  record coincide with the Weissert CIE end (C in Fig. 2) and the Valangian/Hauterivian boundary, detached from the Weissert Event. The two cooling intervals are separated by a (<900 kyr) warming interlude. The main  $\text{TEX}_{86}$  decrease (B–C in Fig. 2) of almost 0.1 (translating in a 3–4 °C cooling, discussion below in  $\text{TEX}_{86}$  calibration section) is significantly larger than the analytical uncertainty of  $\text{TEX}_{86}$  analysis (0.004 following published<sup>26</sup> analytical methodology; see ‘Methods’ section).

In order to assess whether the local Weddell Sea cooling represents a global climate signal, we used a published compilation of Cretaceous  $\text{TEX}_{86}$  data<sup>27</sup>, focusing only on Valangian sites (e.g. DSDP Sites 603<sup>17</sup> and 534<sup>17</sup>, ODP Site 766<sup>17</sup>, and including also 5 published sample data from the stratigraphic study interval at ODP Site 692<sup>17</sup>). Palaeographic locations (Fig. 1) and a summary overview of these datasets are presented in Fig. 3, following our revised and updated biochemostratigraphic framework of the Weissert Event. The  $\text{TEX}_{86}$ -derived cooling trend at Site 692 is in stark contrast with records of time-equivalent strata at sub-tropical sites (603 and 534; ~18–25 °N) from the proto-North Atlantic<sup>17</sup>, which show stable

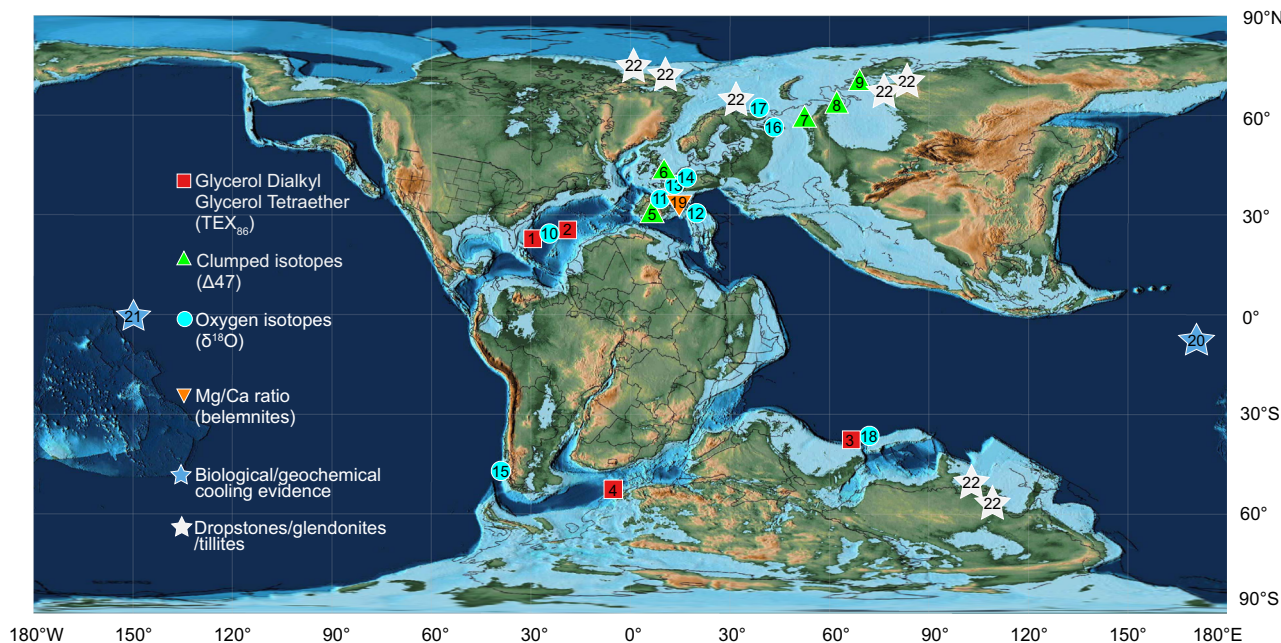


**Fig. 1 Paleogeographic reconstruction of the Valanginian-Early Hauterivian (-133 Myr).** Paleogeographic map by C.R. Scotese, PALEOMAP project<sup>64</sup> modified in this work to show the location of available Valanginian-Early Hauterivian multi-proxy-based temperature records (e.g.  $TEX_{86}$ , oxygen carbonate clumped isotopes, oxygen isotopes and belemnite Mg/Ca ratios) from Deep Sea Drilling Project/Ocean Drilling Project (DSDP/ODP) Sites and other worldwide sections: (1) 534, (2) 603, and (3) 766<sup>17</sup>; (4) 692<sup>this study and 17</sup>; (5) Caravaca, (6) Speeton, (7) Izmha, (8) Yatria and (9) Boyarka<sup>20</sup>; (10) Proto North Atlantic compilation<sup>16</sup>; (11) South East (SE) France compilation<sup>6, 18</sup>; (12) Northwestern Tethys compilation<sup>18</sup>; (13) Southern Boreal compilation<sup>18</sup>; (17) Festningen and Janusfjellet<sup>19</sup>; (18) 765<sup>15</sup>; (19) Vocontian Trough compilation<sup>15</sup>. Biological and geochemical cooling evidence in sub-tropical oceans (blue stars) from calcareous nannofossils at (20) Site 1049<sup>9</sup> and from steryl ethers at (21) Site 1213<sup>33</sup>; (22) compilation of Late Valanginian geologic cooling evidence in sub-polar regions (white stars) from dropstones, glendonites and tillites<sup>16</sup>. Red box symbols indicate  $TEX_{86}$  data, green triangles clumped isotopes, turquoise circles oxygen isotopes, orange down-pointing triangles Mg/Ca ratio (belemnite).

and high  $TEX_{86}$  values across the perturbation ( $\sim 0.9$  and  $0.93$  between the stratigraphic interval identifying the Weissert CIE). However, the  $\delta^{13}C_{org}$  data from Site 766 do not unequivocally identify the CIE, and magnetostratigraphy<sup>17</sup> suggests an age slightly younger than the end of the CIE (i.e., the base of this record starts in the uppermost CM11 polarity chron, and thus it sits slightly above the end of the Weissert Event; Fig. 3).

We conclude that this study presents the first robust  $TEX_{86}$ -based evidence of a cooling episode coinciding with the end of the Weissert CIE that contrasts the stable SSTs in the sub-tropical North Atlantic<sup>17</sup>. We will resolve this apparent contrast by comparing the  $TEX_{86}$ -based results with a global compilation of other independent temperature proxies in the following section.

**Integrating global ocean temperatures and cooling evidence.** In order to explore the global nature of the Weissert Event, we evaluate available upper ocean temperature reconstructions from other geochemical proxies, such as carbonate clumped isotopes<sup>20</sup>, oxygen isotopes<sup>6,16,18,19,28</sup> and belemnite Mg/Ca ratios<sup>15</sup> positioned in our revised and updated bio-chemostratigraphic framework (Fig. 3). A summary table of all available temperature records encompassing the Weissert CIE is reported in Supplementary Table 1. Oxygen isotopes on belemnites and/or benthic foraminifera<sup>6,18</sup>, consistent with Mg/Ca measurements on belemnites<sup>15</sup>, document a  $\sim 1-2^\circ C$  cooling at the end of the Weissert Event in South East France ( $\sim 26^\circ N$ ) and a cooling of up to  $4^\circ C$  in the southern and arctic part of the Boreal Realm ( $\sim 38-65^\circ N$ )<sup>18</sup>. Notably, our detailed stratigraphic re-analysis of these datasets also indicates that the cooling coinciding with the end of the Weissert CIE is followed by an intermittent warming, and a second minor cooling period that continues in the earliest Hauterivian (Fig. 3); a pattern also noted at the Weddell Sea study

site. Moreover, a recent overview of oxygen isotopes on bulk carbonate in the proto-North Atlantic and in the North-West and Southern Tethys<sup>16</sup> also documents a cooling in both hemispheres coinciding with the end of the Weissert Event. We note a strong correlation of the cooling trend documented at Site 692 with the only other available detailed record in the Southern Hemisphere at Site 765 (see ref. <sup>16</sup>). The stratigraphic resolution of available Valanginian clumped isotope data<sup>20</sup> impedes identification of the Weissert CIE but according to biostratigraphy document average temperature values of the warm initial phase of the Weissert CIE and/or of the interval shortly preceding the onset of the perturbation (Fig. 3). Within chronological uncertainties, we conclude that the temperature trends at Site 692 are in agreement with these independent global cooling signals. The absolute cooling of about  $3-4^\circ C$  in the Weddell Sea is larger than for most low-to-mid-latitude sites, which is consistent with the concept of polar amplification<sup>29</sup>, leading to a more pronounced high-latitude temperature change. Finally, we consider indirect and geological evidence supporting cooler conditions during the Early Cretaceous. Limited palynoflora data at Site 692<sup>30</sup> suggest the presence of a cool temperate forest on the Antarctic continent, with high moisture levels and strong seasonality with temperature below freezing. From the analysis of a qualitative dataset<sup>30</sup>, we observe that the sample at 84.95 mbsf yields the most diverse palynofloral assemblage. Relying on previous work botanical affinities and ecological preferences<sup>31</sup>, we postulate that this assemblage, which comprises ferns, Lycopods, Pteridosperms and conifers, is expression of cooler and more humid climatic conditions compared to assemblages above and below. The occurrence of *Podocarpidites*, a typical boreal floral element with broad temperature range but preference for cool and humid conditions<sup>32</sup> is worth noting as this taxon is absent from samples above and

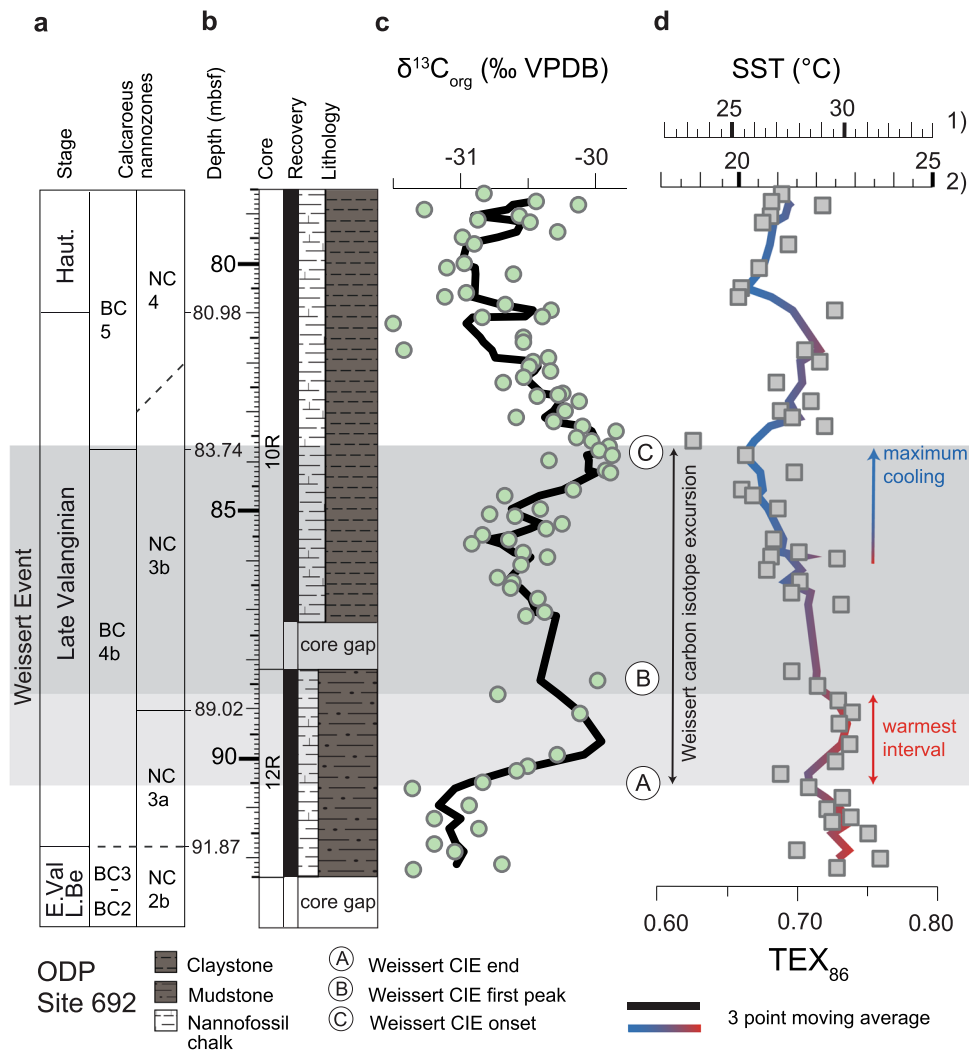


**Fig. 2 Carbon isotopes and sea surface temperatures (SSTs) of cores 10R and 12R at ODP Site 692.** **a** Stage and calcareous nannofossil zonation (Boreal Realm, BC<sup>65</sup> zonation and Tethys, NC<sup>66</sup> zonation). **b** Depth in metres below sea floor (mbsf), cores (12R and 10R), core recovery, and lithology. **c** Stable carbon isotope record measured on bulk organic matter ( $\delta^{13}\text{C}_{\text{org}}$  with green circles and a black curve reporting the calculated three point moving average) and identification of the Weissert positive carbon isotope excursion (CIE) segments (A, Weissert CIE onset; B, Weissert CIE first peak; C, Weissert CIE end). **d** Organic  $\text{TEX}_{86}$  paleothermometry (grey boxes and a shaded red (warmer values)—blue (colder values) curve reporting the calculated three point moving average) and the calibration to SSTs in degree °C showing (1) BAYSPAR and (2) restricted basin calibrations, representing maximum and minimum temperature estimates based on  $\text{TEX}_{86}$ , respectively.

below 84.95 mbsf. Interestingly, sample 84.95 mbsf is the closest to  $\text{TEX}_{86}$  minimum (i.e., coolest temperature) recorded in this study (at 83.74 mbsf) and coinciding with the Weissert Event end (C in Fig. 2). Moreover, latest Valanginian Steryl ethers (ODP 1213, Shatsky Rise, Central Pacific<sup>33</sup>) and changes in calcareous nannofossil assemblages (ODP 1049, Nadezhda Basin, Western Pacific<sup>11,34</sup>) have been reported in sub-tropical sites, suggesting biological evidence of cooler waters in these regions. Furthermore, several findings of latest Valanginian glendonites, dropstones, tillites deposits and ice-rafted debris both in the Arctic and Antarctic sub-polar regions (>50°N/S) (see ref. 16 compilation and locations in Fig. 1) are documented. However, the supporting evidence from sub-polar regions<sup>21,35,36</sup> has to be interpreted with caution due to large stratigraphic uncertainties covering the Berriasian to the Early Valanginian, but not specifically the target period of the Weissert Event. Despite stratigraphic and calibration uncertainties from all available geological and proxy evidence we note that the parallel temperature response of both hemispheres centered around the Weissert

Event is consistent and argues for a global process, with fluctuations in atmospheric  $p\text{CO}_2$  driving temperature.

**Absolute  $\text{TEX}_{86}$ -derived sea surface temperatures.** A variety of calibrations have been proposed to convert measured  $\text{TEX}_{86}$  ratios to upper ocean temperatures (see ref. 27 and ‘Methods’). The aim of this study is neither to discuss advantages and disadvantages nor the ecological and statistical justification of individual approaches, but rather to apply multiple calibrations to generate a plausible range of absolute sea surface temperatures for each site. We will then use our multi-proxy compilation and Valanginian climate model simulations to constrain this proxy uncertainty and derive climatic implications by a best-fit approach between all datasets.

In our analysis, the BAYSPAR model<sup>37,38</sup> provides the upper end estimate of absolute  $\text{TEX}_{86}$ -derived ocean temperatures (i.e., max- $\text{TEX}_{86}$ ). We also report the outcomes from all calibrations in the Supplementary Data Appendix. Applying the default BAYSPAR Deep-Time settings, SSTs in the Weddell Sea record

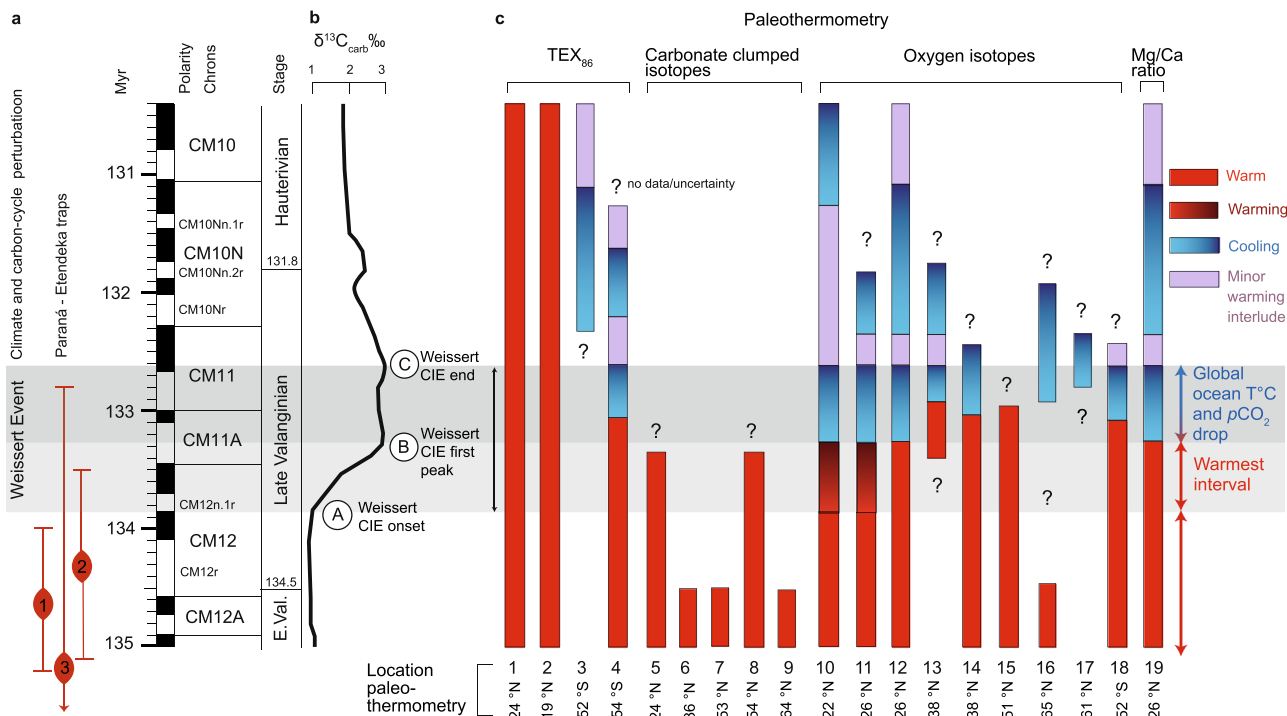


**Fig. 3 Chronological framework of the Weissert Event and evolution of worldwide multi-proxy ocean temperature trends.** **a** Chronostratigraphy of climate and carbon-cycle (Weissert) perturbation event and Paraná-Etendeka timing after (1)<sup>67</sup>, (2)<sup>68</sup> and (3)<sup>69</sup>; numerical ages in Myr are based on boundary ages of polarity chrons<sup>57</sup> revised in this study for the position of the Valanginian/Hauterivian boundary<sup>56</sup>. **b** Identification of the Weissert positive carbon isotope excursion (CIE) is based on the reference carbon isotope record measured on bulk carbonate ( $\delta^{13}C_{carb}$ )<sup>25</sup> calibrated in the Southern Alps in the uppermost part of magnetic chron CM12 (A, CIE onset) and in the upper part of magnetic chron CM11 (C, CIE end)<sup>9</sup>. **c** A detailed correlation to available global multi-proxy-based ocean temperature records is presented by coloured bars (e.g., red (relatively stable warm interval), graded red to darker red (warming interval), blue to darker blue (cooling interval), and lilac (minor warming interlude)), which graphically represent the reconstructed ocean temperature trends organized by type of proxy (e.g.,  $TEX_{86}$ , carbonate clumped isotopes, oxygen isotopes and Mg/Ca ratio paleothermometry). Note that numbered section/site locations of the reported proxy compilation are shown in Fig. 1.

decrease from  $\sim 30^{\circ}C$  (warm A–B interval in Fig. 2) to a minimum of  $\sim 25.6^{\circ}C$  at the cold CIE end (C in Fig. 2). Importantly, results for the logarithmic  $TEX_{86}$  calibration<sup>39</sup> (Supplementary Data Appendix) are similar to the BAYSPAR method for the Weddell Sea  $TEX_{86}$  range of 0.63 to 0.77. We compare these results to published Valanginian BAYSPAR-derived SSTs<sup>27</sup> (Supplementary Table 1). At Site 766, the temperatures calculated from the 8 lowermost data points ( $\sim 25^{\circ}C$ <sup>27</sup>) possibly represent the coolest temperatures at the end of the Weissert Event (see Fig. 3). The stable BAYSPAR SSTs in the subtropical proto-North Atlantic exceed  $40^{\circ}C$ <sup>27</sup> across the perturbation. These high surface temperatures seem irreconcilable with Cretaceous climate model results<sup>20,24</sup>, and foster the debate about the maximum heat stress tolerated by Cretaceous plants and mammals<sup>40</sup>.

An alternative explanation for these high  $TEX_{86}$  ratios may come from a distinct sedimentary isoprenoid-GDGT (i-GDGT) distribution leading to a different  $TEX_{86}$ -temperature relation in young and restricted Mesozoic ocean basins<sup>24</sup>. It is important to note that Site 766 offshore Australia represents an open marine setting with unrestricted connection to the Early Cretaceous ocean<sup>41</sup>. In contrast, proto-North Atlantic Sites 534 and 603 represent more restricted settings in a young and evolving ocean basin. As recently proposed<sup>24</sup>, these special environmental conditions might have enhanced the contribution of i-GDGTs from deep-dwelling Thaumarchaeota populations, similar to observations from the modern Mediterranean and Red Sea<sup>42</sup> that lead to a regional warm bias in  $TEX_{86}$ -derived temperatures. Like the proto-North Atlantic, Site 692 in the emerging Weddell

Sea also represents a highly restricted depositional environment, although with different climate conditions<sup>16,17,30</sup>, i.e., arid and warm versus humid and rather cool, respectively. Importantly, a consistent warm bias in  $TEX_{86}$ -SSTs has also been found in Pleistocene sapropels from the Mediterranean Sea<sup>43</sup>, a highly stratified depositional environment more comparable to the Valanginian Weddell Sea (Supplementary ‘Anomalous GDGT distributions’ section). We also find similarities in the i-GDGT distributions of Site 692 and present-day samples from the Mediterranean Sea (Supplementary Fig. 4). Our benthic foraminiferal data from Site 692 further indicate an intermediate-deep basin with an outer neritic to upper bathyal paleowater depth up to 500 m (Supplementary ‘Benthic foraminifera’ section). Such a paleowater depth would allow enhanced contribution of deeper water Thaumarchaeota communities producing the distinct i-GDGT distribution recorded in the sediments. Moreover, we document a high GDGT-2/GDGT-3 ratio  $>5$  (on average 5.7; Supplementary Data Appendix) in the study samples, which also corroborates a contribution from Archaea living in the deeper water column<sup>44</sup>. Further supporting evidence for a restricted Early Cretaceous Weddell Basin with persistent ocean stratification comes from plate-tectonic reconstructions that show early stages of basin evolution with closed or limited ocean gateways<sup>22</sup> and very high TOC concentrations (range 3.2–12.5%; Supplementary Data Appendix) in black shales at Site 692.

For Sites 603, 534, and 692, the restricted basin calibration accounting for the regional  $TEX_{86}$ -temperature relation<sup>42</sup> (Eq. 2) yields overall  $\sim 6$ – $14^{\circ}C$  cooler SSTs compared to the BAYSPAR



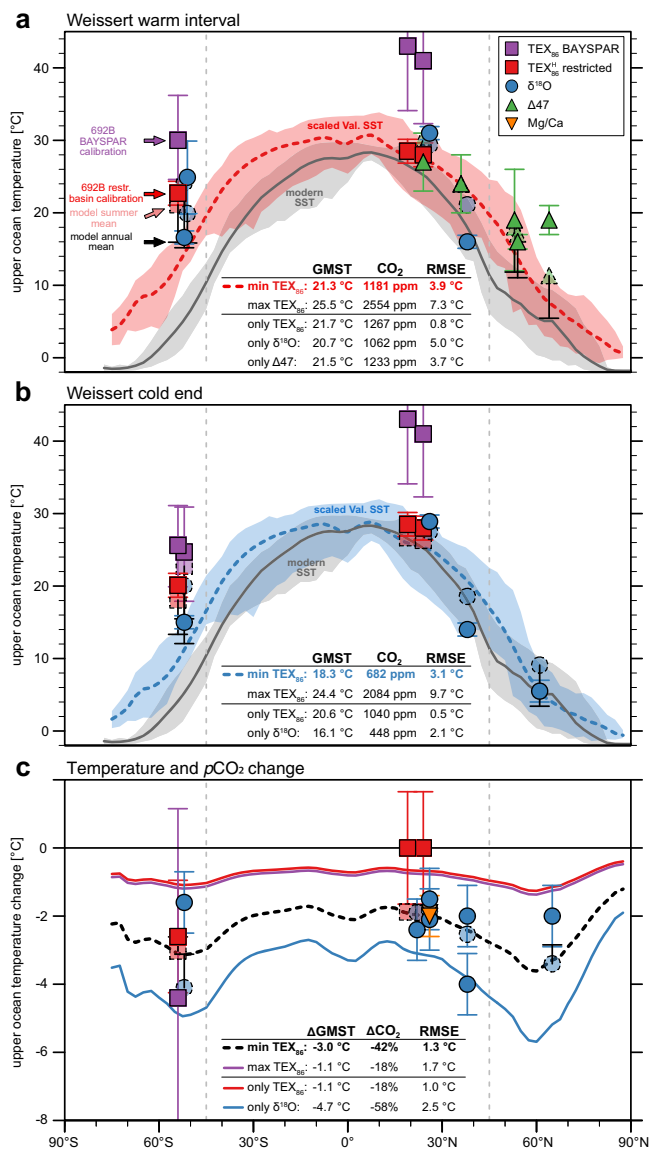


**Fig. 4 Best-fit model-proxy comparison of upper ocean temperatures and model CO<sub>2</sub> estimates.** Estimates of global mean surface temperatures (GMSTs) and associated model CO<sub>2</sub> levels are calculated for the whole dataset as well as for three different subsampling experiments including only single proxy techniques (only-TEX<sub>86</sub>, only-δ<sup>18</sup>O and only-Δ47). In addition, TEX<sub>86</sub>-derived temperatures are calculated from either the calibration for modern deep, restricted basins (min-TEX<sub>86</sub>) or the BAYSPAR calibration (max-TEX<sub>86</sub>) for DSDP/ODP sites 534, 603 and 692. Error bars document 90% confidence intervals for the TEX<sub>86</sub> calibration and uncertainties for other proxies as reported in Supplementary Table 1. **a** Model SSTs are linearly scaled to the best-fit CO<sub>2</sub> estimate of 1181 ppm during the Weissert warm interval (see Supplementary Equation 5). Root-mean-square-error (RMSE) between scaled model temperatures and local proxy data are discussed in the Supplementary ‘Global mean surface temperature and pCO<sub>2</sub> estimates’ section. Shading around the zonal mean shows the range of annual mean SSTs at each latitude, for modern<sup>70</sup> (grey) and Valanginian (red and blue). Dashed symbols represent simulated annual (summer) mean SSTs at low (high) latitude proxy locations for the derived mean CO<sub>2</sub> concentrations. Black bars show the difference between the warmest 3-months and annual mean temperature for high-latitude sites. **b** Model SSTs linearly scaled to the mean CO<sub>2</sub> estimates of 682 ppm during the Weissert cold end. **c** Model temperature and pCO<sub>2</sub> change from the Weissert warm interval to Weissert cold end.

results. Even though the exact ecological justification for the distinct i-GDGT distributions remains uncertain<sup>24</sup>, we interpret the results as a possible lower end estimate (i.e., min-TEX<sub>86</sub>) of absolute SSTs in these restricted environments. Notably, a recent study has also demonstrated that semi-enclosed basins document systematically offset from zonal mean temperatures, and are unusually warm and seasonal compared to the majority of open ocean locations situated at the same latitudes, especially in the higher latitudes<sup>45</sup>. We next validate the possible temperature range against our multi-proxy compilation and independent climate model results.

In summary, absolute temperatures for the Weddell Sea decrease from ~22.7/30 °C (min-/max-TEX<sub>86</sub>) for the Weissert warm interval to a minimum of ~20.1/25.6 °C (min-/max-TEX<sub>86</sub>) at the cold CIE end. It is important to note that while absolute temperature reconstructions change significantly with the applied calibration model, the relative cooling of ~3–4 °C observed at Site 692 is similar for all calibrations.

**Global mean surface temperature and pCO<sub>2</sub> estimates.** We estimate the global mean surface temperature (GMST) evolution across the Weissert Event by comparing our proxy compilation (Fig. 3; Supplementary Table 1) with model-simulated SSTs. This approach assumes that the global mean surface temperature scales linearly with local SSTs and that this scaling factor can be estimated from two model simulations at ×2 and ×4 preindustrial atmospheric pCO<sub>2</sub> concentrations (e.g., 560 and 1120 ppm)<sup>46</sup>. This approach allows us to derive an independent GMST estimate for each proxy site via a single transfer function (Supplementary Equation 3). We then calculate average GMSTs across all sites for both the Weissert warm interval between the Weissert CIE onset to the first peak CIE (warm A–B interval in Fig. 3) and the cold Weissert CIE end (C in Fig. 3). We further use the associated standard errors across all proxy sites as a measure of overall consistency between different proxy techniques and the model results.

Combining our multi-proxy compilation, the lower-end estimates of TEX<sub>86</sub>-derived SSTs (min-TEX<sub>86</sub>), and annual mean temperatures we estimate GMSTs of 24.4 °C (±1.8 °C) and 21.5 °C (±1.6 °C) for the Weissert warm interval and cold CIE end, respectively (Supplementary Table 2). Assuming a linear climate sensitivity this indicates a model-derived atmospheric pCO<sub>2</sub> concentration above 2000 ppm for the Weissert warm interval (Supplementary Fig. 6 and Equation 6). Even though these estimates depend on the climate sensitivity of the model, with higher climate sensitivity resulting in lower CO<sub>2</sub> values and vice-versa, they clearly exceed the plausible range of available Valanginian pCO<sub>2</sub> reconstructions (~500–1700 ppm;<sup>10</sup>). These high pCO<sub>2</sub> estimates are related to very warm GMSTs derived from mid to high latitude sites of both hemispheres (Supplementary Fig. 5). High-latitude proxy reconstructions significantly warmer than climate model temperatures are a long-standing challenge for the model-data comparison of past greenhouse climates, including the Valanginian<sup>20</sup>. A potential reason for this mismatch is a strong seasonality in available sunlight and food web dynamics, which has the potential to skew higher latitude proxy reconstructions towards seasonal rather than annual mean temperatures (e.g., refs. 47–49). We explore this hypothesis by repeating the analysis with simulated warmest 3-month mean instead of annual mean temperatures for mid to high latitude sites poleward of 45 °. The assumption of a summer bias in high-latitude proxy reconstructions reduces absolute GMST estimates to 21.3 °C (±1.2 °C) for the Weissert warm interval and 18.3 °C (±1.1 °C) for the Weissert cold end, a reduction of about 3 °C for

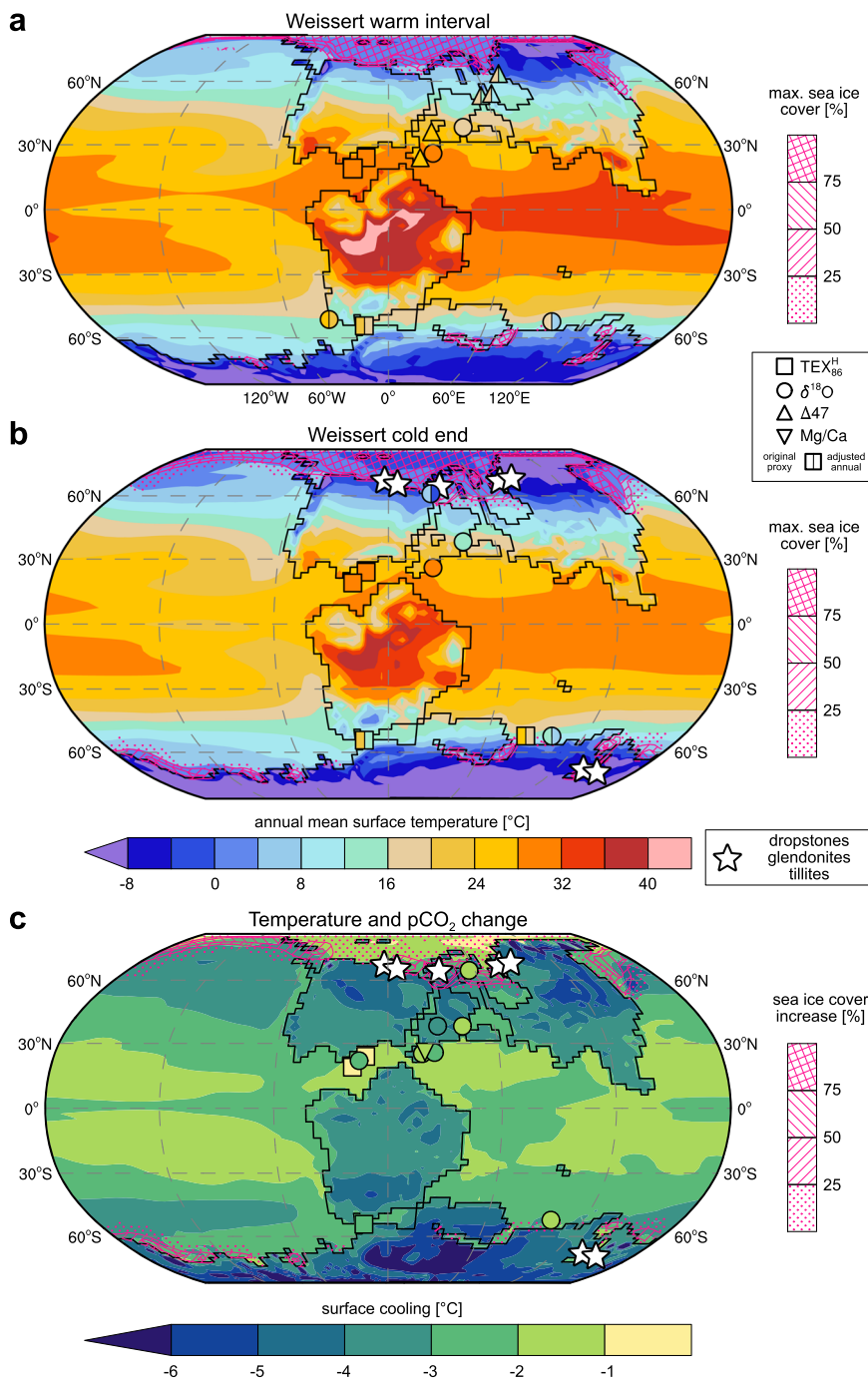


**Fig. 5 Simulated and reconstructed annual mean surface temperatures and cooling across the Weissert Event.** **a** Model fields combine surface air temperatures over land with sea surface temperatures (SSTs) over the ocean and are linearly scaled to the calculated mean  $p\text{CO}_2$  estimates of 1181 ppm during the Weissert warm interval (Supplementary Equation 5). Pink contours show associated maximum monthly mean sea ice concentrations. Symbols represent available proxy information. High-latitude sites (poleward of  $45^\circ$ ) also show approximated annual mean temperatures where the model-estimated difference between summer and annual mean values is subtracted from the original proxy temperatures to correct for a possible seasonal warm bias and to facilitate the model-data comparison. **b** Annual mean surface temperatures during the Weissert cold end scaled to the mean  $p\text{CO}_2$  estimate of 682 ppm. **c** Estimated surface cooling from the Weissert warm interval to the Weissert cold end, i.e. panel **a** minus **b**, with an associated  $p\text{CO}_2$  drop of  $\sim 40\%$ .

both periods (Supplementary Table 2). The reduced standard errors compared to the annual mean analysis document an overall more consistent distribution in simulated and reconstructed surface temperatures. Associated  $p\text{CO}_2$  concentrations under this assumption are  $\sim 1180$  ppm (940–1480 ppm) and  $\sim 680$  ppm (550–840 ppm) for the Weissert warm interval and cold CIE end, respectively (Fig. 4), and therefore within the range

of independent  $p\text{CO}_2$  reconstructions<sup>10</sup>. Our results indicate a drop in GMST of  $3.0^\circ\text{C}$  ( $\pm 1.7^\circ\text{C}$ ) towards the Weissert CIE end (Fig. 4c). This global cooling and the corresponding  $\sim 40\%$  reduction in  $p\text{CO}_2$  is independent of any seasonal bias assumption (Supplementary Fig. 6), and in good agreement with proxy estimates from carbon isotopes on terrestrial plant records<sup>13</sup>.

We further repeat our analysis for four different variations of the proxy data to assess the sensitivity of our results to the selected proxy techniques and temperature calibrations. The max-TEX<sub>86</sub> data-set (BAYSPAR) increases local proxy temperatures by ~6–14 °C in the proto-Weddell Sea and proto-North Atlantic sites and therefore overall GMST estimates (Supplementary Table 2). The corresponding model *p*CO<sub>2</sub> concentration of more than 2500 ppm for the Weissert warm interval by far exceeds the upper end of available reconstructions and results in overall higher root-mean-square-errors in the model-data comparison (Fig. 4). The increased standard errors of the mean for max-TEX<sub>86</sub> compared to min-TEX<sub>86</sub> (Supplementary Table 2) indicate an overall worse fit between BAYSPAR-derived GMST estimates and those based on other proxy methods. We, therefore, observe that the highest degree of consistency between model temperatures and our proxy compilation is achieved by application of a regional TEX<sub>86</sub> calibration for restricted Mesozoic ocean basins for selected sites in combination with a seasonal warm bias in high-latitude SST proxies. Only this specific combination permits a model-data congruence within the plausible range of *p*CO<sub>2</sub> reconstructions for the Valanginian<sup>10,50,51</sup> and will be further discussed in the next section.

**High-latitude cooling and ice formation during the end of the Weissert Event.** The cold Weissert CIE end is associated with a drop in the GMST of 3.0 °C (±1.7 °C) compared to the Weissert warm interval, but the modelling results indicate large contrasts in the regional cooling patterns (Fig. 5c). Minimum cooling of 1–2 °C is simulated for the subtropics, while it exceeds 6 °C in polar, continental regions. The reduced sensitivity of proto-Arctic Ocean temperatures can be explained by already near-freezing temperatures during the Weissert warm onset (Fig. 5a). The model supports the possibility for seasonal sea ice formation in the Arctic and around Antarctica for both Weissert *p*CO<sub>2</sub> scenarios. The seasonal sea ice coverage however expands during the cool end of the event, with largest increases around the Arctic. The latitudes of maximum simulated cooling and sea ice extension (~50–70 ° in both hemispheres) coincide with the location of upper Valanginian dropstones, glendonites and tillites<sup>16</sup> (Fig. 5c), indicating cooler surface waters, sea ice and drifting ice conditions. We quantify net snow mass accumulation rates as a first-order approximation for the potential of ice formation on Antarctica (Supplementary Fig. 7). The total snow mass surviving the Antarctic summer increases by ~58% in the ×2 *p*CO<sub>2</sub> simulation (~cold Weissert CIE end) compared to the ×4 *p*CO<sub>2</sub> results (~warm Weissert interval). Areas of potential land ice formation are restricted to southern and western coastal, high-elevation (>2000 m) regions. Previous modelling results support a *p*CO<sub>2</sub> threshold for the onset of Antarctic glaciation between ×2 to ×4 pre-industrial levels for the Early Cretaceous<sup>52</sup> and the Cenozoic<sup>53</sup>, even though absolute numbers depend on the climate model<sup>54</sup>. Within model and paleogeographic uncertainties, our simulations support small scale continental glaciation during the Valanginian, consistent with geological observations. Moreover, calcareous nannofossil data from Site 692 (this study) confirm coeval braarudosphaerid-enrichments documented offshore Antarctica (ODP Sites 766 and 765<sup>55</sup>; and Supplementary ‘Paleoecology of braarudosphaerids’ section), and at high latitudes in the northern hemisphere (e.g., ref. 34, Supplementary ‘Paleoecology of braarudosphaerids’ section) in the latest Valanginian–Early Hauterivian (Supplementary Fig. 3). These braarudosphaerid-enrichments thus suggest temporary salinity lowering possibly triggered by discharges of fresh, deglacial melt water during the warming interlude following the cold Weissert CIE end, in high latitude and subpolar regions. Unfortunately, there are significant discrepancies in recent Early Cretaceous

global sea level changes and variations in ocean water salinity in high-latitude basins from oxygen isotopes (see ref. 16).

## Discussion

Our findings from geological evidence, proxy records and climate model simulations provide a calibrated context of global climate perturbation for the ~2 million years history of the Early Cretaceous Weissert Event. This study documents the first TEX<sub>86</sub>-based evidence of a relevant cooling episode coinciding with the end of the Weissert perturbation in the sub-polar proto-Weddell Sea. The observed cooling (3–4 °C) is consistent with global signals based on different types of SST proxies that overall document a more pronounced temperature response in the most climate sensitive high-latitude regions (polar amplification). This outcome not only contributes to the long-lasting discussion about the potential for polar ice during greenhouse conditions but also offers a strategy to investigate other periods with comparable temperature-*p*CO<sub>2</sub> boundary conditions and inconsistent proxy reconstructions. The strength of the presented best-fit approach between modelling and multi-proxy data compilation is that it is largely decoupled from uncertainties and limitations of individual proxy estimates and other constraints (chronology, paleobathymetry and paleolatitude). Instead, the approach statistically identifies one solution where all available data and model configurations converge towards a single (most) plausible scenario. The described strategy implies that the best-solution approach can be adapted as new evidence and understanding emerges, without being skewed or biased by individual observations. The ongoing discussion on SST estimates from GDGT-based TEX<sub>86</sub> paleothermometry is one area where a consensus cannot easily be reached, leading to inconsistent and often opposing interpretations. We propose that moving away from such individual observations and discussions towards more integrated solutions, as shown in this study, bear large potential to better recognize large scale inter-relationships and quantify climate and environmental change back in time, setting further constraints for projecting the future.

## Methods

**Calcareous nannofossils and benthic foraminifera.** A total of 69 samples were investigated for calcareous nannofossils; samples were prepared using the simple smear slide technique and examined under polarising light microscope, at ×1250 magnification. Notably, we adopt a revised<sup>56</sup> timescale<sup>57</sup> for the position of the Valanginian/Hauterivian boundary relative to polarity chrons (Supplementary calcareous nannofossils section and Supplementary Fig. 1). Samples for benthic foraminifera analysis were disaggregated in hydrogen peroxide (H<sub>2</sub>O<sub>2</sub>), washed under tap water over >63 μm mesh and dry sieved. All residues of the size-fraction >63 μm were picked, identified, counted, and permanently stored in Plummer slides for benthic foraminifera (Supplementary ‘Benthic foraminifera’ section).

**Carbon isotope and TOC analysis.** Bulk dried and ground samples (*N* = 81, avg. resolution ~25–50 kyr) were analyzed for bulk organic stable carbon isotope ratios (δ<sup>13</sup>C<sub>org</sub>) and TOC at Iso-Analytical, Crewe Cheshire UK, by a Europa Scientific Elemental Analyser–Isotope Ratio Mass Spectrometry (EA–IRMS). Weighed powdered samples were acidified with 2 M hydrochloric acid, mixed, left for 24 h, then washed and oven dried at 60 °C. Weighed samples were loaded into an autosampler. The temperature of the furnace was held at 1000 °C, reaching up ~1700 °C in the region of the sample. Repeat analysis on check samples (e.g., IA-R005 and IA-R006) and the reference material used during δ<sup>13</sup>C analysis (e.g., IA-R001–Iso-Analytical standard wheat flour), ensure standard deviation <0.1. All reference materials were calibrated against and traceable to an inter-laboratory comparison standard distributed by the International Atomic Energy Agency (IAEA), Vienna (e.g., IAEA-CH-6). Carbon isotope results are shown in the Vienna Pee Dee Bee δ notation (‰ VPDB) and TOC results are reported in weight percentage (%) in the Supplementary Data Appendix.

**Glycerol dialkyl glycerol tetraethers extraction and TEX<sub>86</sub> analysis.** Extraction of freeze-dried powdered samples (*N* = 48; 1–5 grams) was performed by Dionex accelerated solvent extraction (DIONEX ASE 350) using a mixture of dichloromethane (DCM)/methanol (MeOH) (5:1, v/v) at a temperature of 100 °C and a pressure of 69 ± 10 psi. Sulfur-free extracts (desulfurization by acid-activated copper turnings) were purified by column chromatography over self-packed silica gel (deactivated with 1% ultrapure H<sub>2</sub>O) columns using hexane, hexane:DCM (2:1,

v/v), and MeOH as subsequent eluents. The MeOH-fraction containing the GDGTs was dissolved in hexane/isopropanol (95:5, v/v) and 20  $\mu\text{L}$  of  $\text{C}_{46}$  GDGT tetraether idol lipid standard was added prior to filtering through 0.45 mm Teflon filters. Samples were analysed at the University of Cologne using an Agilent 1290 Infinity ultra high performance liquid chromatography (HPLC) paired with an Agilent GDGT 6460 Triple Quadrupole MS system. Published chromatographic conditions were applied<sup>58</sup> in selected ion monitoring mode, following previous work for GDGTs identification<sup>23,26</sup>. Peak areas were integrated and calibrated against the internal  $\text{C}_{46}$  standard. The  $\text{TEX}_{86}$  index (Eq. 1) was calculated as originally defined<sup>23</sup>:

$$\text{TEX}_{86} = \frac{[\text{GDGT} - 2] + [\text{GDGT} - 3] + [\text{Cren}]}{[\text{GDGT} - 1] + [\text{GDGT} - 2] + [\text{GDGT} - 3] + [\text{Cren}]} \quad (1)$$

We note that our high-resolution record from Site 692 is consistent with 5 available published sample data for the study stratigraphic interval from same site location<sup>17</sup>. Repeat analysis of an in-house standard and the application of published analytical techniques<sup>23,26</sup> suggest that the analytical error associated with  $\text{TEX}_{86}$  analysis is well below the observed variable  $\text{TEX}_{86}$  range (0.77–0.63) and the mean  $\text{TEX}_{86}$  decrease from the Weissert warmest interval (~0.74 between A and B in Fig. 2) to the Weissert cold end (~0.66 in C in Fig. 2) documented at Site 692. Therefore, the highest error uncertainty in SST estimates comes calibration errors themselves (see also ref. 27).

**$\text{TEX}_{86}$  calibration.** Based on a published compilation of Cretaceous  $\text{TEX}_{86}$  data and calibration methods<sup>27</sup>, we present in our Supplementary Data Appendix all temperature results based on different calibrations for the Valanginian sites (603<sup>17</sup>, 534<sup>17</sup>, 766<sup>17</sup> and 692<sup>17</sup> and this study), including the BAYSPAR calibration model that reports in the main text the upper end  $\text{TEX}_{86}$  estimates max- $\text{TEX}_{86}$  calculated in our analysis. Notably, following a recent study<sup>24</sup> it was further applied a regional calibration, based on a deep-water  $\text{TEX}_{86}^{\text{H}}$  dataset for deep restricted modern basins<sup>42</sup> (Eq. 2), to the restricted Sites 534 and 603, and 692.

$$\text{TEX}_{86}^{\text{H}} - \text{Deep restricted basin SST } (^{\circ}\text{C}) = 56.3 \times (\text{TEX}_{86}^{\text{H}}) + 30.2; \pm 1^{\circ}\text{C} \quad (2)$$

**Glycerol dialkyl glycerol tetraethers screening.** A strict GDGT screening procedure was applied (see ref. 27) to rule out secondary effects, such as thermal alteration, overprint by terrestrial input, and methanogenesis. To this end, we verified that the following indices are within the boundaries deemed to represent suitable organic matter for  $\text{TEX}_{86}$ -based SST reconstructions: a Methane Index (MI) < 0.5, GDGT-0 percentage >67% and the crenarchaeol index ( $f_{\text{Cren}^{\text{H}}:\text{Cren}^{\text{H}} + \text{Cren}^{\text{H}}}$ ) < 0.25. The laminated sediments and high TOC values (3.2–12.5%) in the analysed samples indicate deoxygenated bottom waters in the restricted Weddell Sea basin. To test for possible physiological controls on  $\text{TEX}_{86}$  we calculated the Ring Index ( $\Delta\text{RI}$ )<sup>59</sup> during our initial quality screening. This measure is explicitly designed to identify whether  $\text{TEX}_{86}$  samples might be significantly influenced by non-temperature factors, like low dissolved oxygen levels. Importantly all  $\text{TEX}_{86}$  samples show  $|\Delta\text{RI}|$  values well below the threshold of 0.3 (maximum of 0.16) and therefore indicate an overall dominant control of environmental temperature on measured  $\text{TEX}_{86}$ . Note that the branched and isoprenoid tetraether (BIT) index was not calculated in our samples because the concentrations of branched GDGTs were below detection limit. We thus assume the BIT index to be 0 or very low for all investigated samples as shown in previous work at this site<sup>17</sup>. Further details in Supplementary ‘Organic matter quality and thermal maturation’ section.

**Climate model simulations.** Climate model simulations are based on published work<sup>46</sup> and were performed with the coupled atmosphere-ocean-vegetation climate model HadCM3BL-M2.1aD<sup>60</sup>. The model uses a horizontal resolution of 3.75  $^{\circ}$  in longitude by 2.5  $^{\circ}$  in latitude with 19 vertical levels in the atmosphere and 20 ocean depth levels. Two simulations employing a Valanginian (~138 Myr) paleogeography<sup>61</sup> at  $\times 2$  and  $\times 4$  pre-industrial atmospheric  $\text{CO}_2$  concentrations (e.g., 560 and 1120 ppm) build the foundation for the model-data comparison. Atmospheric  $\text{CO}_2$  levels during the Valanginian–Hauterivian are currently not well constrained but were probably lower than during the peak greenhouse conditions of the mid-Cretaceous<sup>10,50</sup>, and most likely between  $\times 2$  to  $\times 4$  preindustrial level<sup>10,50,51</sup>. The general circulation model is coupled to the dynamic global vegetation model TRIFFID via the land surface scheme MOSES 2.1. Orbital parameters are set to present-day values, but with a reduced solar constant of 1349.1  $\text{W}/\text{m}^2$  following published work<sup>62</sup>.

The  $\times 4$  simulation is initialized with a globally homogeneous salinity of 35 ppt and an idealized zonal mean ocean temperature profile that changes with latitude<sup>61</sup>. The  $\times 2$  simulation is branched off at model year 422 and both integrations are continued for a further 10,000 years. Remaining model temperature drifts in both simulations are very small with radiation imbalances at the top of the atmosphere over the last 100 years <0.05  $\text{W}/\text{m}^2$  and changes in volume-integrated ocean temperatures over the last 1000 years <0.04  $^{\circ}\text{C}$ . We note that both simulations show a continuous increase in global mean ocean salinity, even though the influence of this drift on the resulting ocean circulation and surface temperature distribution is probably small (see discussion in ref. 46).

We follow published methods<sup>46,63</sup> to calculate global mean surface temperature (GMST) estimates for each site by comparing the reconstructed Valanginian ocean temperatures with the simulated sea surface temperatures (SSTs) at the individual

paleopositions (Supplementary ‘Global mean surface temperature and p $\text{CO}_2$  estimates’ section and Supplementary Tables 1 and 2).

## Data availability

The  $\text{TEX}_{86}$  and stable carbon isotopes data and the complete calcareous nannofossil range chart generated in this study are provided in the Supplementary Source data file. Source data are provided with this paper.

Received: 8 January 2021; Accepted: 12 August 2021;

Published online: 13 September 2021

## References

- Wagner, T. et al. Rapid warming and salinity changes of Cretaceous surface waters in the subtropical North Atlantic. *Geology* **36**, 203 (2008).
- Jenkyns, H. C., Schouten-Huibers, L., Schouten, S. & Sinninghe Damsté, J. S. Warm Middle Jurassic–Early Cretaceous high-latitude sea-surface temperatures from the Southern Ocean. *Clim. Past* **8**, 215–226 (2012).
- Bottini, C. & Erba, E. Mid-Cretaceous paleoenvironmental changes in the western Tethys. *Clim. Past* **14**, 1147–1163 (2018).
- Klages, J. P. et al. Temperate rainforests near the South Pole during peak Cretaceous warmth. *Nature* **580**, 81–86 (2020).
- McAnena, A. et al. Atlantic cooling associated with a marine biotic crisis during the mid-Cretaceous period. *Nat. Geosci.* **6**, 558–561 (2013).
- Bodin, S., Meissner, P., Janssen, N. M. M., Steuber, T. & Mutterlose, J. Large igneous provinces and organic carbon burial: Controls on global temperature and continental weathering during the Early Cretaceous. *Glob. Planet. Change* **133**, 238–253 (2015).
- Bottini, C. et al. Climate variability and ocean fertility during the Aptian Stage. *Clim. Past* **11**, 383–402 (2015).
- Miller, K. G. Broken greenhouse windows. *Nat. Geosci.* **2**, 465–466 (2009).
- Erba, E., Bartolini, A. & Larson, R. L. Valanginian Weissert oceanic anoxic event. *Geology* **32**, 149 (2004).
- Foster, G. L., Royer, D. L. & Lunt, D. J. Future climate forcing potentially without precedent in the last 420 million years. *Nat. Commun.* **8**, 14845 (2017).
- Weissert, H. & Erba, E. Volcanism,  $\text{CO}_2$  and palaeoclimate: a Late Jurassic–Early Cretaceous carbon and oxygen isotope record. *J. Geol. Soc.* **161**, 695–702 (2004).
- Erba, E. & Tremolada, F. Nannofossil carbonate fluxes during the Early Cretaceous: Phytoplankton response to nitrification episodes, atmospheric  $\text{CO}_2$ , and anoxia. *Paleoceanogr.* **19**, PA1008 (2004).
- Gröcke, D. et al. The Upper Valanginian (Early Cretaceous) positive carbon–isotope event recorded in terrestrial plants. *Earth Planet. Sci. Lett.* **240**, 495–509 (2005).
- Bornemann, A. & Mutterlose, J. Calcareous Nannofossil and  $\delta^{13}\text{C}$  records from the Early Cretaceous of the Western Atlantic Ocean: Evidence for enhanced fertilization across the Berriasian–Valanginian transition. *Palaios* **23**, 821–832 (2008).
- Price, G. D. et al. A high-resolution Belemnite geochemical analysis of early Cretaceous (Valanginian–Hauterivian) environmental and climatic perturbations. *Geochem. Geophys. Geosyst.* **19**, 3832–3843 (2018).
- Charbonnier, G. et al. A global palaeoclimatic reconstruction for the Valanginian based on clay mineralogical and geochemical data. *Earth-Sci. Rev.* **202**, 103092 (2020).
- Littler, K., Robinson, S. A., Bown, P. R., Nederbragt, A. J. & Pancost, R. D. High sea-surface temperatures during the Early Cretaceous Epoch. *Nat. Geosci.* **4**, 169–172 (2011).
- Meissner, P., Mutterlose, J. & Bodin, S. Latitudinal temperature trends in the northern hemisphere during the Early Cretaceous (Valanginian–Hauterivian). *Palaeogeogr. Palaeoclimatol. Palaeoecol.* **424**, 17–39 (2015).
- Price, G. D. & Nunn, E. V. Valanginian isotope variation in glendonites and belemnites from Arctic Svalbard: transient glacial temperatures during the Cretaceous greenhouse. *Geology* **38**, 251–254 (2010).
- Price, G. D., Bajnai, D. & Fiebig, J. Carbonate clumped isotope evidence for latitudinal seawater temperature gradients and the oxygen isotope composition of Early Cretaceous seas. *Palaeogeogr. Palaeoclimatol. Palaeoecol.* **552**, 109777 (2020).
- Alley, N. F., Hore, S. B. & Frakes, L. A. Glaciations at high-latitude Southern Australia during the Early Cretaceous. *Aust. J. Earth Sci.* **67**, 1045–1095 (2020).
- Mutterlose, J. & Wise, S. W. Lower Cretaceous nannofossil biostratigraphy of ODP Leg 113 Holes 692B and 693A, continental slope off East Antarctica, Weddell Sea. In *Proc. ODP Sci. Res. Vol. 113* (eds Barker, P. R., Kennett, J. P., et al.), 325–351 (Ocean Drilling Program, 1990).
- Schouten, S., Hopmans, E. C., Schefuÿ, E. & Sinninghe Damsté, J. S. Distributional variations in marine crenarchaeal membrane lipids: a new

- tool for reconstructing ancient sea water temperatures? *Earth Planet. Sci. Lett.* **204**, 265–274 (2002).
24. Steinig, S. et al. Evidence for a regional warm bias in the Early Cretaceous TEX<sub>86</sub> record. *Earth Planet. Sci. Lett.* **539**, 116184 (2020).
  25. Sprovieri, M., Coccioni, R., Lirer, F., Pelosi, N. & Lozar, F. Orbital tuning of a lower Cretaceous composite record (Maiolica Formation, central Italy). *Paleoceanogr.* **21**, PA4212 (2006).
  26. Schouten, S., Forster, A., Panoto, F. E. & Sinninghe Damsté, J. S. Towards calibration of the TEX<sub>86</sub> palaeothermometer for tropical sea surface temperatures in ancient greenhouse worlds. *Org. Geochem.* **38**, 1537–1546 (2007).
  27. O'Brien, C. L. et al. Cretaceous sea-surface temperature evolution: Constraints from TEX<sub>86</sub> and planktonic foraminiferal oxygen isotopes. *Earth Sci. Rev.* **172**, 224–247 (2017).
  28. Gómez Dacal, A. R. et al. Evidence of warm seas in high latitudes of southern South America during the Early Cretaceous. *Cretac. Res.* **95**, 8–20 (2019).
  29. Stuecker, M. F. et al. Polar amplification dominated by local forcing and feedbacks. *Nat. Clim. Change* **8**, 1076–1081 (2018).
  30. Mohr B. A. R. Early Cretaceous palynomorphs from ODP Sites 692 and 693, the Weddell Sea, Antarctica. In *Proc. ODP Sci. Res.* Vol. 113 (eds et al.) 325–351 (Ocean Drilling Program, 1990).
  31. Kujau, A. et al. Reconstructing Valanginian (Early Cretaceous) mid-latitude vegetation and climate dynamics based on spore-pollen assemblages. *Rev. Palaeobot. Palynol.* **197**, 50–69 (2013).
  32. Hochuli, P. A. & Kelts, K. Palynology of Middle Cretaceous black clay facies from DSDP sites 417 and 418 of the western North Atlantic. In *Initial Reports DSDP*. Vol. 51 (eds Donnelly et al.) 897–935 (Deep Sea Drilling Project, 1980).
  33. Brassell, S. C. Steryl ethers in a Valanginian claystone: molecular evidence for cooler waters in the central Pacific during the Early Cretaceous? *Paleoogeogr. Palaeoclimatol. Palaeoecol.* **282**, 45–57 (2009).
  34. Kessels, K., Mutterlose, J. & Michalzik, D. Early Cretaceous (Valanginian – Hauterivian) calcareous nannofossils and isotopes of the northern hemisphere: proxies for the understanding of Cretaceous climate. *Lethaia* **39**, 157–172 (2006).
  35. Vickers, M. L. et al. The duration and magnitude of Cretaceous cool events: Evidence from the northern high latitudes. *GSA Bull.* **131**, 1979–1994 (2019).
  36. Rogov, M. et al. Database of global glendonite and ikaite records throughout the Phanerozoic. *Earth Syst. Sci. Data* **13**, 343–356 (2021).
  37. Tierney, J. E. & Tingley, M. P. A TEX<sub>86</sub> surface sediment database and extended Bayesian calibration. *Sci. Data* **2**, 150029 (2015).
  38. Tierney, J. E. & Tingley, M. P. A Bayesian, spatially-varying calibration model for the TEX<sub>86</sub> proxy. *Geochim. Cosmochim. Ac.* **127**, 83–106 (2014).
  39. Kim, J. –H. et al. New indices and calibrations derived from the distribution of crenarchaeal isoprenoid tetraether lipids: Implications for past sea surface temperature reconstructions. *Geochim. Cosmochim. Ac.* **74**, 4639–4654 (2010).
  40. Hay, W. W. & Floegel, S. New thoughts about the Cretaceous climate and oceans. *Earth-Sci. Rev.* **115**, 262–272 (2012).
  41. Holbourn, A. E. L. & Kaminski, M. A. Valanginian to Barremian Benthic Foraminifera from ODP Site 766 (Leg 123, Indian Ocean). *Micropal* **41**, 197 (1995).
  42. Kim, J. –H. et al. Influence of deep-water derived isoprenoid tetraether lipids on the TEX<sub>86</sub><sup>H</sup> paleothermometer in the Mediterranean Sea. *Geochim. Cosmochim. Ac.* **150**, 125–141 (2015).
  43. Polik, C. A., Elling, F. J. & Pearson, A. Impacts of Paleocology on the TEX<sub>86</sub> sea surface temperature proxy in the Pliocene-Pleistocene Mediterranean Sea. *Paleoceanogr. Palaeoclimatol.* **33**, 1472–1489 (2018).
  44. Taylor, K. W. R., Huber, M., Hollis, C. J., Hernandez-Sanchez, M. T. & Pancost, R. D. Re-evaluating modern and Palaeogene GDGT distributions: Implications for SST reconstructions. *Glob. Planet. Change* **108**, 158–174 (2013).
  45. Judd, E. J., Bhattacharya, T. & Ivany, L. C. A dynamical framework for interpreting ancient sea surface temperatures. *Geophys. Res. Lett.* **47**, e2020GL089044 (2020).
  46. Farnsworth, A. et al. Climate sensitivity on geological timescales controlled by nonlinear feedbacks and ocean circulation. *Geophys. Res. Lett.* **46**, 9880–9889 (2019).
  47. Bijl, P. K. et al. Early Palaeogene temperature evolution of the southwest Pacific Ocean. *Nature* **461**, 776–779 (2009).
  48. Price, G. D. & Passey, B. H. Dynamic polar climates in a greenhouse world: evidence from clumped isotope thermometry of Early Cretaceous belemnites. *Geology* **41**, 923–926 (2013).
  49. Super, J. R. et al. Late Cretaceous climate in the Canadian Arctic: multi-proxy constraints from Devon Island. *Paleoogeogr. Palaeoclimatol. Palaeoecol.* **504**, 1–22 (2018).
  50. Wang, Y. et al. Paleo-CO<sub>2</sub> variation trends and the Cretaceous greenhouse climate. *Earth-Sci. Rev.* **129**, 136–147 (2014).
  51. Jing, D. & Bainian, S. Early Cretaceous atmospheric CO<sub>2</sub> estimates based on stomatal index of *Pseudofrenelopsis papillosa* (Cheirolepidiaceae) from southeast China. *Cretac. Res.* **85**, 232–242 (2018).
  52. Ladant, J.-B. & Donnadieu, Y. Palaeogeographic regulation of glacial events during the Cretaceous supergreenhouse. *Nat. Commun.* **7**, 12771 (2016).
  53. DeConto, R. M. & Pollard, D. Rapid Cenozoic glaciation of Antarctica induced by declining atmospheric CO<sub>2</sub>. *Nature* **421**, 245–249 (2003).
  54. Gasson, E. et al. Uncertainties in the modelled CO<sub>2</sub> threshold for Antarctic glaciation. *Clim* **10**, 451–466 (2014).
  55. Mutterlose, J. Lower Cretaceous nannofossil biostratigraphy off northwestern Australia (Leg 123). In *Proc. ODP, Sci. Res.* Vol. 123 (eds et al.) 343–368 (Ocean Drilling Project, 1992).
  56. Ogg, J. G., Ogg, G. M., & Gradstein, F. M. *A Concise Geologic Time Scale* (Elsevier, Amsterdam, 2016).
  57. Malinverno, A., Hildebrandt, J., Tominaga, M. & Channell, J. E. T. M-sequence geomagnetic polarity time scale (MHTC12) that steadies global spreading rates and incorporates astrochronology constraints. *J. Geophys. Res.* **117**, B6 (2012).
  58. Hopmans, E. C., Schouten, S. & Sinninghe Damsté, J. S. The effect of improved chromatography on GDGT-based palaeoproxies. *Org. Geochem.* **93**, 1–6 (2016).
  59. Zhang, Y. G., Pagani, M. & Wang, Z. Ring Index: A new strategy to evaluate the integrity of TEX<sub>86</sub> paleothermometry: quality control for TEX<sub>86</sub> temperatures. *Paleoceanography* **31**, 220–232 (2016).
  60. Valdes, P. J. et al. The BRIDGE HadCM3 family of climate models: HadCM3@Bristol v1.0. *Geosci. Model Dev.* **10**, 3715–3743 (2017).
  61. Lunt, D. J. et al. Palaeogeographic controls on climate and proxy interpretation. *Clim. Past* **12**, 1181–1198 (2016).
  62. Gough, D. O. Solar interior structure and luminosity variations. *Sol. Phys.* **74**, 21–34 (1981).
  63. Inglis, G. N. et al. Global mean surface temperature and climate sensitivity of the early Eocene Climatic Optimum (EECO), Paleocene–Eocene Thermal Maximum (PETM), and latest Paleocene. *Clim. Past* **16**, 1953–1968 (2020).
  64. Scotese, C. R. Map Folio 29, Early Cretaceous (Hauterivian, 132.0 Ma), <https://doi.org/10.13140/2.1.1284.1768> (2013).
  65. Bown, P. R., Rutledge, D. C., Crux, J. A. & Gallagher, L. T. Early Cretaceous. In *Calcareous Nannofossil Biostratigraphy* (ed Bown, P. R.) 86–131 (Chapman and Hall, Cambridge, 1998).
  66. Bralower, T. J., Leckie, R. M., Sliter, W. V., & Thierstein, H. R. An integrated Cretaceous microfossil biostratigraphy. In *Geochronology, Time Scales and Global Stratigraphic Correlation* (eds Berggren W. A., Kent D. V., Aubry M.-P. & Hardenbol J.) Vol. 54, 65–79 (Spec. Publ. Soc. Econ. Paleontol. Mineral., 1995).
  67. Thiede, D. S. & Vasconcelos, P. M. Paraná flood basalts: rapid extrusion hypothesis confirmed by new 40Ar/39Ar results. *Geology* **38**, 747–750 (2010).
  68. Janasi, V., de, A., de Freitas, V. A. & Heaman, L. H. The onset of flood basalt volcanism, Northern Paraná Basin, Brazil: A precise U–Pb baddeleyite/zircon age for a Chapecó-type dacite. *Earth Planet. Sci. Lett.* **302**, 147–153 (2011).
  69. Dodd, S. C., Mac Niocaill, C. & Muxworthy, A. R. Long duration (>4 Ma) and steady-state volcanic activity in the early Cretaceous Paraná–Etendeka Large Igneous Province: New palaeomagnetic data from Namibia. *Earth Planet. Sci. Lett.* **414**, 16–29 (2015).
  70. Rayner, N. A. Global analyses of sea surface temperature, sea ice, and night marine air temperature since the late nineteenth century. *J. Geophys. Res.* **108**, 4407 (2003).

## Acknowledgements

We thank the ODP repository teams in Bremen and Kochi for providing sample material for this project. We also thank Eni Spa for financial support and permission to publish this study. The project has strongly benefited from technical support by M. Pegoraro in Milan and D. Warok in Cologne. Funding was provided by Erasmus+ Traineeship scholarship to LC, the Milano group benefited of the fund PRIN 2017RX9XXXY awarded to E.E. and Eni SpA Research & Development provided financial support for research to E.E. and T.W. The authors also acknowledge the financial support from the University of Milan through the APC initiative and from the Italian Ministry of University (MUR) through the project “Dipartimenti di Eccellenza 2018–2022, Le Geoscienze per la Società: Risorse e loro evoluzione”.

## Author contributions

L.C. conducted all isotopic and molecular geochemical analyses and led the writing of the study. T.W. conceptualized the study, established the data-model synergies, and co-lead the writing, in close partnership with E.E. C.B., G.G. and V.G.-G. conducted chronostratigraphic and paleoenvironmental analyses, led by E.E. D.L. and A.F. provided all climate model simulations, S.S. performed the model-data comparison and led the writing of the modelling part. S.F. contributed to the model-data comparison. The biomarker work and TEX<sub>86</sub> analyses conducted by L.C. were supported by W.D., J.R., P.H. and O.E. S.T. contributed to the revision and discussion of palynology data available at ODP site 692. All co-authors contributed to the writing of the manuscript.

## Competing interests

The authors declare no competing interests.

**Additional information**

**Supplementary information** The online version contains supplementary material available at <https://doi.org/10.1038/s41467-021-25706-0>.

**Correspondence** and requests for materials should be addressed to Thomas Wagner.

**Peer review information** *Nature Communications* thanks Gregory Price and the anonymous reviewer(s) for their contribution to the peer review of this work. Peer reviewer reports are available.

**Reprints and permission information** is available at <http://www.nature.com/reprints>

**Publisher's note** Springer Nature remains neutral with regard to jurisdictional claims in published maps and institutional affiliations.



**Open Access** This article is licensed under a Creative Commons Attribution 4.0 International License, which permits use, sharing, adaptation, distribution and reproduction in any medium or format, as long as you give appropriate credit to the original author(s) and the source, provide a link to the Creative Commons license, and indicate if changes were made. The images or other third party material in this article are included in the article's Creative Commons license, unless indicated otherwise in a credit line to the material. If material is not included in the article's Creative Commons license and your intended use is not permitted by statutory regulation or exceeds the permitted use, you will need to obtain permission directly from the copyright holder. To view a copy of this license, visit <http://creativecommons.org/licenses/by/4.0/>.

© Crown 2021

## 6. Global and local dynamics on biogeochemical carbon cycling in the Early Cretaceous proto-Weddell Sea (Eastern Antarctica)

**Draft article in preparation**

**Author(s):** L. Cavalheiro, C. Bottini, W. Dumann, E. Erba, G. Gambacorta, V. Giraldo-Gómez, P. Hofmann, T. Wagner

### **Abstract**

Marine sediments enriched in organic carbon (OC) in the geological record are often associated with extreme perturbations in the atmospheric and oceanic carbon-cycle which impacted the global climate. Examples of C-org rich records from emerging ocean basins that developed during the breakup of Pangea in the Early Cretaceous (~ 145–100.5 Ma) are widely studied. A general gap in detailed proxy records from sub-polar/polar regions has been recognised. This study provides critical new inorganic and organic proxy records from Ocean Drilling Project (ODP) Site 692 covering the Berriasian to the Barremian interval in a high latitude Southern Ocean position. The site, located along the continental slope off Dronning Maud Land (Weddell Sea) of East Antarctica, confirms exceptional high and well preserved organic matter preservation. Stable carbon isotope records identify a prominent excursion (CIE) that documents the Valanginian carbon-cycle/climate perturbation of the Weissert Event and later periods, linked to new proxy data on sea surface ocean temperature (SST) fluctuations. This study presents detailed inorganic (calcium carbonate and X-ray fluorescence based elements) and organic (biomarkers, TEX<sup>86</sup>-based sea surface temperatures, and total organic carbon) geochemical proxy data covering the Early Cretaceous that are integrated to develop a new conceptual and temporal framework to study the interplay between global and local factors as they controlled and sustained high C<sub>org</sub> burial rates and fluctuations over a long geological period of about 10 Myrs. This multi-scale and multi proxy approach has not been shown before and opens new opportunities to ascertain how small and large climate perturbations were translated into the shallow marine sedimentary record of the Early Cretaceous Antarctica.

## 1. Introduction

Early Cretaceous (~ 145–100.5 Ma) emerging ocean basins that developed during the breakup of Pangea are widely studied as important hot spots for deposition of marine organic-carbon-rich black shales (Stein et al., 1986; Zimmerman et al., 1987; McAnena et al 2013). Black shales enriched in organic carbon (OC) are very important in the geological record as they are generally linked to important perturbations in the atmospheric and oceanic carbon-cycle impacting the global climate (e.g., Weissert and Erba, 2004; Jenkyns, 2010). Integrated modelling and biochemical results (McAnena et al 2013) from the late Aptian revealed global bio-geochemical perturbations in the oceans and a 5 degree global cooling linked to over proportionately high rates of excess carbon burial in restricted emerging ocean basins. The study reconstructed that the incipient South Atlantic and Southern Ocean basins recorded 16% and 19% of the total global carbon burial, respectively, i.e., ~132,000 and 160,000 Gt of carbon. Recent work (i.e., Dumman et al. 2021; 2020) discussed in detail the complex interplay between different processes acting on different timescales in the emerging Early Cretaceous South Atlantic basins, controlling primary productivity, preservation, and dilution dynamics, and ultimately changes in OC burial and/or preservation. Examples on a relatively short-time scale are intense carbon-cycle and climate perturbation episodes associated to carbon isotope excursions in the  $\delta^{13}\text{C}$  record (Jenkyns, 2010; Weissert and Erba, 2004), and orbital cycles driving changes in oceanic and atmospheric circulation on timescales of tens of thousands to hundreds of thousands of years (Beckmann et al., 2005; Behrooz et al., 2018; Hofmann and Wagner 2001; Wagner et al., 2013). Particularly, also plate-tectonic processes transforming basin physiography, ocean gateways, and circulation also played a key role in C-cycle dynamics on a multimillion-year (geological) timescale (Dummann et al., 2020; Donnadieu et al., 2016; McAnena et al 2013; Arthur and Natland, 1979; Wagner and Pletsch, 1999). Therefore, the incipient bathymetric and hydrographic isolation of young basins is crucial in controlling nutrient and oxygen exchange dynamics, and the overall biogeochemical carbon-cycling. In the Early Cretaceous, the continuous seafloor spreading and the gradual widening of ocean gateways connecting the South Atlantic and Southern Ocean with the S Pacific and Indian oceans is associated with a progressive, gradual decreasing trend in C-org rich sedimentation (e.g., Barker et al., 1988; Dummann et al. 2021; 2020). By the Albian time, the final ventilation of the Weddell Basin and South Atlantic terminated deposition of C-org rich black shales (Barker et al., 1988; Dummann et al., 2020; 2021). Nonetheless, to date, only the Ocean Drilling Project Site 692 covers the stratigraphic time interval from the Berriasian to the



Barremian in the Southern Ocean (Mutterlose and Wise, 1990; Giraldo-Gomez et al., 2021). Notably, in this very early emerging phase of the southern ocean basins, the position of the Antarctic Peninsula, the depth and width of the proto-Drake passage and Madagascar channel, thus the level of restriction of the Proto-Weddell Basin, are poorly constrained (Miller, 2007; Sewall et al., 2007; Eagles, 2016; Donnadiou et al., 2016; Uenzelmann-Neben et al., 2016; Dummann et al., 2020).

This study aims to provide a unique, multi-proxy based, geochemical dataset to examine how local and global climate impacted on carbon production and burial and SST in the most restricted, initial phase of the proto-Weddell Sea, with a focus on the relationships between biogeochemical carbon cycling and the marine organic carbon (OC) preserved offshore Eastern Antarctica. This is achieved by studying a Berriasian–Barremian, high-resolution sample set from Ocean Drilling Program (ODP) Site 692, drilled in 1987. The site, located along the continental slope off Dronning Maud Land (Weddell Sea, Fig.1) of East Antarctica, records exceptional high and well preserved organic matter (OM) rates (Cavalheiro et al., 2021). Site 692 represents a unique, high-latitude example to study and disentangle the different contributions of local and global dynamics controlling OC burial and preservation. Deposition of the organic-rich Early Cretaceous black shales occurred in the isolated and restricted Weddell Basin (WB), from a paleo-latitude of  $\sim 55^\circ\text{S}$ , and at a paleo water depth of about 500 m (Barker et al., 1988; Giraldo-Gomez et al., 2021). A recently revised biostratigraphy study assigned Berriasian to lower Barremian age to the study site (see Giraldo-Gomez et al., 2021). Notably, the lower stratigraphic interval identifies the carbon-climate perturbation of the Valanginian Weissert Event, which drastically impacted SST and global atmospheric  $p\text{CO}_2$  (Cavalheiro et al., 2021). Moreover, across the recovered section at Site 692, abundant volcanic ash component has been reported, with the Mozambique Ridge further east as a possible source region (Barker et al., 1998). Particularly, in other Early Cretaceous black shales, it has been investigated how the presence of abundant ash material may have acted as fertiliser and productivity stimulus in down-drift ocean regions (Lee et al., 2018).

In this study, we combine OC and calcium carbonate records with geochemical inorganic and molecular proxy data to track fluctuations in biogeochemical cycling and associated organic carbon burial. Reconstruction of paleo-redox conditions is based on Fe-S-TOC relationships, redox sensitive trace metals, manganese/aluminium ratios, and molecular proxies. Other X-ray fluorescence derived geochemical data (Si/Al; K/Al; Ti/Al) are used to track changes in composition, provenance, and weathering state of the analysed sediments.

Moreover, a new detailed SST record – based on the TEX<sub>86</sub> organic paleothermometry – is presented.

## **1.1 Geological framework**

The Ocean Drilling Program (ODP) Site 692 (70°43.432'S, 13°49.195'W) lies on a continental slope off Dronning Maud Land (Weddell Sea) of East Antarctica (Fig.1.a). ODP Site 692 was drilled in 1987 during ODP Leg 113 in a water depth of 2875 m. Paleo-position in the Early Cretaceous, in the incipient and restricted proto-Weddell Basin, near the eastern tip of the Falkland Plateau (Smith et al., 1981), is shown in Fig.1.b–d. Following Barker and Kennet 1988, during the Berriasian-Barremian interval, a triangular-shaped restricted and anoxic basin south of the Falkland Plateau was bound to the west by the Antarctic Peninsula and the southeast and east to East Antarctica and Madagascar, respectively, as illustrated in Fig.1.b–d. By the Middle Jurassic, the individual continents of Gondwana had drifted apart and opened up parts of the Southern Ocean (König and Jokat, 2006). This rifting continued into the Early Cretaceous and led to the early opening of the South Atlantic from ~140 Ma to ~130 Ma ago (König and Jokat, 2006). This ultimately resulted in a separation of South America and the Falkland Plateau from Antarctica at around 135 Ma before today (König and Jokat, 2006). Only in the early Albian, the final ventilation of the Weddell Basin allowed sufficiently strong flows terminating black shale deposition, and causing upwelling and the accumulation of diatom ooze in a well oxygenated environment, as documented at ODP Site 693, offshore Eastern Antarctica (Mutterlose and Wise, 1990).

## **2. Material and methods**

### **2.1 Sampling and stratigraphy**

At ODP Site 692, in a modern water depth of 2875 m, 97.9 m were penetrated and 29.3 m (30%) were recovered in 11 cores (plus 2 wash cores). All depths referred to in this study are depths below sea-floor. High-resolution samples (N =216), approximately every 10–15 cm, were taken from the interval 53.54 to 92.34 mbsf (cores 113-692B-7R through 113-692B-12R).

Sampling avoided intervals with dominant ash lenses and beds. The study section is described from the top-down, following Barker et al., 1988, and core observations in this work (Fig. 2).

**Lithology.** The study interval is a 44.7 m-thick carbonate and organic-rich hemipelagic claystone, rich in nannofossils; the clay fraction contains between 85 and 100 percent of smectite (Barker et al., 1988).

Claystones are common at the top of the unit (core 7R) and are underlain by a mixed assemblage of ash and nannofossil-bearing claystone, organic and nanno-fossil-bearing mudstone, organic-bearing muddy nannofossil chalk. Carbonate-bearing nannofossil claystone and mudstones characterize the middle of the unit (cores 8R to 10R). The bottom part of the unit (core 12R) is mainly carbonate-bearing and nanofossil bearing clayey mudstone. Minor to moderate bioturbation is observed at several levels, especially in the following intervals: 113-692B-7R-1, 100–110 cm, 113-692B-8R-2, 10–40 cm, 113-692B-8R-3, 70–80 cm, and 113-692B-9R-1, 80–90 cm. In all sections abundant pyrite nodules, fragments, and framboids are identified

**Volcanic Ash and Lenses.** All cores (cores 113-692B-7R through 113-692B-12R; 53.2–97.9 mbsf) are characterized by the presence of several volcanic layers (beds, laminae, and lenses), commonly with a high percentage of calcium carbonate. The volcanic ash lenses generally decrease in abundance toward the bottom core 113-692B-12R. The volcanic beds are mostly grey in colour (N 5/0), and/or pale yellow-olive (5Y 6/6). Some of the ash layers and lenses are pyritized and are likely broken fragments of pumice.

## **2.2 Analytical methods**

### **2.2.1 Total carbon, total organic carbon and total inorganic carbon**

A total of 216 samples were analysed for total carbon (TC), total inorganic carbon (TIC), and derived total organic carbon (TOC = TC-TIC) contents using a DIMATOC 2000 carbon analyser (Dimatec Corp., Germany). An aliquot (25–30 milligrams) of each core ground sample (pulverised and homogenized) is mixed with an aliquot (12–14 grams) of MilliQ water. Afterward, sonification is applied to stir and homogenized the particles in a sample, using an ultrasonic processor UP200Ht, and a magnetic stir bar is also applied. The TOC measurement is based on the principle of thermal-catalytic oxidation at 900° C, which guarantees the complete conversion of all relevant carbon compounds to CO<sub>2</sub>. The instrument uses two independent measurement channels and a zero-entrainment sampling system. The processing of the sample rack is fully automatic, including acidification (using 40% phosphoric acid), outgassing, and homogenizing. The measuring range is 0–20.000 ppm C, and the detection limit is 0.05 ppm C. All measurements are repeated in triplicate. In accordance with the DIMATOC Standard Protocol, blank and standard samples are run for calibration and quality check control of the machine. Quantitative calculations and data processing is automatically operated through an external PC with DIMAQS operating software. Calcium carbonate (CaCO<sub>3</sub>) content was calculated stoichiometrically from TIC content.

### **2.2.2 Carbon isotope analysis**

A total of 143 samples including a published data-set from Cavalheiro et al., 2021 (see also methodology details) were analysed for bulk organic stable carbon isotope ratios ( $\delta^{13}\text{C}_{\text{org}}$ ) by Europa Scientific Elemental Analyser – Isotope Ratio Mass Spectrometry (EA – IRMS). Analysis was carried out at Iso-Analytical, Crewe Cheshire (UK). Repeat analysis on reference materials (e.g., IAEA-CH-6, IA-R001, IA-R005, and IA-R006) and duplicate sample measurements yielded a standard deviation < 0.1. Carbon isotope results are reported in the standard Vienna Pee Dee Bee  $\delta$  notation (VPDB).

### 2.2.3 Major and trace element analyses

The elemental concentration of 178 samples was measured by X-ray fluorescence core scanning (XRFcs) using an Itrax XRF Core Scanner (Cox Analytical Systems, Germany), equipped with a Cr-tube. The XRF analyses were performed non-destructively and without sample contact. Samples were milled, pressed into plastic pads (2x1 cm), and aligned under the core scanner. Analyses were performed with X-ray beam size of 7 x 0.2 millimetres, and a measuring time of 16 seconds at each position, yielding nine to twelve individual measurements per sample. For each sample and individual element, arithmetic means were calculated. XRF raw data are stored as spectra from each point of analysis, and element data are available as peak areas as well as concentrations of each element. Absolute element concentrations were derived from the semi-quantitative counts, verifying the calibration curves based on 30 reference samples of known elemental composition, which were measured alongside the samples. Regression analysis of linear calibration curves used to calculate absolute elemental concentrations yielded good correlation coefficients with  $R^2 > 0.80$  for all the reported elements.

Total nitrogen (TN) and total sulphur (TS) concentrations were analysed using a vario MICRO CUBE elemental analyser (elementar Corp., USA). An aliquot (2–5 milligrams) of dry sample (pulverized and homogenized) is jet-injected directly into the combustion zone with approximately 20 milligrams of chemical catalyst Com-Cat Accelerator and combusted at ~1,150°C in an oxygen atmosphere; any carbon present is converted to CO<sub>2</sub>, which mass is then converted to percent carbon based on the dry sample weight. Quantitative calculations and data processing are automatically operated through an external PC with Windows-based operating software. In accordance with the Vario MICRO cube CNS protocol, the equipment is tuned to check for drift and standardized, and a continuing calibration check standard is analysed every 10 samples: one Standard Reference Material (SRM) is equally replicated twice to check for the reproducibility of the results.

**Normalization of XRF data and proxies.** All resulted elements are reported as Aluminium-normalized elemental ratios to account for dilution by CaCO<sub>3</sub> and OC. Moreover, redox-sensitive elements trace metals (TMs), e.g., Ni, Cu, V, and Zn, are also related to average shale values (Wedepohl, 1971, 2004) in order to access the degree of authigenic enrichment beyond detrital background levels.

## 2.2.4 Lipid biomarker analysis

Aliquots (~1–5 grams) of dry and pulverised sample material were extracted with an Accelerated Solvent Extractor (DIONEX ASE 350 System), using a mixture of dichloromethane (DCM)/methanol (MeOH) (5:1, v/v) at a temperature of 100 °C and pressure of 69±10 psi. Sulphur-free extracts were obtained with desulfurization using acid-activated copper turnings; extracts were thus purified by column chromatography over self-packed silica gel (deactivated with 1% ultrapure H<sub>2</sub>O) columns using hexane, hexane:DCM (2:1, v/v), and MeOH as subsequent eluents.

The saturated aliphatic fractions (dissolved in 50µL hexane) were screened at Heriot-Watt University, on a Thermo Scientific Trace 1310 GC fitted with a split splitless injector (at 280 °C) and linked to a Single Quadrupole Mass Spectrometer using electron ionization (electron voltage 70eV, source temperature 230 °C, quadrupole temperature 150 °C, multiplier voltage 1800V, interface temperature 310 °C). Samples were investigated both in selected ion monitoring (SIM) and in full scan acquisition mode (50–600 amu/sec), using a thermo fused silica capillary column (60 m x 0.25 mm i.d) coated with 0.25 µm 5 % phenylmethylpolysiloxane phase. The GC temperature was gradually (5 °C/min) increased from 50 to 310 °C, holding the final temperature for 10 minutes and using helium as carrier gas (flow rate of 1 ml/min, the initial inlet pressure of 50 kPa, split at 30 ml/min). Reproducibility was monitored using an in-house standard containing all targeted compounds at similar concentrations levels. Note that data reproducibility varied between different compounds and was generally better than 1–5%, but always better than 10% for all reported biomarker ratios.

Pilot analyses on a sub-set of 63 samples analysed the distribution of acyclic hydrocarbons (i.e., *n*-alkanes, acyclic isoprenoids) and sterane distributions (42 samples) were investigated to explore basic molecular proxies to infer OC sources. The average chain length ratio (ACL) (equation 1), was calculated according to a modified formula by Peters et al. (2005), including all ranges of odd and even *n*-alkanes (*n*-C<sub>17</sub> → *n*-C<sub>33</sub>) as follows

$$ACL_{17-33} = \left[ \frac{(17 \cdot C_{17} + 18 \cdot C_{18} + n \cdot C_{n...} + 33 \cdot C_{33})}{(C_{17} + C_{18} + C_{19} + C_{20} + C_{21} + C_{22} + C_{23} + C_{24} + C_{25} + C_{26} + C_{27} + C_{28} + C_{29} + C_{30} + C_{31} + C_{32} + C_{33})} \right] \quad (1)$$

Furthermore, the terrigenous/aquatic ratio  $TAR_{HC}$  - used as a crude indicator of relative terrigenous versus aquatic organic matter input (equation 2) - was calculated using a modified formula based on Bourbonniere and Meyers, (1996). This proxy shows relative changes in the composition between aquatic and terrestrial fauna (Meyers, 1997).

$$TAR_{HC} = \frac{(C_{29} + C_{31} + C_{33})}{(C_{17} + C_{19} + C_{21})} \quad (2)$$

Other relations between acyclic isoprenoids, i.e., pristane/phytane (Pr/Ph) proxy, and *n*-alkanes, are used as indicators of redox conditions, organic carbon source, and thermal maturity assessment (Didyk et al., 1978; Peters et al., 2005).

### 2.2.5 Glycerol Dialkyl Glycerol Tetraether and derived SSTs

A total of 100 samples were screened for Glycerol Dialkyl Glycerol Tetraether (GDGTs) compounds at the University of Cologne using an Agilent 1290 Infinity ultra-high performance liquid chromatography (HPLC) paired with an Agilent GDGT 6460 Triple Quadrupole MS system. Published chromatographic conditions and previous work for GDGTs identification were applied. Refer to Cavalheiro et al., 2021, which includes 68 recently published sample results of this data-set, for details of the methodology, analytical error, GDGT-screening, and calibration discussion to SSTs. The  $TEX_{86}$  index (equation 3) was calculated as originally defined<sup>23</sup>:

$$TEX_{86} = \frac{[GDGT-2]+[GDGT-3]+ [Cren']}{[GDGT-1]+[GDGT-2]+[GDGT-3]+ [Cren']} \quad (3)$$

Based on a published compilation of Cretaceous  $TEX_{86}$  data and calibration methods<sup>27</sup>, we report in the Supplementary Data Appendix all temperatures resulting from different calibrations. Particularly, following Cavalheiro et al., 2021, only the results from two main calibrations, the BAYSPAR calibration model (Tierney and Tingley 2014, 2015; MATLAB script) and a regional calibration for deep restricted modern basins (Kim et al., 2015; equation 4), are discussed in this work.

$$SST \text{ (deep restricted basin)} = 56.3 * TEX_{86} + 30.2 \quad (4)$$

### 3. Results

#### 3.1 Stable carbon isotopes

Stable carbon isotopes range between -31.9 and -28.7‰ (from sample 692B-12R-3-112-115 to 692B-7R-1-32-34, e.g., 92.34 to 53.53 mbsf in Fig. 2.a). As detailed in Cavalheiro et al. (2021), the lower portion of the studied section documents the positive carbon isotope excursion (CIE) of about 1.5 ‰ at ODP Site 692 identifying the Valanginian Weissert Event. Following the original definition of Erba et al. (2004), the onset of the Weissert Event is placed at the base of the positive CIE (A in Fig. 2.a), and the end of the event at the top of the CIE plateau (C in Fig.2.a). Following the recovery phase of the Weissert CIE (C–D in Fig.2.a), a small positive CIE ( $\delta^{13}\text{C}_{\text{org}}$ ) at 80.98 mbsf marks the upper Valanginian – Early Hauterivian boundary (Cavalheiro et al., 2021 Supplementary). Carbon isotope values are relatively stable across the Hauterivian – lowermost Barremian interval, documenting average values of  $\sim -30$ ‰ until  $\sim 68.80$  mbsf (top core 9); starting from the base of core 8, at  $\sim 64$  mbsf,  $\delta^{13}\text{C}_{\text{org}}$  exhibits complex patterns with swings between maximum and minimum excursions of about 1–2 ‰, showing a strong inverse relation with TOC ( $R^2 \sim 0.5$  in core 8 and  $\sim 0.7$  in core 7; see cross plots in Data Appendix). However, relevant core gaps and the lack of calcareous nanofossils in the interval from 60.32 to 53.20 mbsf impede chemostratigraphic and chronostratigraphic framing of the upper part of cores 8 and 7.

#### 3.2 Total organic carbon content

A broad range of TOC contents are documented, i.e., 1.3 to 19.9% (Fig. 2.c) but overall high background levels, on avg. 7.5 % are documented across the study section. Particularly, we observe that changes in TOC content are unrelated to visible changes in sedimentary facies and/or to volcanic ash lenses/beds distribution (Fig. 2).

In the Berriasian–Valanginian interval, from the section bottom until about the Valanginian–Hauterivian boundary, TOC ranges between  $\sim 3$  and 11%, on avg.  $\sim 6$ %. Starting from the Upper Valanginian and Hauterivian transition, higher TOC rates, ranging between  $\sim 6$  and 12% (avg. values of  $\sim 9$ %), are documented up to the end of the Hauterivian. In the lower Barremian, TOC becomes highly variable, with fluctuations between 1.3 and 19.9%, showing a strong inverse relation with  $\delta^{13}\text{C}_{\text{org}}$  both in cores 8 and 7 ( $R^2 = 0.5$  and 0.7, respectively; cross-



plots in Data Appendix). In the first interval of the lower Barremian, at ~70 mbsf, TOC documents a sharp rise up to the highest documented results, ranging between ~10 and 20%, with an average of 13.5%. TOC gradually decreases at the base of core 8, reaching average values of 5%, ranging between ~2.5 and 6%, with minima between 62 and 63 mbsf; TOC sharply rises again in the upper part of core 8, ranging from ~8 to 15.5 % TOC (on avg. 12.5%) between 61.06 mbsf and the top core 8. At the base of core 7, TOC values are high, with maxima of ~16, a progressively decrease but ranging 5 and 10% TOC, with avg. values of ~7.5%.

### 3.3 Calcium carbonate

Calcium carbonate values are largely scattered, varying between 0 and 86.13% (Fig. 3.d), and show different trend relations with TOC and  $\delta^{13}\text{C}_{\text{org}}$  across the study section. A weak co-variation ( $R^2 \sim 0.3$ ; cross-plots in Data Appendix) with Fe and Ti/Al is documented. During the Berriasian and lower interval of the Upper Valanginian,  $\text{CaCO}_3$  values vary between 0–33.58%; a general decreasing trend from avg. values of 20% is identified between the section bottom and the early onset of Weissert Event (interval A–B), during which  $\text{CaCO}_3$  content is close to zero.  $\text{CaCO}_3$  recovers in the second phase of the Weissert Event, showing scattered values between ~2 and 50% (on avg. 25%) in the uppermost Upper Valanginian and across the Hauterivian. No co-variation with TOC and redox-sensitive TMs is recorded in these intervals. During the lower Barremian, the  $\text{CaCO}_3$  record registers increased fluctuations from ~0 to 86.13% (on avg. ~30%). The base of core 8 is characterized by a  $\text{CaCO}_3$  increasing trend, with maximum values >80% coinciding with the minima in TOC and TM EFs between 62 and 63 mbsf; afterward, it follows a decreasing trend in  $\text{CaCO}_3$ , reaching minimum avg. values of 10% in the upper, not zoned, core 8. In the uppermost, not zoned, core 7, except from one single high value at the core bottom (~50%  $\text{CaCO}_3$ ), the calcium carbonate content becomes extremely low ranging between 20 and 0%, on avg. ~5%. Particularly, if maximum and minima are smoothed using a 3 point moving average, a strongly negative co-variation between TOC and  $\text{CaCO}_3$  is registered ( $R^2 \sim 0.7$ ; cross-plots in Data Appendix) in the carbonate-rich interval from ~60 to 64 mbsf (core 8). This may occur because, in a carbonate-dominated environment, enhanced silicate content goes along with enhanced nutrient supply and thus bio-productivity leading to higher organic matter (Ghassal et al., 2016). In contrast, the low-carbonate interval

from ~53 to 56 mbsf (core 7) shows a positive correlation between CaCO<sub>3</sub> and TOC ( $R^2 \sim 0.7$ ; cross-plots in Data Appendix), indicating that during this episode nutrient supply was not a limiting factor for organic matter.

### 3.4 Distribution of sulphur and iron

Sulphur contents are generally unrelated to TOC (cross plot in Data appendix), varying between 0.6 and 3.89%, and a mean value of 2.3% in either “low, high and extremely high TOC black shales” (Fig.4). Only in the lower Barremian, between 62.0 and 63.0 mbsf, TS is below 1%, reaching minima of 0.6% (Fig.4.b). Note that 5 samples exceed 4% (Supplementary Data), reaching maximum of 10.4%, probably having measured abundant pyrite powder. Fe, S and TOC relationships (Fig. 4.d) are used to differentiate between paleo-redox states based on diagnostic S/C and S/Fe ratios (Dean and Arthur, 1989; Arthur and Sageman, 1994; Raiswell et al., 1988). Overall all samples show S/Fe ratios well above or about the threshold value of 0.45, which is generally used to discriminate oxic from “restricted” (i.e., sub-anoxic-anoxic) conditions (Raiswell et al., 1988). S/Fe ratios show a relatively high scatter between 0.45 and the pyrite line (S/Fe = 1.15; Worthmann *et al.*, 1999), with values often above 0.75, indicating strictly anoxic-euxinic conditions (Raiswell et al., 1988). Particularly, the Fe-S cross-plot (see Data Appendix) shows that most samples have excess Fe. During the Berriasian and lower interval of the Upper Valanginian in samples above 0.75. Values decrease at the base of core 8, mostly ranging between 0.40 and 0.75 until ~62 mbsf). Fluctuations in S/Fe ratios of ~0.4 to >1 are again documented between 61.62 and 59.30 mbsf (i.e., top core 8). In the upper, not zoned, core 7, S/Fe ratios decrease to a range of 0.4–0.75.

### 3.5 Distribution of redox-sensitive trace metals and major elements

Distribution of redox-sensitive trace metals (TMs) Ni, Cu, Vn, and Zn are presented as enrichment factors (EFs) relative to average shale (AS) values from Wedephol (2004, 1971) in Fig. 5b–f. Generally, all TM EFs co-vary closely with each other and with TOC (Fig.5.a–f). Across the overall section, TM EFs only moderately exceed AS values, showing EFs of ~1–8, 1–7, 1–12, and 1–16 for Ni, V, Zn, and Cu, respectively. Cross-plots of TM EFs against TOC

(see Data appendix) provide additional information on the mechanisms of sedimentary TM enrichment and thus paleo-redox conditions (Tribovillard et al., 2066; Algeo and Maynard, 2004). Average EFs of about 2 (1.7–4.5), 1.5 (0–2.2), 3 (0.7–6.9), and 3.5 (1.8–6.8) of Ni, V, Zn, and Cu, respectively, are documented during the Berriasian and lowermost Upper Valanginian interval (core 12, 92.34–88.33 mbsf), including the first warmest phase of the Weissert Event. In the top part of the upper Valanginian, starting from the base of core 12 (including the cooling and recovery phase of the Weissert) and across the Hauterivian, EFs of Ni, V, Zn, and Cu slightly increase to average values of about 3 (1.9–6.5), 2 (1.1–3.3), 4 (2.1–8.1), and 5 (1.7–9.2), respectively. In the first interval of the lower Barremian, a sharp peak in EFs of all redox-sensitive TMs is documented. Average values of ~6 (2.8–7.8), 4.5 (1.5–6.6), 7 (2.0–12.1), and 8 (2.3–11.6) are reported for Ni, V, Zn, and Cu respectively. Particularly, in the upper part of the lower Barremian (~62 to 63 mbsf), concurrent with a sharp drop in TOC and a decrease in S to 0.6–0.9%, a fall of all redox sensitive TMs close to average shales is documented. Moreover, all samples are poor in Mn, indicating anoxic bottom water conditions with only the interval at ~62–63 mbsf showing a peak in Mn/Al to 0.02, with an increase in Mn contents suggesting a shift to more dysoxic conditions (Calvert and Pedersen, 1993; Aquit et al., 2013). In contrast, in the uppermost, not zoned, core 7, TM EFs exhibit complex patterns of enrichment and depletion, lacking clear parallel trends neither between TOC, S/Fe ratios nor with the different TMs.

We note that diagnostic element ratios for continental supply (e.g., Si/Al, K/Al, and Ti/Al) are just below or at average shale levels (Fig.3.a–d) suggesting low or limited connectivity to adjacent landmasses.

### **3.6 Thermal maturity**

Consistently with previous studies (Barker et al., 1988; Littler et al., 2011; Cavalheiro et al., 2021), sediments at Site 692 are thermally immature, reporting Rock-Eval  $T_{max}$  values of ~420 °C (see Fig. 6). This interpretation is consistent with Pr/*n*-C<sub>17</sub> and Ph/*n*-C<sub>18</sub> relationships (Fig. 7) and the dominant presence of the least stable 5  $\alpha$ , 14  $\alpha$ , 17 $\alpha$  (H)-20R stereoisomeric configuration of regular steranes (Fig.8).

### 3.7 Biomarkers, organic matter sources, and paleo-redox conditions

Variations in OM sources are assessed based on the relative abundances of *n*-alkanes and desmethylsteranes. Chain lengths of *n*-alkanes range from C<sub>15</sub> to C<sub>35</sub>. The proxy ACL indicates mean values below 25 (20.5–26.5; avg. 23.2; Fig. 6), which can be used as a threshold to specify the dominance of lower molecular weight *n*-alkanes, indicative of algal and/or bacterial OC input (Han and Calvin, 1969). The ratio of terrestrial to aquatic *n*-alkanes (TAR<sub>Hc</sub>) is consistently below one except for a few samples (0.2–3.; avg. 0.8; Fig. 6), indicating a dominant aquatic origin of sedimentary OM, consistent with a dominance of C<sub>27</sub> and C<sub>28</sub> over C<sub>29</sub> regular steranes (Fig.8). Pristane to phytane (Pr/Ph) ratios are below 1 (0.14–1; avg. 0.42; Fig. 6) are documented in all samples. Pristane and phytane are two of the most prominent isoprenoids in black shales that originate partly from the phytol side chain of chlorophyll a (Brooks et al., 1969; Powell and McKirdy, 1973; Didyk et al., 1978). Depending on the oxygen availability the diagenesis of phytol leads either to pristane under more oxic conditions or to phytane under more anoxic conditions (Koopmans et al., 1999; Peters et al., 2005). Therefore, Pr/Ph ratios lower than 1.0 usually support anoxic seawater conditions during deposition. Pr/*n*-C<sub>17</sub> versus Ph/*n*-C<sub>18</sub> relationships support immature, marine OM under reducing conditions (cross-plot in Fig. 7).

We note high concentrations of lycopane, a tail-to-tail linked acyclic isoprenoid, as a diagnostic proxy for anoxic depositional settings (Sinninghe Damste' et al. 2003). Lycopane/*n*-C<sub>31</sub> ratios range from 0.3 to 8.1, with a mean value of 1.6 (Fig 7.d).

### 3.8 TEX<sub>86</sub>-based sea surface temperatures

TEX<sub>86</sub> values range between 0.63 and 0.77 in the Berriasian – Barremian section (Fig. 2.b). No TEX<sub>86</sub> covariation with CaCO<sub>3</sub> and TOC is observed (see Data Appendix). TEX<sub>86</sub>-based sea surface temperatures presented include data from the Valanginian Weissert Event, discussed earlier by Cavalheiro et al. (2021). Following the recent Weissert Event study TEX<sub>86</sub>-based sea surface temperature have been calibrated using the BAYSPAR model (Tierney and Tingley 2014; 2015) (Fig. 2.b); while the regional TEX<sub>86</sub>-temperature relation (Equation 4; Kim et al., 2015) yields the lower end estimates (i.e., min-TEX<sub>86</sub>) of absolute SSTs in the

restricted Weddell Basin. Across the Hauterivian, following the Weissert Event, sea surface temperatures values gradually return to warmer and rather stable values that continue across the lower Barremian, showing values of  $\sim 0.72$ , corresponding to  $\sim 22/30$  °C (min/max–TEX<sub>86</sub>).

## 4. Discussions

### 4.1 Local versus global drivers controlling bio-geochemical carbon cycle dynamics

The new high-resolution geochemical data from ODP Site 692 confirm consistent and long-term black shale deposition (avg. 7.5% TOC) in the proto-Weddell Basin from the Berriasian to the lower Barremian. Such long-term high OC burial trend is modulated by episodes of enhanced and depleted OC burial, with the highest OC variabilities registered in the lower Barremian ( $\sim 2\%$  to 20%). However, because of the presence of core gaps, we can only speculate about the controls of these probably Ma-year long carbon cycles. We observe even shorter-term internal fluctuations of about 2% TOC, which may occur at frequencies of orbital or sub-orbital cycles.

A fundamental observation of this study is that OC burial rates in the Weddell Basin were unrelated to the Weissert Event, documenting no relevant changes in TOC concentration across the upper Valanginian CIE. Moreover, SST changes at ODP Site 692, including the observed latest Valanginian cooling event of  $\sim 3\text{--}4$  °C (Cavalheiro et al., 2021), are also decoupled from OC variations, with no influence on the dominant marine OM source. SSTs in the Weddell Sea after the Weissert Event document a gradually increasing trend across the Hauterivian, which reports average values of about 21 °C. In the lower Barremian, SSTs return to rather stable and warmer values, on average 22 °C. These relationships exclude a strong local climate and SST control on OC fluctuations for the lower Barremian. This relationship may have been different for the upper Barremian (not zoned intervals of cores 8 and 7) with C<sub>org</sub> dynamics closely related to carbon isotope chemistry, suggesting a closer coupling between local carbon fluctuations in the Weddell Sea and global carbon controls. The lack of stratigraphic control of this interval complicates further interpretations of forcing-response mechanisms.

We observe two intervals of CaCO<sub>3</sub> drop with values close to zero, the first coinciding with the warmest phase of the Valanginian Weissert Event (A–B), and the latter in the not zoned topmost interval. Both interludes are unrelated to peaks in TOC and/or redox sensitive trace metals but coincide with a drop in calcareous nannofossils and benthic foraminifera (Giraldo-

Gomez et al., 2021). We suggest that these CaCO<sub>3</sub> drops represent intermittent carbonate dissolution events, possibly related to a shoaling of the calcite compensation depth (CCD) in the study region. Ocean acidification linked to the onset of the Parana'-Etendeka large igneous province and the warmest phase of the Valanginian Weissert Event (A-B) has been shown for the Tethys Ocean (Casellato and Erba, 2004) and might explain the pause in calcium carbonate deposition in the Weddell Sea. Better time control and additional research, including climate-ocean modelling, are required to validate the proposed relationships. From a general paleoceanographic perspective it seems feasible that fluctuations in ocean current exchange across the Indian and Pacific gateways and internal modulations of the current patterns within the proto Weddell Sea may have occurred throughout the early Cretaceous. Such large-scale oceanographic modulations may have had the potential to impact ocean chemistry and accordingly the position of the CCD, however, at this stage, we can only speculate about such process chains in the Southern Ocean and their link with the global ocean (see further discussion below).

Different from indirect and vague evidence supporting fluctuations in ocean carbon chemistry the new inorganic and organic proxy data clearly show support persistent dysoxia-anoxia in the study region across the Berriasian-Barremian interval. The new molecular data are consistent with a continuous reducing depositional setting, favouring excellent preservation of diagnostic compounds like lycopane and phytane in all samples analysed. The molecular redox assessment is supported by Fe-S-TOC relationships of dysoxia-anoxia to strictly anoxia-euxinia and records of abundant framboidal pyrite (Barker et al., 1988). The fact that peaks in TOC are generally associated with an increase in total sulphur, S/Fe ratios, redox-sensitive TMs, and depletion in manganese, supports the conclusion that ocean redox (anoxia) added to the enhanced preservation and burial of OC.

Different from that, the data do not support that fluctuations in nutrient discharge from the Antarctic controlled the marked TOC variabilities. The molecular data, despite low stratigraphic resolution, confirm a dominance of marine OM both from *n*-alkane ratios and dominance of isoprenoid-GDGT compounds, excluding relevant terrestrial input across the section. Moreover, K/Al ratios show little variability below average shale levels, again supporting low continental supply. This interpretation is in accordance with previous work (Mohr et al., 1990) that placed ODP 692 well offshore ( $\geq 100$  km), based on low percentages of organic terrestrial debris. Studies on clay mineralogy associations at ODP 692 report abundant smectite, suggesting that the adjacent continent was low-lying and that erosional

processes towards the shelf margin were rather weak (Barker and Kennet 1988). Moreover, Si/Al and K/Al ratios lack parallel trends across the study section, without any correlation to each other and other diagnostic proxies. Si/Al ratios are generally constant across the section but generally higher than in average shale. Previous work has reported nodules containing carbonate fluorapatite and abundant radiolarians at ODP 692 (O'Connell et al., 1990). This leads us to suggest that the relatively high and constant Si/Al ratios are related to the presence of an important biosiliceous component. Therefore, if the hypothesis of enhanced nutrient runoff does not seem convincing – both from previous work (Mutterlose and Wise 1990; Mohr 1990; O'Connell et al., 1990) and new data from this study – additional mechanisms might have contributed to the delivery of such elements and enhancing of OC burial and preservation rates.

During the study Berriasian–Valanginian interval, most plate tectonic reconstructions (Matthews et al., 2016), and recent modelling results (Donnadieu et al., 2016; Uenzelmann-Neben et al., 2016; Dummann et al., 2020; 2021) suggest the presence of bathymetric barriers in the regions of the proto-Drake Passage (i.e. the gateway between S-America and the Antarctic Peninsula), the Madagascan- African, and the Indian–Antarctic gateways (Fig. 9). Our new data show a lack of considerable TM enrichment beyond average shale levels, supporting possible exhaustion of TMs in the water column due to weak replenishment of water masses and dissolved TMs (Algeo and Maynard, 2004; Algeo and Rowe, 2012). We thus relate the perseverance of reducing conditions to the high degree of hydrographic and bathymetric isolation of the incipient proto-Weddell Sea. However, to date, the depth and width of such bathymetric barriers and the level of hydrographic isolation of the entire Southern Ocean during the pre-Aptian period remain poorly constrained (Matthews et al., 2016; Dummann et al., 2021; 2021). Nonetheless, the high-resolution geochemical data presented in this study might suggest that the increased amplitude of  $C_{org}$  cycles from the Berriasian–Valanginian to the Barremian interval might be related to the result of a progressively more dynamic ocean system. These modulations would have enabled more exchange with the S Pacific Ocean and replenishment of water masses with elevated dissolved nutrients and TMs. This hypothesis can be tested by future biogeochemical modelling supporting a causal link between evolving ocean circulation, nutrient (re)supply, and its transport along the Antarctica peninsula.

## 4.2 Possible mechanisms sustaining continuous and elevated ocean fertilization

Another important consideration at ODP Site 692 is that the average organic content recorded in the study section (TOC on avg. > 6%) is very high, at least for modern upwelling areas (O'Connell et al., 1990). Continuing high levels of organic matter and the presence of biosiliceous sediments might suggest, as speculated by O'Connell et al. (1990), deposition under conditions of high productivity across the overall Berriasian–lower Barremian interval. Particularly, understanding how ocean waters could sustain such fertile states over long-time periods raises a major paleoceanographic challenge (Meyer and Kump, 2008), especially in the case of the proto-Weddell Sea for a period over 10 Ma with limited or no direct continental runoff. We speculate that the abundance of ash material at ODP Site 692 throughout the Berriasian–lower Barremian may have played a central role in sustaining continuous and elevated ocean fertilization. Volcanic ash fertilization would be one mechanism to maintain high nutrients and productivity levels across the proto Weddell Sea (and beyond?), pushing the restricted basin conditions towards even lower dissolved oxygen contents, as documented in other Early Cretaceous black shales (Lee et al., 2018). We note that the volcanic ash at Site 692 is absent from coeval samples on the Falkland Plateau. There is no tectonic evidence to explain this discrepancy, as the two areas had the closest plate boundary lying between them (Lawver et al., 1985). In contrast, ash is found in coeval sediments at Site 249 (Mozambique Ridge), however in a much more condensed section (Barker et al., 1988). We, therefore, speculate that winds and/or ocean currents may have transported volcanic ash from the Mozambique Ridge region to the location of ODP 692. Particularly, the location of Site 692 on the eastern side of Antarctica, in the hydrographic and bathymetric isolated proto-Weddell Basin, might have acted as a 'nutrient trap' of all such nutrients delivered to the basin. This process cascade would explain continuous and elevated ocean fertilization and persistent high OC preservation in the sediments. Further climate modelling simulations are needed to validate a possible east-west eolian transport and/or marine transfer and 'trap model' of ash material and nutrients along the Early Cretaceous Antarctica peninsula. Moreover, future investigation of specific paleo-productivity proxies, and a detailed geochemical and stratigraphic study of these volcanic ash beds/lenses might shed new light on the link between primary productivity, southern volcanic activity, and C<sub>org</sub>-rich black shales recorded offshore the Early Cretaceous southeast Antarctica peninsula.



## 5. Conclusions and implications for further research

This study presents a new conceptual and temporal framework of the crucial interplay between concurrent global and local factors that sustained and controlled extreme  $C_{org}$  burial rates and fluctuations, as well as exceptional preservation of OM, over a long period of about 10 Ma in the Early Cretaceous Weddell Sea.

1. The new high-resolution data reveal long-term (Berriasian to Barremian) black shale deposition with unusual and persistent high OC burial (avg. 7.5% TOC) in the proto-Weddell Basin. Particularly, OC burial rates are unrelated to the Weissert Event and the Barremian interval registers the highest episodes of peak carbon burial, with OC variabilities up to 20%. We speculate that the location of Site 692, in the hydrographic and bathymetric isolated proto-Weddell Basin, might have acted as a ‘nutrient trap’, sustaining high productivity across the overall Berriasian–lower Barremian. Indeed, continuing high levels of OM are recorded together with abundant biosiliceous and ash material. Further climate modelling simulations will be necessary to validate a possible east-west eolian transport and/or marine transfer and ‘trap model’ of ash material and nutrients along the Antarctica peninsula.
2. The study excludes a main local climate control on OC fluctuations in the Early Cretaceous Weddell Sea from new evidence showing that OC burial rates are unrelated to the reconstructed  $TEX_{86}$ -based SST variations. Following the Weissert Event, SSTs gradually increase across the Hauterivian (avg. values  $\sim 21$  °C) and return to rather stable and warmer values (avg.  $\sim 22$  °C) in the lower Barremian. In contrast, the warmest phase of the Valanginian Weissert Event (A–B) marks a relevant change in carbon chemistry with  $CaCO_3$  decreasing below 5% and coinciding with a major drop in calcareous benthic foraminifera (Giraldo-Gomez et al., 2021). This may indicate a dissolution event, possibly related to a shoaling of the calcite compensation depth (CCD).
3. Consistent multi-proxy evidence supports persistent dysoxia-anoxia that is related to the high degree of hydrographic and bathymetric isolation of the Early Cretaceous proto-Weddell Sea. Notably, fluctuations in OC are generally correlated to changes in redox sensitive proxies. OM type and quality remain generally constant and of well-preserved marine OM, consistent with the evidence of very low continental supply. Therefore, the increased amplitude of  $C_{org}$  cycles from the Berriasian–Valanginian to the Barremian interval might be related to the result of a progressively more dynamic ocean system,

enabling more exchange with the S Pacific. This hypothesis can be tested by future biogeochemical modelling supporting a causal link between evolving ocean circulation, nutrient (re)supply, and its transport along the Antarctica peninsula. This research emphasizes the major role of the local basin physiography of the emerging Weddell Sea plays in controlling OC rates even across the occurrence of extreme Weisert global carbon cycle and climate perturbation.

## 6. Figures

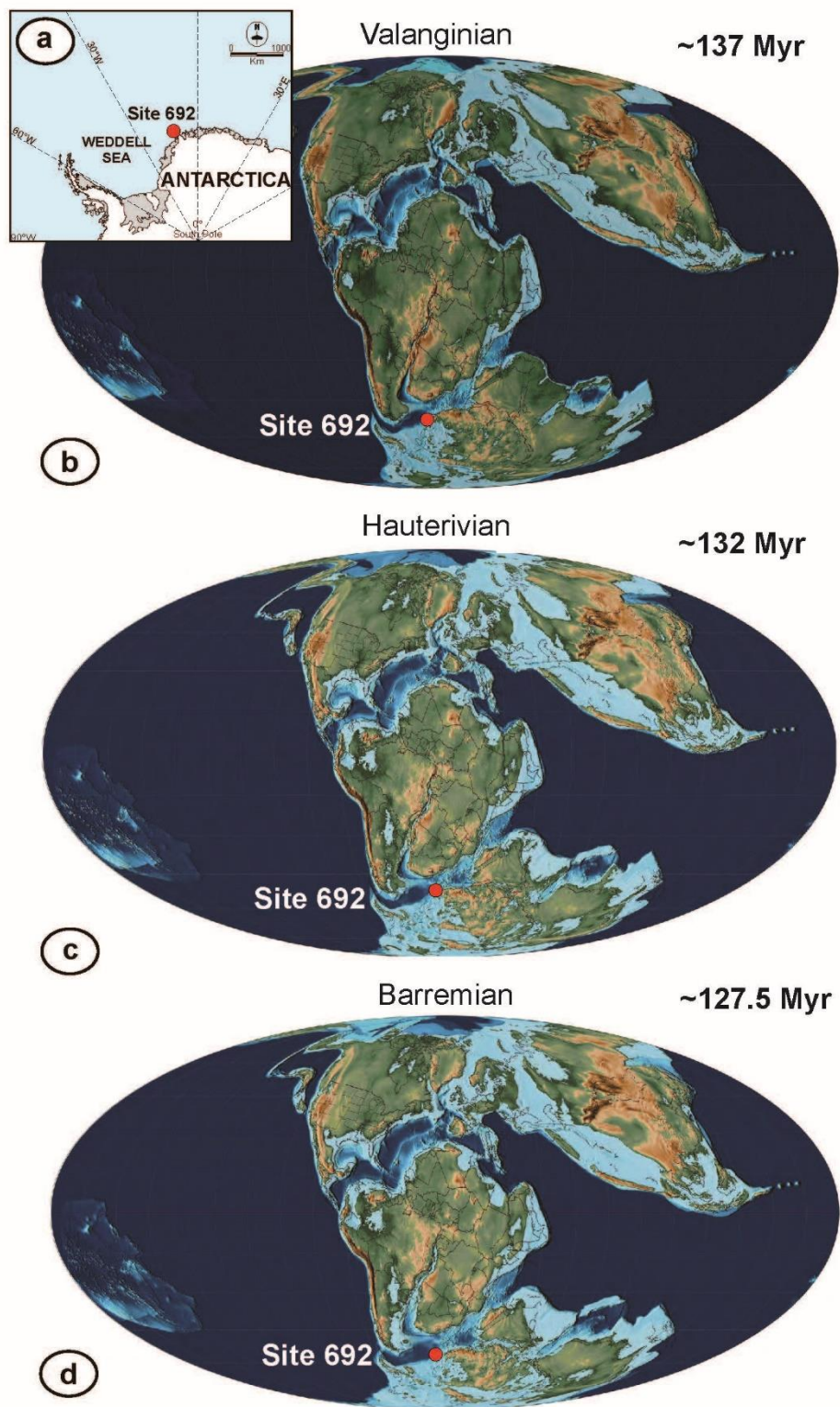


**Fig. 1:** (a) Location of the Ocean Drilling Program (ODP) Site 692 (70°43.432'S, 13°49.195'W) in the Weddell Sea, Eastern Antarctica. Paleogeographic reconstruction of the Gondwana continent during the (b) Valanginian (~137 Ma), (c) Hauterivian (~132 Ma), and

(c) Barremian (~127.5 Ma) by C.R. Scotese, PALEOMAP project showing the position of ODP Site 692 along the Antarctica margin.

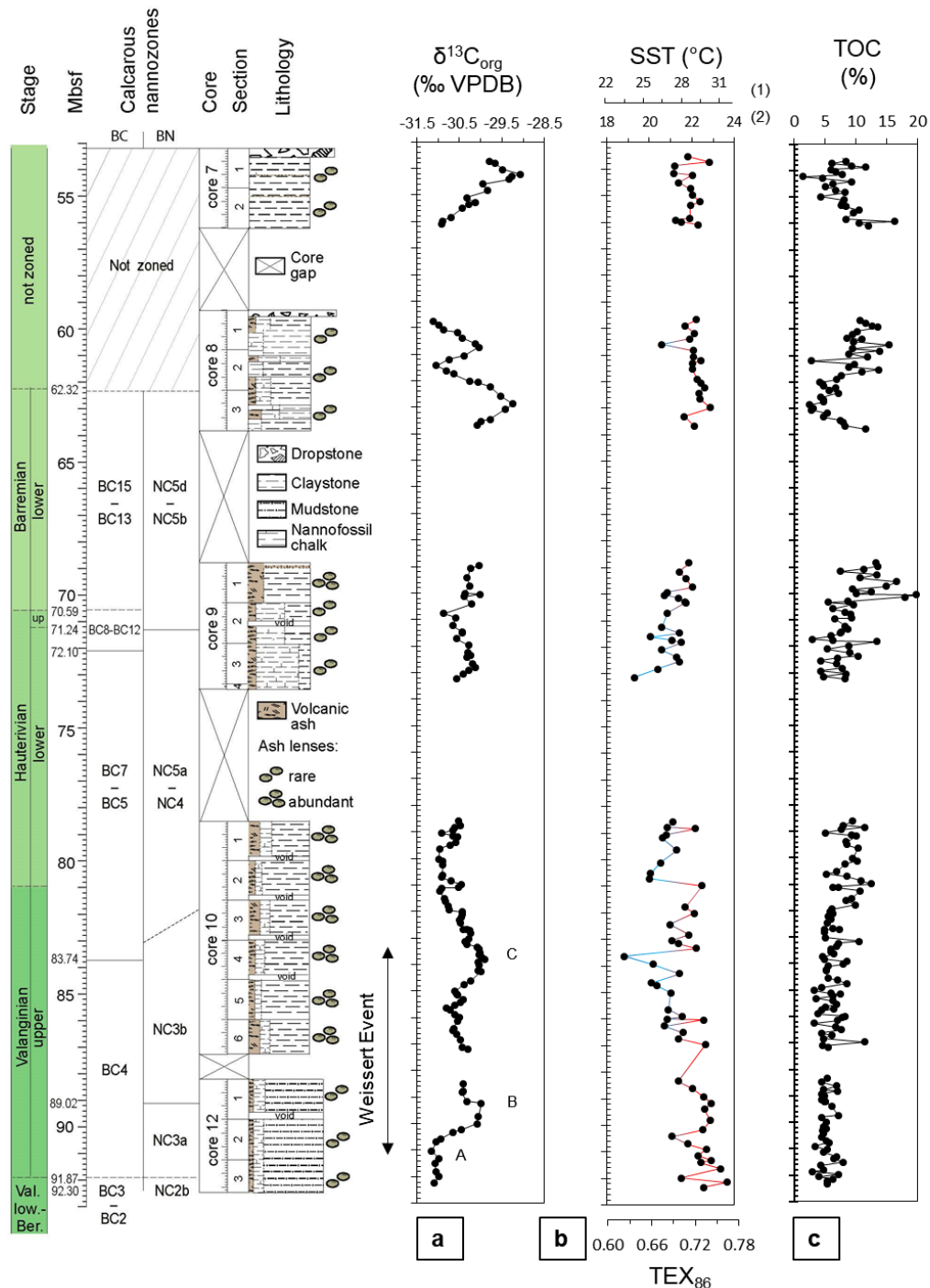


**Fig. 2:** Stage and calcareous nannofossil zonation, Boreal (BC; Bown et al., 1988) and Tethys (NC; Bralower et al., 1995) zonations of cores 7R, 8R, 9R, 10R, and 12R of Ocean Drilling Site 692 (Cavalheiro et al. 2021). Depth in metres below seafloor (mbsf) and lithology log. (a) Stable carbon isotope record measured on bulk organic matter ( $\delta^{13}\text{C}_{\text{org}}$  three points moving average; Cavalheiro et al., 2021; Giraldo-Gomez et al., 2021); identification of the

Weissert positive carbon isotope excursion (CIE segments: A, Weissert CIE onset; B, Weissert CIE first peak; C, Weissert CIE end); **(b)** organic TEX<sub>86</sub> paleothermometry curve reporting TEX<sub>86</sub> raw values and the calibrations to SSTs in degree °C showing (1) BAYSPAR and (2) restricted basin calibrations, representing maximum and minimum temperature estimates. **(c)** Total organic carbon content (TOC).



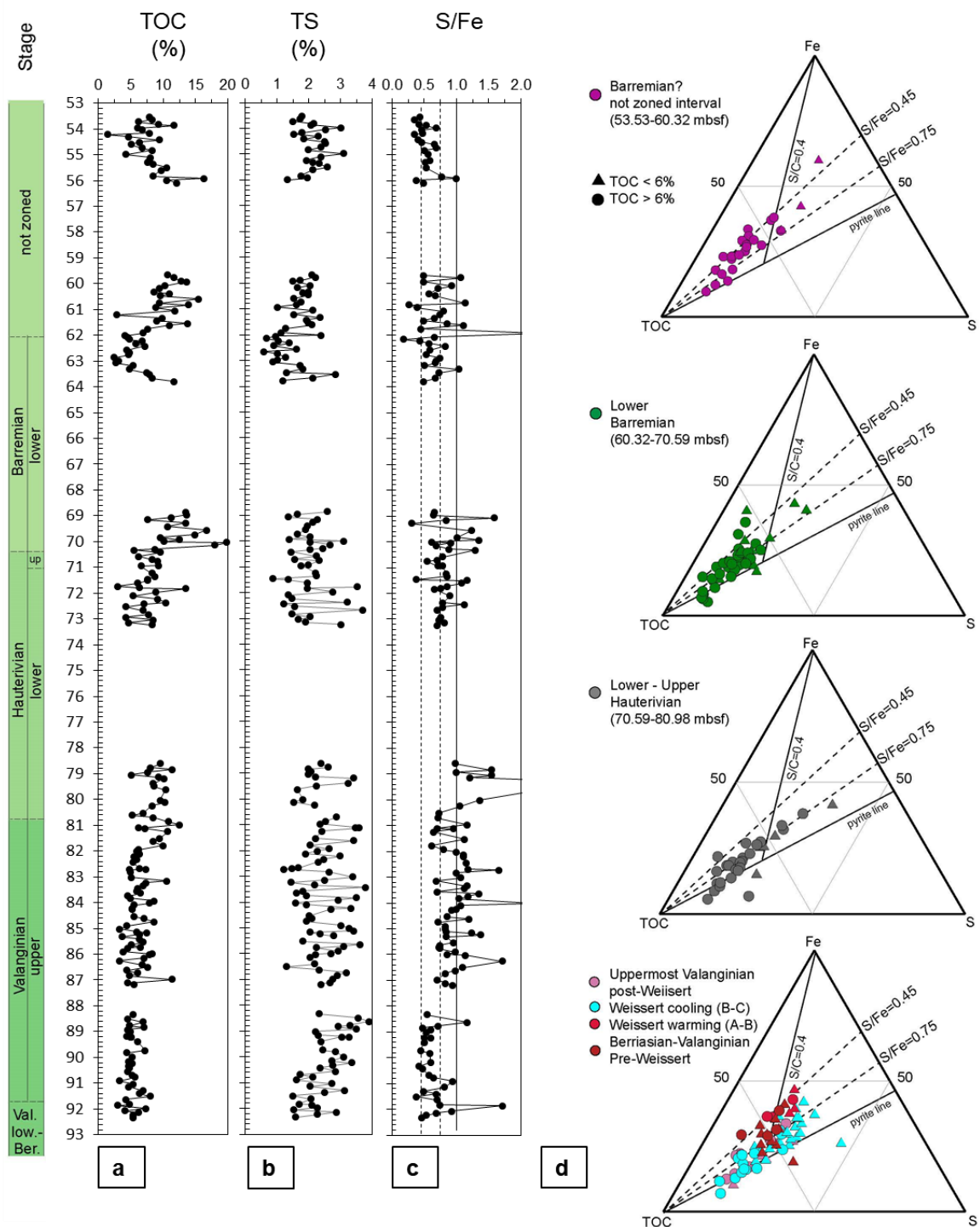


**Fig. 4:** Stratigraphic distribution of (a) total organic carbon content (TOC), (b) bulk total sulphur content (TS), (c) sulphur/iron (S/Fe) ratio. (d) Ternary diagrams showing the Fe/S/TOC relationships for different time intervals. Characteristic ratios used to reconstruct paleo-redox conditions are plotted in (d), following Berner and Raiswell (1983), Leventhal (1983), and Raiswell et al. (1988).

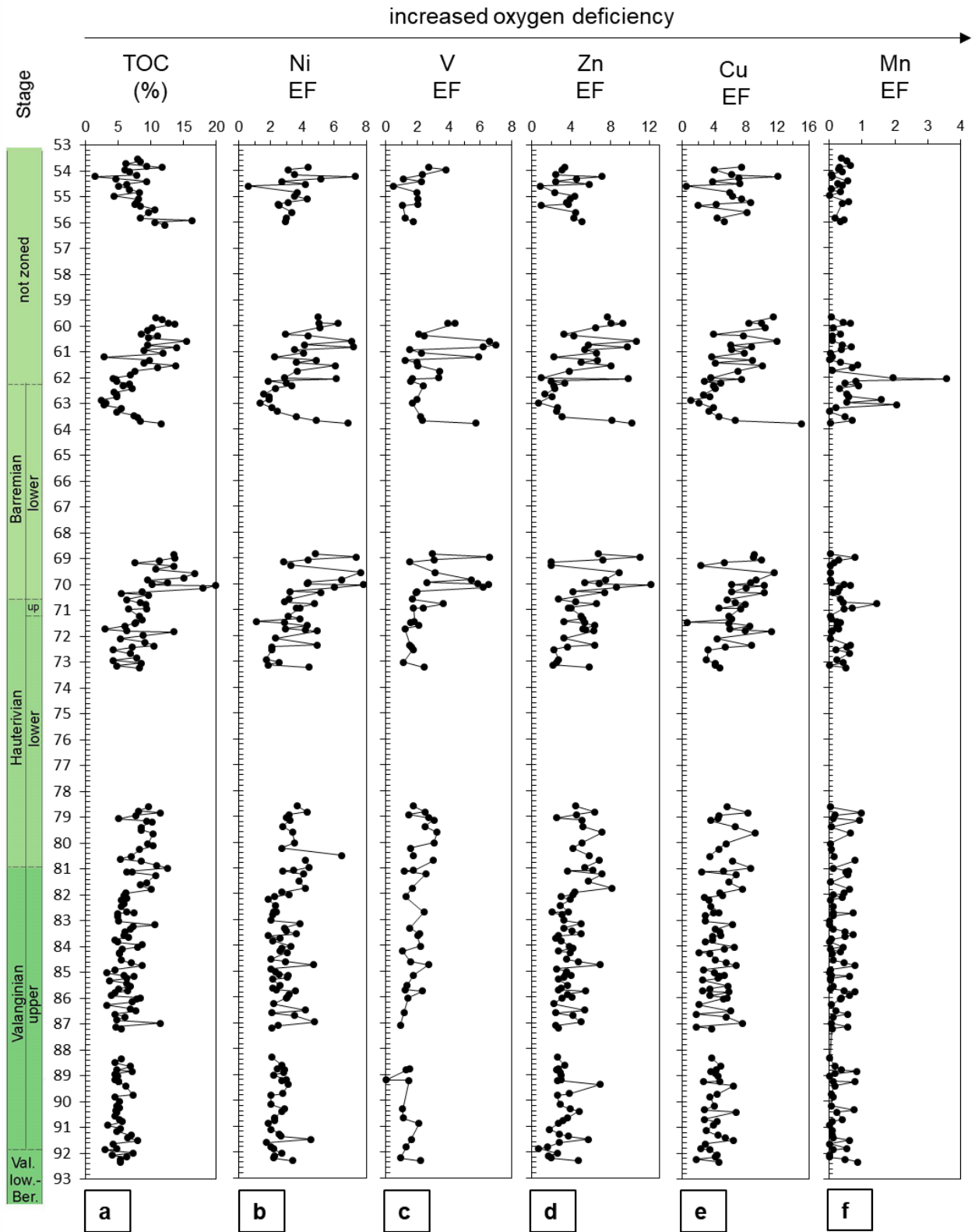


**Fig. 5:** Stratigraphic distribution of (a) total organic carbon content (TOC) and average shale-normalized enrichment factors ( $EF_{AS}$ ) of (b) Ni, (c) V, (d) Zn, and (e) Cu. (f) Mn/Al ratio.



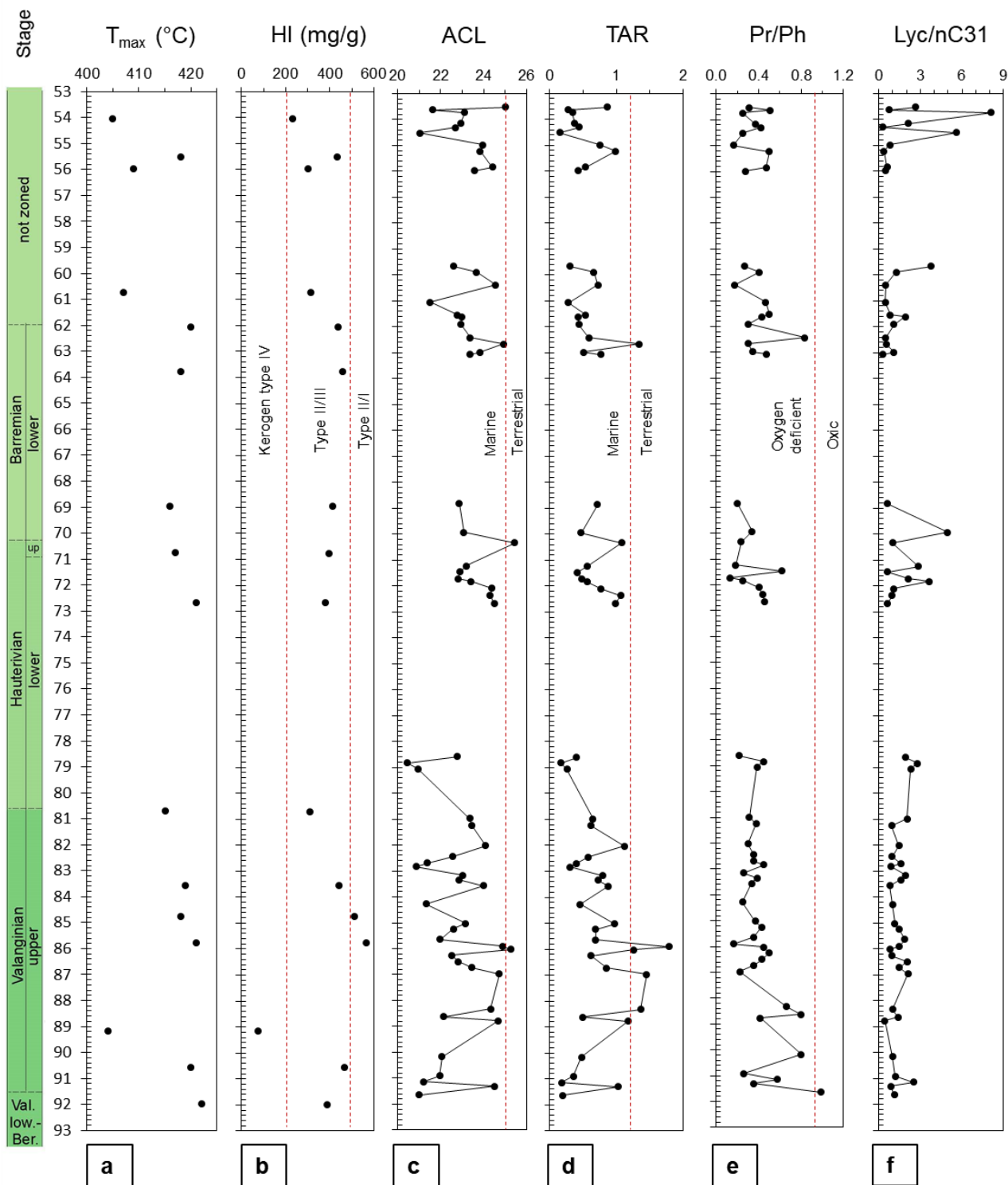


**Fig. 6:** Distribution of selected biomarker parameters used to reconstruct organic carbon (OC) source and paleo-redox conditions: (a) total organic carbon content (TOC), (b) average chain length ratio (ACL), (c) terrigenous/aquatic ratio  $TAR_{HC}$ , and (d) lycopane/*n*-C<sub>31</sub> ratio.

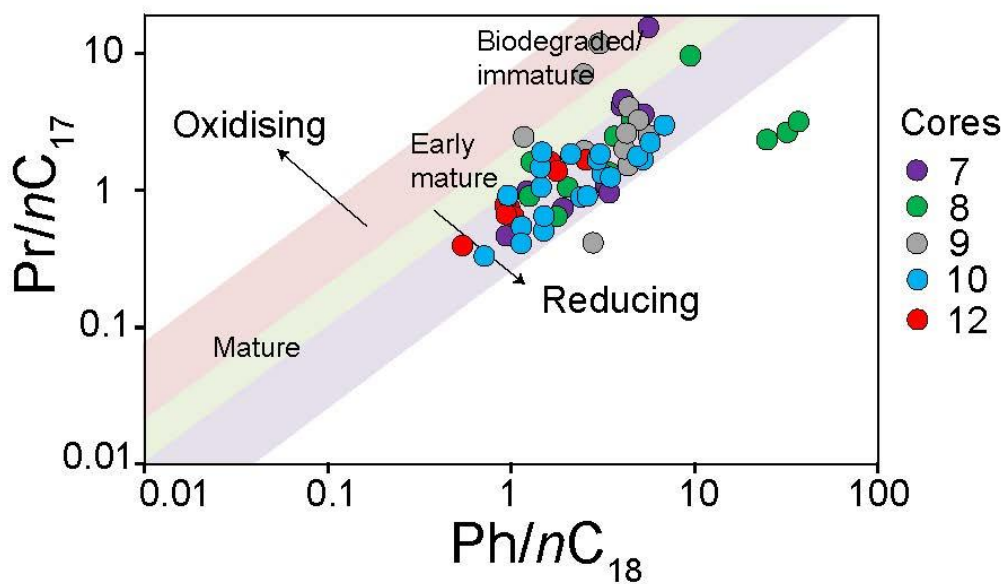


**Fig. 7:** Cross-plot of ratios of pristane to *n*-heptadecane ( $Pr/nC_{17}$ ) vs. phytane to *n*-octadecane ( $Ph/nC_{18}$ ) with classification method adapted from Shanmungam (1985).

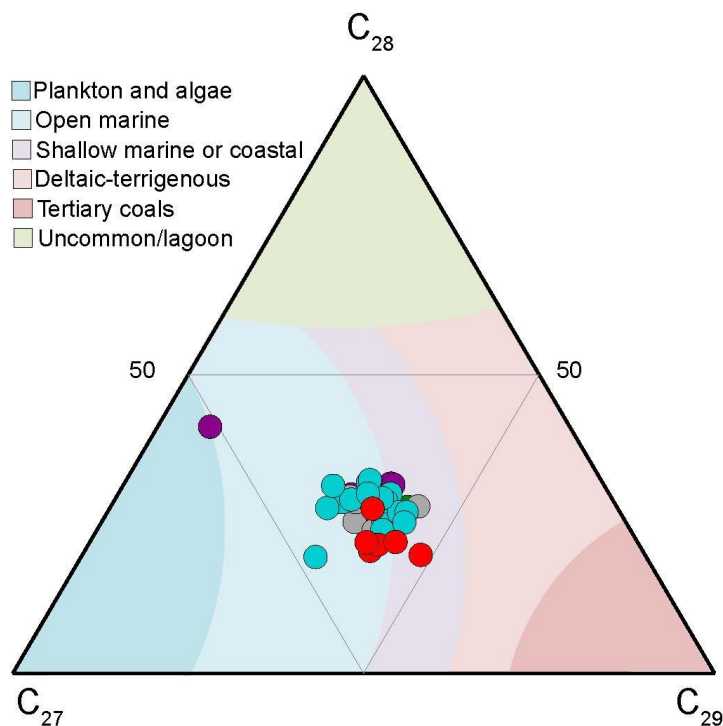


**Fig. 8:** Ternary diagram showing the distribution of conventional steroids  $C_{27}$ ,  $C_{28}$  and  $C_{29}$  related to parent material sources. The classification method is adapted from Huang and Meinschein (1979).

**a** Isolated basins (>~124 Ma)

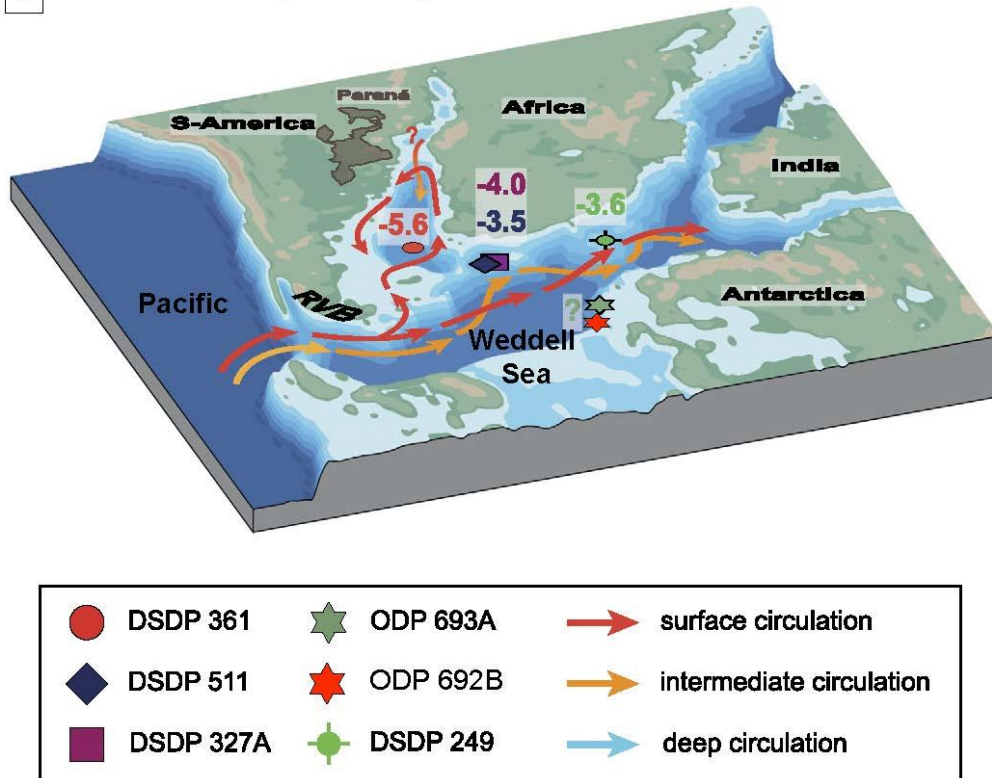


**Fig. 9:** Scheme of ocean circulation modelling during the Late Barremian and Early Aptian prior to gateway opening (>124 Ma) from Dummann et al., 2020. Note that the topography shown is idealized and does not claim to be a detailed paleotopographic reconstruction. Numbers next to coring sites represent average seawater  $\epsilon\text{Nd}(t)$ . RVB: Rocas Verdes Basin.

## 7. References

1. Algeo, T. J., Maynard, J. B., 2004. Trace-element behavior and redox facies in core shales of Upper Pennsylvanian Kansas-type cyclothems, *Chemical Geology* 206, 289–318.
2. Algeo, T.J., Rowe, H., 2012. Paleooceanographic applications of trace-metal concentration data. *Chemical Geology*, 324, 6–18.
3. Aquit, M., Kuhnt, W., Holbourn, A., Chellai, E., Stattegger, K., Kluth, O., Jabour, H., 2013. Late Cretaceous paleoenvironmental evolution of the Tarfaya Atlantic coastal Basin, SW Morocco. *Cretaceous Research* 45, 288–305.
4. Arthur, M.A., Natland, J.H., 1979. Carbonaceous sediments in the North and South Atlantic: the role of salinity in stable stratification of Early Cretaceous Basins. In: Talwani, M., Hay, W.W., Ryan, W.B.F. (Eds.), *Deep Drilling Results in the Atlantic Ocean: Continental Margins and Paleoenvironment*. American Geophysical Union, Washington DC (USA), 375–401.
5. Arthur, M.A., Brumsack, H.J., Jenkyns, H.C., Schlanger, S.O., 1990. Stratigraphy, geochemistry, and paleoceanography of organic carbon-rich Cretaceous sequences. In *Cretaceous resources, events and rhythms* (Springer, Dordrecht), 75–119.
6. Arthur, M. A., Sageman, B. B., 1994. Marine Black Shales: Depositional Mechanisms and Environments of Ancient Deposits, *Annual Review Earth and Planetary Science*, 22, 499–551.
7. Barker, P.F., Kennett, J.P., 1988. Leg 113. In *Proceedings of the Ocean Drilling Program Initial Reports of Leg 113*, 785.
8. Beckmann, B., Flögel, S., Hofmann, P., Schulz, M., Wagner, T., 2005. Orbital forcing of Cretaceous river discharge in tropical Africa and ocean response. *Nature* 437, 241–244.
9. Behrooz, L., Naafs, B. D. A., Dickson, A. J., Love, G. D., Batenburg, S. J., Pancost, R. D., 2018. Astronomically driven variations in depositional environments in the South Atlantic during the Early Cretaceous. *Paleoceanography and Paleoclimatology* 33, 894–912.
10. Berner, R. A., Raiswell, R., 1983. Burial of organic carbon and pyrite sulfur in sediments over Phanerozoic time: a new theory, *Geochimica et Cosmochimica Acta* 47, 855–862.
11. Boucot, A. J., Xu, C., Scotese, C. R., Morley, R. J., 2013. *Phanerozoic Paleoclimate: An Atlas of Lithologic Indicators of Climate*, *SEPM Concepts in Sedimentology and Paleontology*, SEPM Society for Sedimentary Geology, Tulsa (USA) No 11 Map Folio.

12. Bourbonniere, R.A., Meyers, P.A., 1996. Sedimentary geolipid records of historical changes in the watersheds and productivities of Lakes Ontario and Erie. *Limnology and Oceanography* 41, 352–359.
13. Bown, P. R., Rutledge, D. C., Crux, J. A., Gallagher, L. T., 1998. Early Cretaceous. In *Calcareous Nannofossil Biostratigraphy* (ed Bown, P. R.) (Chapman and Hall, Cambridge,), 86–131.
14. Bralower, T. J., Leckie, R. M., Sliter, W. V., Thierstein, H. R., 1995. An integrated Cretaceous microfossil biostratigraphy. In *Geochronology, Time Scales and Global Stratigraphic Correlation* (eds Berggren W. A., Kent D. V., Aubry M.-P. and Hardenbol J.), Special Publication Society of Economic Paleontologists and Mineralogists, 54, 65–79.
15. Brooks, J.D., Gould, K., Smith, J.W., 1969. Isoprenoid hydrocarbons in coal and petroleum. *Nature* 222, 257–259.
16. Calvert, S.E., Pedersen, T.F., 1993. Geochemistry of Recent oxic and anoxic marine sediments: Implications for the geological record. *Marine Geology* 113(1–2), 67–88.
17. Cao, W., Williams, S., Flament, N., Zahirovic, S., Scotese, C., Müller, R. D., 2019. Palaeolatitudinal distribution of lithologic indicators of climate in a palaeogeographic framework. *Geological Magazine* 156, 331–354.
18. Casellato, C. E., Erba, E., 2015. Calcareous nannofossil biostratigraphy and paleoceanography of the Toarcian Oceanic Anoxic Event at Colle di Sogno (Southern Alps, Northern Italy). *Rivista Italiana di Paleontologia e Stratigrafia* 105, 343–376.
19. Cavalheiro, L., Wagner, T., Steinig, S., Bottini, C., Dummann, W., Esegbue, O., Gambacorta, G., Giraldo-Gómez, V., Farnsworth, A., Flögel, S., Hofmann, P., 2021. Impact of global cooling on Early Cretaceous high pCO<sub>2</sub> world during the Weissert Event. *Nature communications* 12(1), 1–11.
20. Charbonnier, G., Duchamp-Alphonse, S., Deconinck, J. F., Adatte, T., Spangenberg, J. E., Colin, C., Föllmi, K. B., 2020. A global palaeoclimatic reconstruction for the Valanginian based on clay mineralogical and geochemical data. *Earth-Science Reviews* 202, 103092.
21. Dean, W. E., Arthur, M. A., 1989. Iron-sulfur-carbon relationships in organic-carbon-rich sequences I: Cretaceous Western Interior Seaway. *American Journal of Science* 289, 708–743.
22. Didyk, B.M., Simoneit, B.R.T., Brassell, S.C., Eglinton, G., 1978. Organic geochemical indicators of palaeoenvironmental conditions of sedimentation. *Nature* 272, 216–222.

23. Donnadieu, Y., Pucéat, E., Moiroud, M., Guillocheau, F., Deconinck, J.F., 2016. A better-ventilated ocean triggered by Late Cretaceous changes in continental configuration. *Nature communications* 7(1), 1–12.
24. Dummann, W., Steinig, S., Hofmann, P., Flögel, S., Osborne, A.H., Frank, M., Herrle, J.O., Bretschneider, L., Sheward, R.M., Wagner, T., 2020. The impact of Early Cretaceous gateway evolution on ocean circulation and organic carbon burial in the emerging South Atlantic and Southern Ocean basins. *Earth Planet Science Letters* 530, 115890.
25. Dummann, W., Hofmann, P., Herrle, J.O., Wennrich, V., Wagner, T., 2021. A refined model of Early Cretaceous South Atlantic–Southern Ocean gateway evolution based on high-resolution data from DSDP Site 511 (Falkland Plateau). *Palaeogeography, Palaeoclimatology, Palaeoecology* 562, 110113.
26. Eagles G., 2016. Plate kinematics of the Rocas Verdes Basin and Patagonian orocline. *Gondwana Research* 37, 98–109.
27. Erba, E., Bartolini, A., Larson, R. L., 2004. Valanginian Weissert oceanic anoxic event. *Geology* 32(2), 149–152.
28. Farquharson, G W., 1983. The Nordenskjöld Formation of the northern Antarctic Peninsula: an upper Jurassic radiolarian mudstone and tuff sequence. *British Antarctic Survey Bulletin* 60, 1–22.
29. Ghassal B. I., Littke R., Sachse V., Sinderen S., Schwarzbauer J., 2016. Depositional environment and source rock potential of Cenomanian and Turonian sedimentary rocks of the Tarfaya Basin, Southwest Morocco. *Geologica Acta* 14(4), 419–41.
30. Han, J., Calvin, M., 1969. Hydrocarbon distribution of algae and bacteria, and microbiological activity in sediments. *Proceedings of the National Academy of Sciences* 64(2) 436–443.
31. Hofmann, P., Wagner, T., 2011. ITCZ controls on Late Cretaceous black shale sedimentation in the tropical Atlantic Ocean. *Paleoceanography and Paleoclimatology* 26(4).
32. Huang, W.Y., Meinschein, 1979. Sterols as ecological indicators. *Geochimica et Cosmochimica Acta* 43, 739–745.
33. Jenkyns, H. C., 2010. Geochemistry of oceanic anoxic events. *Geochemistry, Geophysics, Geosystems* 11(3), Q03004.
34. Kim, J.H., Schouten, S., Rodrigo-Gámiz, M., Rampen, S., Marino, G., Huguet, C., Helmke, P., Buscail, R., Hopmans, E.C., Pross, J., Sangiorgi, F., 2015. Influence of deep-

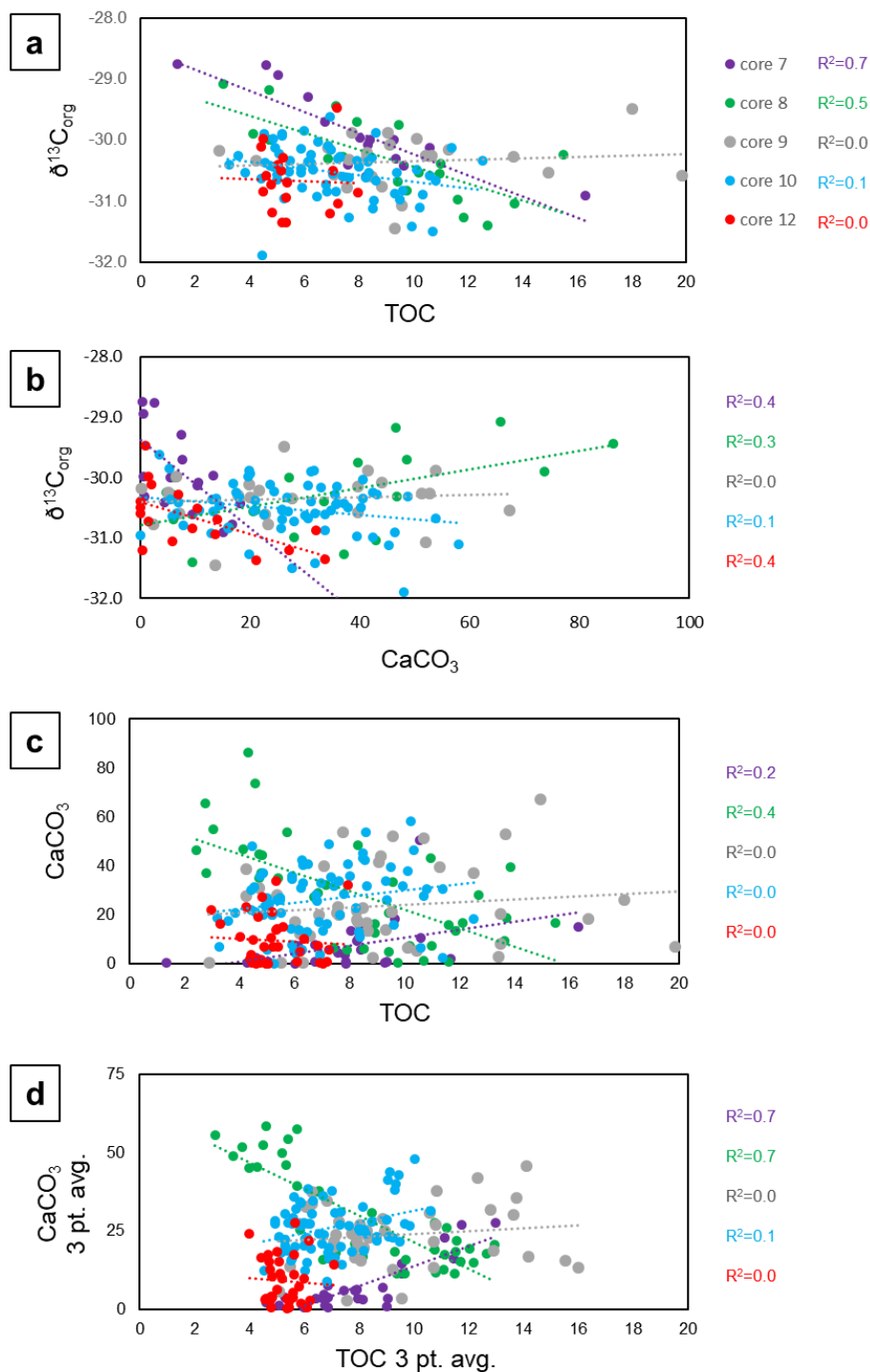
- water derived isoprenoid tetraether lipids on the TEX86H paleothermometer in the Mediterranean Sea. *Geochimica et Cosmochimica Acta* 150, 125–141.
35. König, M., Jokat, W., 2006. The Mesozoic breakup of the Weddell Sea. *Journal of Geophysical Research: Solid Earth* 111, B12102.
  36. Koopmans, M.P., Irene; W., Rijpstra, C., Klapwijk, M.M., de Leeuw, J.W., Lewan, M.D., Damsté, J.S.S., 1999. A thermal and chemical degradation approach to decipher pristane and phytane precursors in sedimentary organic matter. *Organic Geochemistry* 30, 1089–1104.
  37. Koopmans, M. P., Köster, J., Van Kaam-Peters, H. M. E., Kenig, F., Schouten, S., Hartgers, W. A., de Leeuw, J. W., Sinninghe Damsté, J. S., 1996. Diagenetic and catagenetic products of isorenieratene: molecular indicators for photic zone anoxia, *Geochimica et Cosmochimica Acta* 60, 4467–4496.
  38. Lawver, L. A., Sclater, J. G., Meinke, L., 1985. Mesozoic and Cenozoic reconstructions of the South Atlantic. *Tectonophysics* 114, 233–254.
  39. Lee C. T., Jiang H., Ronay E., Minisini D., Stiles J., Neal M., 2018. Volcanic ash as a driver of enhanced organic carbon burial in the Cretaceous. *Scientific reports* 8(1), 1–9.
  40. Leventhal, J. S., 1983. An interpretation of carbon and sulfur relationships in Black Sea sediments as indicators of environments of deposition. *Geochimica et Cosmochimica Acta* 47, 133–137.
  41. Littler, K., Robinson, S.A., Bown, P.R., Nederbragt, A.J., Pancost, R.D., 2011. High sea-surface temperatures during the Early Cretaceous Epoch. *Nature Geoscience* 4(3), 169–172.
  42. Matthews K. J., Maloney K.T., Zahirovic S., Williams S.E., Seton M., Mueller R. D., 2016. Global plate boundary evolution and kinematics since the late Paleozoic. *Global and Planetary Change*. 146, 226–50.
  43. McAnena A, Flögel S, Hofmann P, Herrle JO, Griesand A, Pross J, Talbot HM, Rethemeyer J, Wallmann K, Wagner T., 2013. Atlantic cooling associated with a marine biotic crisis during the mid-Cretaceous period. *Nature Geoscience* 6(7), 558–61.
  44. Meyers, P.A., 1997. Organic geochemical proxies of paleoceanographic, paleolimnologic, and paleoclimatic processes. *Organic Geochemistry* 27, 213–250.
  45. Meyer K. M., Kump L. R., 2008. Oceanic euxinia in Earth history: causes and consequences. *Annu. Rev. Earth Planet.* 36, 251–88.

46. Miller H., 2007. History of views on the relative positions of Antarctica and South America: a 100-year tango between Patagonia and the Antarctic Peninsula. *Antarctica: A Keystone in a Changing World-Online Proceedings of the 10th ISAES*.
47. Mohr B., 1990. Early Cretaceous palynomorphs from ODP Sites 692 and 693, The Weddell Sea, Antarctica. In *Proceedings of the Ocean Drilling Program: Scientific results*, 449.
48. Mutterlose, J., Wise, S. W., 1990. Lower Cretaceous nannofossil biostratigraphy of ODP Leg 113 Holes 692B and 693A, continental slope off East Antarctica, Weddell Sea. In *Proceedings of Ocean Drilling Program: Scientific Results 113*, 325–351.
49. O'Connell S. B., 1990. Sedimentary response to paleoclimate from downhole LOGS at Site 693, Antarctic continental margin. In *proceedings of the Ocean Drilling Program: Scientific Results*, 71.
50. Peters, K.E., Peters, K.E., Walters, C.C., Moldowan, J.M., 2005. *The biomarker guide*. Cambridge university press, 1.
51. Powell, T.G., McKirdy, D.M., 1973. Relationship between ratio of pristane to phytane, crude oil composition and geological environment in Australia. *Nature* 243, 37–39.
52. Raiswell, R., Buckley, F., Berner, R. A., Anderson, T. F., 1988. Degree of pyritization of iron as a paleoenvironmental indicator of bottomwater oxygenation. *Journal of Sedimentary Research* 58, 812–819.
53. Sewall J. V., Van De Wal R.S., Van Der Zwan K., Van Oosterhout C., Dijkstra H. A., Scotese C. R., 2007. Climate model boundary conditions for four Cretaceous time slices. *Climate of the Past* 3(4), 647–57.
54. Sinninghe Damsté, J. S., Kuypers, M. M. M., Schouten, S., Schulte, S., Rullkötter, J., 2003. The lycopane/C31 n-alkane ratio as a proxy to assess palaeoacidity during sediment deposition, *Earth and Planet Science Letters* 209, 215–226.
55. Smith, A. G., Hurley, A. M., Briden, J. J., 1981. *Phanerozoic Paleogeographic World Maps*. Cambridge University Press.
56. Sprovieri, M., Coccioni, R., Lirer, F., Pelosi, N., Lozar, F., 2006. Orbital tuning of a lower Cretaceous composite record (Maiolica Formation, central Italy). *Paleoceanography* 21(4).
57. Stein, R., Rullkötter, J., Welte, D. H., 1986. Accumulation of organic-carbon-rich sediments in the Late Jurassic and Cretaceous Atlantic Ocean—A synthesis, *Chemical Geology* 56, 1–32.

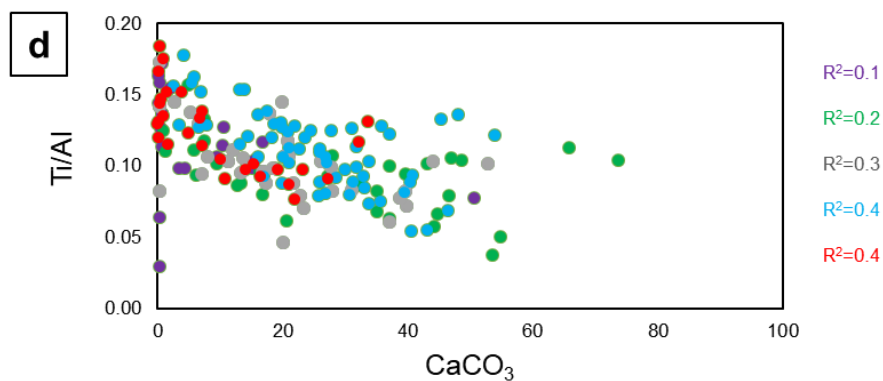
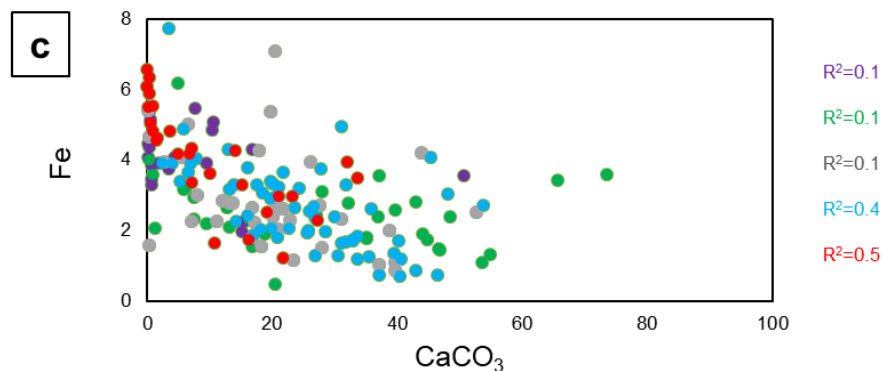
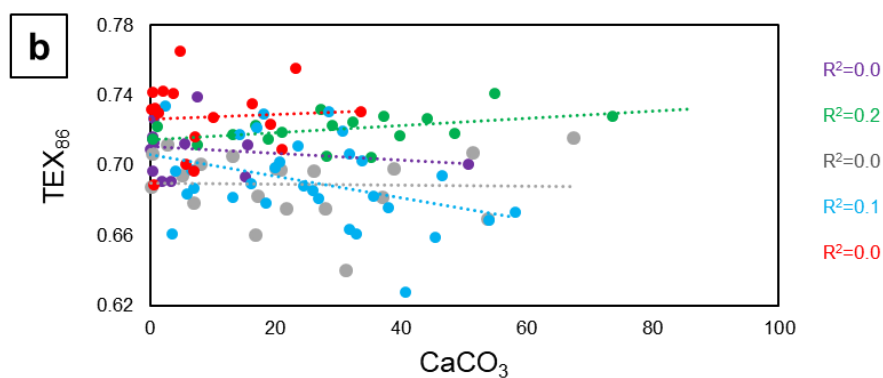
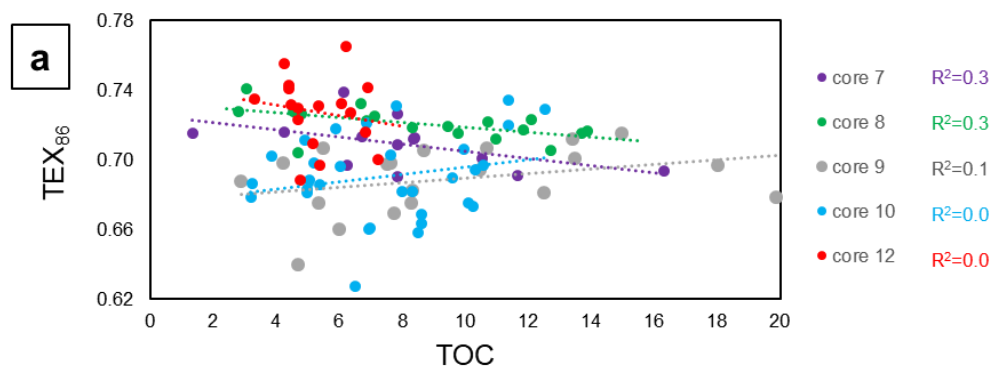


58. Tierney, J.E., Tingley, M.P., 2014. A Bayesian, spatially-varying calibration model for the TEX86 proxy. *Geochimica et Cosmochimica Acta* 127, 83–106.
59. Tierney, J.E., Tingley, M.P., 2015. A TEX 86 surface sediment database and extended Bayesian calibration. *Scientific data* 2(1), 1–10.
60. Uenzelmann-Neben G., Weber T., Grützner J., Thomas M., 2017. Transition from the Cretaceous ocean to Cenozoic circulation in the western South Atlantic—A twofold reconstruction. *Tectonophysics* 716, 225–40.
61. Wagner, T., Pletsch, T., 1999. Tectono-sedimentary controls on Cretaceous black shale deposition along the opening Equatorial Atlantic Gateway (ODP Leg 159). Geological Society, London, Special Publications 153(1), 241–265.
62. Wagner, T., Hofmann, P., Flögel, S., 2013. Marine black shale deposition and Hadley Cell dynamics: A conceptual framework for the Cretaceous Atlantic Ocean, *Marine and Petroleum Geology* 43, 222–238.
63. Wedepohl, K. H., 1971. Environmental influences on the chemical composition of shales and clays. *Physics and Chemistry of the Earth* 8, 307–333.
64. Wedepohl, K. H., 2004. The Composition of Earth's Upper Crust, Natural Cycles of Elements, Natural Resources, in: *Metals and Their Compounds in the Environment*, Merian, E., Anke, M., Ihnat, M., Stoepler, M., Wiley-VCH, Weinheim (Eds.) 3–17.
65. Weissert, H., Erba, E., 2004. Volcanism, CO<sub>2</sub> and palaeoclimate: a Late Jurassic–Early Cretaceous carbon and oxygen isotope record. *Journal of the Geological Society* 161(4), 695–702.
66. Tribouillard, N., Algeo, T. J., Lyons, T., Riboulleau, A., 2006. Trace metals as paleoredox and paleoproductivity proxies: an update. *Chemical Geology* 232, 12–32.
67. Zimmerman, H. B., Boersma, A., McCoy, F. W., 1987. Carbonaceous sediments and paleoenvironment of the Cretaceous South Atlantic Ocean. Geological Society London, Special Publications 26, 271–286.

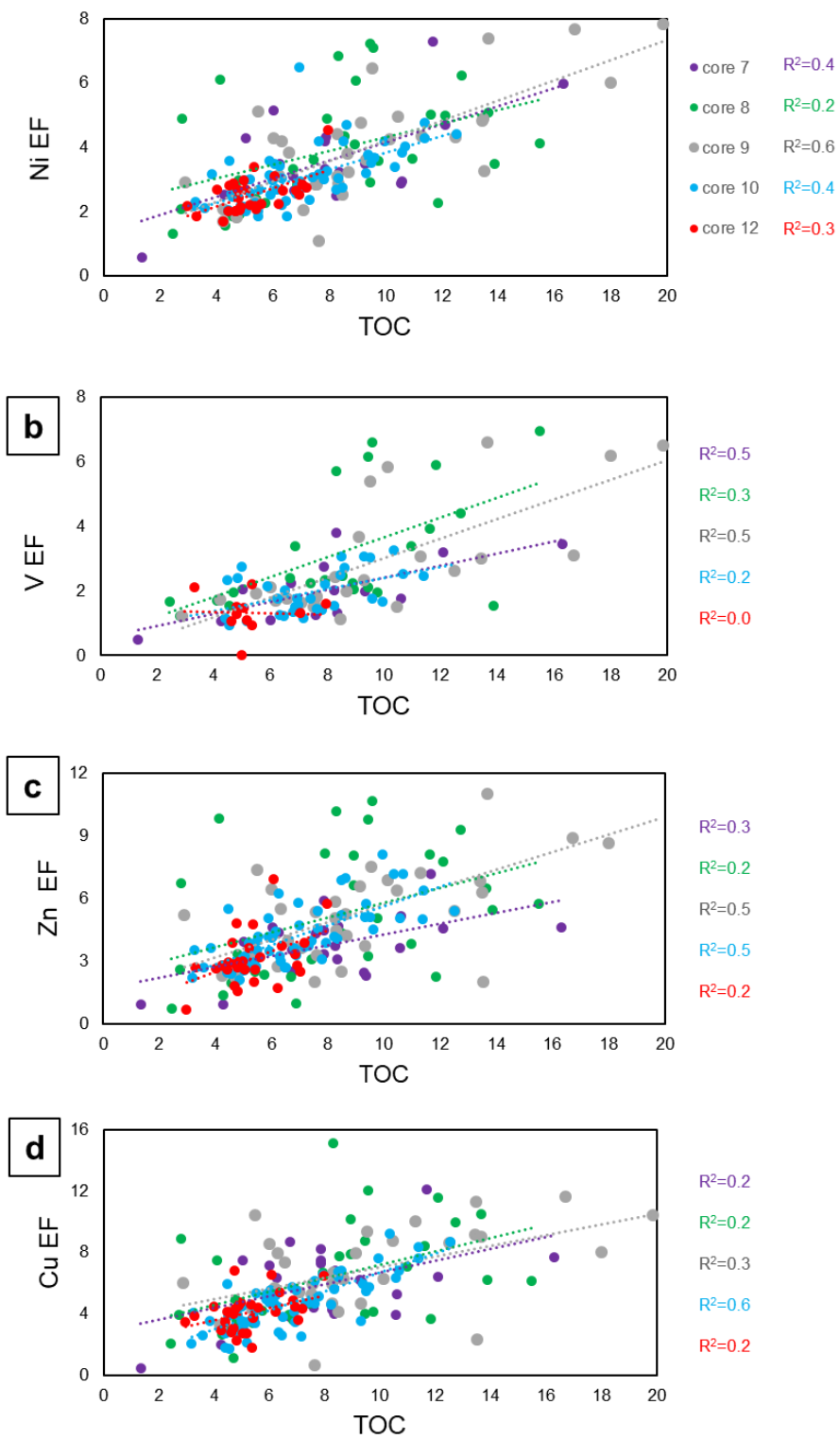
## 8. Data Appendix



**Supplementary Fig. 1 (a):** Cross-plots of stable carbon isotopes measured on bulk organic matter ( $\delta^{13}\text{C}_{\text{org}}$ ) vs. total organic carbon (TOC), and **(b)** vs. calcium carbonate content ( $\text{CaCO}_3$ ). **(c)** Cross-plots of  $\text{CaCO}_3$  vs. TOC, **(d)** and tree point moving average  $\text{CaCO}_3$  vs. TOC.  $R^2$  values of linear trend lines of each core set are reported.



**Supplementary Fig. 2 (a):** Cross-plots of organic paleo-thermometer TEX<sub>86</sub> vs. total organic carbon (TOC), and **(b)** vs. calcium carbonate content (CaCO<sub>3</sub>). **(c)** Cross-plots of Fe vs. CaCO<sub>3</sub>, **(d)** and Ti/Al ratios vs. CaCO<sub>3</sub>. R<sup>2</sup> values of linear trend lines of each core set are reported.



**Supplementary Fig. 3 (a–d):** Cross-plots of redox sensitive trace metal enrichment factor (EF), Ni, V, Zn, and Cu vs. total organic carbon (TOC).  $R^2$  values of linear trend lines of each core set are reported.

---

## 7. Bottom water conditions during the Early Cretaceous at ODP Hole 692B - Weddell Sea (Antarctica) - paleoenvironmental changes through the Weissert Event

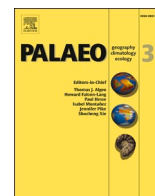
In *Palaeogeography, Palaeoclimatology, Palaeoecology*, 587, 1–02, 2022

<https://doi.org/10.1016/j.palaeo.2021.110795>

**Author(s):** V. M. Giraldo-Gómez, C. Bottini, C. Möller, T. Wagner, O. Esegbue, L. Cavalheiro, M. R. Petrizzo, G. Gambacorta

### Abstract

Benthic foraminifera at the Ocean Drilling Program (ODP) Hole 692B were studied to characterize changes of the oxygen and organic-matter fluxes, and their relationships to paleoceanographic changes in the bottom waters during the Early Cretaceous. The upper Berriasian/lower Valanginian – lower Barremian black shales recovered at ODP Hole 692B are characterized by high values of the total organic carbon (TOC) ranging between 1.3 and 18%, and the benthic foraminiferal assemblages suggest a depositional setting corresponding to an outer neritic-upper bathyal environment (~200 – 500 m). Benthic foraminiferal assemblages recorded throughout ODP Hole 692B show fluctuation of the benthic foraminiferal numbers (BFN) and/or the diversities indices (D: Dominance and H<sub>s</sub>: Shannon) suggestive of paleoenvironmental changes at the seafloor. The most dominant taxa recorded at ODP Hole 692B are the infaunal genus *Eoguttulina* and the epifaunal-infaunal taxa *Lenticulina*, *Laevidentalina*, *Saracenaria*, and *Marginulina*. The increases of the infaunal taxa are related to the decrease of the epifaunal-infaunal taxa that show a peculiar distribution pattern through the analyzed samples. Genera of both morphogroups (infaunal and epifaunal-infaunal) are characterized by thriving under depleted-oxygen conditions and high organic-matter fluxes. Low abundances and diversities of benthic foraminifera during the upper Berriasian/lower Valanginian to the lower Barremian indicate strongly dysoxic-anoxic conditions. A slight increase in the oxygenation is experienced at the seafloor during the upper part of the upper Valanginian after a short period of deprivation of benthic foraminifera during the Weissert Event. It is suggested that oxygen availability is the dominant environmental factor in the bottom waters, whereas the organic flux played a secondary role in the seafloor in controlling the benthic foraminiferal distribution during the Early Cretaceous.



# Bottom water redox dynamics during the Early Cretaceous Weissert Event in ODP Hole 692B (Weddell Sea, Antarctica) reconstructed from the benthic foraminiferal assemblages

Victor M. Giraldo-Gómez<sup>a,\*</sup>, Maria Rose Petrizzo<sup>a</sup>, Cinzia Bottini<sup>a</sup>, Carla Möller<sup>a,c</sup>, Thomas Wagner<sup>b</sup>, Liyenne Cavalheiro<sup>a,b</sup>, Onoriode Esegbue<sup>b,e</sup>, Gabriele Gambacorta<sup>d</sup>, Elisabetta Erba<sup>a</sup>

<sup>a</sup> Università degli Studi di Milano, Dipartimento di Scienze della Terra "Ardito Desio", Via Mangiagalli 34, 20133 Milano, Italy

<sup>b</sup> Lyell Centre, Heriot-Watt University, EH14 4AP Edinburgh, UK

<sup>c</sup> Ruhr - University Bochum, Institute for Geology, Mineralogy and Geophysics, Universitätsstraße 150, 44801 Bochum, Germany

<sup>d</sup> Eni S.p.A. Natural Resources - Geology and Geophysics Research and Technological Innovation, Milan, Italy

<sup>e</sup> Newcastle University, School of Natural and Environmental Sciences, NE1 7RU Newcastle upon Tyne, UK

## ARTICLE INFO

Editor: Isabel Montanez

### Keywords:

Benthic foraminifera  
Early Cretaceous  
Weissert event  
Bottom-water redox  
Paleoceanography  
Antarctica

## ABSTRACT

Benthic foraminifera at Ocean Drilling Program (ODP) Hole 692B were studied to understand variations in oxygen and organic-matter fluxes in bottom waters during the Early Cretaceous. The upper Berriasian to lower Barremian black shales, characterized by high concentrations of total organic carbon (TOC) ranging between 1.3 and 18%, were deposited in an outer neritic-upper bathyal environment (~200–500 m) according to benthic foraminifera assemblages. A new high-resolution record of benthic foraminiferal assemblages of high-latitude, dominated by infaunal taxa (*Citharina*, *Eoguttulina*, *Laevidentalina*, *Lagena*, *Lenticulina*, *Marginulina*, *Nodosaria*, *Planularia*, *Saracenaria*, and *Vaginulinopsis*), is described in depleted-oxygen and high organic-carbon flux conditions.

Extremely dysoxic conditions are recorded at the onset of the carbon isotope excursion (CIE) marking the Weissert Event (late Valanginian), followed by a period of anoxic conditions in bottom waters. A repopulation event of benthic foraminifera, linked to an increase in oxygen concentrations, coincided with the global cooling episode that characterized the late part of the Weissert Event.

Subsequently, there were short periods in the late Valanginian and the late early Hauterivian when the bottom waters experienced increased oxygen concentrations. Possibly, bottom currents related to the influx of Southern Ocean waters favored short-term pulses of ventilation under constant increased organic-carbon flux during the late Valanginian and late Hauterivian.

## 1. Introduction

The Early Cretaceous represents a greenhouse period with phases of high atmospheric CO<sub>2</sub> concentrations and high global mean temperatures (Royer et al., 2007; Littler et al., 2011). However, multiproxy studies (e.g., Weissert and Erba, 2004; O'Brien et al., 2017; Bottini and Erba, 2018) have shown significant climate variability associated with global oceanic anoxic events (OAEs), the emplacement of large igneous

provinces and the opening or closure of oceanic gateways.

As evidenced by different proxies, the response of the biota unravels the changes in disturbed and stable environments of the oceanic biosphere. Records from high paleolatitudes and restricted basins are of particular relevance, as they provide new evidence about biotic reactions to regional and global changes.

During the Cretaceous, the accumulation of organic-rich strata (black shale) was recorded both in epicontinental seas and oceanic

\* Corresponding author.

E-mail addresses: [victor.giraldo@unimi.it](mailto:victor.giraldo@unimi.it) (V.M. Giraldo-Gómez), [mrose.petrizzo@unimi.it](mailto:mrose.petrizzo@unimi.it) (M.R. Petrizzo), [cinzia.bottini@unimi.it](mailto:cinzia.bottini@unimi.it) (C. Bottini), [carla.moeller@rub.de](mailto:carla.moeller@rub.de) (C. Möller), [t.wagner@hw.ac.uk](mailto:t.wagner@hw.ac.uk) (T. Wagner), [liyenne.cavalheiro@unimi.it](mailto:liyenne.cavalheiro@unimi.it) (L. Cavalheiro), [onoriode.esegbue@newcastle.ac.uk](mailto:onoriode.esegbue@newcastle.ac.uk) (O. Esegbue), [gabriele.gambacorta@eni.com](mailto:gabriele.gambacorta@eni.com) (G. Gambacorta), [elisabetta.erba@unimi.it](mailto:elisabetta.erba@unimi.it) (E. Erba).

<https://doi.org/10.1016/j.palaeo.2021.110795>

Received 22 July 2021; Received in revised form 9 December 2021; Accepted 9 December 2021

Available online 17 December 2021

0031-0182/© 2021 Elsevier B.V. All rights reserved.

basins (Arthur and Sageman, 1994), and was used to define Oceanic Anoxic Events (OAEs) that implied oxygen-depletion of intermediate and bottom-waters, promoting enhanced burial of organic matter on a global scale (Schlanger and Jenkyns, 1976; Arthur and Schlanger, 1979; Arthur et al., 1990). During the Valanginian, a major environmental change is evidenced from a positive  $\delta^{13}\text{C}$  excursion (CIE) named the Weissert Event by Erba et al. (2004). The event was associated with multiple climatic and paleoceanographic changes (e.g., Weissert, 1989; Erba et al., 2004; Westermann et al., 2010; Meissner et al., 2015), which probably were triggered by volcanic activity of the Paraná-Etendeka Large Igneous Province (LIP) (Erba et al., 2004, 2019; Weissert and Erba, 2004; Sprovieri et al., 2006; Thiede and Vasconcelos, 2010; Gréselle et al., 2011; Martínez et al., 2015).

In this study, we analyze benthic foraminiferal assemblages in the upper Berriasian - lower Barremian section recovered at Ocean Drilling Program (ODP) Hole 692B drilled in the Weddell Sea (Fig. 1), intending to characterize the paleoceanographic changes that occurred in a basin formed during the initial separation of Antarctica from Gondwana. During the Early Cretaceous, Antarctica was the centerpiece of a large landmass extending from South America across the southern latitudes to Australasia (Zinsmeister, 1987). From Hauterivian times, an incipient separation began between Antarctica and Madagascar-India, which finished during the mid-Cretaceous (Wilford and Brown, 1994). Meanwhile, the Southern Ocean (Atlantic and SW Indian oceans) was characterized by extensive continental shelves and deeper basins (Fig. 1).

Benthic foraminifera in ODP Hole 692B were described by the Shipboard Scientific Party of ODP Leg 113 (Barker and Kennett, 1988), in which a few analyzed samples were interpreted to be characterized by low levels of bottom water oxygen in a middle bathyal (500–1000 m) paleobathymetric setting (Barker and Kennett, 1988).

We conducted a high-resolution study of the benthic foraminiferal assemblages of the upper Berriasian to lower Barremian interval integrated with stable carbon isotope and total organic carbon data. For that, we used a revised chronostratigraphic framework based on calcareous nannofossil biostratigraphy. (Cavalheiro et al., 2021). The primary aims of this study are the identification of: 1) quantitative changes in benthic foraminiferal assemblages to derive oxygen and organic-matter fluxes to the seafloor; 2) the paleobathymetric setting; 3) the paleoecological preferences of benthic foraminifera; and thus, paleoenvironmental changes in bottom water conditions before, during and after the Weissert Event.

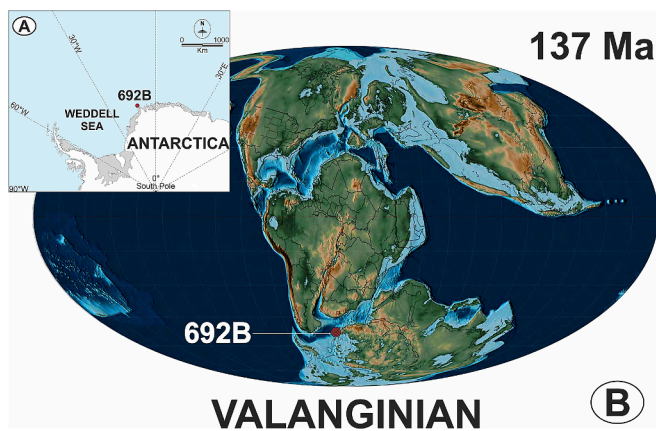


Fig. 1. A. Location of ODP Hole 692B in the Weddell Sea, Antarctica. B. Paleogeographic reconstruction of the Gondwana continent during the Valanginian (137 Ma), showing the position of ODP Hole 692B along the Antarctica margin (modified from Scotese, 2014).

## 2. Material and methods

### 2.1. ODP Hole 692B

ODP Hole 692B is located in the Weddell Sea (70°43.432'S, 13°49.195'W, East Antarctica) at water depth of 2875 m (Fig. 1A, B) and was cored for a total length of 97.9 m with only 30% (29.3 m) of sediment recovery due to operational problems (Barker and Kennett, 1988).

Cretaceous sedimentary rocks corresponding to Unit III (cores 113-692B-7R to 113-692B-12R; Barker and Kennett, 1988) are characterized from top to bottom (Fig. 2) by common claystone (core 113-692B-7R), mixed sedimentary rocks composed of ash and nannofossil-bearing claystone, organic and nannofossil-bearing mudstone, organic-bearing muddy nannofossil chalk, carbonate-bearing nannofossil claystone and mudstone (cores 113-692B-8R to 113-692B-10R), and carbonate-bearing and nannofossil-bearing clayey mudstone (core 113-692B-12R). Moreover, volcanic beds, layers, and lenses with a high percentage of carbonate are recorded commonly through Unit III (Barker and Kennett, 1988).

### 2.2. Calcareous nannofossils

A total of 112 samples were examined for calcareous nannofossil biostratigraphy in the interval between 93 mbsf (meters below seafloor) (sample 113-692B-12R, CC) and 53.53 mbsf (sample 113-692B-7R-1, 32 cm) (see Supplementary data, Table S1). Samples were prepared using a simple smear slide technique: a small piece of rock was powdered, adding a few drops of bi-distillate water without centrifuging, ultrasonic cleaning, or settling the sediment, thus retaining the original rock composition. Investigations were performed with a polarizing light microscope at 1250 X magnification. Since calcareous nannofossil assemblages in ODP Hole 692B include a combination of high latitude taxa, cosmopolitan species, and a few Tethyan species (Mutterlose and Wise Jr, 1990), biostratigraphy has been derived regarding standard zonation schemes for the Boreal Realm (BC zonation after Bown et al., 1988) and the Tethys Ocean (NC zonation after Bralower et al., 1995).

### 2.3. Geochemistry ( $\delta^{13}\text{C}_{\text{org}}$ and TOC)

A total of 143 samples, including a published data set (Cavalheiro et al., 2021), were analyzed for bulk organic stable carbon isotope ratios ( $\delta^{13}\text{C}_{\text{org}}$ ) by Europa Scientific Elemental Analyser - Isotope Ratio Mass Spectrometry (EA - IRMS). Analysis was carried out at Iso-Analytical, Crewe Cheshire (UK). Measurements of the TOC content of 67 samples were also carried out along with  $\delta^{13}\text{C}_{\text{org}}$  analysis. Repeated analysis on reference materials (e.g., IAEA-CH-6, IA-R001, IA-R005 and IA-R006) and duplicate sample measurements yielded a standard deviation <0.1. Carbon isotope and TOC results are reported in the standard Vienna Pee Dee Bee  $\delta$  notation (VPDB) and weight percentage (%), respectively.

### 2.4. Benthic foraminifera

A total of 69 samples (from samples 113-692B-7R-1, 42–45 cm to 113-692B-12R-3, 112–115 cm; Supplementary data, Table S2) of about 3–17 g in weight (an average of 7 g/sample) were processed to obtain washed residues using hydrogen peroxide ( $\text{H}_2\text{O}_2$ ). Samples were washed under tap water through different sieves (meshes of 355  $\mu\text{m}$ , 250  $\mu\text{m}$ , 125  $\mu\text{m}$ , and 63  $\mu\text{m}$ ). Because of the small size of the samples, all residues of the size-fractions >63  $\mu\text{m}$  were picked for benthic foraminifera (BF) and, when possible, at least 200 specimens were picked, identified, counted, and permanently stored in Plummer slides. The abundance of radiolaria, calcispheres, and pyrite observed in the washed residues are reported in Supplementary data, Table S2.

Benthic foraminiferal numbers (BFN) were calculated for the >63  $\mu\text{m}$  size fraction as specimens per 10 g of dry sediment (n/10 g). Based on

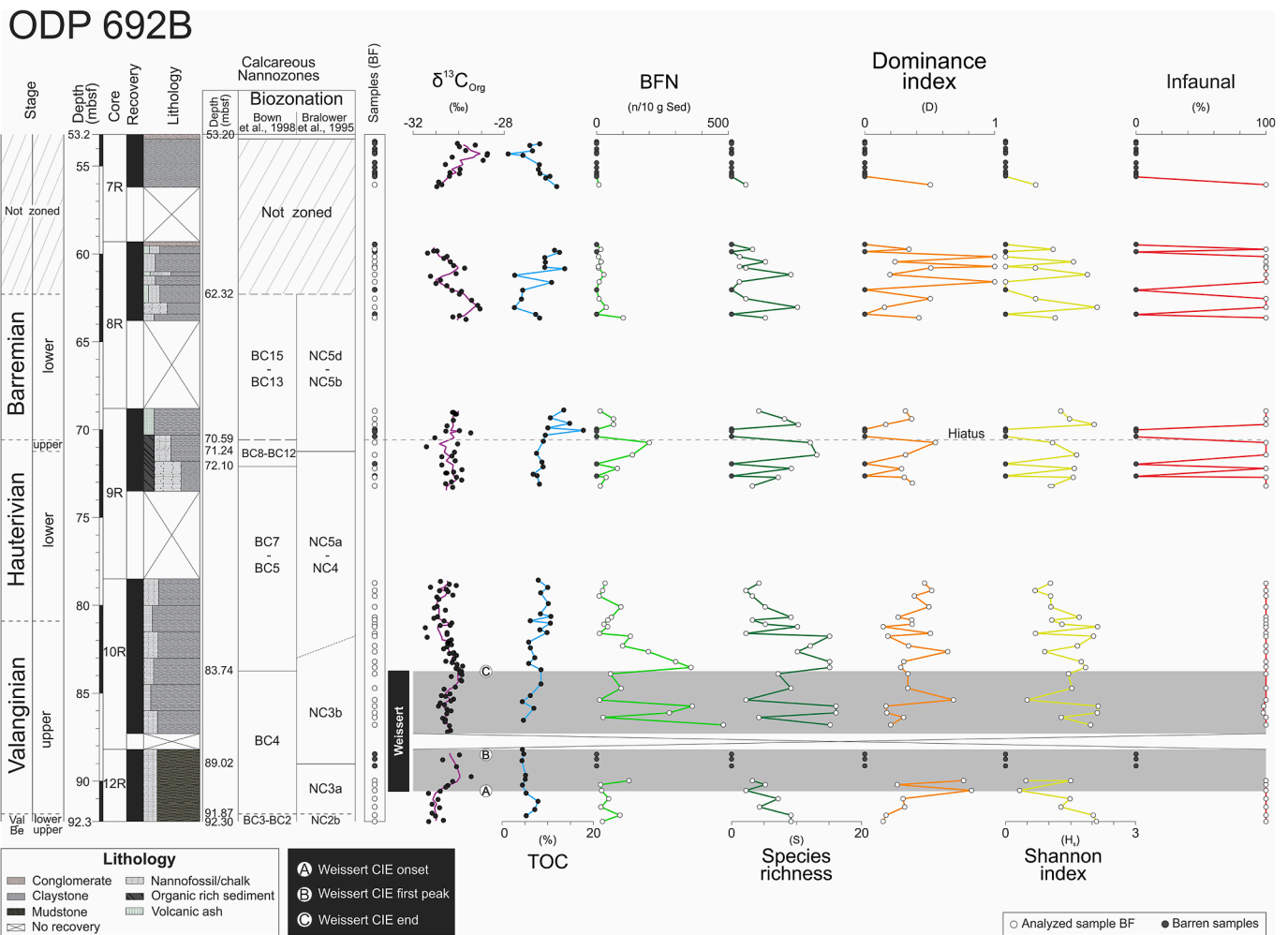


**Fig. 2.** Lithological, geochemical, and benthic foraminiferal assemblage data from ODP Hole 692B: benthic foraminiferal numbers (BFN), species richness (S), dominance (D), Shannon Index ( $H_s$ ), and infaunal morphogroup of benthic foraminifera. Lithology according to Barker et al. (1988). Age and calcareous nannofossils biozonation from this study and Cavalheiro et al. (2021). Organic carbon isotopes ( $\delta^{13}C_{Org}$ ), total organic carbon (TOC), the position of the Weissert Event (grey band) and peaks A, B, C are according to Cavalheiro et al. (2021).

the counts of BF, three faunal indices were calculated for all samples as follows: 1) species richness (S), which is the number of different species in a community, 2) dominance (D) is the degree to which a taxon is more or less abundant in a community (Abundant:  $D = 0$ ; scarce:  $D = 1$ ), and 3) Shannon diversity index ( $H_s$ ) that measures the heterogeneity of a population, taking into account the evenness of species abundances (Shannon and Weaver, 1949).

Statistical analyses were applied using the PAST software 3.1 (Hammer et al., 2001). A non-metric multidimensional scaling (NMDS; Q-mode) and a detrended correspondence analysis (DCA; R-mode) were performed on the abundance data of benthic foraminifera to reconstruct environmental changes. The NMDS and DCA are based on the Bray-Curtis similarity index (in two dimensions - samples) and the Pearson correlation (in two dimensions - taxa), respectively.

Taxa were subdivided into morphogroups according to their ecological preferences, specifically infaunal and epifaunal (e.g., Koutsoukos, 1989; Murray, 1991; Jorissen et al., 2007). Although some opportunistic foraminifera are characterized by their high adaptive capacity to live on top (epifauna) or within (infauna) of the uppermost centimeter of the sediment (e.g., Koutsoukos, 1989; Kaminski et al., 1995; Erbacher et al., 1998; Holbourn et al., 2001a; Friedrich et al., 2003, 2009), we have inferred in this study that most of the benthic foraminifera assemblages are dominated by taxa with infaunal preferences.

The marker species, BFN,  $H_s$  and D were used to reconstruct the oxygen availability and increases/decreases in organic carbon fluxes in bottom waters (e.g., Koutsoukos, 1989; Jorissen et al., 1995; van der Zwaan et al., 1999; Holbourn et al., 2001b; Friedrich et al., 2003; Friedrich and Hemleben, 2007).

The paleo-bathymetric subdivisions used in this study are according to Nyong and Olsson (1984) and van Morkhoven et al. (1986). They are inner-neritic (IN: 0–50 m), middle-neritic (MN: 50–100 m), outer-neritic (ON: 100–200 m), upper bathyal (UB: 200–500 m), middle bathyal (MB: 500–1000 m), and lower bathyal (LB: 1000–2000 m). The bottom water-oxygenation has been evaluated as anoxic (without detectable oxygen concentration) and dysoxic (with some oxygen concentration) following Jorissen et al. (2007). The dysoxic conditions were subdivided into three categories, according to the increase and decrease of the abundances (BFN) and diversity indices ( $H_s$  and D) of benthic foraminifera, allowing interpretation of the oxygen availability in the bottom waters as follows: extremely dysoxic (low BFN and  $H_s$ , high D), severely dysoxic (low BFN and  $H_s$ , moderate D) and moderately dysoxic (high BFN and  $H_s$ , moderate to low D). For this interpretation, we identify a range of values for each variable (BFN,  $H_s$ , and D) to constrain the categories (low, moderate, and high) as follow: BFN (minimum value: 1 specimen - maximum value: 500 specimens): low values: 1–166 specimens; moderate values: 167–333 specimens; high values: 334–500 specimens;  $H_s$  (minimum value: 0 - maximum value: 3): low values: 0–1;



moderate values: 1–2; high values: 2–3; D (minimum value: 0 - maximum value: 1): low values: 0–0.33; moderate values: 0.34–0.66; high values: 0.67–1.

The most important taxa identified in ODP Hole 692B were photographed using the Scanning Electron Microscopy (SEM - Jeol JSM-IT500) at the Department of Earth Sciences “A. Desio” of the Università degli Studi di Milano.

### 3. Results

#### 3.1. Calcareous nannofossil biostratigraphy

The new calcareous nannofossil biostratigraphy of ODP Hole 692B allowed a revision of the age assignment by Mutterlose and Wise Jr (1990) for the stratigraphic interval comprised between 93 mbsf and 53.53 mbsf, initially interpreted to be Valanginian- Hauterivian. The revised calcareous nannofossil biostratigraphy applies the chronostratigraphic framework of the Berriasian - Barremian interval reported in Cavalheiro et al. (2021). Calcareous nannofossil assemblages (Supplementary Fig. S1, Table S1) contain relatively diverse and moderate to well-preserved specimens. The nannoflora is dominated by a few species, most prominently *Watznaueria barnesiae*, and in the interval between 91.87 mbsf (sample 113-692B-12R-3, 65–68 cm) and 80.52 mbsf (sample 113-692B-10R-2, 50–54 cm), *Biscutum constans* and *Crucibiscutum salebrosum*. A few barren samples were detected in core 12R (91.31, 90.57, 90.42, 89.4, 89.22, 88.93, 88.78 and 88.50 mbsf), in core 8R (59.67 mbsf) and in core 7R (55.23, 54.31, 53.87, and 53.2 mbsf). The topmost part of the investigated section, from 61.91 mbsf (113-692B-8R-2, 12–14 cm) to 53.2 mbsf, is characterized by poorly preserved and scarce nannofossils (Fig. 2).

The lowermost studied sample at 93 mbsf (sample 113-692B-12R-CC) is not older than late Berriasian and corresponds to Zone BC2 (Bown et al., 1988) and subzone NC2b (Bralower et al., 1995) is characterized by the presence of the boreal taxon *Crucibiscutum ryazanicum* and the Tethyan taxon *Percivalia fenestrata*.

The interval 93–91.87 mbsf (sample 113-692B-12R-3, 65–68 cm) is attributed to the late Berriasian - early Valanginian (Zones BC2-BC3 and NC2b). A more precise age assignment of this interval is not possible due to the absence of Boreal (i.e. *Triquetrorhabdulus shetlandensis* and *Michrantolitus speetonensis*) and Tethyan (i.e. *Calcicalathina oblongata*) marker species for the base of the Valanginian. The first occurrence (FO) of *Zeugrhabdodus trivectis* at 91.87 mbsf that shortly precedes the onset of the positive  $\delta^{13}\text{C}$  isotopic excursion of the Weissert Event was also identified in worldwide sections (Kessels et al., 2006; Duchamp-Alphonse et al., 2007; Barbarin et al., 2012; Charbonnier et al., 2013; Aguado et al., 2018; see Cavalheiro et al., 2021 for further discussion) and indicates subzone NC3a and Zone BC4.

The base of subzone NC3b is identified at the last occurrence (LO) of *Rucinolitus wisei* detected at 89.02 mbsf (sample 113-692B-12R-1, 80–83 cm), suggestive of a late Valanginian age. In ODP Hole 692B, the LO of *R. wisei* correlates with the early phase of the Weissert Event similarly to other records worldwide (SE France: Duchamp-Alphonse et al., 2007, Charbonnier et al., 2013; Central Atlantic: Bornemann and Mutterlose, 2008; and SE Spain: Aguado et al., 2018).

Disarticulated elements of possible *Micrantholitus speetonensis* were found in ODP Hole 692B in the interval between 84.03 mbsf (sample 113-692B-10R-4, 101–104 cm) and 83.74 mbsf (sample 113-692B-10R-4, 73–75 cm) in correspondence with the topmost part of the CIE. This finding is consistent with the recent revision of the LO of *M. speetonensis*, placed in the late Valanginian, close to the topmost part of the Weissert Event (Möller et al., 2015). The LO of *M. speetonensis* marks the base of Zone BC5 and the NC3/NC4 zonal boundary is tentatively placed between 82 mbsf and 83 mbsf just above the CIE of the Weissert Event following the inter-calibration of *Tubodiscus veranae* (absent in ODP Hole 692B) concerning the chemo- and magneto-stratigraphy (see Cavalheiro et al., 2021 for further discussion).

The absence of low and high latitude markers such as *Tubodiscus veranae* (Bralower et al., 1995) and *Triquetrorhabdulus shetlandensis* and/or *Eprolithus antiquus* (Bown et al., 1988), respectively, makes the identification of the Valanginian/Hauterivian boundary not straightforward in ODP Hole 692B. Since in the literature, the last common occurrence (LCO) of *Cyclagelosphaera deflandrei* was documented in the latest Valanginian after the LO of *T. veranae*, within subzone NC4a and close to the Valanginian/Hauterivian boundary (Roth, 1983; Thierstein, 1976; Erba and Quadrio, 1987), the Valanginian/Hauterivian boundary is here constrained using the LCO of *C. deflandrei* detected at 80.98 mbsf (sample 113-692B-10R-2, 96–99 cm). Moreover, in ODP Hole 692B, the LCO of *C. deflandrei* is above the CIE of the Weissert Event, thus, in the equivalent stratigraphic position reported in several works (e.g., Channell et al., 1993; Roth, 1983; Littler et al., 2011; Applegate and Bergen, 1988; Kessels et al., 2006).

The FO of *Tranolithus octiformis* at 72.10 mbsf (sample 113-692B-9R-3, 29–31 cm) marks the base of Zone BC8 (Bown et al., 1988). This event is shortly followed by the FO of *Rucinolitus terebrodentarius* at 71.24 mbsf (sample 113-692B-9R-2, 92–95 cm), which defines the base of subzone NC5b (Bralower et al., 1995), indicating a late Hauterivian age (Supplementary Fig. S1).

A distinctive change in the nannofossil assemblage composition is detected at 70.59 mbsf (sample 113-692B-9R-2, 27–30 cm): *C. salebrosum* is no longer present, while *Cyclagelosphaera margerelii* is frequent-common and, from 69.28 mbsf upwards (sample 113-692B-9R-1, 47–49 cm), *Watznaueria britannica* is also frequent. *Diazomatolithus lehmanii* is present up to 62.32 mbsf (sample 113-692B-8R-3, 1–3 cm), where its LCO is detected (Supplementary Fig. S1). In the biozonation of Bown et al. (1988) and boreal records (Jeremiah, 2001), abundant *C. margerelii* is recorded in the late early Barremian within Zones BC13 and BC14, together with relatively frequent *W. britannica* (Bown et al., 1988; Jeremiah, 2001). The LCO of *D. lehmanii* is reported in Zone BC15 (Bown et al., 1988; Jeremiah, 2001).

We, therefore, interpret the nannoflora assemblages detected in ODP Hole 692B between 70.59 and 62.32 mbsf to correspond to Zones BC13 - BC15 of Bown et al. (1988). In the same interval, low latitude marker species are absent, and thus the identification of Zones NC5b to NC5d (Bralower et al., 1995) was based on the Boreal-Tethyan correlation of Bown et al. (1988). The sharp change in nannofossil assemblages and the marked thin thickness of the upper Hauterivian stratigraphic interval suggest a hiatus at 70.59 mbsf, probably eliding part of the late Hauterivian. Samples from 61.91 mbsf to the top of the studied interval are barren of nannofossils or contain very rare *W. barnesiae* specimens, making the age determination impossible.

#### 3.2. $\delta^{13}\text{C}_{\text{org}}$ and TOC

$\delta^{13}\text{C}_{\text{org}}$  values recorded in ODP Hole 692B range between  $-31.9$  and  $-28.7\text{‰}$  (from sample 113-692B-12R-3, 112–115 cm to 113-692B-7R-1, 42–45 cm, 92.34 to 53.65 mbsf in Fig. 2). As detailed in Cavalheiro et al. (2021), the lower portion of the studied section documents the positive CIE that identifies the Valanginian Weissert Event that is comprised between the top of calcareous nannofossil subzone NC3a and the top of subzone NC3b of Bralower et al. (1995) and Zone BC4 of Bown et al. (1988) (see the chronostratigraphic revision in Cavalheiro et al., 2021) (Fig. 2). Following the original definition by Erba et al. (2004), the onset of the Weissert Event is placed at the base of the positive CIE (sample 113-692B-12R-2, 71–73 cm; 90.57 mbsf; A in Fig. 2) and the end of the event coincides with the top of the CIE plateau (sample 113-692B-10R-4, 61–65 cm; 83.63 mbsf; C in Fig. 2) (Cavalheiro et al., 2021). Carbon isotope values are relatively stable in the Hauterivian - lowermost Barremian interval in core 9R, documenting average values of  $\sim -30\text{‰}$ . Notably, relevant fluctuations of about 2‰ are documented in the topmost intervals in cores 8R (early Barremian in age) and 7R (no age assignment).

The total organic carbon (TOC) values in ODP Hole 692B range from

1.3 to 18%, with an average of 8.0% (Fig. 2). The highest TOC values, up to 14.9–18% (samples 113-692B-9R-1, 92–95 cm and 113-692B-9R-1, 132–135 cm, respectively), are observed in the middle part of the section (Hauterivian - lower Barremian). The lowest TOC content (e.g., 1.3% in sample 113-692B-7R-1, 101–103 cm) is recorded in the topmost stratigraphic interval (core 7).

### 3.3. Benthic foraminifera

Twenty-two out of 69 samples are barren of BF and, therefore, quantitative analyses were performed on 47 samples that contained scarce (especially in cores 113-692B-7R, 113-692B-8R, and 113-692B-9R) to abundant BF assemblages (Figs. 2, 3), which are composed only of calcareous benthic foraminifera (Figs. 2–4).

The preservation of BF is good throughout the studied section (Fig. 4). Nevertheless, some tests show moderate etching, suggesting dissolution or slight overgrowth and breakages (especially in samples 113-692B-9R-2, 45–48 cm, 113-692B-9R-1, 60–63 cm, 113-692B-9R-2, 10–13 cm, and 113-692B-10R-6, 39–42 cm). A possible explanation for the diagenetic alteration in terms of dissolution is related to early post-depositional changes in pore water chemistry, which provoke an imbalance with the foraminiferal tests (Murray and Alve, 1999; Kozdon et al., 2013).

The BFN vary between 1 and 481 specimens/10 g of dry sediment (Fig. 2). The highest BFN (481 specimens /10 g sed) is found in the upper Valanginian (sample 113-692B-10R-6, 82–85 cm) coinciding with the middle part of the Weissert Event, while the lowest BFN value (1 n/10 g

sed) is recorded at 60.73 mbsf (sample 113-692B-8R-1, 143–146 cm; Fig. 2). The S reaches a high value of 16 taxa in the upper Valanginian (samples 113-692B-10R-5, 125–128 cm and 113-692B-10R-6, 13–16 cm) and the middle part of the Weissert Event (Fig. 2). The D values are highest (=1) in the Barremian (samples 113-692B-8R-1, 87–90 cm, 692B-8R-1, 143–146 cm and 113-692B-8R-2, 80–83 cm; Fig. 2), in which the H<sub>S</sub> recorded the lowest values (0). The lowest value of D (=0.13) is detected in the upper Berriasian/lower Valanginian (sample 113-692B-12R-3, 112–115 cm). The highest value of H<sub>S</sub> (2.14) was recorded in the upper Valanginian (sample 113-692B-10R-5, 125–128 cm; Fig. 2).

Thirty-three BF taxa (12 genera and 28 species; Supplementary Table S2) were identified in the upper Berriasian to lower Barremian stratigraphic interval in ODP Hole 692B (Fig. 3). The most abundant taxa are represented by the genus *Eoguttulina* (*Eoguttulina bilocularis*, *Eoguttulina biserialis*, *Eoguttulina fusus*, *Eoguttulina guttifera*), ranging from 1 specimen/10 g (in samples at 92.32 mbsf, 79.48 mbsf, 61.19 mbsf, and 60.81 mbsf) to 205 specimens/10 g (at 83.55 mbsf). *Eoguttulina bilocularis* is the most abundant species in the BF assemblages, fluctuating from 0.39% (at 85.75 mbsf) to 90.00% (at 90.55 mbsf) (Fig. 3).

The absolute abundance of *Lenticulina* (*Lenticulina* sp. 1., *Lenticulina involvens*, *Lenticulina lideri*, *Lenticulina pulchella*, *Lenticulina turgidula*) ranges from 1 specimen/10 g (samples at 91.49 mbsf, 85.40 mbsf, and 70.75 mbsf) to 319 specimens/10 g (at 86.82 mbsf; Fig. 3). The most abundant species is *L. turgidula*, which varies from 0.48% (at 70.75 mbsf) to 33.33% (91.02 mbsf; Fig. 3).

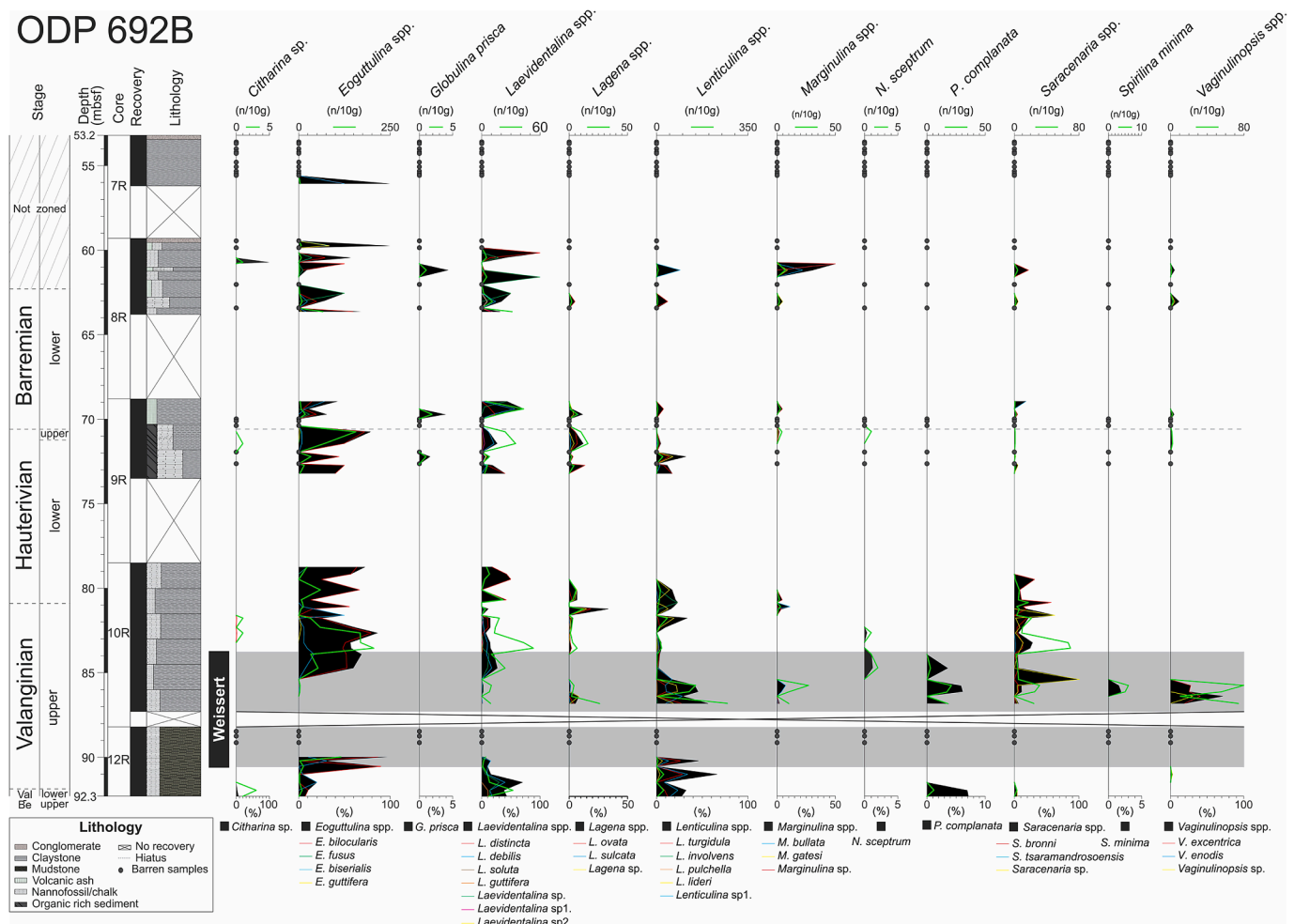


Fig. 3. Absolute and relative abundances of the most important benthic foraminiferal taxa in ODP Hole 692B. Lithology according to Barker et al. (1988).

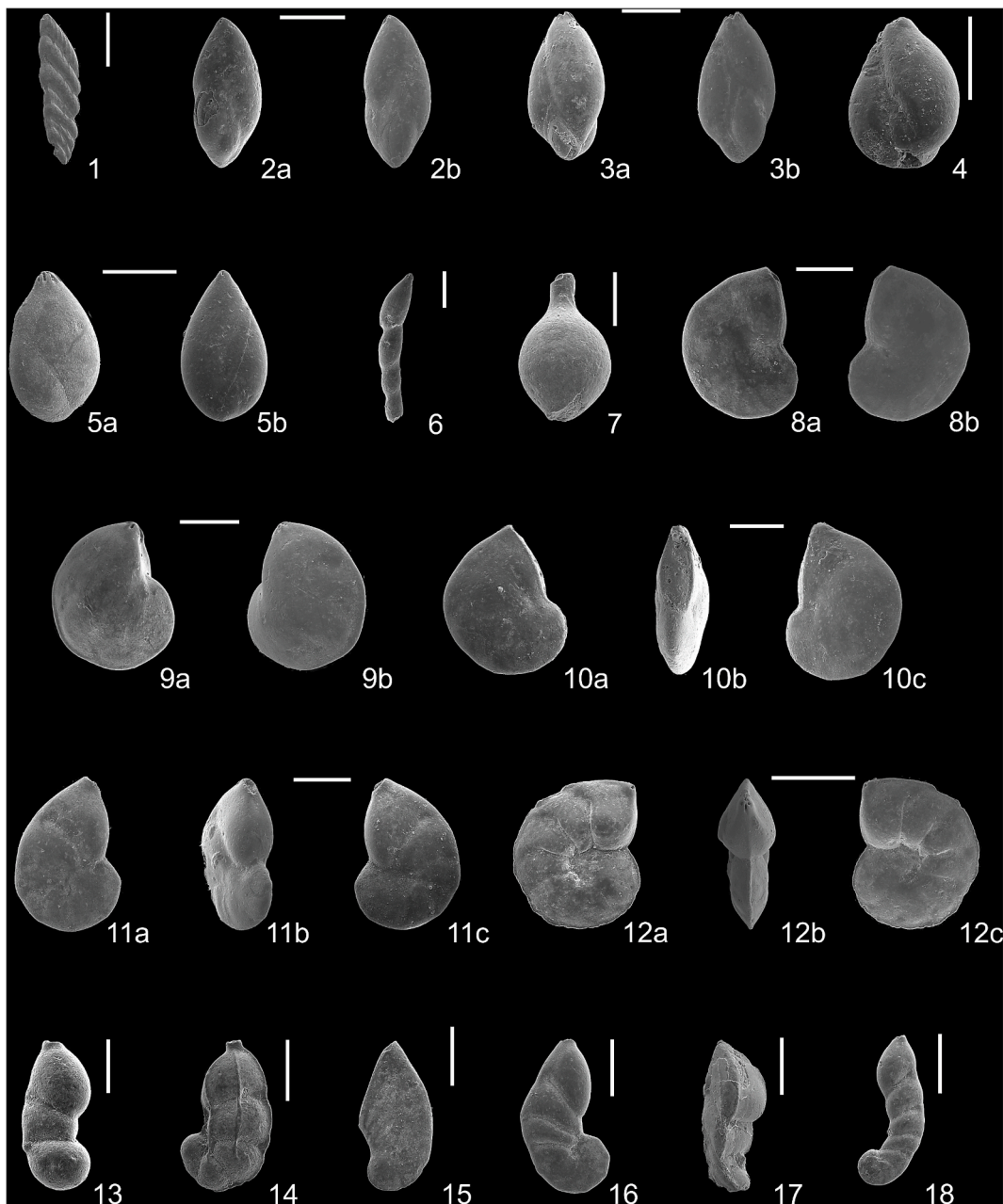


Fig. 4. Benthic foraminifera from the Lower Cretaceous in ODP Hole 692B organized according to genera. Scale-bars are 100  $\mu$ m.

1. *Citharina* sp. (113-692B-12R-3, 112–115 cm). 2. a/b *Eoguttulina bilocularis* (113-692B-8R-3, 75–78 cm). 3. a/b *Eoguttulina fusus* (113-692B-9R-2, 10–13 cm). 4. *Eoguttulina guttifera* (113-692B-9R-2, 45–48 cm). 5. a/b *Globulina prisca* (113-692B-9R-3, 42–45 cm). 6. *Laevidentalina debilis* (113-692B-9R-1, 60–63 cm). 7. *Lagena ovata* (113-692B-9R-1, 60–63 cm). 8. a/b *Lenticulina involvens* (113-692B-10R-3, 27–30 cm). 9. a/b *Lenticulina lideri* (113-692B-9R-3, 42–45 cm). 10. a/b/c *Lenticulina pulchella* (113-692-10R-6, 13–16 cm). 11. a/b/c *Lenticulina turgidula* (113-692B-10R-6, 82–85 cm). 12. a/b/c *Lenticulina* sp. 1. (113-692B-10R-6, 82–85 cm). 13. *Marginulina bullata* (113-692B-9R2, 45–48 cm). 14. *Marginulina gatesi* (113-692B-8R-3, 75–78 cm). 15. *Planularia complanata* (113-692B-10R-6, 82–85 cm). 16. *Saracenaria bronni* (113-692B-10R-3, 27–30 cm). 17. *Saracenaria tsaramandroensis* (113-692B-10R-6, 39–42 cm). 18. *Vaginulinopsis enodis* (113-692B-9R-2, 115–117.5 cm).

Genus *Laevidentalina* (*Laevidentalina* sp., *Laevidentalina* sp. 1., *Laevidentalina* sp. 2., *Laevidentalina debilis*, *Laevidentalina distincta*, *Laevidentalina guttifera*, *Laevidentalina soluta*), displays low absolute abundance, varying from 1 specimen/10 g (samples at 90.55 mbsf, 61.19 mbsf, and 70.75 mbsf) to 53 specimens/10 g (at 83.55 mbsf; Fig. 3). *Laevidentalina distincta* is the most abundant species, ranging from 0.52% (at 86.82 mbsf) to 100% (at 60.17 mbsf; Fig. 3).

Genus *Saracenaria* (*Saracenaria* sp., *Saracenaria bronni*, *Saracenaria tsaramandroensis*) is characterized by low absolute values varying from 1 specimen/10 g (at samples of 92.32 mbsf, 79.48 m, 72.73 mbsf, 72.22 mbsf, 71.45 mbsf, 70.75 mbsf, and 68.95 mbsf) to 69 specimens/10 g (at

83.55 mbsf; Fig. 3). *Saracenaria* sp. displays high abundance, fluctuating from 0.48% (70.75 mbsf) to 80% (at 85.40 mbsf) (Fig. 3).

The absolute abundance of *Vaginulinopsis* (*Vaginulinopsis* sp., *Vaginulinopsis enodis*, *Vaginulinopsis excentrica*) is characterized by intermediate values, ranging from 1 specimen/10 g (samples at 91.02 mbsf, 70.75 mbsf, and 61.19 mbsf) to 82 specimens/10 g (at 85.75) (Fig. 3). The species most abundant is *V. excentrica*, which fluctuates between 15.74% (at 86.82) and 33.33% (at 86.39 mbsf) (Fig. 3).

The previously described assemblages represent about 95% of the total BF and are recorded mainly in the Valanginian-Hauterivian interval (cores 113-692B-9R and 113-692B-10R; Fig. 3). The remaining

5% of the BF assemblages show low abundances and are characterized by *Citharina* sp., which ranges from 1 specimen/10 g to 3 specimens/10 g (Fig. 3). The abundance of the genus *Lagena* (*Lagena* sp., *Lagena sulcata*, and *Lagena ovata*) ranges from 1 specimen/10 g to 26 specimens/10 g (Fig. 3). Genus *Marginulina* (*Marginulina* sp., *Marginulina bullata*, *Marginulina gatesi*) fluctuates from 1 specimen/10 g to 27 specimens/10 g (at 85.75 mbsf) (Fig. 3). *Nodosaria sceptrum* shows a lower value of abundance, between 1 specimen/10 g and 2 specimens/10 g (Fig. 3). The abundance of *Planularia complanata* fluctuates from 1 specimen/10 g to 21 specimens/10 g (at 85.75 mbsf) (Fig. 3). *Spirulina minima* is recorded in the upper Valanginian with abundances of up to 5 specimens/10 g in a sample at 86.13 mbsf and 6 specimens/10 g in a sample at 85.75 mbsf (Fig. 3).

Benthic foraminifera assemblages display high dominance of the taxa belonging to the infaunal morphogroup (mean value of 98.3%) throughout the studied succession (Fig. 2). The dominant morphogroup is represented by the genera *Citharina*, *Eoguttulina*, *Laevidentalina*, *Lagena*, *Lenticulina*, *Marginulina*, *Nodosaria*, *Planularia*, *Saracenaria*, and *Vaginulinopsis* (Fig. 3). The remaining 1.7% of the assemblages correspond to the occurrence of *Spirulina minima*, which is considered an epifaunal species that is only registered in the middle part of the Weisert Event (samples 113-692B-10R-5, 125–128 cm and 113-692B-10R-6, 13–16 cm) (Fig. 3).

#### 4. Discussion

##### 4.1. Paleobathymetric evolution

The current configuration of the Antarctic continental margin of the

eastern Weddell Sea off Kapp Norvegia (Fig. 5A) shows a very steep and narrow upper continental slope that abruptly passes into a gently sloping mid-slope bench. The transition between the continental rise and the abyssal plain (>4000 m water depth) is characterized by the steep and narrow Explora Escarpment (Hinz and Krause, 1982; Barker and Kennett, 1988).

The ODP Hole 692B was drilled at 2875 m water depth, and the oldest sedimentary rocks were recovered at 97.9 mbsf, approximately in the mid-slope bench of the Wegener Canyon (upper scarp), corresponding to the abyssal zone (Fig. 5A).

The most abundant genus is *Eoguttulina*, which has been described as inhabiting in shelf environments (e.g., Georges Bank basin - USA; Scholle and Wenkam, 1982) and outer neritic to upper bathyal settings (e.g., Sergipe - Brazil; Koutsoukos, 1989). *Eoguttulina bilocularis*, the most abundant species in the studied interval at Hole 692B, was documented by Riegraf (1989) on a shallow shelf in the Indian Ocean (DSDP Site 249). *Laevidentalina*, *Lenticulina*, *Lagena*, and *Nodosaria* have a broad paleobathymetric range, occurring from inner neritic to lower bathyal environments (Table 1). *Saracenaria* was allocated to an inner-to outer neritic setting by Frenzel (2000) and a neritic to a middle bathyal environment by Koutsoukos (1989). *Vaginulinopsis* is reported as bathyal in the Indian Ocean (e.g., Holbourn and Kaminski, 1995a). Based on the known paleobathymetric distribution of the taxa detected in this study (Table 1) and thanks to the high-resolution sampling adopted, an outer neritic-upper bathyal (~200–500 m) bathymetric deposition is inferred for ODP Hole 692B at the upper Berriasian - Barremian interval (Fig. 5B), contrasting with the earlier estimation (500–1000 m) given by Barker and Kennett (1988).

According to Barker and Kennett (1988), the BF taxa recorded in the

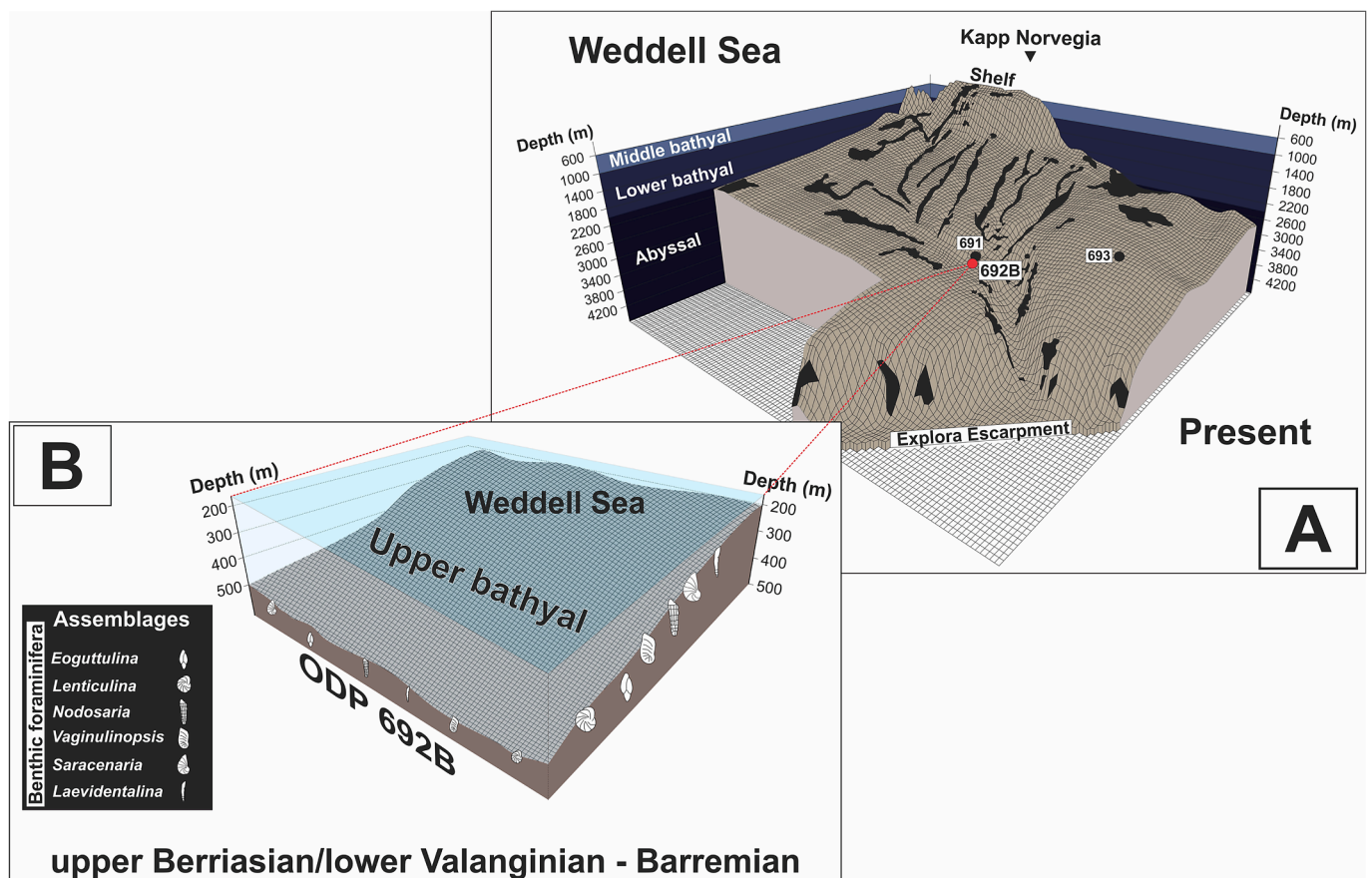


Fig. 5. A. Present bathymetry of the Antarctic continental margin and the Wegener Canyon (modified after Fütterer et al., 1990). B. Paleobathymetric reconstruction of ODP Hole 692B during the Lower Cretaceous based on the occurrence of benthic foraminiferal assemblages that indicate an outer neritic - upper bathyal environment (see text for further explanation).

**Table 1**

Paleoecological preferences of the benthic foraminifera according to the morphogroups identified by Corliss and Chen (1988). Paleoecological and paleobathymetric interpretation are based on different studies: Løfdali and Nagy (1980)<sup>1</sup>; Scholle and Wenkam (1982)<sup>2</sup>; Nyong and Olsson (1984)<sup>3</sup>; De Azevedo et al. (1987)<sup>4</sup>; Koutsoukos (1989)<sup>5</sup>; Rieggraf (1989)<sup>6</sup>; Koutsoukos and Hart (1990)<sup>7</sup>; Tyszka (1994)<sup>8</sup>; Kaiho (1994)<sup>9</sup>; Kaiho and Hasegawa (1994)<sup>10</sup>; Hart and Fitzpatrick, (1995)<sup>11</sup>; Holbourn and Kaminski (1995a, 1995b)<sup>12</sup>; Decker and Rögl (1988)<sup>13</sup>; Frenzel (2000)<sup>14</sup>; Schnack (2000)<sup>15</sup>; Holbourn et al. (2001b)<sup>16</sup>; Alegret et al. (2003)<sup>17</sup>; Kouwenhoven and van der Zwaan (2006)<sup>18</sup>; Friedrich et al. (2006)<sup>19</sup>; Friedrich and Erbacher (2006)<sup>20</sup>; Reolid et al. (2008)<sup>21</sup>; Cetaan et al. (2011)<sup>22</sup>; Reolid and Martínez-Ruiz (2012)<sup>23</sup>; Koch and Friedrich (2012)<sup>24</sup>; Reolid et al. (2013)<sup>25</sup>; Reolid et al. (2015)<sup>26</sup>; Ashckenazi-Polivoda et al. (2018)<sup>27</sup>; Giraldo-Gómez et al. (2018)<sup>28</sup>; Reolid et al. (2019)<sup>29</sup>.

Benthic foraminifera	Morphogroups		Oxygen			Organic matter			Paleodepth						References	
	Epifauna	Infauna	Low	Middle	High	Low	Middle	High								
									50 m	100	200	500	1000	2000		
									IN	MN	ON	UB	MB	LB		
<i>Citharina</i>	X	X	█									█	█			5, 14, 22
<i>Eoguttulina</i>		X	█	█				█				█	█			2, 5, 6, 11, 25, 29
<i>Globulina</i>	X	X	█									█	█			5, 8, 14, 17
<i>Laevidentalina</i>	X	X		█				█				█	█			8, 10, 14, 16, 17, 20, 21, 24, 27
<i>Lagena</i>	X	X		█			█					█	█			5, 8, 9, 14, 17, 22
<i>Lenticulina</i>	X	X	█				█					█	█			4, 5, 7, 8, 9, 12, 13, 14, 15, 16, 17, 18, 19, 21, 22, 27, 28, 29
<i>Marginulina</i>	X	X	█				█					█	█			5, 8, 13, 14, 25, 26
<i>Nodosaria</i>	X	X	█				█					█	█			3, 4, 5, 8, 14, 18, 21, 24
<i>Planularia</i>	X	X	█				█					█	█			5, 8, 14, 21, 27
<i>Saracenaria</i>	X	X		█								█	█			5, 7, 8, 12, 14, 17
<i>Spirillina</i>	X		█									█	█			5, 8, 14, 21, 22, 23
<i>Vaginulinopsis</i>	X	X	█					█				█	█			1, 6, 12, 13

Pliocene and Pleistocene sediments in ODP Hole 692B indicate a bathymetry not significantly different from the present water depth (2875 m). Furthermore, at the nearby ODP Site 693, benthic foraminifera also indicate an outer neritic-upper bathyal setting (200–500 m) during the Aptian - Albian, and a paleodepth similar to the present water depth (about 2400 m) is inferred for the Miocene - Pleistocene time interval (Barker and Kennett, 1988; Leckie, 1990). Therefore, according to these data, the evolution of the Weddell Sea displays a progressive deepening of the basin, passing from an outer neritic-upper bathyal setting during the Early Cretaceous (Berriasian-Barremian in ODP Hole 692B, Aptian - Albian at ODP Site 693) to ultra-deep waters (abyssal) at present.

#### 4.2. Paleoecological significance of benthic foraminifera

Despite the lack of a continuous sedimentary record and the low abundance of benthic foraminifera (BFN; Fig. 2) throughout the ODP Hole 692B, the BFN, the diversity indices (D-H<sub>s</sub>; Fig. 2), paleoecological preferences of the identified taxa, and statistical analyses (NMDS and DCA; Fig. 6A, B), allowed a detailed palaeoenvironmental reconstruction of the bottom-water conditions during the Lower Cretaceous.

The BFN and diversity indices (D - H<sub>s</sub>) are well established in the literature and used to estimate the oxygen content and the organic-matter flux to bottom waters (e.g., Sen Gupta and Machain-Castillo, 1993; Kaiho and Hasegawa, 1994; Jorissen et al., 1995; van der Zwaan et al., 1999; Friedrich et al., 2006; Jorissen et al., 2007). The BFN changes recorded in ODP Hole 692B probably reflect fluctuations in organic matter flux associated with dissolved oxygen availability. The increase in BFN recorded in the upper Valanginian (samples 113-692B-10R-6, 82–85 cm, 113-692B-10R-6, 13–16 cm, 113-692B-10R-5, 125–128 cm, 113-692B-10R-4, 55–58 cm, 113-692B-10R-4, 22–25 cm, 113-692B-10R-3, 115–118 cm, and 113-692B-9R-2, 115–117.5 cm) and upper Hauterivian (sample 113-692B-9R-2, 45–48 cm) could represent the response to enhanced organic-matter flux and/or decreased oxygen availability in bottom waters (e.g., Gooday, 2003; Schmiedl et al., 1998; Holbourn et al., 2001b; Friedrich et al., 2006; Friedrich and Hemleben,

2007). Diversity (H<sub>s</sub>) in ODP Hole 692B is characterized by low to intermediate values, fluctuating between 0 and 2.1, indicating stressing conditions under low oxygen and high organic-matter fluxes to the seafloor. In turn, the high values of D in the upper Valanginian (samples 113-692B-12R-2, 85–88 cm, 113-692B-12R-2, 29–32 cm, 113-692B-10R-5, 90–93 cm, and 113-692B-10R-3, 11–14 cm), lower Hauterivian (sample 113-692B-10R-1, 67–70 cm), upper Hauterivian (sample 113-692B-9R-2, 45–48 cm), and Barremian (samples 113-692B-8R-2, 26–29 cm, 113-692B-8R-2, 80–83 cm, 113-692B-8R-2, 1–4 cm, 113-692B-8R-1, 143–146 cm, 113-692B-8R-1, 87–90 cm, and 113-692B-7R-2, 138–141 cm) suggest a decline in oxygen but high nutrient availability in bottom waters (Fig. 2). Similar bottom water conditions have been described in various locations worldwide during the Cretaceous (e.g., Holbourn et al., 2001b; Friedrich et al., 2005a; Friedrich et al., 2006).

The significance of BF assemblages in reconstructing the link between organic carbon flux (food availability) and oxygenation of the bottom waters has been shown by several authors (e.g., Bernhard, 1986; Jorissen et al., 1995; van der Zwaan et al., 1999; Jorissen, 1999; Jorissen et al., 2007). The Lower Cretaceous BF assemblages in ODP Hole 692B display an absolute predominance of infaunal taxa (Fig. 2), which are characterized by their dependence on the intermittent flux of labile and easily metabolized organic matter to the seafloor and oxygen-depleted environments (e.g., Corliss and Chen, 1988; Sen Gupta and Machain-Castillo, 1993; Kaiho, 1994; Kaminski et al., 1995; Jorissen et al., 1995; Erbacher et al., 1998; Jorissen, 1999; Holbourn et al., 2001b; Friedrich et al., 2003, 2006; see Table 1).

*Eoguttulina*, the most abundant genus within the assemblage in Hole 692B (Fig. 3), is interpreted to be an opportunist taxon at different locations, characterized by preferring environments with reduced levels of oxygen and high organic matter at the sediment-water interface during Jurassic times (e.g., Dorset Coast-England: Hart and Fitzpatrick, 1995; Middle Atlas-Morocco: Reolid et al., 2013; Lusitanian Basin-Portugal: Reolid et al., 2019; Cueva del Agua-Spain: Reolid, 2020). Moreover, *Eoguttulina* was recorded in the oxygen-depleted sediments of the

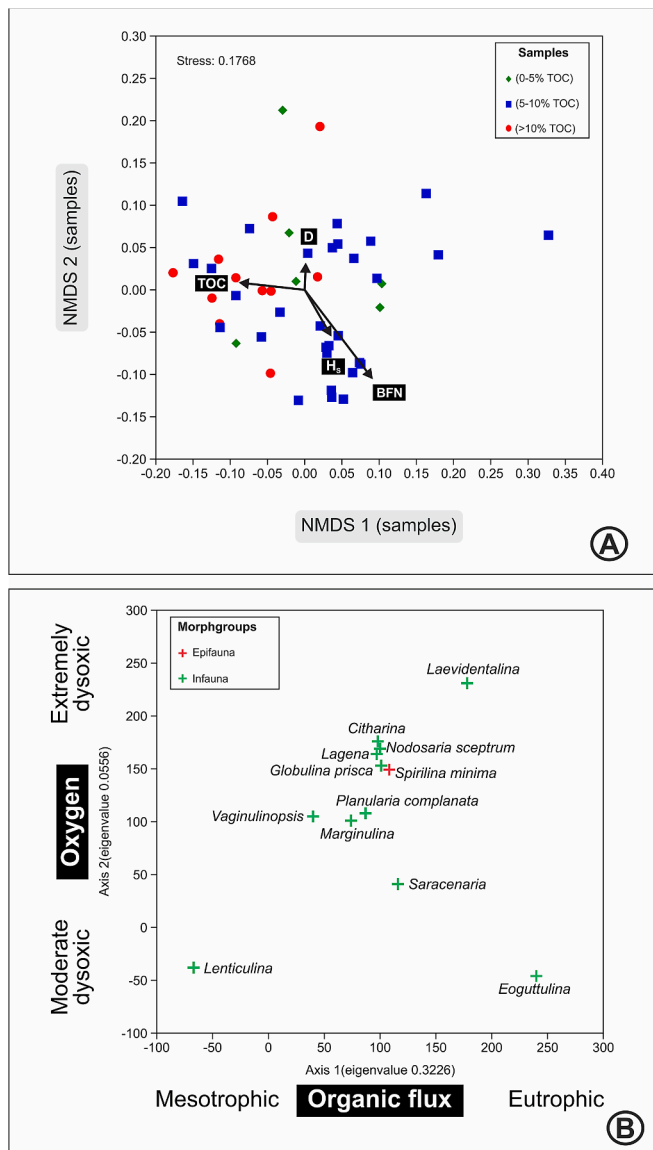


**Fig. 6.** Multivariate analyses of benthic foraminiferal assemblages in ODP Hole 692B. A. Non-Metric Multidimensional Scaling (NMDS: Q-mode) showing a relationship between the TOC content and the benthic foraminiferal parameters: benthic foraminifera numbers (BFN) and diversity indices (D: Dominance index and H<sub>5</sub>: Shannon index). From fitted environmental vectors, the TOC content and the BFN are related to the NMDS axis 1, which is controlled by benthic foraminiferal assemblages. Samples with high TOC values (left side) and D (right side) show an opposite trend to those with high BFN and H<sub>5</sub> values. B. Detrended Correspondence Analyses (DCA: R-mode) of benthic foraminiferal abundances of Hole 692B. The first axis (eigenvalue 0.3226) is associated with the organic carbon flux, while the second axis (eigenvalue 0.0556) is linked to oxygen depletion (see text for further explanation).

Cretaceous Sergipe Basin in Brazil (e.g., Koutsoukos, 1989). The genus *Laevidentalina* is known as a dysoxic indicator, able to live under depleted oxygen conditions (Kaiho and Hasegawa, 1994; Frenzel, 2000) and is interpreted from Cretaceous black-shale intervals as highly tolerant to low oxygen levels and high organic carbon fluxes (Friedrich and Erbacher, 2006; Koch and Friedrich, 2012). Genus *Saracenaria* was found in dysaerobic to quasi-anaerobic environments of the upper Aptian-lower Albian in the Sergipe Basin (Koutsoukos, 1989; Koutsoukos and Hart, 1990) and is considered to thrive under suboxic conditions (Alegret et al., 2003).

The genus *Lenticulina* is an opportunist taxon thriving under low

oxygen concentrations and high organic-matter fluxes; it has been documented worldwide in different basins during the Jurassic and Cretaceous (Koutsoukos and Hart, 1990; Tyszka, 1994; Kaiho, 1994; Frenzel, 2000; Holbourn et al., 2001b; Reolid et al., 2013; Ashckenazi-Polivoda et al., 2018; Giraldo-Gómez et al., 2018).

*Vaginulinopsis excentrica* was recorded in dark claystones at DSDP Site 263 in the Indian Ocean during the Valanginian-Barremian time interval and interpreted as an indicator of high organic-matter influx coupled with oxygen-depletion (Holbourn and Kaminski, 1995b). *Vaginulinopsis enodis* was found in restricted bottom waters associated with a considerable supply of organic matter during the Jurassic (e.g., Svalbard: Løfaldli and Nagy, 1980). The genus *Marginulina* was recorded in oxygen-depleted bottom waters characterized by an ample supply of organic matter during the Jurassic (Løfaldli and Nagy, 1980) and was also observed in dysaerobic conditions with changing oxygen concentration at the seafloor during the Hauterivian in Austria (Eastern Alps: Decker and Rögl, 1988).

High organic-matter fluxes are also evidenced by the occurrence of diagnostic taxa in ODP Hole 692B such as *Eoguttulina* (e.g., Koutsoukos, 1989; Hart and Fitzpatrick, 1995; Reolid et al., 2013; Reolid et al., 2019; Reolid, 2020), *Lenticulina* (e.g., Koutsoukos and Hart, 1990; Tyszka, 1994; Kaiho, 1994; Frenzel, 2000; Holbourn et al., 2001b; Reolid et al., 2013; Ashckenazi-Polivoda et al., 2018; Giraldo-Gómez et al., 2018), *Laevidentalina* (e.g., Friedrich and Erbacher, 2006; Koch and Friedrich, 2012), *Marginulina* (e.g., Løfaldli and Nagy, 1980; Decker and Rögl, 1988), and *Vaginulinopsis* (e.g., Svalbard: Løfaldli and Nagy, 1980; Holbourn and Kaminski, 1995b), which are more abundant under eutrophic conditions (higher organic-matter fluxes), where they can reach high relative abundance (> 90%) (Fig. 7). In summary, the assemblages recorded in ODP Hole 692B display typical taxa that thrived under depleted oxygen conditions with an enhanced increase of organic carbon flux under eutrophic conditions, where bottom water oxygenation become the dominant control on the composition of foraminiferal assemblages (e.g., Jorissen et al., 1995; van der Zwaan et al., 1999).

Non-metric multidimensional scaling (NMDS) ordination displays an arrangement of the Lower Cretaceous BF in ODP Hole 692B that shows different relationships with various proxies such as TOC, BFN, D, and H<sub>5</sub> in two dimensions (Fig. 6A). The correlation between BFN and H<sub>5</sub> with TOC values shows different combinations according to the NMDS, as follows (Fig. 6A): a) highest TOC with very few or no BFN and very low H<sub>5</sub>; b) moderate to elevate TOC with high BFN and H<sub>5</sub> values; c) low TOC with high BFN and H<sub>5</sub> values. High TOC content is interpreted to reflect increased organic-matter fluxes (food) that might result from enhanced preservation, deriving from an additional supply of terrestrial organic matter or increased surface water productivity (Wahyudi and Minagawa, 2013; Gooday et al., 2009; Lowery et al., 2014).

A Detrended Correspondence Analysis (DCA) was carried out to evaluate the principal environmental gradients controlling the distribution of benthic foraminifera. The first axis of the DCA (Fig. 6B) mainly separates two BF patterns. The right side of the DCA displays positive scores and is characterized by *Citharina*, *Eoguttulina*, *Laevidentalina*, *Lagena*, *Marginulina*, *N. sceptrum*, *P. complanata*, *Saracenaria*, *S. minima* and *Vaginulinopsis*, while on the left side is only observed *Lenticulina* with negative scores. Based on the ecological preferences described above, the first axis likely represents changes in productivity (carbon-organic flux) in bottom-waters. In addition, the low negative scores of *Eoguttulina* and *Lenticulina* are opposite to the remaining taxa (*Citharina*, *Laevidentalina*, *Lagena*, *Marginulina*, *N. sceptrum*, *P. complanata*, *Saracenaria*, *S. minima* and *Vaginulinopsis*) that display positive scores. According to this distribution, the second axis of the DCA (Fig. 6B) probably reflects oxygen-depletion conditions (moderate to extremely dysoxic conditions) in bottom waters.

However, the potential changes in the bottom waters, evidenced by different proxies, allow concluding that the short-term fluctuations in the BFN and an increase in H<sub>5</sub> in ODP Hole 692B reflect the presence of oxygen in the seabed during short intervals in the upper Valanginian

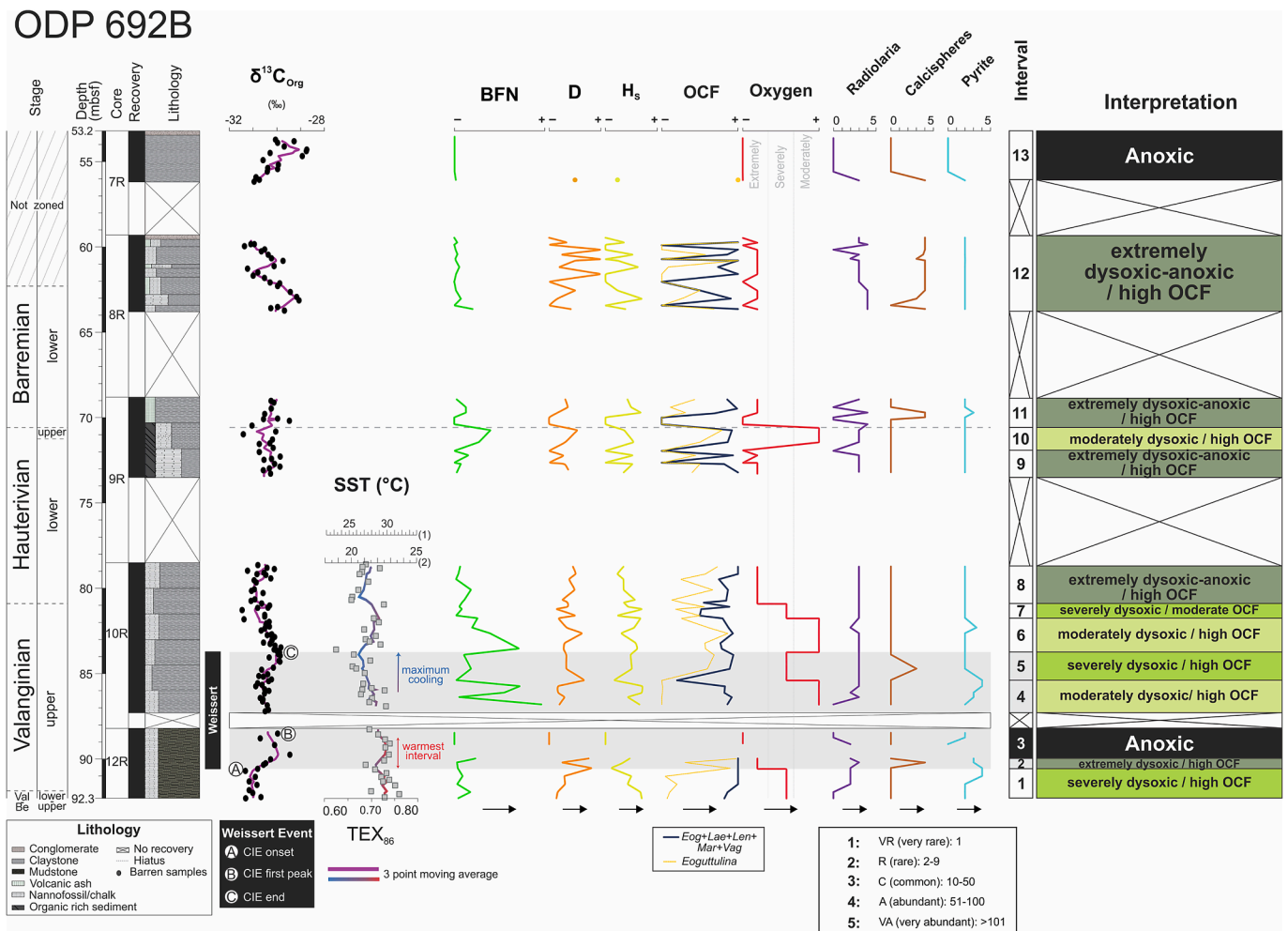


**Fig. 7.** Paleoceanographic reconstruction of bottom-water conditions in ODP Hole 692B is based on the abundances and composition of the benthic foraminiferal assemblages during the Lower Cretaceous. Changes in organic carbon fluxes (OCF) gained from the abundance of diagnostic benthic foraminiferal taxa (*Eogu*: *Eoguttulina*; *Laev*: *Laevidentalina*; *Lent*: *Lenticulina*; *Mar*: *Marginulina*; *Vag*: *Vaginulinopsis*) and oxygen estimations derived from BFN, diversity indices (D -  $H_S$ ), palaeoecological preferences of each taxon, and statistical analyses (NMDS and DCA) (see text for further explanation). Thirteen intervals have been identified as follows: I) upper Berriasian - lower Valanginian (interval 1); II) Hauterivian (intervals 8, 9 and 10), and III) Barremian and post-Barremian (intervals 11, 12 and 13). Radiolaria, calcspheres, and pyrite abundances from this study (Supplementary data, Table S1). Organic carbon isotopes ( $\delta^{13}C_{org}$ ), the position of the Weissert Event (grey band) and peaks A (CIE onset), B (CIE first peak), and C (CIE end) are according to Cavalheiro et al. (2021). Sea surface temperatures (SSTs) from  $TEX_{86}$  paleothermometry (red curve: warmer values; blue curve: colder values) showing the calibration in degree °C (1: Bayspar and 2: restricted basin calibrations) are according to Cavalheiro et al. (2021). (For interpretation of the references to colour in this figure legend, the reader is referred to the web version of this article.)

(samples 113-692B -10R-6, 82–85 cm, 113-692B-10R-5, 125–128 cm, 113-692B-10R-4, 55–58 cm, 113-692B -10R-4, 22–25 cm, and 113-692B-10R-3, 115–118 cm) and upper Hauterivian (sample 113-692B-9R-2, 45–48 cm). These temporary oxygenation episodes coincide with a slight increase in abundance of the genus *Lenticulina* and a decrease in TOC values, especially in the upper Valanginian (Figs. 2, 3). In turn, an opposite correlation between *Lenticulina* and *Eoguttulina* is evidenced by the DCA, indicating that *Lenticulina* is more controlled by the availability of oxygen than *Eoguttulina*; the latter taxon is more dependent on food (organic carbon flux), and both thrived under low oxygen conditions (Fig. 6B).

#### 4.3. The Weissert Event in the Weddell Sea

The late Valanginian Weissert Event corresponds to a large-scale perturbation in the global carbon cycle, affecting both the atmosphere and ocean systems, as evidenced by a positive carbon isotope excursion (CIE) in marine and terrestrial settings (e.g., Erba et al., 2004; Meissner et al., 2015). In ODP Hole 692B, a well-defined  $\delta^{13}C$  carbon isotopic

excursion is documented by Cavalheiro et al. (2021) (Figs. 2, 7).

The new data gathered in this study of the benthic foraminiferal assemblages across the Weissert Event reveals variations in abundances (BFN), diversity indices (D and  $H_S$ ) and composition, allowing identification of intervals characterized by specific environmental conditions coinciding with decreases and increases in organic carbon fluxes and oxygen content in bottom waters (Fig. 7).

Before the perturbation (pre-Weissert Event), the bottom-waters experienced dysoxic conditions with high organic-matter fluxes (interval 1; Fig. 7). At the onset of the Weissert Event (A in Figs. 2, 7), a progressive deterioration of the bottom waters under extremely dysoxic conditions and high organic carbon flux were recorded (interval 2; Fig. 7). The absence of BF suggests a transition to anoxic conditions recorded in the bottom waters, which coincides with the first peak of the Weissert CIE (B in Figs. 2, 7). Between the first peak of the Weissert perturbation (peak B in Fig. 7) and the end of the carbon isotopic plateau (peak C in Figs. 2, 7), and above the interval barren of BF, the assemblages suggest a sporadic increase in oxygen concentration (moderate dysoxic conditions), which favored the recolonization of bottom waters

(interval 4; Fig. 7). Similar repopulation events have been described for other Oceanic Anoxic Events (e.g., Friedrich, 2010; Friedrich et al., 2005b, 2011), indicating short-term amelioration of bottom waters during overall hostile conditions. The latest part of the Weissert CIE near the end of the carbon isotopic plateau displays a sudden decrease in the oxygen concentration of the seafloor, with severe dysoxia, marked by an abrupt reduction in the BFN (interval 5; Fig. 7).

In the recovery state of the Weissert CIE (post-peak C in Fig. 7), it is evident that the BFN rapidly increases, indicating a reinvigorated repopulation phase whose magnitude is similar to the previous one detected after the interval of most severe anoxia. An improvement in the seafloor as evidenced by an increase in oxygen concentration is compared with the preceding interval marked by several dysoxic conditions under high organic carbon flux (interval 6; Fig. 7). Moreover, this increase in BF abundance and species richness correlates with a cooling episode documented by micropaleontological, mineralogical, and geochemical proxies (Erba et al., 2004; Cavalheiro et al., 2021; Fig. 7) and, thus, might have been triggered by the downwelling of colder and denser surface waters, resulting in oxygen-rich bottom waters that favored benthic organisms. The Valanginian - Hauterivian boundary was characterized by a significant decrease in the BFN, indicating oxygen-depleted bottom waters characterized by severe dysoxic conditions under moderate organic-carbon flux (interval 7; Fig. 7).

#### 4.4. Paleooceanography of the Weddell Sea during the Early Cretaceous

The paleooceanography in the Antarctic region during the Early Cretaceous was closely related to the stretching and eventual separation of the West Antarctic Peninsula from East Antarctica, which originated the Weddell Sea in response to the early evolution of the South Atlantic and the western Indian Ocean (Owen, 1983; Crame, 1999).

According to the data collected in this study, the Lower Cretaceous sedimentary sequence recovered in ODP Hole 692B was deposited at a paleo-water depth of 200–500 m in an outer neritic-upper bathyal setting, characterized by high TOC contents (Fig. 2) and abundant pyrite framboids (Fig. 7), which are generally used to reconstruct paleo-redox conditions. These high-TOC values resulted from the enhanced burial of organic-carbon deposited under anoxic and euxinic bottom water conditions. The distribution of pyrite framboids allows determining their syngenetic (formed in the water column) or diagenetic (originated within the sediment) origin, suggesting anoxic-euxinic or dysoxic conditions, respectively (Wignall and Newton, 1998; Bond and Wignall, 2010; Dummann et al., 2021).

The frequent abundance of radiolarians throughout the investigated interval may indicate enhanced nutrient levels in the surface waters (Fig. 7). Similarly, the occurrence of abundant calcispheres, possibly colonizing the niches left vacant by the collapse of the dinoflagellate cyst population (e.g., Hart, 1991), supports stressing conditions in the surface waters (Fig. 7).

A relevant cooling episode coinciding with the end of the Weissert Event is documented in ODP 692B in the Weddell Sea, displaying a ~3–4 °C decline in the sea surface temperature (SST) derived from TEX<sub>86</sub> analyses (Cavalheiro et al., 2021; Fig. 7). This cooling is consistent with global signals based on different SST-proxies, which show higher sensitivity temperatures in high-latitude regions (Cavalheiro et al., 2021). The presence of abundant benthic foraminifera during the Weisser Event cooling episode (interval 4; Fig. 7) indicates a significant increase in oxygen after a period of anoxic conditions in bottom waters (interval 3; Fig. 7), which can be regarded as a benthic foraminiferal repopulation event.

Similar repopulation events have been reported for various OAEs (OAE 1b: Friedrich et al., 2005b; OAE 2: Friedrich et al., 2011) and from Quaternary Mediterranean sapropels (e.g., Rohling et al., 1997; Schmiedl et al., 2003; Friedrich et al., 2005b). Different mechanisms have been postulated to explain these repopulation events, which could be triggered either by a decrease in nutrient input from the surface

waters or/and by an increase in the ventilation of bottom waters during cooling periods characterized by short-term climate variability (Rohling et al., 2002; Friedrich et al., 2005b, 2011). Based on benthic foraminiferal assemblages recorded in ODP Hole 692B, we hypothesize that the repopulation event in the Weddell Sea is presumably related to short periods of oxygen-ventilation rather than to a decrease in the supply of nutrients to the bottom waters (interval 4; Fig. 7).

In the lower Hauterivian, a continuous decline in oxygen availability induced severely dysoxic to anoxic conditions with increased organic-carbon fluxes (interval 8; Fig. 7). In the uppermost lower Hauterivian, the bottom waters display a depleted-oxygen availability under dysoxic to anoxic conditions and increases in organic carbon fluxes. Subsequently, a sudden increase in oxygen availability under moderate dysoxic conditions is associated with high organic carbon fluxes to the seafloor (intervals 9 and 10; Fig. 7). The previously mentioned bottom-water conditions remained during the upper Hauterivian (interval 10; Fig. 7).

The lower Barremian and the post-Barremian stratigraphic interval display a transition to a more stressful environmental setting with extremely dysoxic to anoxic bottom conditions and high organic carbon fluxes (intervals 11 and 12; Fig. 7), whereas the topmost studied interval, characterized by the absence of benthic foraminifera, indicates anoxic-water conditions (interval 13; Fig. 7).

Micropaleontological, geochemical, and sedimentological data from ODP Hole 692B delineate paleooceanographic changes that influenced the Weddell Sea during the Early Cretaceous. A dominance of anoxic-euxinic and dysoxic conditions is envisaged based on the scarcity of benthic foraminiferal assemblages and the presence of organic-rich sediments with high TOC content and pyrite framboids.

Food availability is strongly related to organic-carbon fluxes and the transport of organic matter to the seafloor. Marine coastal settings are generally characterized by organic-rich sediments resulting from enriched supplies of terrestrial organic matter and enhanced productivity via runoff. However, the lack of terrestrial siliciclastic and organic material in ODP Hole 692B (O'Connell, 1990; Robert and Maillot, 1990) discards a relationship between high TOC content and primary productivity associated with a runoff system.

We hypothesize that the enhanced organic matter availability in bottom waters (as a food supply), as evidenced by the infaunal benthic foraminifera in the Weddell Sea, probably reflect a local upwelling system favored by climatic and atmospheric circulation (O'Connell, 1990). The abundant radiolarians in ODP Hole 692B support the idea of an upwelling system as suggested by modern radiolarian blooms in high-fertility upwelling regions where increased nutrient loadings (phosphates and nitrates) are combined with enhanced silica availability (Racki and Cordey, 2000). Recent studies on modern upwelling systems indicate variability of climate factors such as changes in local wind forcing, ventilation processes, or the source-water pathways, which influence oxygen concentration, nutrient supply, and CO<sub>2</sub> concentrations in the surface waters (Ryckaczewski et al., 2015; García-Reyes et al., 2015).

The proto-Drake Passage between South America and the Antarctic Peninsula has been described as a narrow and shallow connection during the Barremian - Albian interval (Sewall et al., 2007; Eagles, 2016). However, new circulation models in the proto-Drake Passage suggest that from Berriasian to Hauterivian, there was a sluggish water mass exchange between the Southern Ocean and the South Pacific with the adjacent proto-Indian and Tethys Oceans (Dummann et al., 2021). On the contrary, a West-to-East transport of intermediate water masses between the Pacific and the Southern Ocean is proposed to have occurred since the Barremian (Dummann et al., 2021).

We therefore infer that possible bottom currents related to the influx of Southern Ocean waters favored short-term pulses of ventilation in the Weddell Sea under constantly increased organic carbon fluxes during the late Valanginian and late Hauterivian (intervals 4, 6, and 10; Fig. 7).

The documented BF assemblages occurring in the Weddell Sea show



similarities to those observed in the Boreal and Tethyan bioprovinces and reveal a strong affinity with the Austral bioprovince of the southern hemisphere (Scheibnerová, 1973; Scheibnerová, 1976). In particular, Lower Cretaceous BF recorded in ODP Hole 692B display an affinity with assemblages from South-America (e.g., the Austral Basin of southern Patagonia and the Andean Basin: Riccardi, 1988; Bertels, 1988), the Indian Ocean (e.g., Mozambique ridge - DSDP Site 249: Riegraf, 1989, Holbourn and Kaminski, 1994), and Australia (e.g., Great Australian Basin: Scheibnerová, 1976; Exmouth Plateau off northwest Australia ODP Site 766: Holbourn and Kaminski, 1994; Holbourn and Kaminski, 1995a).

Such affinities of benthic foraminifera argue for an efficient circulation across the Southern Ocean sub-basins, with cosmopolitan BF populating the Austral realm (e.g., Scheibnerová, 1973; Scheibnerová, 1976), thus excluding restricted conditions at the Weddell Sea during the Lower Cretaceous.

## 5. Conclusions

Detailed benthic foraminiferal data from the Weddell Sea (ODP Hole 692B, Antarctica) suggests variable bottom water conditions in the latest Berriasian to Barremian time interval in terms of organic-carbon fluxes and oxygenation at the seafloor.

1. A paleodepth corresponding to an outer neritic-upper bathyal setting (~200–500 m) is inferred by benthic foraminiferal assemblages through the late Berriasian to early Barremian time interval.
2. Benthic foraminiferal assemblages show significant variation in the BFN and diversity indices (D and H<sub>5</sub>), indicating changes in bottom waters. Low abundances and diversities of benthic foraminiferal assemblages suggest prevailing high organic matter-fluxes and strongly dysoxic-to anoxic conditions at the seafloor in the Weddell Sea. Brief interruptions with a slight increase in bottom-water oxygenation occurred during and after the Weissert Event, in the latest Valanginian and late Hauterivian.
3. Benthic foraminiferal assemblages are dominated by infaunal taxa (*Eoguttulina*, *Laevidentalina*, *Lagena*, *Lenticulina*, *Marginulina*, *Nodosaria*, *Planularia*, *Saracenaria*, and *Vaginulinopsis*) tolerant to depleted-oxygen conditions and high organic-matter fluxes.
4. Food supply, identified by high organic-matter fluxes, was not the main factor controlling benthic foraminiferal assemblages. Instead, the redox state of bottom waters seems to have had overall control in the Weddell Sea.
5. During the Weissert Event, stressful bottom water conditions include short-term severely dysoxic conditions (Weissert CIE onset), culminating in an anoxic interval characterized by the absence of benthic foraminifera (peak B of the Weissert Event). Re-oxygenation interludes favored the return of benthic foraminifera, known as a repopulation event, which coincided with a global cooling episode at the end of the Weissert Event (between peaks B and C).
6. Brief pulses of increased oxygen concentrations in the bottom waters during and after the Weissert Event (late Valanginian) and late Hauterivian were probably originated by bottom currents, which promoted the ventilation under a constant increase in organic carbon flux.

Supplementary data to this article can be found online at <https://doi.org/10.1016/j.palaeo.2021.110795>.

## Declaration of Competing Interest

The authors declare that they have no known competing financial interests or personal relationships that could have appeared to influence the work reported in this paper.

## Acknowledgments

We thank the Ocean Drilling Program (ODP) for providing samples used in this study. Eni Spa is acknowledged for financial support and permission to publish this study. This research was funded through PRIN 2017RX9XXY to E. Erba. The authors also acknowledge the support of the Italian Ministry of University (MUR) through the project “Dipartimenti di Eccellenza 2018-2022, Le Geoscienze per la Società: Risorse e loro evoluzione”. We thank the editor and anonymous reviewers for their helpful comments and suggestions. Thanks to Stefania Crespi for her assistance at the Scanning Electron Microscope.

## Appendix A. Taxonomic appendix

The list of benthic foraminifera cited in the text are based on the works by Ellis and Messina (1940–2015), Riergraf (1989), and Holbourn and Kaminski (1995a, 1995b).

- Citharina* d'Orbigny, 1839.  
*Laevidentalina* Loeblich & Tappan, 1986.  
*Laevidentalina debilis* (Hantken) = *Dentalina debilis* Hantken, 1868.  
*Laevidentalina distincta* (Reuss) = *Dentalina distincta* Reuss, 1868.  
*Laevidentalina guttifera* (d'Orbigny) = *Dentalina guttifera* d'Orbigny, 1846.  
*Laevidentalina soluta* (Reuss) = *Dentalina soluta* Reuss, 1851.  
*Globulina prisca* Reuss, 1863.  
*Lagena* Reuss, 1863.  
*Lagena sulcata* (Walker & Jacob, 1798).  
*Lagena ovata* (Terquem, 1858).  
*Lenticulina* Lamarck, 1804.  
*Lenticulina lideri* Romanova, 1960.  
*Lenticulina involvens* (Wiśniowski, 1890).  
*Lenticulina pulchella* (Reuss, 1863).  
*Lenticulina turgidula* (Reuss, 1863).  
*Marginulina* d'Orbigny, 1826.  
*Marginulina bullata* Reuss, 1845.  
*Marginulina gatesi* Tappan, 1957.  
*Nodosaria sceptrum* Reuss, 1863.  
*Planularia complanata* (Reuss, 1845).  
*Saracenaria* DeFrance, 1824.  
*Saracenaria bronni* (Roemer, 1841).  
*Saracenaria tsaramandrosoensis* Espitalié & Sigal, 1963.  
*Vaginulinopsis* Silvestri, 1904.  
*Vaginulinopsis enodis* Loeblich & Tappan, 1950.  
*Vaginulinopsis excentrica* Cornuel, 1848.

## References

- Aguado, R., Company, M., Castro, J.M., de Gea, G.A., Molina, J.M., Nieto, L.M., Ruiz-Ortiz, P.A., 2018. A new record of the Weissert episode from the Valanginian succession of Cehegín (Subbetic, SE Spain): Bio-and carbon isotope stratigraphy. *Cretac. Res.* 92, 122–137.
- Alegret, L., Molina, E., Thomas, E., 2003. Benthic foraminiferal turnover across the cretaceous/Paleogene boundary at Agost (southeastern Spain): paleoenvironmental inferences. *Mar. Micropaleontol.* 48 (3–4), 251–279.
- Applegate, J.L., Bergen, J.A., 1988. Cretaceous calcareous nannofossil biostratigraphy of sediments recovered from the Galicia Margin, ODP Leg 103. *Proc. Ocean Drill. Program Sci. Results* 103, 293–348.
- Arthur, M.A., Sageman, B.B., 1994. Marine black shales: depositional mechanisms and environments of ancient deposits. *Annu. Rev. Earth Planet. Sci.* 22 (1), 499–551.
- Arthur, M.A., Schlanger, S.O., 1979. Cretaceous “Oceanic Anoxic Events” as causal factors in development of reef-reservoired giant oil fields. *AAPG Bull.* 63, 870–885.
- Arthur, M.A., Brumsack, H.J., Jenkyns, H.C., Schlanger, S.O., 1990. Stratigraphy, geochemistry, and paleoceanography of organic carbon-rich Cretaceous sequences. In: *Cretaceous Resources, Events and Rhythms*. Springer, Dordrecht, pp. 75–119.
- Ashckenazi-Polivoda, S., Titelboim, D., Meilijson, A., Almogi-Labin, A., Abramovich, S., 2018. Bathymetric trend of Late Cretaceous southern Tethys upwelling regime based on benthic foraminifera. *Cretac. Res.* 82, 40–55.
- Barbarin, N., Bonin, A., Mattioli, E., Pucéat, E., Cappetta, H., Gréselle, B., Joachimski, M., 2012. Evidence for a complex Valanginian nannoconid decline in the Vocontian basin (South East France). *Mar. Micropaleontol.* 84, 37–53.
- Barker, P.F., Kennett, J.P., 1988. Sites 691 and 692. *Init. Rep. Deep Sea Drill. Proj.* 113, 293–328.

- Bernhard, J.M., 1986. Characteristic assemblages and morphologies of benthic foraminifera from anoxic, organic-rich deposits; Jurassic through Holocene. *J. Foraminiferal Res.* 16 (3), 207–215.
- Bertels, A., 1988. Cretaceous foraminifera of Argentina: biogeographic tendencies. *Rev. Bras. Geociênc.* 18 (3), 299–311.
- Bond, D.P., Wignall, P.B., 2010. Pyrite framboid study of marine Permian-Triassic boundary sections: a complex anoxic event and its relationship to contemporaneous mass extinction. *Geol. Soc. Am. Bull.* 122, 1265–1279.
- Bornemann, A., Mutterlose, J., 2008. Calcareous Nannofossil and  $\delta^{13}\text{C}$  records from the early cretaceous of the Western Atlantic Ocean: evidence for enhanced fertilization across the Berriasian-Valanginian transition. *Palaios* 23, 821–832.
- Bottini, C., Erba, E., 2018. Mid-cretaceous paleoenvironmental changes in the western Tethys. *Clim. Past* 14 (8), 1147–1163.
- Bown, P.R., Rutledge, D., Crux, J.A., Gallagher, L.T., 1988. Lower cretaceous. In: Bown, P. (Ed.), *Calcareous Nannofossil Biostratigraphy*. Chapman and Hall, London, pp. 86–131.
- Bralower, T.J., Leckie, R.M., Sliter, W.V., Thierstein, H.R., 1995. An integrated Cretaceous microfossil biostratigraphy. In: *Geochronology, Time Scales and Global Stratigraphic Correlation*. SEPM Special Publication, 54. Society for Sedimentary Geology, Tulsa, pp. 65–79.
- Cavalheiro, L., Wagner, T., Steinig, S., Bottini, C., Dummann, W., Esegbue, O., Gambacorta, G., Giraldo-Gómez, V., Farnsworth, A., Flögel, S., Hofmann, P., Lunt, D., Rethemeyer, J., Torricelli, S., Erba, E., 2021. Impact of global cooling on Early Cretaceous high  $p\text{CO}_2$  world during the Weissert Event. *Nat. Commun.* 12 (1), 1–11. <https://doi.org/10.1038/s41467-021-25706-0>, 5411.
- Cetean, C.G., Bălc, R., Kaminski, M.A., Filipescu, S., 2011. Integrated biostratigraphy and palaeoenvironments of an upper Santonian–upper Campanian succession from the southern part of the Eastern Carpathians, Romania. *Cretaceous Res.* 32 (5), 575–590.
- Channell, J.E.T., Erba, E., Lini, A., 1993. Magnetostratigraphic calibration of the late Valanginian carbon isotope event in pelagic limestones from Northern Italy and Switzerland. *Earth Planet. Sci. Lett.* 118 (1–4), 145–166.
- Charbonnier, G., Boulila, S., Gardin, S., Duchamp-Alphonse, S., Adatte, T., Spangenberg, J.E., Galbrun, B., 2013. Astronomical calibration of the Valanginian “Weissert” episode: the Orpierre marl–limestone succession (Vocontian Basin, southeastern France). *Cretac. Res.* 45, 25–42.
- Corliss, B.H., Chen, C., 1988. Morphotype patterns of Norwegian Sea deep-sea benthic foraminifera and ecological implications. *Geology* 16 (8), 716–719.
- Crame, J.A., 1999. An evolutionary perspective on marine faunal connections between southernmost South America and Antarctica. *Sci. Mar.* 63, 1–14.
- De Azevedo, R.L.M., Gomide, J., Viviers, M.C., 1987. Geo-história da Bacia de Campos, Brasil: do Albiano ao Maastrichtiano. *Rev. Bras. Geociênc.* 17 (2), 139–146.
- Decker, K., Rögl, F., 1988. Early cretaceous agglutinated foraminifera from limestone-rich rhythmites of the Gresten Klippen Belt (Eastern Alps Austria). *Abh. Geol. Bundesanst.* 41, 41–59.
- Duchamp-Alphonse, S., Gardin, S., Fiet, N., Bartolini, A., Blamart, D., Pagel, M., 2007. Fertilization of the northwestern Tethys (Vocontian basin, SE France) during the Valanginian carbon isotope perturbation: evidence from calcareous nannofossils and trace element data. *Palaeogeogr. Palaeoclimatol. Palaeoecol.* 243 (1–2), 132–151.
- Dummann, W., Hofmann, P., Herrle, J.O., Wennrich, V., Wagner, T., 2021. A refined model of Early Cretaceous South Atlantic–Southern Ocean gateway evolution based on high-resolution data from DSDP Site 511 (Falkland Plateau). *Palaeogeogr. Palaeoclimatol. Palaeoecol.* 562, 1–14.
- Eagles, G., 2016. Plate kinematics of the Rocas Verdes Basin and Patagonian orocline. *Gondwana Res.* 37, 98–109.
- Ellis, B.F., Messina, A.R., 1940. *Catalogue of Foraminifera*, vol. 149. American Museum of Natural History. <http://www.micropress.org>.
- Erba, E., Quadrio, B., 1987. Biostratigrafia a Nannofossili calcarei Calpionellidi e Foraminiferi planctonici della Maiolica (Titoniano superiore–Aptiano) nelle Prealpi Bresciane (Italia settentrionale). *Riv. Ital. Paleontol. Stratigr.* 93 (1), 3–108.
- Erba, E., Bartolini, A., Larson, R.L., 2004. Valanginian Weissert oceanic anoxic event. *Geology* 32 (2), 149–152.
- Erba, E., Bottini, C., Faucher, G., Gambacorta, G., Visentin, S., 2019. The response of calcareous nannoplankton to Oceanic Anoxic Events: the Italian pelagic record. *Soc. Paleontol. Ital.* 58, 51–71.
- Erbacher, J., Gerth, W., Schmiedl, G., Hemleben, C., 1998. Benthic foraminiferal assemblages of late Aptian–early Albian black shale intervals in the Vocontian Basin, SE France. *Cretaceous Res.* 19 (6), 805–826.
- Frenzel, P., 2000. Die benthischen Foraminiferen der Rügiger Schreibkreide (Unter-Maastricht, NE-Deutschland). *Neues Palaontol. Abh.* 3, 1–361.
- Friedrich, O., 2010. Benthic foraminifera and their role to decipher paleoenvironment during mid-cretaceous Oceanic Anoxic Events–the “anoxic benthic foraminifera” paradox. *Rev. Micropaleontol.* 53 (3), 175–192.
- Friedrich, O., Erbacher, J., 2006. Benthic foraminiferal assemblages from Demerara Rise (ODP Leg 207, western tropical Atlantic): possible evidence for a progressive opening of the Equatorial Atlantic Gateway. *Cretac. Res.* 27 (3), 377–397.
- Friedrich, O., Hemleben, C., 2007. Early Maastrichtian benthic foraminiferal assemblages from the western North Atlantic (Blake Nose) and their relation to paleoenvironmental changes. *Mar. Micropaleontol.* 62 (1), 31–44.
- Friedrich, O., Reichelt, K., Herrle, J.O., Lehmann, J., Pross, J., Hemleben, C., 2003. Formation of the late Aptian Niveau Fallot black shales in the Vocontian Basin (SE France): evidence from foraminifera, palynomorphs, and stable isotopes. *Mar. Micropaleontol.* 49 (1–2), 65–85.
- Friedrich, O., Herrle, J.O., Hemleben, C., 2005a. Climatic changes in the late Campanian–early Maastrichtian: Micropaleontological and stable isotopic evidence from an epicontinental sea. *J. Foraminiferal Res.* 35 (3), 228–247.
- Friedrich, O., Nishi, H., Pross, J., Schmiedl, G., Hemleben, C., 2005b. Millennial-to centennial-scale interruptions of the Oceanic Anoxic Event 1b (Early Albian, mid-Cretaceous) inferred from benthic foraminiferal repopulation events. *Palaios* 20 (1), 64–77.
- Friedrich, O., Erbacher, J., Mutterlose, J., 2006. Paleoenvironmental changes across the Cenomanian/Turonian boundary event (oceanic anoxic event 2) as indicated by benthic foraminifera from the Demerara Rise (ODP Leg 207). *Rev. Micropaleontol.* 49 (3), 121–139.
- Friedrich, O., Erbacher, J., Wilson, P.A., Moriya, K., Mutterlose, J., 2009. Paleoenvironmental changes across the Mid Cenomanian Event in the tropical Atlantic Ocean (Demerara Rise, ODP Leg 207) inferred from benthic foraminiferal assemblages. *Mar. Micropaleontol.* 71 (1–2), 28–40.
- Friedrich, O., Voigt, S., Kuhn, T., Koch, M.C., 2011. Repeated bottom-water oxygenation during OAE 2: timing and duration of short-lived benthic foraminiferal repopulation events (Wunstorf, northern Germany). *J. Micropaleontol.* 30 (2), 119–128.
- Fütterer, D., Kuhn, G., Schenke, H.W., 1990. Wegener Canyon bathymetry and results from rock dredging near ODP Sites 691–693, eastern Weddell Sea, Antarctica. *Proc. Ocean Drill. Program Sci. Results* 113, 39–48.
- García-Reyes, M., Sydeman, W.J., Schoeman, D.S., Rykaczewski, R.R., Black, B.A., Smit, A.J., Bograd, S.J., 2015. Under pressure: climate change, upwelling, and eastern boundary upwelling ecosystems. *Fron. Mar. Sci.* 2 (109), 1–10.
- Giraldo-Gómez, V.M., Beik, I., Podlaha, O.G., Mutterlose, J., 2018. A paleoenvironmental analyses of benthic foraminifera from Upper Cretaceous–lower Paleocene oil shales of Jordan. *Cretac. Res.* 91, 1–13.
- Goody, A.J., 2003. Benthic foraminifera (Protista) as tools in deep-water palaeoceanography: Environmental influences on faunal characteristics. In: Southward, A.J., Tyler, P.A., Young, C.M., Fuiman, L.A. (Eds.), *Advances in Marine Biology*, vol. 46. Academic Press, London, UK, pp. 3–90.
- Goody, A.J., Jorissen, F., Levin, L.A., Middelburg, J.J., Naqvi, S.W.A., Rabalais, N.N., Zhang, J., 2009. Historical records of coastal eutrophication-induced hypoxia. *Biogeosciences* 6 (8), 1707–1745.
- Gréselle, B., Pittet, B., Mattioli, E., Joachimski, M., Barbarin, N., Riquier, L., Pucéat, E., 2011. The Valanginian isotope event: a complex suite of paleoenvironmental perturbations. *Palaeogeogr. Palaeoclimatol. Palaeoecol.* 306 (1–2), 41–57.
- Hammer, O., Harper, D.A.T., Ryan, P.D., 2001. PAST: paleontological statistics software package for education and data analysis. *Palaeontol. Electronica.* 4 (1), p4.
- Hart, M.B., 1991. The Late Cenomanian calcispher global bioevent. *Proc. Ussher Soc.* 7 (4), 413–417.
- Hart, M.B., Fitzpatrick, M.E.J., 1995. Kimmeridgian paleoenvironments; a micropaleontological perspective. *Proc. Ussher Soc.* 8, 433.
- Hinz, K., Krause, W., 1982. The continental margin of Queen Maud Land/Antarctica: Seismic sequences, structural elements and geological development. *Reihe E. Geol. Jahrb.* 23, 17–41.
- Holbourn, A.E., Kaminski, M.A., 1994. Lower Cretaceous benthic foraminifera from DSDP and ODP sites of the Indian Ocean: A review and synthesis. In: *Microfossils and Oceanic Environments. Proceedings of the Symposium on the Ocean Drilling Program and the Marine Biosphere*, Aberystwyth, Wales, pp. 77–90.
- Holbourn, A.E., Kaminski, M.A., 1995a. Valanginian to Barremian benthic foraminifera from ODP site 766 (Leg 123, Indian ocean). *Micropaleontol.* 197–250.
- Holbourn, A.E., Kaminski, M.A., 1995b. Lower Cretaceous benthic foraminifera from DSDP Site 263: micropaleontological constraints for the early evolution of the Indian Ocean. *Mar. Micropaleontol.* 26 (1–4), 425–460.
- Holbourn, A., Kuhn, W., Erbacher, J., 2001a. Benthic foraminifera from lower Albian black shales (Site 1049, ODP Leg 171): evidence for a non “uniformitarian” record. *J. Foraminiferal Res.* 31 (1), 60–74.
- Holbourn, A., Kuhn, W., Soeding, E., 2001b. Atlantic paleobathymetry, paleoproductivity and paleocirculation in the late Albian: the benthic foraminiferal record. *Palaeogeogr. Palaeoclimatol. Palaeoecol.* 170 (3–4), 171–196.
- Jeremiah, J., 2001. A Lower Cretaceous nannofossil zonation for the North Sea Basin. *J. Micropaleontol.* 20 (1), 45–80.
- Jorissen, F.J., 1999. Benthic foraminiferal microhabitats below the sediment-water interface. In: *Modern Foraminifera*. Springer, Dordrecht, pp. 161–179.
- Jorissen, F.J., Destigter, H.C., Widmark, J.G.V., 1995. A conceptual model explaining benthic foraminiferal microhabitats. *Mar. Micropaleontol.* 26, 3–15.
- Jorissen, F.J., Fontanier, C., Thomas, E., 2007. Paleocceanographical proxies based on deep-sea benthic foraminiferal assemblage characteristics. *Dev. Mar. Geol.* 1, 263–325.
- Kaiho, K., 1994. Benthic foraminiferal dissolved-oxygen index and dissolved-oxygen levels in the modern ocean. *Geology* 22 (8), 719–722.
- Kaiho, K., Hasegawa, T., 1994. End-Cenomanian benthic foraminiferal extinctions and oceanic dyoxic events in the northwestern Pacific Ocean. *Palaeogeogr. Palaeoclimatol. Palaeoecol.* 111 (1–2), 29–43.
- Kaminski, M.A., Boersma, E., Tyszka, J., Holbourn, A.E.L., 1995. Response of deep-water agglutinated foraminifera to dyoxic conditions in the California Borderland basins. *Gzryb Found Spec Pub.* 131–140.
- Kessels, K., Mutterlose, J., Michalzik, D., 2006. Early Cretaceous (Valanginian–Hauterivian) calcareous nannofossils and isotopes of the northern hemisphere: proxies for the understanding of cretaceous climate. *Lethaia.* 39 (2), 157–172.
- Koch, M.C., Friedrich, O., 2012. Campanian–Maastrichtian intermediate- to deep-water changes in the high latitudes: Benthic foraminiferal evidence. *Paleoceanography.* 27, 1–11.
- Koutsoukos, E.A.M., 1989. Mid-to Late Cretaceous Microbiostratigraphy, Palaeo-Ecology and Palaeogeography of the Sergipe Basin, Northeastern Brazil. Ph.D. Thesis University of Plymouth, Plymouth, England, p. 471p.
- Koutsoukos, E.A.M., Hart, M.B., 1990. Cretaceous foraminiferal morphogroup distribution patterns, palaeocommunities and trophic structures: a case study from

- the Sergipe Basin, Brazil. *Earth and Environmental Science Transactions of the Royal Society of Edinburgh*. 81 (03), 221–246.
- Kouwenhoven, T.J., van der Zwaan, G.J., 2006. A reconstruction of late Miocene Mediterranean circulation patterns using benthic foraminifera. *Palaeogeogr. Palaeoclimatol. Palaeoecol.* 238, 373–385.
- Kozdon, R., Kelly, D.C., Kitajima, K., Strickland, A., Fournelle, J.H., Valley, J.W., 2013. In situ  $\delta^{18}\text{O}$  and Mg/calc analyses of diagenetic and planktic foraminiferal calcite preserved in a deep-sea record of the Paleocene-Eocene thermal maximum. *Palaeoceanography*. 28, 517–528.
- Leckie, R.M., 1990. Middle Cretaceous planktonic foraminifera of the Antarctic margin: Hole 693A, ODP Leg 113. *Proc. Ocean Drill. Program Sci. Results* 113, 319–324.
- Littler, K., Robinson, S.A., Bown, P.R., Nederbragt, A.J., Pancost, R.D., 2011. High sea-surface temperatures during the Early Cretaceous Epoch. *Nat. Geosci.* 4 (3), 169.
- Lofaldli, M., Nagy, J., 1980. Foraminiferal stratigraphy of Jurassic deposits on Kongsoya, Svalbard. *Norsk Polarinst. Skr.* 172, 63–96.
- Lowery, C.M., Corbett, M.J., Leckie, R.M., Watkins, D., Romero, A.M., Pramudito, A., 2014. Foraminiferal and nannofossil paleoecology and paleoceanography of the Cenomanian–Turonian Eagle Ford Shale of southern Texas. *Palaeogeogr. Palaeoclimatol. Palaeoecol.* 413, 49–65.
- Martinez, M., Deconinck, J.-F., Pellenard, P., Riquier, L., Company, M., Reboulet, S., Moiroud, M., 2015. Astrochronology of the Valanginian–Hauterivian stages (Early Cretaceous): chronological relationships between the Paraná–Etendeka large igneous province and the Weissert and the Faraoni events. *Glob. Planet. Change*. 131, 158–173.
- Meissner, P., Mutterlose, J., Bodin, S., 2015. Latitudinal temperature trends in the northern hemisphere during the Early Cretaceous (Valanginian–Hauterivian). *Palaeogeogr. Palaeoclimatol. Palaeoecol.* 424, 17–39.
- Möller, C., Mutterlose, J., Alsen, P., 2015. Integrated stratigraphy of lower cretaceous sediments (Ryazanian–Hauterivian) from North-East Greenland. *Palaeogeogr. Palaeoclimatol. Palaeoecol.* 437, 85–97.
- Murray, J.W., 1991. *Ecology and Paleoecology of Benthic Foraminifera*. Longman, Harlow, p. 397.
- Murray, J.W., Alve, E., 1999. Taphonomic experiments on marginal marine foraminiferal assemblages: how much ecological information is preserved? *Palaeogeogr. Palaeoclimatol. Palaeoecol.* 149, 183–197.
- Mutterlose, J., Wise Jr., S.W., 1990. Lower Cretaceous nannofossil biostratigraphy of ODP Leg 113 holes 692b and 693a, continental slope off east Antarctica, Weddell Sea. *Proc. Ocean Drill. Program Sci. Results* 113, 325–353.
- Nyong, E.E., Olsson, R.K., 1984. A paleoslope model of Campanian to lower Maestrichtian foraminifera in the North American basin and adjacent continental margin. *Mar. Micropaleontol.* 8 (6), 437–477.
- O'Brien, C.L., Robinson, S.A., Pancost, R.D., Damste, J.S.S., Schouten, S., Lunt, D.J., Wrobel, N.E., 2017. Cretaceous sea-surface temperature evolution: Constraints from TEX<sub>86</sub> and planktonic foraminiferal oxygen isotopes. *Earth-Sci. Rev.* 172, 224–247.
- O'Connell, S.B., 1990. Sedimentary facies and depositional environment of the Lower Cretaceous East Antarctic margin: sites 692 and 693. *Proc. Ocean Drill. Program Sci. Results* 113, 71–88.
- Owen, H.G., 1983. *Atlas of Continental Displacement, 200 Million Years to the Present*. Cambridge University Press, England, p. 170.
- Racki, G., Cordey, F., 2000. Radiolarian palaeoecology and radiolarites: is the present the key to the past? *Earth-Sci. Rev.* 52 (1–3), 83–120.
- Reolid, M., 2020. Microfossil assemblages and geochemistry for interpreting the incidence of the Jenkyns Event (early Toarcian) in the south-eastern Iberian Palaeomargin (External Subbetic, SE Spain). *J. Micropaleontol.* 39 (2), 233–258.
- Reolid, M., Martínez-Ruiz, F., 2012. Comparison of benthic foraminifera and geochemical proxies in shelf deposits from the Upper Jurassic of the Prebetic (southern Spain). *J. Iber. Geol.* 38 (2), 449–465.
- Reolid, M., Rodríguez-Tovar, F.J., Nagy, J., Olóriz, F., 2008. Benthic foraminiferal morphogroups of mid to outer shelf environments of the Late Jurassic (Prebetic Zone, southern Spain): characterization of biofacies and environmental significance. *Palaeogeogr. Palaeoclimatol. Palaeoecol.* 261 (3–4), 280–299.
- Reolid, M., Chakiri, S., Bejjaji, Z., 2013. Adaptive strategies of the Toarcian benthic foraminiferal assemblages from the Middle Atlas (Morocco): palaeoecological implications. *J. Afr. Earth Sci.* 84, 1–12.
- Reolid, M., Sánchez-Quinónez, C.A., Alegret, L., Molina, E., 2015. Palaeoenvironmental turnover across the Cenomanian–Turonian transition in Oued Bahloul, Tunisia: foraminifera and geochemical proxies. *Palaeogeogr. Palaeoclimatol. Palaeoecol.* 417, 491–510.
- Reolid, M., Duarte, L.V., Rita, P., 2019. Changes in foraminiferal assemblages and environmental conditions during the T-OAE (early Jurassic) in the northern Lusitanian Basin. *Portugal. Palaeogeogr. Palaeoclimatol. Palaeoecol.* 520, 30–43.
- Riccardi, A.C., 1988. *The Cretaceous System of Southern South America*, vol. 168. Geological Society of America (161p).
- Riegraf, W., 1989. Benthonische Schelf-Foraminiferen aus dem Valanginium–Hauterivium (Unterkreide) des Indischen Ozeans südwestlich Madagaskar (Deep Sea Drilling Project Leg 25, Site 249). *Geol. Rundsch.* 78 (3), 1047–1061.
- Robert, C., Maillot, H., 1990. Palaeoenvironments in the Weddell Sea area and Antarctic climates, as deduced from clay mineral associations and geochemical data, ODP Leg 113. *Proc. Ocean Drill. Program Sci. Results* 113, 51–70.
- Rohling, E.J., Jorissen, F.J., De Stigter, H.C., 1997. 200 year interruption of Holocene sapropel formation in the Adriatic Sea. *J. Micropaleontol.* 16 (2), 97–108.
- Rohling, E., Mayewski, P., Abu-Zied, R., Casford, J., Hayes, A., 2002. Holocene atmosphere-ocean interactions: records from Greenland and the Aegean Sea. *Clim. Dyn.* 18 (7), 587–593.
- Roth, P.H., 1983. Jurassic and lower cretaceous calcareous nannofossils in the western North Atlantic (Site 534): biostratigraphy, preservation, and some observations on biogeography and palaeoceanography. In: Sheridan, R.E., Gradstein, F.M. (Eds.), *Init. Reports DSDP 76*. Init. Rep. Deep Sea Drill. Proj. pp. 587–621.
- Royer, D.L., Berner, R.A., Park, J., 2007. Climate sensitivity constrained by CO<sub>2</sub> concentrations over the past 420 million years. *Nature*. 446 (7135), 530–532.
- Rykaczewski, R.R., Dunne, J.P., Sydean, W.J., García-Reyes, M., Black, B.A., Bograd, S. J., 2015. Pole ward intensification of coastal upwelling in response to global warming. *Geophys. Res. Lett.* 42, 6424–6431.
- Scheibnerová, V., 1973. A comparison of the austral and boreal Lower Cretaceous foraminiferal and ostracodal assemblages. In: *Proceedings of the International Symposium on the Boreal Lower Cretaceous (1972)*. Seel House, Liverpool, pp. 407–414.
- Scheibnerová, V., 1976. Cretaceous foraminifera of the Great Australian Basin. *Mem. Geol. Surv. N.S.W.* 17, 1–265.
- Schlanger, S.O., Jenkyns, H.C., 1976. Cretaceous oceanic anoxic events: causes and consequences. *Geol. Mijnb.* 55, 179–184.
- Schmiedl, G., Hemleben, C., Keller, J., Segl, M., 1998. Impact of climatic changes on the benthic foraminiferal fauna in the Ionian Sea during the last 330,000 years. *Palaeoceanography*. 13, 447–458.
- Schmiedl, G., Mitschele, A., Beck, S., Emeis, K.C., Hemleben, C., Schulz, H., Weldeab, S., 2003. Benthic foraminiferal record of ecosystem variability in the eastern Mediterranean Sea during times of sapropel S5 and S6 deposition. *Palaeogeogr. Palaeoclimatol. Palaeoecol.* 190, 139–164.
- Schnack, K., 2000. *Biostratigraphie und fazielle Entwicklung in der Oberkreide und im Altertär im Bereich der Kharga Schwelle, Westliche Wüste, southwest Ägypten*. Ph. D. Thesis Nr. 151. Universität Bremen, Bremen (142 p).
- Scholle, P.A., Wenkam, C.R., 1982. Geological studies of the COST Nos. G-1 and G-2 wells, United States North Atlantic Outer Continental Shelf: Introduction. *Geological Studies of the cost Nos. G-1 and G-2 Wells, US North Atlantic Outer Continental Shelf*, p. 194.
- Scotese, C.R., 2014. *Atlas of Early Cretaceous Paleogeographic Maps, Paleomap Atlas for ArcGIS, volume 2, The Cretaceous, Maps 23-31, Mollweide Projection, Paleomap Project, Evanston, IL*. <https://doi.org/10.13140/2.1.4099.4560>.
- Sen Gupta, B.K., Machain-Castillo, M.L., 1993. Benthic foraminifera in oxygen poor habitats. *Mar. Micropaleontol.* 20, 183–201.
- Sewall, J.V., Van De Wal, R.S.W., van Der Zwan, K., Van Oosterhout, C., Dijkstra, H.A., Scotese, C.R., 2007. Climate model boundary conditions for four cretaceous time slices. *Clim. Past* 3 (4), 647–657.
- Shannon, C.E., Weaver, W., 1949. *The Mathematical Theory of Communication*. University of Illinois Press, Urbana, p. 125.
- Sprovieri, M., Coccioni, R., Lirer, F., Pelosi, N., Lozar, F., 2006. Orbital tuning of a lower Cretaceous composite record (Maiolica Formation, central Italy). *Palaeoceanography*. 21 (4), 1–19.
- Thiede, D.S., Vasconcelos, P.M., 2010. Paraná flood basalts: rapid extrusion hypothesis confirmed by new <sup>40</sup>Ar/<sup>39</sup>Ar results. *Geology* 38 (8), 747–750.
- Thierstein, H.R., 1976. Mesozoic calcareous nannoplankton biostratigraphy of marine sediments. *Mar. Micropaleontol.* 1, 325–362.
- Tyszkaj, J., 1994. Response of Middle Jurassic benthic foraminiferal morphogroups to dyoxic/anoxic conditions in the Pieniny Klippen Basin. *Polish Carpathians. Palaeogeogr. Palaeoclimatol. Palaeoecol.* 110 (1–2), 55–81.
- van der Zwaan, G.J., Duijnste, I.A.P., Den Dulk, M., Ernst, S.R., Jannink, N.T., Kouwenhoven, T.J., 1999. Benthic foraminifera: proxies or problems? A review of paleoecological concepts. *Earth-Sci. Rev.* 46 (1–4), 213–236.
- van Morkhoven, F.P., Berggren, W.A., Edwards, A.S., Oertli, H.J., 1986. *Cenozoic Cosmopolitan Deep-Water Benthic Foraminifera: Bulletin Des Centres de Recherches Exploration-Production Elf-Aquitaine, Pau* (421 p).
- Wahyudi, W., Minagawa, M., 2013. The last 41,000 years fluctuation in Atmospheric CO<sub>2</sub> Concentration Inferred from the changes in Oxygen and Carbon Stable Isotopes Ratios of the Marine Sediment. *Eksplorium*. 33 (1), 15–24.
- Weissert, H., 1989. C-isotope stratigraphy, a monitor of paleoenvironmental change: a case study from the early cretaceous. *Surv. Geophys.* 10 (1), 1–61.
- Weissert, H., Erba, E., 2004. Volcanism, CO<sub>2</sub> and palaeoclimate: a Late Jurassic–Early Cretaceous carbon and oxygen isotope record. *J. Geol. Soc. Lond.* 161, 695–702.
- Westermann, S., Föllmi, K.B., Adatte, T., Matera, V., Schnyder, J., Fleitmann, D., Duchamp-Alphonse, S., 2010. The Valanginian  $\delta^{13}\text{C}$  excursion may not be an expression of a global oceanic anoxic event. *Earth Planet. Sci. Lett.* 290 (1–2), 118–131.
- Wignall, P., Newton, R., 1998. Pyrite framboid diameter as a measure of oxygen deficiency in ancient mudrocks. *Am. J. Sci.* 298, 537–552.
- Wilford, G.E., Brown, P.J., 1994. In: Hill, Robert S. (Ed.), *Maps of Late Mesozoic–Cenozoic Gondwana Break-Up: Some Palaeogeographical Implications. History of the Australian Vegetation: Cretaceous to Recent*. University of Adelaide Press, South Australia, pp. 5–13.
- Zinsmeister, W.J., 1987. Cretaceous paleogeography of Antarctica. *Palaeogeogr. Palaeoclimatol. Palaeoecol.* 59, 197–206.

## 8. Discussions and implications

This Ph.D. thesis studies two paleo-environments under extreme modes of the Mesozoic climate-carbon cycle, identified by the distinct carbon isotope excursions (CIEs) of the Early Jurassic (T-OAE) and the Early Cretaceous (Weissert-Event). The two case studies are used to identify how global perturbations translate into local paleo-environmental responses in the sedimentary record. The settings are (a) restricted shallow (outer shelf/upper margin) environments along nascent/emerging open marine basins (Early Cretaceous Weddell Sea) and (b) deepwater corridors along-shelf seaways (Sogno and Gajum locations in the Early Jurassic Lombardy Basin).

The analytical approach has not been identical for both case studies. The outcomes suggest, however, that the more comprehensive analyses of the Weddell Sea example may serve as a template to advance research on the Italian T-OAE sections and other OAE examples. The power of the Weddell Sea approach lies in the combination and integration of new high-resolution proxy records, including SST and carbon, with other published proxy and geological evidence and advanced climate simulations. This approach not only offers a unifying climate solution consistent with all available evidence but also provides a clue to connect temperature with atmospheric  $p\text{CO}_2$ . The latter relationship is of fundamental importance to ascertain climatic boundary conditions and associated carbon production and burial.

This chapter is composed of two components.

First, an overview (subsections 8.1 and 8.2) of the data generated for the two case studies, summarised in the six independent chapters above, (chapters 2, 3, and 4 for the T-OAE and chapters 5, 6, and 7 for the Early Cretaceous Weissert Event).

Second, a summary that highlights the uniqueness of each case study and the integrated approach (sub-section 8.3), including comparison and integration of both case studies provides recommendations for further research.

### 8.1 The Valanginian (Early Cretaceous) Weissert Event

The data presented in Cavalheiro et al. (2021) (chapter 5) document the first carbon-isotope chemostratigraphy resolving the  $\delta^{13}\text{C}_{\text{org}}$  positive excursion that records the Late Valanginian Weissert Event in the southern hemisphere high latitudes (Weddell Sea, at ODP Site 692). Based on the extremely detailed chemostratigraphic study carried out complemented by nannofossil biostratigraphy, and following the original definition of Erba et al. (2004), precise identification of the beginning and

end of Weissert CIE was achieved. The Weissert Event is subdivided into lower A–B and upper B–C segments, based on the globally documented trends recognized within the Late Valanginian  $\delta^{13}\text{C}$  anomaly.

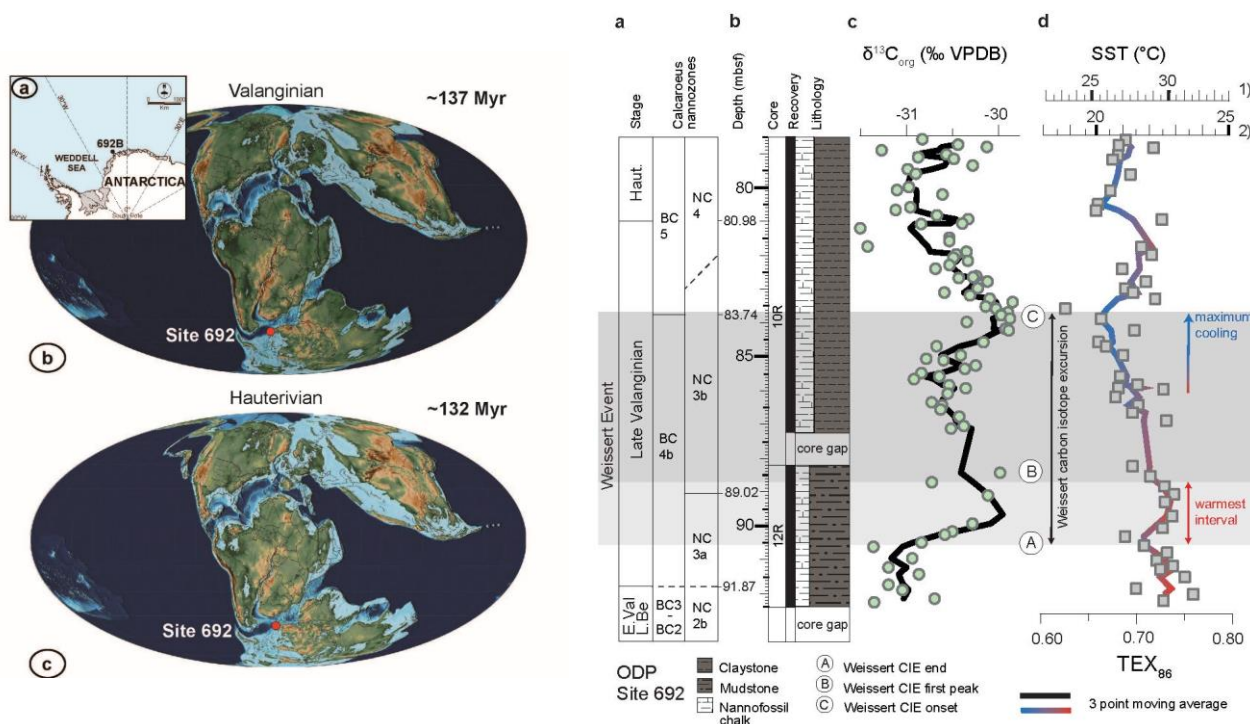


**Fig. 8:** Location of the Ocean Drilling Program (ODP) Site 692 ( $70^{\circ}43.432'S$ ,  $13^{\circ}49.195'W$ ) in the Weddell Sea, Eastern Antarctica, and the paleogeographic reconstruction of the Gondwana continent during the Valanginian and Hauterivian by C.R. Scotese, PALEOMAP project. To the right, chemostratigraphic framing of ODP Site 692 showing stage and calcareous nannofossil zonation (Boreal Realm, BC zonation; Bown et al., 1998. Tethys, NC zonation; Bralower et al., 1995). Depth in meters below seafloor (mbsf), cores (12R and 10R), core recovery, and lithology. Stable carbon isotope record measured on bulk organic matter ( $\delta^{13}\text{C}_{\text{org}}$  with green circles and a black curve reporting the calculated three points moving average) and identification of the Weissert positive carbon isotope excursion (CIE) segments (A, Weissert CIE onset; B, Weissert CIE first peak; C, Weissert CIE end). Organic  $\text{TEX}_{86}$  paleothermometry reporting the calculated three points moving average and the calibration to SSTs in degree  $^{\circ}\text{C}$  showing 1) BAYSPAR and 2) restricted basin calibrations, representing maximum and minimum temperature estimates based on  $\text{TEX}_{86}$ , respectively. Figure from Cavalheiro et al., 2021 (Chapter 5).

OC burial rates and bottom water anoxia linked to the Weissert CIE were investigated by the combination of high-resolution  $\delta^{13}\text{C}$  data, lithostratigraphy, Fe-S-TOC relationships, molecular and redox sensitive trace metal analyses. The new high-resolution TOC record at ODP Site 692 (chapter 6)

shows continuous elevated values of about 6% TOC across the overall Valanginian, consistently with documentation of continuous anoxic to euxinic conditions. During the Valanginian, ODP Site 692 was indeed located in a restricted basin with weak replenishment of water masses due to the high degree of hydrographic and bathymetric isolation of the young Early Cretaceous Southern Ocean, which was overall prone to constantly record high OC burial and preservation rates. Nonetheless, the extremely well preserved marine OM recorded at ODP Site 692, allowed detailed investigation of other geochemical proxies tracking major perturbations linked to the Weissert Event and the main phases preceding and following the Valanginian CIE.

The new data (Cavalheiro et al., 2021; chapter 5) document the first TEX<sub>86</sub>-based evidence of a relevant SST cooling episode coinciding with the end of the Weissert Event in the sub-polar proto-Weddell Sea. The observed cooling (3–4 °C) is consistent with worldwide signals of ocean temperature records, which overall depict a more pronounced temperature response in the most climate sensitive high-latitude regions (polar amplification). The detailed stratigraphic re-analysis of worldwide datasets in Cavalheiro et al. (2021) also indicate that the cooling coinciding with the end of the Weissert CIE is followed by intermittent warming and a second minor cooling period that continues in the earliest Hauterivian. Particularly, the warming interlude coincides with braarudosphaerid-enrichments (Cavalheiro et al., 2021) suggesting temporary salinity lowering possibly triggered by discharges of fresh, deglacial meltwater following the cold Weissert end. Unfortunately, in the Early Cretaceous high-latitude basins, there are yet major discrepancies in global sea level changes and variations in ocean water salinity based on oxygen isotopes (see Charbonnier et al., 2020 review).

Molecular analyses (chapter 6) on bulk organic matter from the black shales recovered at ODP Site 692 revealed a good quality of dominant pelagic marine organic matter, consistently with a kerogen type II/III inferred by Rock-Eval analysis and T<sub>max</sub> values of ~420 °C. Particularly, dominant pelagic organic matter is also in accordance with an estimation of a ~500 m paleo-water depth at ODP Site 692 (Giraldo- Gómez et al., 2021) and palynology data (Mohr et al., 1990) that placed ODP Site 692 well offshore ( $\geq 100$  km from the coastline), based on low percentages of organic terrestrial debris. The extremely well preserved and C-org rich black shales from the Weddell Sea are thus suggested as new reference records for the pelagic Early Cretaceous interval in the sub-Antarctic region. Therefore, chapter 6 of this thesis also presents a new conceptual and temporal framework of the crucial interplay between concurrent global and local factors, which sustained and controlled extreme OC burial rates and fluctuations in the young Berriasian–Barremian and restricted Weddell Sea.

ODP Site 692, in contrast to steady OC contents and/or redox conditions (chapter 6) across the Valanginian, documents a drastic drop in CaCO<sub>3</sub> content and benthic foraminifera (Giraldo- Gómez et

al., 2021.) coinciding with the warmest phase (A–B) of the Weissert Event. Possible bottom water anoxia and/or ocean acidification and warming linked to the onset of the Parana’-Etendeka LIP might explain bottom water anoxia and/or a carbonate decline episode during the Weissert CIE, as documented for the Tethys Ocean (Erba and Tremolada, 2004).

The overall novel and integrated analytical approach adopted in this Ph.D. thesis for the study of past carbon cycle dynamics and climate perturbations are discussed in detail in chapter 5 for the study of the Weissert Event. The integration of the new Weddell Sea data with a compilation of available worldwide multi-proxy-based data was crucial for climate simulations towards one unifying solution, providing a best-fit between all lines of evidence. The outcome confirms a 3 °C ( $\pm 1.7$  °C) global mean surface cooling across the last part of the Weissert Event culminating in the latest Valanginian. In accordance with geochemical proxy estimations (Gröcke et al., 2005), the new climate simulation results suggest that the reconstructed SST cooling at the end of the Weissert Event translates into a ~40% drop in atmospheric  $p\text{CO}_2$ . Notably, based on a solid geologic characterization and climate modelling, the outcome of this study sheds new light on the long-lasting discussion about the potential for polar ice during greenhouse conditions in the Early Cretaceous.

## **8.2 The early Toarcian (Early Jurassic) T-OAE.**

The first description of the drilling operations, complete sedimentology, and chemostratigraphy description of the Sogno and Gajum cores (Southern Alps, northern Italy) were published in Erba et al. (2019b; in press; chapters 2 and 3). The detailed sedimentological characterization of the two cores and subdivisions in defined lithostratigraphic units revealed that drilling at both sites resulted in 100% recovery of unweathered material (Erba et al., 2019b). Both the pelagic successions comprise a relatively expanded interval enriched in organic carbon (OC), the Fish Level, which represents the sedimentary expression of the “Jenkyns Event” within the T-OAE in the Lombardy Basin. The Fish Level consist of ~5m and ~16m in the Sogno and in the Gajum Cores, respectively (Fig. 8) (Erba et al., 2019b).

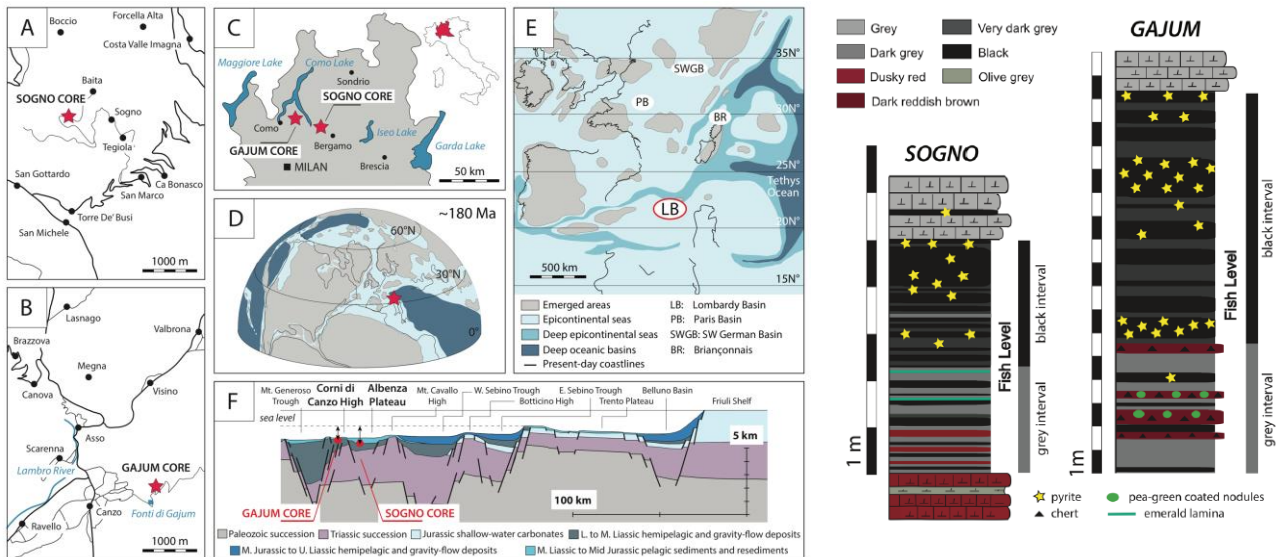


**Fig. 9:** The paleo-locations of the two studied sites are indicated. Panels A and B show the present day location of the Sogno and Gajum drilling sites. C. Present day map of the Lombardy area. D. Paleogeographic location of the studied successions during the Toarcian (~180 Ma) (modified after Scotese, 2011). E. Early Toarcian paleogeographic map of the western Tethys and European epicontinental sea (modified after Fantasia et al., 2019). F. Schematic section across the Lombardy basin during the Toarcian (modified after Erba et al., 2019b). To the right, detailed lithostratigraphy of the Fish Level in the Sogno and Gajum Cores, respectively. Two distinctive parts, namely a lower grey interval and an upper black interval are distinguished. Figures from Erba et al., in press.

A new high-resolution carbon-isotope chemostratigraphy resolves a  $\delta^{13}\text{C}_{\text{carb}}$  negative excursion of ~3‰ at Sogno and ~6‰ at Gajum, and a  $\delta^{13}\text{C}_{\text{org}}$  negative excursion of ~7‰ at both locations (Erba et al., in press). Based on the extremely detailed chemostratigraphic study, within the T-OAE the  $\delta^{13}\text{C}$  negative excursion has been defined as the “Jenkyns Event” further subdivided into a lower J1 and an upper J2 segments, based on the globally documented trends.



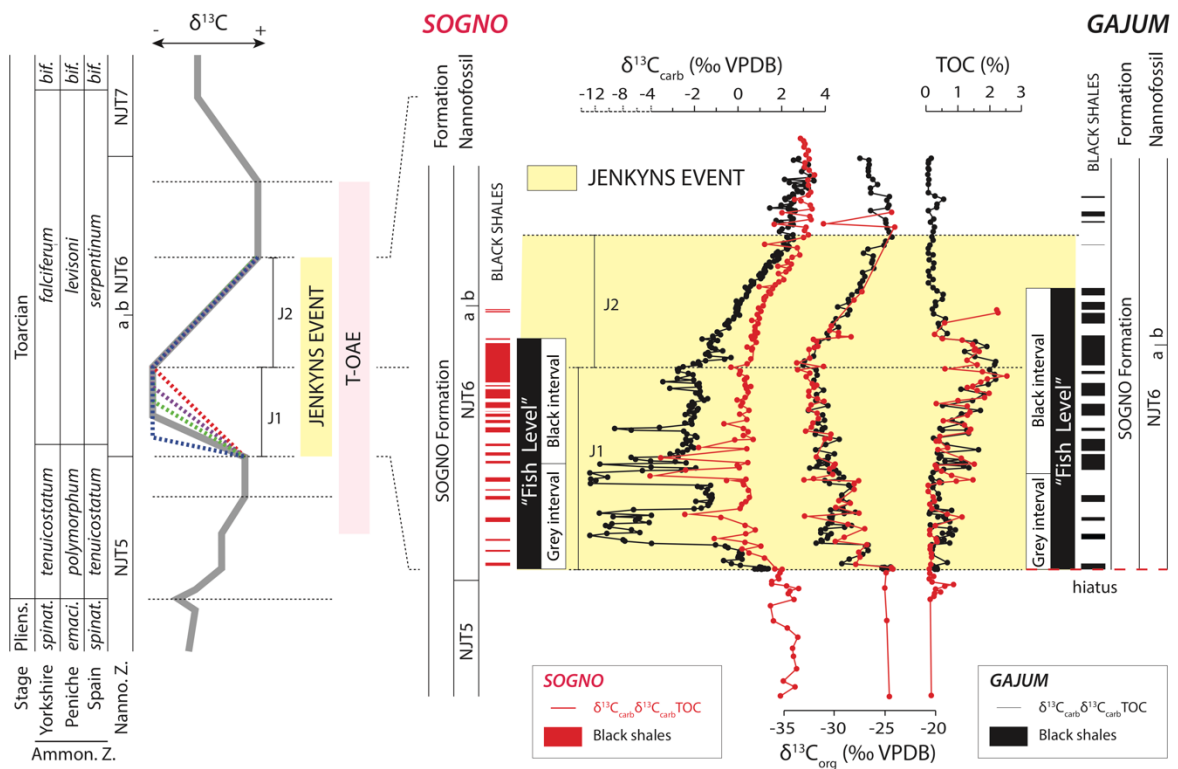


**Fig. 10:** Schematic  $\delta^{13}\text{C}$  reference curve for the latest Pliensbachian–Toarcian time interval (modified after Ruebsam and Al-Husseini (2020), with minor modifications by Hougård et al. 2021). The stratigraphic extent of the T-OAE is indicated with a light red rectangle and a yellow band indicates the proposed interval of the Jenkyns Event, including the lower J1 and the upper J2 segments. Coloured dashed lines in the reference plot represent the different trends documented in the lower part of the Jenkyns Event (J1). On the right, chemostratigraphic correlation of the Sogno and Gajum Cores is based on overlapped  $\delta^{13}\text{C}_{\text{carb}}$  and  $\delta^{13}\text{C}_{\text{org}}$  isotope profiles and TOC data. The extent of the Fish Level and its internal subdivision into a grey interval and a black interval are reported for the two records. Figure from Erba et al., in press.

Organic carbon (OC) burial rates and bottom water anoxia linked to the Jenkyns Event were investigated based on the combination of high-resolution  $\delta^{13}\text{C}$  data, lithostratigraphy, and TOC analyses. Ongoing analyses exploring redox-sensitive trace metals, sulphur content, and specific biomarker compounds have been resulting in the high-resolution characterization of the development of dysoxic-anoxic conditions during the T-OAE and specifically across the Jenkyns Event. Current data document in both the Sogno and Gajum Cores a progressive upward increase in the TOC content, with maxima up to 2.5 % in the uppermost part of the Fish Level (Erba et al., in press). The correlation of the Sogno and Gajum data to other sections showed that the onset of C-org enriched sediments (Fish

Level) was coeval in different basins in the western Tethys, and started at the beginning of the Jenkyns Event. In contrast, the return to more oxygenated bottom waters and the termination of black shale deposition were anachronous, either in long distance or in relatively close-by Tethyan basins, such as the case of the Sogno and Gajum sites. Therefore, it can be concluded that the organic-rich and/or carbonate-poor lithologies (black shales) are anachronous relative to carbon-isotope stratigraphy (Erba et al., in press), as documented in other OAEs (see also discussion in Tsikos et al., 2004 and Kolonic et al., 2005 for OAE2, and Wagner et al., 2013 for OAE3).

Preliminary molecular analyses (chapter 4) on bulk organic matter from the Fish Level of the Sogno Core revealed a good quality of dominant pelagic marine organic matter, consistently with a kerogen type II/III inferred from Rock-Eval analysis and  $T_{\max}$  values of 430–440 °C. Particularly, the investigated sections represent some of the deepest records of the T-OAE in the western Tethyan region, with an estimated paleo-water depth of ~1500 m, and are proposed as new reference sections for the pelagic lower Toarcian interval of the western Tethys. Ongoing analyses aim to further investigate the link between paleoenvironmental and biogeochemical changes using multi-organic and -inorganic proxies to track possible fluctuations in organic matter type, terrestrial input, and nutrient levels.

Consistently with global temperature estimates (e.g., Ruebsam et al., 2020), the new data oxygen-isotope ratios ( $\delta^{18}\text{O}$ ) from Erba et al. (in press) document a progressive shift to lighter values suggestive of warmer paleo-water conditions starting before the deposition of the Fish Level. The lowest oxygen ratios within the Fish Level suggest that the warmest conditions occurred during its deposition in the early Toarcian. The  $\delta^{18}\text{O}$  data indicate a return to higher oxygen isotope values before the end of the black shale interval in the uppermost Fish Level, thus indicating a drop to cooler conditions before the termination of the Jenkyns Event. In order to corroborate and quantify the observed warming and cooling trends, absolute sea surface temperatures (SSTs) reconstructions are planned to be completed using a molecular paleothermometry, based on the  $\text{TEX}_{86}$  proxy (Schouten et al. 2004), both at Sogno and Gajum. The release of high amounts of  $\text{CO}_2$ , presumably related to the degassing of the Karoo–Ferrar LIP (Percival et al., 2015; Heimdal et al., 2021), is interpreted as the trigger of warming associated with the onset of the Jenkyns Event, in addition to extreme paleoenvironmental changes, e.g., biocalcification crisis (Erba, 2004; Mattioli et al., 2004; Casellato and Erba, 2015; Erba et al., 2019a; Reolid et al., 2020), enhanced primary productivity (Erba, 2004; Jenkyns, 2010), and ocean acidification (Erba, 2004; Trecalli et al., 2012; Casellato and Erba, 2015; Posenato et al., 2018). In both the Sogno and Gajum Cores, indeed, the onset of Fish Level is marked by a lower part characterized by minimum  $\text{CaCO}_3$  values (5–10 %), which gradually rise upwards, returning to average values of ~50% above the Fish Level.

Further inorganic and organic geochemical data integrated with available worldwide multi-proxy data compilation and climate model simulations, as discussed below for the Weissert Event study at ODP Site 692, are predicted to result in estimates of temperature-CO<sub>2</sub> relations and changes across the T-OAE.

### **8.3 Implications from this research and future perspectives**

This Ph.D. thesis was designed to study two distinct carbon cycle anomalies evidenced in the carbon isotope record of the Early Jurassic and Early Cretaceous, exploring how such global perturbations translated into local paleo-environmental settings. For both case studies, my specific contribution consisted in geochemical characterization based on C and O stable isotopes, inorganic and organic geochemistry inserted in a solid chronostratigraphic framework to date and measure duration of positive and negative feedback. High-resolution C isotopic chemostratigraphy allowed the univocal definition of the beginning and end of both the T-OAE and the Weissert Event. Moreover, high-resolution integrated bio-chemostratigraphy, changes in OC and CaCO<sub>3</sub> burial/preservation rates, redox conditions, and SSTs in relation to the respective T-OAE and Weissert Event were investigated and paleo-climate modelling was successfully applied. The planned analytical workflow was completed only for the Weissert Event studied at ODP Site 692, due to delays and restrictions during the COVID-19 pandemic. Ongoing integrative geochemical analyses and climate simulations are being carried out for the T-OAE case study.

Some unique features of the two study sites are presented below emphasising the uniqueness of this study compared to the wider literature.

#### Early Cretaceous Weddell Sea

- The study of the Weissert Event is carried out in an understudied, subpolar and restricted basin. This presents a different perspective to the common data available for the Valanginian CIE as well as other global OAEs, which are studied in open marine settings, where OC records are much lower in content and quality, in addition to being usually restricted only to the interval of the CIE.
- ODP Site 692 was drilled in a relatively outer shelf/upper continental margin environment (~500 m paleo-water depth) presenting a rather unique geochemical expression of the Weissert Event, closely connected to surface ocean processes.
- The Weddell Sea record offers the unique opportunity to explore an extended OC record encompassing the entire Weissert CIE, and especially the precedent and following phases.

- This research finds that the restricted setting of the Early Cretaceous Southern Ocean shows that the Weddell Basin was continuously prone to produce high rates and well preserved OC during the Valanginian, consistently with evidence of persistent anoxia-euxinia. Therefore, OC burial rates and redox proxies were not specifically used in this case study to explore the response of the Weissert Event in the proto-Weddell Sea. Instead, the exceptional preservation of high OM levels allowed detailed paleo-environmental investigations based on organic geochemistry proxies, exploring in high-resolution  $\delta^{13}\text{C}_{\text{org}}$  chemostratigraphy,  $\text{TEX}_{86}$ -based SSTs, and biomarker records.
- The design and application of a new integrated approach integrating modelling and multi-proxy data compilation for the Weissert event case-study, which is largely decoupled from uncertainties and limitations of individual proxy results.

#### Early Jurassic deep settings in the Lombardy Basin

- The study of the T-OAE in the Sogno and Gajum cores, consistently with Western Tethys records, documents moderate OC accumulation and preservation rates even during the peak of the Jenkyns Event compared to other coeval worldwide Toarcian records (Jenkyns, 2010).
- These pelagic sections recorded from deep (1000-1500 m) pelagic settings of the Western Tethys, explore in large detail the link of carbon-chemostratigraphy with the gradual onset of bottom water anoxia in an originally well-oxygenated environment. These deep-water sections are significantly more expanded compared to the neighboring shallow shelf settings, and therefore provide an unprecedented record of redox and carbon burial change of the T-OAE perturbation in the Western Tethys.
- The new records confirm a culmination of more extreme depositional conditions towards the end of the Toarcian negative CIE (namely the Jenkyns Event), as documented in the OC-rich Fish Level interval.

#### Comparison and integration of both case studies

- Both case studies emphasize that basin physiography plays a major role in controlling OC rates even across the global carbon cycle and climate perturbations.
- Both case studies document that the  $\delta^{13}\text{C}$  signals of global perturbations and associated environmental variables are well registered even in the local sedimentary record of restricted and/or deep marine basins. This has been demonstrated showing proxy variations in ocean temperatures, drastic changes in carbonate chemistry, and the biologic response.

- The applied approach, integrating modelling and multi-proxy data compilation, as shown for the Weissert Event case study, demonstrates an innovative way forward to decouple uncertainties and limitations of individual proxy results and locations from regional to global scale interpretations. The T-OAE case study represents an excellent example to apply the conceptual framework established for the Early Cretaceous Weissert perturbation. The foundation for such study is well prepared through this research project.
- More emphasise should be made in understanding temperature/ $p\text{CO}_2$  relationships based on multi-proxy data and modelling to evaluate processes, rates, and dimensions of climate and environmental change back in time, setting boundaries for projecting future climate and environmental response.

---

## 9. References

1. Abramovich, S., Keller, G., Stüben, D., Berner, Z., 2003. Characterization of late Campanian and Maastrichtian planktonic foraminiferal depth habitats and vital activities based on stable isotopes. *Palaeogeography, Palaeoclimatology, Palaeoecology* 202 (1–2), 1–29.
2. Arthur, M.A., Natland, J.H., 1979. Carbonaceous sediments in the North and South Atlantic: the role of salinity in stable stratification of Early Cretaceous Basins. In: Talwani, M., Hay, W.W., Ryan, W.B.F. (Eds.), *Deep Drilling Results in the Atlantic Ocean: Continental Margins and Paleoenvironment*. American Geophysical Union, Washington DC (USA) 375–401.
3. Alley, N. F., Hore, S. B., Frakes, L. A., 2020. Glaciations at high-latitude Southern Australia during the Early Cretaceous. *Australian Journal of Earth Sciences* 67(8) 1045–1095.
4. Bachan, A., van de Schootbrugge, B., Fiebig, J., McRoberts, C.A., Ciarapica, G., Payne, J.L., 2012. Carbon cycle dynamics following the end-Triassic mass extinction: Constraints from paired  $\delta^{13}\text{C}_{\text{carb}}$  and  $\delta^{13}\text{C}_{\text{org}}$  records. *Geochemistry, Geophysics, Geosystems* 13 (9).
5. Bartolini, A., Bonnot A., Chateau-Smith, C., Collin, P.Y., Enay, R., Fortwengler, D., et al., 2013. Integrated stratigraphy of some key Callovian-Oxfordian boundary sections in South-East France. Contribution to the choice of the Global Boundary Stratotype Section and Point (GSSP) of the Oxfordian Stage. Field guide 2013 – Oxfordian GSSP Workshop 30<sup>th</sup> September–2<sup>nd</sup> October 2013. *Groupe Français d' Etude Jurasique* 79.
6. Beckmann, B., Flögel, S., Hofmann, P., Schulz, M., Wagner, T., 2005. Orbital forcing of Cretaceous river discharge in tropical Africa and ocean response. *Nature* 437, 241–244.
7. Behrooz, L., Naafs, B. D. A., Dickson, A. J., Love, G. D., Batenburg, S. J., Pancost, R. D., 2018. Astronomically driven variations in depositional environments in the South Atlantic during the Early Cretaceous. *Paleoceanography and Paleoclimatology* 33, 894–912.
8. Berner, R. A., 2006. GEOCARBSULF: a combined model for Phanerozoic atmospheric O<sub>2</sub> and CO<sub>2</sub>. *Geochimica et Cosmochimica Acta* 70 (23), 5653–5664.
9. Bornemann, A., Mutterlose, J., 2008. Calcareous nannofossil and  $\delta^{13}\text{C}$  records from the Early Cretaceous of the Western Atlantic Ocean: evidence for enhanced fertilization across the Berriasian–Valanginian transition. *Palaios* 23 (12), 821–832.
10. Bornemann, A., Erbacher, J., Heldt, M., Kollaske, T., Wilmsen, M., Lübke, N., Huck, S., Vollmar, N. M., Wonik, T., 2017. The Albian–Cenomanian transition and Oceanic Anoxic Event 1d—an example from the boreal realm. *Sedimentology* 64(1), 44–65.
11. Bown, P. R., Rutledge, D. C., Crux, J. A., Gallagher, L. T., 1998. Early Cretaceous. In *Calcareous Nannofossil Biostratigraphy* (ed Bown, P. R.) (Chapman and Hall, Cambridge,) 86–131.

12. Bralower, T. J., Leckie, R. M., Sliter, W. V., Thierstein, H. R., 1995. An integrated Cretaceous microfossil biostratigraphy. In *Geochronology, Time Scales and Global Stratigraphic Correlation* (eds Berggren W. A., Kent D. V., Aubry M.-P. and Hardenbol J.), Special Publication Society of Economic Paleontologists and Mineralogists 54, 65–79.
13. Cavalheiro, L., Wagner, T., Steinig, S., Bottini, C., Dummann, W., Esegbue, O., Gambacorta, G., Giraldo-Gómez, V., Farnsworth, A., Flögel, S., Hofmann, P., Lunt, D. J., Rethemeyer, J., Torricelli, S., Erba, E., 2021. Impact of global cooling on Early Cretaceous high  $p\text{CO}_2$  world during the Weissert Event. *Nature communications* 12 (1), 1–11.
14. Casellato, C. E., Erba, E., 2015. Calcareous nannofossil biostratigraphy and paleoceanography of the Toarcian Oceanic Anoxic Event at Colle di Sogno (Southern Alps, Northern Italy). *Rivista Italiana di Paleontologia e Stratigrafia* 105 343–376.
15. Channell, J. E. T., Erba, E., Lini, A., 1993. Magnetostratigraphic calibration of the Late Valanginian carbon isotope event in pelagic limestones from Northern Italy and Switzerland. *Earth and Planetary Science Letters* 118 (1–4) 145–166.
16. Channell, J.E., Erba, E., Nakanishi, M., Tamaki, K., 1995. Late Jurassic-Early Cretaceous time scales and oceanic magnetic anomaly block models. In *Geochronology, Time Scales and Global Stratigraphic Correlation* (eds Berggren W.A., Kent D.V., Aubry M.-P. and Hardenbol J.), Special Publication Society of Economic Paleontologists and Mineralogists 54, 51–63.
17. Charbonnier, G., Duchamp-Alphonse, S., Deconinck, J. F., Adatte, T., Spangenberg, J. E., Colin, C., Föllmi, K. B., 2020. A global palaeoclimatic reconstruction for the Valanginian based on clay mineralogical and geochemical data. *Earth-Science Reviews* 202, 103092.
18. Cohen, A. S., Coe, A. L., Harding, S. M., Schwark, L., 2004. Osmium isotope evidence for the regulation of atmospheric  $\text{CO}_2$  by continental weathering. *Geology* 32 (2), 157–160.
19. Gradstein, F. M., Ogg, J. G., 2012. *The Geologic Time Scale*. Elsevier.
20. Gradstein, F. M., Ogg, J. G., Schmitz, M. D., Ogg, G. M., 2020. *The Geologic Time Scale*. Elsevier.
21. Dal Piaz G., 1907. *Le Alpi Feltrine*. Memorie del Reale Istituto Veneto di Scienze Lettere ed Arti 27, 1–176.
22. de Assis Janasi, V., de Freitas, V.A., Heaman, L.H., 2011. The onset of flood basalt volcanism, Northern Paraná Basin, Brazil: a precise U–Pb baddeleyite/zircon age for a Chapecó-type dacite. *Earth and Planetary Science Letters* 302 (1–2), 147–153.
23. Dera, G., Brigaud, B., Monna, F., Laffont R., Pucéat, E., Deconinck, J. F., Pellenard, P., Joachimski, M. M., Durllet, C., 2011. Climatic ups and downs in a disturbed Jurassic world. *Geology* 39 (3), 215–218.

24. Dickson, A. J., Jenkyns, H. C., Porcelli, D., van den Boorn, S., Idiz, E., 2016. Basin-scale controls on the molybdenum-isotope composition of seawater during Oceanic Anoxic Event 2 (Late Cretaceous). *Geochimica et Cosmochimica Acta* 178, 291–306.
25. Dickson, A. J., Saker-Clark, M., Jenkyns, H. C., Bottini, C., Erba, E., Russo, F., Gorbanenko, O., Naafs, B. D., Pancost, R. D., Robinson, S. A., Van den Boorn, S. H., 2017. A Southern Hemisphere record of global trace-metal drawdown and orbital modulation of organic-matter burial across the Cenomanian–Turonian boundary (Ocean Drilling Program Site 1138, Kerguelen Plateau). *Sedimentology* 64 (1), 186–203.
26. Dodd, S. C., Mac Niocaill, C., Muxworthy, A. R., 2015. Long duration (> 4 Ma) and steady-state volcanic activity in the early Cretaceous Paraná–Etendeka Large Igneous Province: new palaeomagnetic data from Namibia. *Earth and Planetary Science Letters* 414, 16–29.
27. Donnadieu, Y., Pucéat, E., Moiroud, M., Guillocheau, F. and Deconinck, J.F., 2016. A better-ventilated ocean triggered by Late Cretaceous changes in continental configuration. *Nature communications* 7 (1), 1–12.
28. Dromart, G., Garcia, J. P., Gaumet, F., Picard, S., Rousseau, M., Atrops, F., Lecuyer, C., Sheppard, S. M., 2003. Perturbation of the carbon cycle at the Middle/Late Jurassic transition: geological and geochemical evidence. *American Journal of Science* 303(8), 667–707.
29. Dumann, W., Steinig, S., Hofmann, P., Flögel, S., Osborne, A.H., Frank, M., Herrle, J.O., Bretschneider, L., Sheward, R.M., Wagner, T., 2020. The impact of Early Cretaceous gateway evolution on ocean circulation and organic carbon burial in the emerging South Atlantic and Southern Ocean basins. *Earth Planet Science Letters* 530, 115890.
30. Dumann, W., Steinig, S., Hofmann, P., Lenz, M., Kusch, S., Flögel, S., Herrle, J.O., Hallmann, C., Rethemeyer, J., Kasper, H.U., Wagner, T., 2021. Driving mechanisms of organic carbon burial in the Early Cretaceous South Atlantic Cape Basin (DSDP Site 361). *Climate of the Past* 17 (1), 469–490.
31. Erba, E., 1994. Nannofossils and superplumes: the early Aptian “nannoconid crisis”. *Paleoceanography* 9 (3), 483–501.
32. Erba, E., Bartolini, A., Larson, R. L., 2004. Valanginian Weissert oceanic anoxic event. *Geology* 32 (2), 149–152.
33. Erba, E., Tremolada, F., 2004. Nannofossil carbonate fluxes during the Early Cretaceous: Phytoplankton response to nutrification episodes, atmospheric CO<sub>2</sub>, and anoxia. *Paleoceanography* 19 (1).
34. Erba, E., Bottini, C., Faucher, G., Gambacorta, G., Visentin, S., 2019a. La risposta del nannoplancton calcareo agli Eventi Anossici Oceanici: il record pelagico in Italia [The response of



- calcareous nannoplankton to Oceanic Anoxic Events: The Italian pelagic record]. In Symposium on Environmental Crises and Biotic Responses in the History of the Earth-An Italian Perspective at the Congress of the Italian-Paleontological-Society (SPI). Società Paleontologica Italiana 58 (1), 51–71.
35. Erba, E., Gambacorta, G., Visentin, S., Cavalheiro, L., Reolon, D., Faucher, G., Pegoraro, M., 2019b. Coring the sedimentary expression of the early Toarcian Oceanic Anoxic Event: new stratigraphic records from the Tethys Ocean. *Scientific Drilling* 26, 17–27.
36. Erbacher, J., Thurow, J., Littke, R., 1996. Evolution patterns of radiolaria and organic matter variations: A new approach to identify sea-level changes in mid-Cretaceous pelagic environments. *Geology* 24 (6), 499–502.
37. Fantasia, A., Föllmi, K.B., Adatte, T., Bernàrdez, E., Spangenberg, J.E., and Mattioli, E., 2018. The Toarcian Oceanic Anoxic Event in southwestern Gondwana: an example from the Andean Basin, northern Chile. *Journal of the Geological Society* 175, 883–902.
38. Foster, G. L., Royer, D. L., Lunt, D. J., 2017. Future climate forcing potentially without precedent in the last 420 million years. *Nature communications* 8 (1), 1–8.
39. Gaetani, M., Poliani, G., 1978. Il Toarciano ed il Giurassico medio in Albenza. *Rivista Italiana di Paleontologia e Stratigrafia* 91, 295–320.
40. Gill, B. C., Lyons, T. W., Jenkyns, H. C., 2011. A global perturbation to the sulfur cycle during the Toarcian Oceanic Anoxic Event. *Earth and Planetary Science Letters* 312(3–4), 484–496.
41. Gomes, M. L., Hurtgen, M. T., Sageman, B. B., 2016. Biogeochemical sulfur cycling during Cretaceous oceanic anoxic events: A comparison of OAE1a and OAE2. *Paleoceanography* 31 (2), 233–251.
42. Gómez, J. J., Comas-Rengifo, M. J., Goy, A., 2016. Palaeoclimatic oscillations in the Pliensbachian (Early Jurassic) of the Asturian Basin (Northern Spain). *Climate of the Past* 12 (5), 1199–1214.
43. Grabowski, J., Bakhmutov, V., Kdýr, Š., Krobicki, M., Pruner, P., Reháková, D., Schnabl, P., Stoykova, K., Wierzbowski, H., 2019. Integrated stratigraphy and palaeoenvironmental interpretation of the Upper Kimmeridgian to Lower Berriasian pelagic sequences of the Velykyi Kamianets section (Pieniny Klippen Belt, Ukraine). *Palaeogeography, Palaeoclimatology, Palaeoecology* 532, 109216.
44. Gröcke, D. R., Price, G. D., Robinson, S. A., Baraboshkin, E. Y., Mutterlose, J., Ruffell, A. H., 2005. The Upper Valanginian (Early Cretaceous) positive carbon-isotope event recorded in terrestrial plants. *Earth and Planetary Science Letters* 240 (2), 495–509.

45. Haq, B. U., Hardenbol, J. A. N., Vail, P. R., 1987. Chronology of fluctuating sea levels since the Triassic. *Science* 235 (4793), 1156–1167.
46. Hardenbol, J. A. N., Thierry, J., Farley, M. B., Jacquin, T., De Graciansky, P. C., Vail, P. R., 1998. Mesozoic and Cenozoic sequence chronostratigraphic framework of European basins. In: de Graciansky, P.-C., Hardenbol, J., Jacquin T., Vail, P.R. (Eds), *Mesozoic and Cenozoic sequence stratigraphy of European basins*. Society for Sedimentary Geology (SEPM), Special Publication, 889 (60), 3–13, Tulsa, Oklahoma.
47. Heimdal, T. H., Godd eris, Y., Jones, M. T., Svensen, H. H., 2021. Assessing the importance of thermogenic degassing from the Karoo Large Igneous Province (LIP) in driving Toarcian carbon cycle perturbations. *Nature communications* 12 (1), 1–7.
48. Hesselbo, S. P., Gr ocke, D., Jenkyns, H. C., Bjerrum, C.J., Farrimond, P., Bell, H. S. M., Green, O. R., 2000. Massive dissociation of gas hydrate during a Jurassic oceanic anoxic event. *Nature* 406, 392–395.
49. Hesselbo, S. P., Jenkyns, H. C., Duarte, L. V., Oliveira, L. C., 2007. Carbon-isotope record of the Early Jurassic (Toarcian) Oceanic Anoxic Event from fossil wood and marine carbonate (Lusitanian Basin, Portugal). *Earth and Planetary Science Letters* 253 (3–4), 455–470.
50. Hofmann, P., Wagner, T., 2011. ITCZ controls on Late Cretaceous black shale sedimentation in the tropical Atlantic Ocean. *Paleoceanography and Paleoclimatology* 26 (4).
51. Holmden, C., Jacobson, A. D., Sageman, B. B., Hurtgen, M. T., 2016. Response of the Cr isotope proxy to Cretaceous Ocean Anoxic Event 2 in a pelagic carbonate succession from the Western Interior Seaway. *Geochimica et Cosmochimica Acta* 186, 277–295.
52. Houg ard, I. W., Bojesen-Koefoed, J. A., Vickers, M. L., Ullmann, C. V., Bjerrum, C. J., Rizzi, M., Korte, C., 2021. Redox element record shows that environmental perturbations associated with the T-OAE were of longer duration than the carbon isotope record suggests—the Aubach section, SW Germany. *Newsletters on Stratigraphy* 54 (2), 229–246.
53. Jarvis, I., Mabrouk, A., Moody, R. T., de Cabrera, S., 2002. Late Cretaceous (Campanian) carbon isotope events, sea-level change and correlation of the Tethyan and Boreal realms. *Palaeogeography, Palaeoclimatology, Palaeoecology* 188 (3–4), 215–248.
54. Jenkyns, H. C., 1985. The Early Toarcian and Cenomanian-Turonian anoxic events in Europe: comparisons and contrasts. *Geologische Rundschau* 74 (3), 505–518.
55. Jenkyns, H., 1988. The early Toarcian (Jurassic) anoxic event-stratigraphic, sedimentary, and geochemical evidence. *American Journal of Science* 288 (2), 101–151.

56. Jenkyns, H. C., 2003. Evidence for rapid climate change in the Mesozoic–Palaeogene greenhouse world. *Philosophical Transactions of the Royal Society of London. Series A: Mathematical, Physical and Engineering Sciences* 361 (1810), 1885–1916.
57. Jenkyns, H. C., 2010. Geochemistry of oceanic anoxic events. *Geochemistry, Geophysics, Geosystems* 11, Q03004.
58. Jenkyns, H. C., Gale, A. S., Corfield, R. M., 1994. Carbon-and oxygen-isotope stratigraphy of the English Chalk and Italian Scaglia and its palaeoclimatic significance. *Geological Magazine* 131 (1), 1–34.
59. Katz, M. E., Wright, J. D., Miller, K. G., Cramer, B. S., Fennel, K., Falkowski, P. G., 2005. Biological overprint of the geological carbon cycle. *Marine Geology* 217 (3–4), 323–338.
60. Kolonic, S., Wagner, T., Forster, A., Sinnighe Damsté, J.S., Waslworth-Bell, B., Erba, E., Turgeon, S., Brumsack, H.-J., Chellai, E.H., Tsikos, H., Kuhnt, W., Kuypers, M.M.M., 2005. Black shale deposition on the northwest African Shelf during the Cenomanian//Turonian oceanic anoxic event: Climate coupling and global organic carbon burial. *Paleoceanography*, 20, PA1006.
61. Korte, C., Hesselbo, S. P., 2011. Shallow marine carbon and oxygen isotope and elemental records indicate icehouse-greenhouse cycles during the Early Jurassic. *Paleoceanography* 26, PA4219.
62. Kuypers, M. M., Pancost, R. D., Nijenhuis, I. A., Sinninghe Damsté, J. S., 2002. Enhanced productivity led to increased organic carbon burial in the euxinic North Atlantic basin during the late Cenomanian oceanic anoxic event. *Paleoceanography* 17 (4), 3–1.
63. Leckie, R. M., Bralower, T. J., Cashman, R., 2002. Oceanic anoxic events and plankton evolution: Biotic response to tectonic forcing during the mid-Cretaceous. *Paleoceanography* 17 (3), 13–1.
64. Lini, A., Weissert, H., Erba, E., 1992. The Valanginian carbon isotope event: a first episode of greenhouse climate conditions during the Cretaceous. *Terra Nova* 4 (3), 374–384.
65. Louis-Schmid, B., Rais, P., Bernasconi, S.M., Pellenard, P., Collin, P.Y., Weissert, H., 2007. Detailed record of the mid-Oxfordian (Late Jurassic) positive carbon-isotope excursion in two hemipelagic sections (France and Switzerland): A plate tectonic trigger? *Palaeogeography, Palaeoclimatology, Palaeoecology* 248 (3–4), 459–472.
66. Louis-Schmid, B., 2006. Feedback mechanisms between carbon cycling, climate and oceanography: a combined geochemical, sedimentological and modeling approach (Doctoral dissertation, ETH Zurich).
67. Lu, Z., Jenkyns, H. C., Rickaby, R. E., 2010. Iodine to calcium ratios in marine carbonate as a paleo-redox proxy during oceanic anoxic events. *Geology* 38 (12), 1107–1110.

68. Lunt DJ, Farnsworth A, Loptson C, Foster GL, Markwick P, O'Brien CL, Pancost RD, Robinson SA, Wrobel N., 2016. Palaeogeographic controls on climate and proxy interpretation. *Climate of the Past* 12 (5), 1181–1198.
69. Malinverno, A., Hildebrandt, J., Tominaga, M., Channell, J. E., 2012. M-sequence geomagnetic polarity time scale (MHTC12) that steadies global spreading rates and incorporates astrochronology constraints. *Journal of Geophysical Research: Solid Earth* 117(B6).
70. Mattioli, E., Pittet, B., Palliani, R., Röhl, H. J., Schmid-Röhl, A., Morettini, E., 2004. Phytoplankton evidence for the timing and correlation of palaeoceanographical changes during the early Toarcian oceanic anoxic event (Early Jurassic). *Journal of the Geological Society* 161 (4), 685–693.
71. McElwain, J. C., Wade-Murphy, J., Hesselbo, S. P., 2005. Changes in carbon dioxide during an oceanic anoxic event linked to intrusion into Gondwana coals. *Nature* 435 (7041), 479–482.
72. Mercuzot, M., Pellenard, P., Durlet, C., Bougeault, C., Meister, C., Dommergues, J.L., Thibault, N., Baudin, F., Mathieu, O., Bruneau, L., Huret, E., 2020. Carbon-isotope events during the Pliensbachian (Lower Jurassic) on the African and European margins of the NW Tethyan Realm. *Newsletters on Stratigraphy* 53, 41–69.
73. Meyer, K.M., Kump, L.R., 2008. Oceanic euxinia in Earth history: causes and consequences. *Annual Reviews Earth Planet Sciences* 36, 251–288.
74. Miller, K. G., 2009. Broken greenhouse windows. *Nature Geoscience* 2 (7), 465–466.
75. Mohr B. A. R., 1990. Early Cretaceous palynomorphs from ODP Sites 692 and 693, the Weddell Sea, Antarctica. In *Proceedings Ocean Drilling Program Scientific Results* 113, 325–351.
76. Montoya-Pino, C., Weyer, S., Anbar, A. D., Pross, J., Oschmann, W., van de Schootbrugge, B., Arz, H. W., 2010. Global enhancement of ocean anoxia during Oceanic Anoxic Event 2: A quantitative approach using U isotopes. *Geology* 38 (4), 315–318.
77. Morettini, E., Santantonio, M., Bartolini, A., Cecca, F., Baumgartner, P.O., Hunziker, J.C., 2002. Carbon isotope stratigraphy and carbonate production during the Early–Middle Jurassic: examples from the Umbria–Marche–Sabina Apennines (central Italy). *Palaeogeography, Palaeoclimatology, Palaeoecology* 184 (3–4), 251–273.
78. Mutterlose, J., Wise, S. W., 1990. Lower Cretaceous nannofossil biostratigraphy of ODP Leg 113 Holes 692B and 693A, continental slope off East Antarctica, Weddell Sea. In *Proceedings of Ocean Drilling Program (ODP) Scientific Results* 113, 325–351.
79. Müller T., Price G.D., Bajnai D, Nyerges A., Kesjár D., Raucsik B., Varga A., Judik K., Fekete J., May Z., Pálffy J., 2017. New multiproxy record of the Jenkyns Event (also known as the Toarcian

- Oceanic Anoxic Event) from the Mecsek Mountains (Hungary): Differences, duration and drivers. *Sedimentology* 64 (1), 66–86.
80. Nielsen, S. G., Goff, M., Hesselbo, S. P., Jenkyns, H. C., LaRowe, D. E., Lee, C. T. A., 2011. Thallium isotopes in early diagenetic pyrite—A paleoredox proxy? *Geochimica et Cosmochimica Acta* 75 (21), 6690–6704.
81. O'Brien C. L., Robinson S. A., Pancost R. D., Damsté J. S., Schouten S., Lunt D. J., Alsenz H., Bornemann A., Bottini C. Brassell S. C., Farnsworth A., 2017. Cretaceous sea-surface temperature evolution: Constraints from TEX86 and planktonic foraminiferal oxygen isotopes. *Earth-Science Reviews* 172, 224–247.
82. O'Dogherty, L., Sandoval, J., Bartolini, A., Bruchez, S., Bill, M., Guex, J., 2006. Carbon–isotope stratigraphy and ammonite faunal turnover for the Middle Jurassic in the Southern Iberian palaeomargin. *Palaeogeography, Palaeoclimatology, Palaeoecology* 239 (3–4), 311–333.
83. Ogg, J. G., Ogg, G. M., Gradstein, F. M., 2016. *A Concise Geologic Time Scale*. Elsevier.
84. Oliveira, L. C. V., Rodrigues, R., Duarte, L. V., Lemos, V., 2006. Avaliação do potencial gerador de petróleo e interpretação paleoambiental com base em biomarcadores e isótopos estáveis do carbono da seção Pliensbaquiano-Toarciano inferior (Jurássico inferior) da região de Peniche (Bacia Lusitânica, Portugal). *Boletim de Geociências da Petrobras* 14 (2) 207–234.
85. Owens J. D., Gill B. C., Jenkyns H. C., Bates S. M., Severmann S., Kuypers M. M., Woodfine R. G., Lyons T.W., 2013. Sulfur isotopes track the global extent and dynamics of euxinia during Cretaceous Oceanic Anoxic Event 2. *Proceedings of the National Academy of Sciences* 110 (46), 18407–18412.
86. Owens, J. D., Lyons, T. W., Hardisty, D. S., Lowery, C. M., Lu, Z., Lee, B., Jenkyns, H. C., 2017. Patterns of local and global redox variability during the Cenomanian–Turonian Boundary Event (Oceanic Anoxic Event 2) recorded in carbonates and shales from central Italy. *Sedimentology* 64 (1), 168–185.
87. Padden, M., Weissert, H., Funk, H., Schneider, S., Gansner, C., 2002. Late Jurassic lithological evolution and carbon-isotope stratigraphy of the western Tethys. *Eclogae Geologicae Helvetiae* 95 (3), 333–346.
88. Pálffy, J., Smith, P. L., 2000. Synchrony between Early Jurassic extinction, oceanic anoxic event, and the Karoo-Ferrar flood basalt volcanism. *Geology* 28 (8), 747–750.
89. Pearce, C. R., Cohen, A. S., Coe, A. L., Burton, K. W., 2008. Molybdenum isotope evidence for global ocean anoxia coupled with perturbations to the carbon cycle during the Early Jurassic. *Geology* 36 (3), 231–234.

90. Percival, L. M. E., Witt, M. L. I., Mather, T. A., Hermoso, M., Jenkyns, H. C., Hesselbo, S. P., Al-Suwaidi, A. H., Storm, M. S., Xu, W., Ruhl, M., 2015. Globally enhanced mercury deposition during the end-Pliensbachian extinction and Toarcian OAE: A link to the Karoo–Ferrar Large Igneous Province. *Earth and Planetary Science Letters* 428, 267–280.
91. Percival, L. M., Cohen, A. S., Davies, M. K., Dickson, A. J., Hesselbo, S. P., Jenkyns, H. C., Leng, M. J., Mather, T. A., Storm, M. S., Xu, W., 2016. Osmium isotope evidence for two pulses of increased continental weathering linked to Early Jurassic volcanism and climate change. *Geology* 44 (9), 759–762.
92. Posenato, R., Bassi, D., Trecalli, A., Parente, M., 2018. Taphonomy and evolution of Lower Jurassic lithiotid bivalve accumulations in the Apennine Carbonate Platform (southern Italy). *Palaeogeography, Palaeoclimatology, Palaeoecology* 489, 261–271.
93. Premoli Silva, I., Erba, E., Salvini, G., Locatelli, C., Verga, D., 1999. Biotic changes in Cretaceous oceanic anoxic events of the Tethys. *The Journal of Foraminiferal Research* 29 (4), 352–370.
94. Price, G. D., Nunn, E. V., 2010. Valanginian isotope variation in glendonites and belemnites from Arctic Svalbard: Transient glacial temperatures during the Cretaceous greenhouse. *Geology* 38(3), 251–254.
95. Price, G. D., Janssen, N. M., Martinez, M., Company, M., Vandeveld, J. H., Grimes, S. T., 2018. A High-Resolution Belemnite Geochemical Analysis of Early Cretaceous (Valanginian–Hauterivian) Environmental and Climatic Perturbations. *Geochemistry, Geophysics, Geosystems* 19 (10), 3832–3843.
96. Rais, P., Louis-Schmid, B., Bernasconi, S. M., Weissert, H., 2007. Palaeoceanographic and palaeoclimatic reorganization around the Middle–Late Jurassic transition. *Palaeogeography, Palaeoclimatology, Palaeoecology* 251(3–4), 527–546.
97. Remírez, M. N., Algeo, T. J., 2020. Carbon-cycle changes during the Toarcian (Early Jurassic) and implications for regional versus global drivers of the Toarcian oceanic anoxic event. *Earth-Science Reviews* 103283.
98. Reolid, M., Mattioli, E., Duarte, L. V., Marok, A., 2020. The Toarcian Oceanic Anoxic Event and the Jenkyns Event (IGCP-655 final report). *Episodes* 43(2), 833–844.
99. Retallack, G. J., 2009. Greenhouse crises of the past 300 million years. *Geological Society of America Bulletin* 121(9–10), 1441–1455.
100. Robert, C., 1987. Clay mineral associations and structural evolution of the South Atlantic: Jurassic to Eocene. *Palaeogeography Palaeoclimatology. Palaeoecology* 58, 87–108.
101. Robinson, S. A., Heimhofer, U., Hesselbo, S. P., Petrizzo, M. R., 2017. Mesozoic climates and oceans—a tribute to Hugh Jenkyns and Helmut Weissert. *Sedimentology* 64 (1), 1–15.

102. Roth, P. H., Bowdler, J. L., 1979. Evolution of the calcareous nannofossil genus *Micula* in the Late Cretaceous. *Micropaleontology*, 272–280.
103. Roth, P. H. Jurassic and Lower Cretaceous calcareous nannofossils in the western North Atlantic (Site 534): biostratigraphy, preservation, and some observations on biogeography and palaeoceanography. In *Initial Reports Deep Sea Drilling Project 76*, 587–621.
104. Ruebsam, W., Mayer, B., Schwark, L., 2019. Cryosphere carbon dynamics control early Toarcian global warming and sea level evolution. *Global and Planetary Change* 172, 440–453.
105. Ruebsam, W., Al-Husseini, M., 2020. Calibrating the Early Toarcian (Early Jurassic) with stratigraphic black holes (SBH). *Gondwana Research* 82, 317–336.
106. Sandoval, J., O'Dogherty, L., Aguado, R., Bartolini, A., Bruchez, S., Bill, M., 2008. Aalenian carbon-isotope stratigraphy: calibration with ammonite, radiolarian and nannofossil events in the Western Tethys. *Palaeogeography, Palaeoclimatology, Palaeoecology* 267 (1–2), 115–137.
107. Sandoval, J., Bill, M., Aguado, R., O'Dogherty, L., Rivas, P., Morard, A., Guex, J., 2012. The Toarcian in the Subbetic basin (southern Spain): Bio-events (ammonite and calcareous nannofossils) and carbon-isotope stratigraphy. *Palaeogeography, Palaeoclimatology, Palaeoecology* 342, 40–63.
108. Schlanger, S.O., Jenkyns, H.C., 1976. Cretaceous oceanic anoxic events: causes and consequences. *Geologie en Mijnbouw* 55, 179–184.
109. Solomon, S., Plattner, G.-K., Knutti, R., Friedlingstein, P., 2009. Irreversible climate change due to carbon dioxide emissions, *Proceedings of the national academy of sciences* 106 (6), 1704–1709.
110. Scotese, C.R., 201. Map Folio 29, Early Cretaceous (Hauterivian, 132.0 Ma) doi:10.13140/2.1.1284.1768.
111. Sprovieri, M., Coccioni, R., Lirer, F., Pelosi, N., Lozar, F., 2006. Orbital tuning of a lower Cretaceous composite record (Maiolica Formation, central Italy). *Paleoceanography*, 21(4).
112. Steinhorsdottir, M., Vajda, V., 2015. Early Jurassic (late Pliensbachian) CO<sub>2</sub> concentrations based on stomatal analysis of fossil conifer leaves from eastern Australia. *Gondwana Research* 27 (3), 932–939.
113. Sucheras-Marx, B., Giraud, F., Fernandez, V., Pittet, B., Lecuyer, C., Olivero, D., Mattioli, E., 2013. Duration of the Early Bajocian and the associated  $\delta^{13}\text{C}$  positive excursion based on cyclostratigraphy. *Journal of the Geological Society* 170 (1), 107–118.
114. Svensen, H., Planke, S., Chevallier, L., Malthe-Sørenssen, A., Corfu, F., Jamtveit, B., 2007. Hydrothermal venting of greenhouse gases triggering Early Jurassic global warming. *Earth and Planetary Science Letters* 256 (3–4), 554–566.

115. Them, T. R., Gill, B. C., Selby, D., Gröcke, D. R., Friedman, R. M., Owens, J. D., 2017. Evidence for rapid weathering response to climatic warming during the Toarcian Oceanic Anoxic Event. *Scientific reports* 7 (1), 1–10.
116. Thiede, D.S., Vasconcelos, P.M., 2010. Paraná flood basalts: rapid extrusion hypothesis confirmed by new  $^{40}\text{Ar}/^{39}\text{Ar}$  results. *Geology* 38 (8), 747–750.
117. Trecalli, A., Spangenberg, J., Adatte, T., Föllmi, K. B., Parente, M., 2012. Carbonate platform evidence of ocean acidification at the onset of the early Toarcian oceanic anoxic event. *Earth and Planetary Science Letters* 357, 214–225.
118. Tsikos, H., Jenkyns, H.C., Walsworth-Bell, B., Petrizzo, M.R., Forster, A., Kolonic, S., Erba, E., Premoli-Silva, I., Baas, M., 2004. Carbon-isotope stratigraphy recorded by the Cenomanian-Turonian Oceanic Anoxic Event: correlation and implications based on three key localities. *Journal of the Geological Society-London* 162 (3), 5761–5761.
119. Van de Schootbrugge, B., Bailey, T.R., Rosenthal, Y., Katz, M.E., Wright, J.D., Miller, K.G., Feist- Burkhardt, S., Falkowski, P.G., 2005. Early Jurassic climate change and the radiation of organic-walled phytoplankton in the Tethys Ocean. *Paleobiology* 31, 73–97.
120. Van de Schootbrugge, B., Payne, J. L., Tomasovych, A., Pross, J., Fiebig, J., Benbrahim, M., Föllmi, K.B., Quan, T. M., 2008. Carbon cycle perturbation and stabilization in the wake of the Triassic-Jurassic boundary mass-extinction event. *Geochemistry, Geophysics, Geosystems* 9(4).
121. Wagner, T., Pletsch, T., 1999. Tectono-sedimentary controls on Cretaceous black shale deposition along the opening Equatorial Atlantic Gateway (ODP Leg 159). *Geological Society, London, Special Publications* 153 (1), 241–265.
122. Wagner, T., Hofmann, P., Flögel, S., 2013. Marine black shale deposition and Hadley Cell dynamics: A conceptual framework for the Cretaceous Atlantic Ocean. *Marine and Petroleum Geology* 43, 222–238.
123. Wagreich, M., Hu, X., Wang, C., Scott, R.W., Jansa, L., 2009. Coniacian-Santonian oceanic red beds and their link to Oceanic Anoxic Event 3. In *Cretaceous Oceanic Red Beds: Stratigraphy, Composition, Origins, and Paleooceanographic and Paleoclimatic Significance*. Society Economic of Paleontologists and Mineralogists, Special Publication 91, 235–242.
124. Wagreich, M., 2012. "OAE 3"—regional Atlantic organic carbon burial during the Coniacian–Santonian. *Climate of the Past* 8 (5), 1447–1455.
125. Weissert, H., 2000. Deciphering methane's fingerprint. *Nature* 406 (6794), 356–357.
126. Weissert, H., Channell, J. E. T., 1989. Tethyan carbonate carbon isotope stratigraphy across the Jurassic-Cretaceous boundary: An indicator of decelerated global carbon cycling? *Paleoceanography* 4 (4), 483–494.



127. Weissert, H., Lini, A., Föllmi, K. B., Kuhn, O., 1998. Correlation of Early Cretaceous carbon isotope stratigraphy and platform drowning events: a possible link? *Palaeogeography, Palaeoclimatology, Palaeoecology* 137 (3–4), 189–203.
128. Weissert, H., Erba, E., 2004. Volcanism, CO<sub>2</sub> and palaeoclimate: a Late Jurassic–Early Cretaceous carbon and oxygen isotope record. *Journal of the Geological Society* 161(4), 695–702.
129. Westermann, S., Föllmi, K.B., Adatte, T., Matera, V., Schnyder, J., Fleitmann, D., Fiet, N., Ploch, I., Duchamp-Alphonse, S., 2010. The Valanginian  $\delta^{13}\text{C}$  excursion may not be an expression of a global oceanic anoxic event. *Earth and Planetary Science Letters* 290 (1–2), 118–131.
130. Westermann, S., Vance, D., Cameron, V., Archer, C., Robinson, S. A., 2014. Heterogeneous oxygenation states in the Atlantic and Tethys oceans during Oceanic Anoxic Event 2. *Earth and Planetary Science Letters* 404, 178–189.
131. Zhou, X., Jenkyns, H.C., Owens, J.D., Junium, C.K., Zheng, X.Y., Sageman, B.B., Hardisty, D.S., Lyons, T.W., Ridgwell, A., Lu, Z., 2015. Upper ocean oxygenation dynamics from I/Ca ratios during the Cenomanian-Turonian OAE2. *Paleoceanography* 30 (5), 510–526.